U.PORTO

FEUP FACULDADE DE ENGENHARIA
UNIVERSIDADE DO PORTO

*Master's Dissertation*

# Simulation of Micro-Scale Failure of Composite Materials: On the Interplay between Bulk and Interface Fracture Mechanisms

Miguel Filipe Ribeiro Campos Monteiro

*Supervisor:*
Dr. Igor Lopes

*Co-Supervisor:*
Eng. Guilherme Gonçalves

Master in Mechanical Engineering

Dissertation submitted to the Faculty of Engineering of the University of Porto in fulfilment of the requirements for the degree of Master in Mechanical Engineering

Porto, September 2025

CM2S

Computational Multi-Scale
Modeling of Solids and Structures

# Simulation of Micro-Scale Failure of Composite Materials: On the Interplay between Bulk and Interface Fracture Mechanisms

**Miguel Filipe Ribeiro Campos Monteiro**

## Abstract

The accurate prediction of failure in composite structures is of great relevance in aerospace and aeronautics. In this context, multi-scale approaches for modelling the structural performance of composites under extreme loading scenarios and in the presence of material and geometrical nonlinearities allow relating the global mechanical response with underlying physical phenomena occurring at lower length-scales. In these approaches, the microstructure of fibre-reinforced polymers (FRP) may be modelled using Representative Volume Elements (RVE), which encapsulate the mechanical properties of its material phases, and account for several damage mechanisms, such as matrix cracking, and fibre breakage. However, crack growth in the presence of an interface depends on the interaction between bulk damage and interfacial failure mechanisms, influencing fracture toughness, crack patterns, and overall failure modes. To tackle this issue, a promising computational modelling approach lies in the combination of cohesive zone models (CZM) and phase-field (PF) fracture. The Park-Paulino-Roesler (PPR) potential-based CZM offers a detailed representation of interfacial damage, where traction-separation laws (TSL) dictate the nucleation and propagation of cracks along material interfaces. Conversely, phase-field models are continuous, energy-based approaches that represent cracks as diffuse fields within a thermodynamically consistent framework, and are well-suited for capturing complex crack propagation in the bulk, without the need to define the crack path a priori. Recently, a phase field - cohesive zone model (PF-CZM) approach was introduced, which embeds a cohesive TSL directly into the PF formulation, while decoupling the length-scale from material strength, therefore unifying bulk and interface fracture in a single, variationally consistent model. By combining these two methods, it is possible to simultaneously model bulk and interfacial failure mechanisms, while addressing the interplay between them and its effects on the overall material response.

In this work, parametric studies of the PPR cohesive formulation illustrate the flexibility of this model to represent mode I, II, and mixed mode fracture at the macro-scale, while highlighting the critical influence of material parameters. In addition, phase-field benchmarks expose the sensitivity of the model to the regularisation length-scale and to the solver strategy. Within a finite element framework, the fracture response of composite microstructures is then assessed in this dissertation using a traditional approach based solely on cohesive zone elements, which is systematically compared with a phase-field formulation, as well as with a combined phase-field and cohesive zone elements approach. Overall, the hybrid approach achieved the best compromise between accuracy and computational cost for the models analysed. These findings highlight the potential for hybrid modelling approaches in the multi-scale analysis of structural failure in engineering components.

To enable the integration of cohesive elements within the composite RVEs, a dedicated Python preprocessing routine is improved to automatically pre-insert cohesive elements between different material phases, and within the bulk material in RVEs. This tool provides a flexible and essential foundation for generating the microstructural models for FRPs, and conducting the required parametric studies.

**Keywords:** Heterogeneous materials, Multi-scale, Finite element method, Finite strains, Cohesive zone model, Phase-field fracture models

# Simulação de Falhas na Microescala de Materiais Compósitos: Sobre a Interação entre Mecanismos de Fractura no Contínuo e na Interface

**Miguel Filipe Ribeiro Campos Monteiro**

## Resumo

A previsão precisa de falhas em estruturas em compósito assume particular relevância na indústria aeroespacial e aeronáutica. Neste contexto, abordagens multi-escala para modelar o comportamento estrutural de compósitos sujeitos a cenários de carregamento extremo e na presença de não-linearidades materiais e geométricas permitem relacionar a resposta mecânica global com fenómenos físicos subjacentes que ocorrem em escalas de comprimento inferiores. Nestas abordagens, a microestrutura de materiais compósitos de polímeros reforçados por fibras (FRP) pode ser modelada através de Elementos de Volume Representativo (RVE), os quais encapsulam as propriedades mecânicas das suas fases materiais e consideram vários mecanismos de dano, como fissuração da matriz e rotura de fibras. Contudo, o crescimento de uma fissura na presença de uma interface depende da interação entre os mecanismos de dano no contínuo e de falha na interface, influenciando a tenacidade à fratura, os padrões de fissura e os modos de fratura. Para abordar esta questão, uma estratégia computacional promissora assenta na combinação de modelos de zona coesiva (CZM) e de campo de fase (PF) para fratura. O modelo coesivo, baseado num potencial, de Park-Paulino-Roesler (PPR) proporciona uma representação detalhada do dano interfacial, onde as leis de tração-separação (TSL) determinam a nucleação e propagação de fissuras ao longo das interfaces materiais. Por outro lado, os modelos de campo de fase para fratura são abordagens contínuas, termodinamicamente consistentes e baseadas em energia, que representam as fissuras como campos difusos, sendo adequados para capturar a propagação de fissuras complexas no contínuo sem necessidade de definir antecipadamente o percurso da fissura. Recentemente, modelo de campo de fase com formulação coesiva foi introduzido, o qual incorpora diretamente uma lei TSL coesiva na formulação do modelo de campo de fase, desacoplando o comprimento de escala do modelo PF da resistência do material, e combinando assim a fratura de contínuo e de interface num único modelo variacionalmente consistente. Ao combinar estes dois métodos, é possível modelar simultaneamente os mecanismos de falha no contínuo e na interface, abordando a interação entre estes e os seus efeitos na resposta global do material.

Neste trabalho, estudos paramétricos da formulação coesiva de PPR demonstram a flexibilidade deste modelo para representar fratura em modo I, modo II e modo misto à escala macro, evidenciando a influência crítica dos parâmetros materiais. Por outro lado, os testes de campo de fase revelaram a elevada sensibilidade do modelo ao parâmetro de comprimento de regularização e à estratégia numérica do *solver*. No âmbito de um modelo de elementos finitos, o comportamento de fratura de FRPs é investigado nesta dissertação recorrendo-se a uma abordagem tradicional, baseada exclusivamente em elementos de zona coesiva, a qual é comparada sistematicamente com uma abordagem de campo de fase, bem como com uma abordagem mista de campo de fase e elementos de zona coesiva. No geral, a abordagem híbrida registou o melhor compromisso entre precisão e custo computacional para os modelos analisados, destacando o seu potencial para a análise multi-escala de fratura em componentes de engenharia.

Para viabilizar a inclusão de elementos coesivos nos RVEs de compósitos, uma rotina de pré-processamento em Python é aperfeiçoada, capaz de inserir automaticamente elementos coesivos entre distintas fases materiais e no interior do volume dos RVEs. Esta ferramenta fornece uma base flexível para gerar os modelos microestruturais de FRPs e conduzir os estudos paramétricos.

**Palavras-chave:** Materiais heterogéneos, Multi-escala, Método de elementos finitos, Deformações finitas, Modelo de zona coesiva, Métodos de campo de fase para fratura

# Agradecimentos

Procuro com as seguintes palavras de agradecimento reforçar o contributo daqueles que ajudaram direta ou indiretamente no desenvolvimento e na escrita desta dissertação, na forma de sugestões, revisões e de apoio moral, sempre bem vindo. Assim, gostaria de destacar alguns nomes.

Em primeiro lugar, manifesto a minha profunda gratidão ao meu supervisor, Dr. Igor Lopes, pela sua constante disponibilidade na partilha de conhecimento e pelos conselhos decisivos que desbloquearam fases mais complexas do trabalho desenvolvido. Ao meu co-supervisor, Eng. Guilherme Gonçalves, expresso igualmente um agradecimento pela sua prontidão em orientar cada fase do projeto, da resolução das dúvidas mais simples às questões burocráticas, pelas suas muitas sugestões práticas e pelo apoio contínuo no decorrer deste longo processo. A ambos, agradeço ainda a compreensão e paciência demonstradas quando conciliei este trabalho académico com um estágio profissional não relacionado com o projeto, e pela flexibilidade na adaptação do calendário e tarefas do projeto que tornou possível conciliar ambos os compromissos e avançar sem obstáculos para as metas traçadas.

À minha família, que me acompanhou desde o início do percurso académico, agradeço todas as palavras de conforto e inspiração determinantes para que levasse a cabo a escrita desta dissertação. Em especial, aos meus pais, Luís Pedro e Maria Eduarda, dedico este trabalho, por depositarem em mim a sua inabalável confiança e serem um pilar central do meu desenvolvimento pessoal. O seu incentivo e confiança permitiram-me dedicar-me com plena serenidade ao estudo com o rigor exigido pela área da mecânica computacional.

A todos, o meu sincero obrigado,
Miguel Filipe Ribeiro Campos Monteiro

# Contents

**List of Figures** ix

**List of Tables** xiii

**List of Symbols** xv

**1 Introduction** 3
- 1.1 Context . . . 3
- 1.2 Sustainable development . . . 4
- 1.3 Main objective . . . 4
- 1.4 Computational framework . . . 4
- 1.5 Dissertation layout . . . 5
- 1.6 Contributions . . . 6

**2 Continuum mechanics and the finite element method** 7
- 2.1 Kinematics of deformation . . . 7
  - 2.1.1 Motion . . . 7
  - 2.1.2 Material and spatial descriptions . . . 9
  - 2.1.3 Deformation gradient . . . 9
  - 2.1.4 Isochoric and volumetric decomposition of the deformation gradient . . . 10
  - 2.1.5 Polar decomposition of the deformation gradient . . . 10
- 2.2 Strain measures . . . 11
- 2.3 Forces and stress measures . . . 12
  - 2.3.1 The Cauchy stress tensor . . . 13
  - 2.3.2 Deviatoric and hydrostatic stress components . . . 13
  - 2.3.3 First Piola-Kirchhoff stress tensor . . . 14
  - 2.3.4 Second Piola-Kirchhoff stress tensor . . . 14
  - 2.3.5 Kirchhoff stress tensor . . . 14
- 2.4 Fundamental conservation principles . . . 14
  - 2.4.1 Conservation of mass . . . 14
  - 2.4.2 Momentum balance . . . 15
  - 2.4.3 First law of thermodynamics . . . 15
  - 2.4.4 Second law of thermodynamics . . . 15
  - 2.4.5 Clausius-Duhem inequality . . . 16
- 2.5 Constitutive theory . . . 16
  - 2.5.1 Thermodynamics with internal variables . . . 16
  - 2.5.2 The constitutive initial value problem . . . 17
- 2.6 Weak equilibrium equations . . . 18
  - 2.6.1 Spatial description . . . 18
  - 2.6.2 Equivalence between weak and strong equilibrium statements . . . 19
- 2.7 The quasi-static initial boundary value problem . . . 20

2.8 Finite Element Method . . . 21
2.8.1 Domain spatial discretisation . . . 21
2.8.2 Discretisation of the equilibrium equations . . . 22
2.8.3 Time discretisation . . . 23
2.8.4 Incremental finite element solution . . . 23
2.8.5 Gaussian quadrature . . . 24

**3 Cohesive zone model for fracture** **27**
3.1 Introduction to the cohesive zone model . . . 27
3.2 On the use of CZMs to model interface and bulk fracture . . . 28
3.3 CZM for the onset and propagation of fracture . . . 28
3.3.1 Boundary value problem . . . 29
3.3.2 Finite element formulation . . . 29
3.3.3 Kinematics of the interface model . . . 30
3.3.4 Constitutive cohesive model . . . 35

**4 Phase-Field** **45**
4.1 Introduction to fracture and continuum damage . . . 45
4.2 A generalised formulation for phase-field fracture . . . 46
4.2.1 Kinematics . . . 46
4.2.2 Differential form of the Griffith thermodynamic balance . . . 47
4.2.3 Variational form of the Griffith thermodynamic balance . . . 47
4.2.4 Crack surface density function . . . 47
4.2.5 Geometric crack function . . . 48
4.2.6 Energy degradation function . . . 49
4.2.7 Total internal energy density . . . 49
4.2.8 Principle of virtual work and balance of forces . . . 50
4.2.9 Damage irreversibility . . . 51
4.3 Weak statement of the phase-field model and finite element discretisation . . . 51
4.3.1 Finite element discretisation of the phase-field equation . . . 52
4.4 Phase-field formulations of interest . . . 54
4.4.1 Hyperelastic constitutive model . . . 54
4.4.2 AT1 phase-field model . . . 55
4.4.3 AT2 phase-field model . . . 56
4.4.4 PF-CZM phase-field model . . . 56

**5 Preprocessing routine for cohesive element insertion** **59**
5.1 Problem statement . . . 59
5.2 Software architecture . . . 60
5.2.1 Implementation workflow . . . 60
5.2.2 Enforcement of periodic boundary conditions . . . 60
5.3 Legacy implementation . . . 61
5.4 Benchmark validation example . . . 61

**6 Numerical applications in fracture mechanics** **67**
6.1 Influence of the cohesive material properties . . . 67
6.2 Influence of the PF-CZM fracture material properties . . . 74
6.3 Comparison between AT2 and PF-CZM fracture models . . . 76
6.4 Comparison between the cohesive zone model and the phase-field fracture model . . . 78

**7 Micro-scale analysis of damage in FRPs** **85**
7.1 Introduction to micro-scale models . . . 85
7.1.1 Representative volume element . . . 85
7.1.2 Boundary conditions . . . 86
7.2 Numerical applications . . . 87
7.2.1 Mesh convergence study . . . 87
7.2.2 Initial studies with PF + intCZM FRP fracture . . . 92
7.2.3 Parametric study of FRP fracture with PF + intCZM and dynamics . . . 97
7.2.4 Parametric study of FRP fracture with allCZM + intCZM and dynamics . . . 112

**8 Conclusions** **119**
8.1 Future works . . . 120

**A Energy decompositions for the phase-field models** **121**
A.1 Standard formulation . . . 121
A.2 Volumetric-deviatoric energy split . . . 122
A.3 Spectral energy split . . . 122

**B Exponential softening curves for the damage models** **125**
B.1 PPR potential approximation . . . 125

**C Rayleigh damping** **127**

**Bibliography** **129**

# List of Figures


2.1 Generic deformation of a tri-dimensional body. Taken from Rodrigues Lopes et al. (2018). . . . . 7

3.1 Schematic representation of six cohesive elements with respective node displacements defined in the local coordinate system. The white circles in the middle lines/planes represent the position of the middle plane nodes. Taken from Vieira de Carvalho (2023). 31
3.2 Schematic representation of the three modes of fracture. Taken from Vieira de Carvalho (2023). . . . . 35
3.3 Schematic representation of the PPR cohesive zone model (traction-separation curves) for different values of the normal and tangential shape parameter, $\alpha$ and $\beta$, respectively. Taken from Vieira de Carvalho (2023). . . . . 41

4.1 Schematic representation of an arbitrary body with a discrete or a diffuse crack. Taken from Gonçalves (2024). . . . . 46
4.2 Crack profiles for various geometric crack functions. Taken from Wu (2024). . . . . 49

5.1 Mean runtime per execution (ten trials) for each script version and mesh type. . . . . 63
5.2 Boxplot distributions of the ten trial runtimes for each script version and mesh type. . 63
5.3 Homogenised stress against prescribed deformation gradient component $\boldsymbol{F}_{xx}$, for each script version and mesh type. . . . . 64
5.4 Deformed configurations (scale factor of 10) of the RVEs after preprocessing. . . . . 65

6.1 Schematic representation of the two-dimensional patch test presented in Park and Paulino (2012) and employed in the cohesive zone model benchmark. The COH2D4 cohesive element is in light green, with zero thickness at the beginning of the analyses, while the two TRI3 continuum elements are in light blue. . . . . 67
6.2 Deformed configuration at the final prescribed displacement of $7.5 \cdot 10^{-5}$ m, for a scale factor of 100. . . . . 70
6.3 Results for the two-element mesh, for mode I fracture, varying the values of the PPR cohesive properties. Vertical reaction force against displacement. . . . . 71
6.4 Results for the two-element mesh, for mode II fracture, varying the values of the PPR cohesive properties. Vertical reaction force against displacement. . . . . 72
6.5 Results for the two-element mesh, for mixed-mode fracture, varying the values of the PPR cohesive properties. Vertical reaction force against displacement. . . . . 73
6.6 A quarter of a rectangular plate with a central circular hole, under tensile load. Taken from Gonçalves (2024). . . . . 74
6.7 Phase-field distribution (plotted in the deformed configuration) corresponding to a model with reference PF-CZM material properties, for a load factor of 0.418 (or a prescribed displacement of 0.1672 mm). . . . . 75
6.8 Vertical reaction force curves with the PF-CZM model for the plate with central circular hole, for a linear softening law and varying the values of the fracture properties. . . 77

6.9 Vertical reaction force curves with the AT2 and PF-CZM models for the plate with central circular hole, varying the values of the fracture toughness. The PF-CZM simulation with $G_c = 2.33$ MPa·mm produces a peak load that matches that of the AT2 model. 78
6.10 Schematic representation of the perforated cantilever beam subjected to mode I fracture presented in Verhoosel et al. (2009). The red dashed line represents the plane where the interface elements are placed. Taken from Vieira de Carvalho (2023). . . . . 79
6.11 Finite element mesh for the perforated cantilever beam with zero-thickness cohesive elements inserted in the centre line (highlighted in green colour). The mesh has 26320 TRI6 elements, 160 COH2D6 elements, and 54490 nodes. . . . . 79
6.12 Finite element mesh for the perforated cantilever beam with 28968 TRI6 elements and 59618 nodes. Zero-thickness cohesive elements are inserted in every interface between continuum elements. The mesh has 28968 TRI6 elements, 42602 COH2D6 elements, and 173808 nodes. . . . . 80
6.13 Vertical reaction force curves with the PF-CZM model for the perforated plate: varying the values of the phase-field length-scale (subfigures 1, 2, 3); and running the simulation until the complete failure (subfigure 4). The model with cohesive elements in the center plate line is shown in red, for comparison. Subfigure 4 also presents in yellow the model with cohesive elements inserted everywhere. . . . . 81
6.14 Phase-field distributions (plotted in the deformed configuration) for two length-scales ($l = 0.10$ left, $l = 0.06$ right) at three time instants. . . . . 82

7.1 Schematic representation of the RVE concept and the principle of separation of scales. Taken from Gonçalves (2024). . . . . 86
7.2 Maximum vertical reaction force (squares) and computational time per increment (circles) against the number of nodes. The QUAD4-FBAR model is in blue, while the TRI6 model is in orange. . . . . 89
7.3 Phase-field distribution in the matrix, plotted in the deformed configuration at the end of the simulation (scale factor of 10), of an RVE with QUAD4-FBAR and TRI3 elements for four distinct mesh sizes. . . . . 90
7.4 Phase-field distribution in the matrix, plotted in the deformed configuration at the end of the simulation (scale factor of 10), of an RVE with TRI6 elements for three distinct mesh sizes. . . . . 91
7.5 Homogenised stress-strain curves. . . . . 92
7.6 Finite element mesh for the RVE with zero-thickness cohesive elements inserted between fibre-matrix material interfaces (highlighted in green colour). The mesh has 42136 TRI6 elements, and 1587 COH2D6 elements and 87983 nodes. . . . . 93
7.7 Homogenised stress-strain curves or the initial parametric study of the quadratic *PF + intCZM* RVE, for three distinct values of the cohesive interface strength, $\sigma_{n/t}$. . . . . 94
7.8 Phase-field distribution in the matrix, plotted in the deformed configuration at the end of the simulation (scale factor of 10), of an *PF + intCZM* RVE model with TRI6 continuum elements, for three distinct values of the PPR cohesive strength ($\sigma_{n/t}$): 30, 45, and 60 MPa. . . . . 95
7.9 Homogenised stress-strain curves or the initial parametric study of the quadratic *intCZM* RVE, for three distinct values of the cohesive interface toughness, $\phi_{n/t}$. . . . . 96
7.10 Homogenised stress-strain curves or the initial parametric study of the quadratic *PF + intCZM* RVE, for three distinct values of the cohesive initial slope indicator, $\lambda_{n/t}$. . . 97
7.11 Homogenised stress-strain curves, for the parametric study of the dynamic parameters of the linear *PF + intCZM* RVE model with a cohesive interface strength of 30 MPa: Rayleigh damping (7.11a) and density (7.11b). . . . . 98
7.12 Detailed view of the homogenised stress-strain curves, for the different Rayleigh coefficients of the interface cohesive elements, for the linear *PF + intCZM* RVE model. . . 99

7.13 Homogenised stress-strain curves, for the different values of the initial slope indicator, $\lambda_{n/t}$, of the interface cohesive elements, for the linear *PF + intCZM* RVE model (full lines), in comparison with the quadratic *PF + intCZM* mesh (dashed line). . . . . 100
7.14 Homogenised stress-strain curves, for the parametric study of the cohesive parameters for the quadratic *PF + intCZM* RVE model, for different values of the cohesive strength, $\sigma_{n/t}$, of the interface cohesive elements. Full lines correspond to dynamic formulation, and dashed lines to a quasi-static formulation. . . . . 101
7.15 Phase-field distribution in the matrix and cohesive damage distribution in the fibre-matrix interfaces, plotted in the deformed configuration at the peak response and at the end of the simulation (scale factor of 10), of an *PF + intCZM* RVE model with TRI6 continuum elements, employing two distinct values of the PPR cohesive strength ($\sigma_{n/t}$): 15 and 30 MPa. . . . . 102
7.16 Phase-field distribution in the matrix and cohesive damage distribution in the fibre-matrix interfaces, plotted in the deformed configuration at the peak response and at the end of the simulation (scale factor of 10), of an *PF + intCZM* RVE model with TRI6 continuum elements, employing two distinct values of the PPR cohesive strength ($\sigma_{n/t}$): 45 and 60 MPa. . . . . 103
7.17 Homogenised stress-strain curves, for the parametric study of the cohesive parameters for the quadratic *PF + intCZM* RVE model, for different values of the fracture energy, $\phi n/t$, of the interface cohesive elements. . . . . 104
7.18 Phase-field distribution in the matrix, plotted in the deformed configuration at the peak response and at the end of the simulation (scale factor of 10), of an *PF + intCZM* RVE model with TRI6 continuum elements, for three distinct values of the PPR cohesive strength, $\phi_{n/t}$. . . . . 105
7.19 Homogenised stress-strain curves, for different values of the shape parameters $\alpha$ and $\beta$ of the interface cohesive elements, for the quadratic *PF + intCZM* RVE model. Full lines correspond a PF linear softening law, and dashed lines to a PF exponential softening law. . . . . 106
7.20 Phase-field distribution in the matrix, plotted in the deformed configuration at the peak response and at the end of the simulation (scale factor of 10), of an *PF + intCZM* RVE model with TRI6 continuum elements, for a PPR cohesive strength of 15 MPa and for three distinct combinations of the softening laws. . . . . 107
7.21 Phase-field distribution in the matrix, plotted in the deformed configuration at the peak response and at the end of the simulation (scale factor of 10), of an *PF + intCZM* RVE model with TRI6 continuum elements, for a PPR cohesive strength of 30 MPa and for three distinct combinations of the softening laws. . . . . 108
7.22 Homogenised stress-strain curves, for different values of the cohesive strength of the interface cohesive elements, for the quadratic *intCZM* RVE model (full lines), with respect to the hybrid configuration, *PF + intCZM* (dashed lines). . . . . 109
7.23 Phase-field distribution in the matrix (deformed configuration, scale factor of 10) at the peak response (1 % displacement) and at the end (2 % displacement) of the simulation, of an *intCZM* RVE model with TRI6 continuum elements, for a PPR cohesive strength of 15 MPa and for three distinct values of the PPR cohesive strength ($\sigma_{n/t}$): 15, 45 and 60 MPa. . . . . 111
7.24 Detail of the homogenised stress-strain curves, showing early-increment oscillations for the linear *allCZM + intCZM* RVE model. . . . . 115
7.25 Homogenised stress-strain curves, for different values of the cohesive strength of the interface cohesive elements, for the linear *allCZM + intCZM* RVE model (full lines), in comparison with the *intCZM* models (dashed lines). . . . . 116

7.26 Detail of homogenised stress-strain curves, for the parametric study of the dynamic parameters of the linear *allCZM* + *intCZM* RVE model with a cohesive interface strength of 30 MPa: Rayleigh damping (7.26a) and spectral radius, $\rho_\infty$ (7.26b). Full lines correspond to an incrementation of $15 \cdot 10^{-5}$ and dashed lines to an incrementation of $30 \cdot 10^{-6} + 12 \cdot 10^{-5}$. . . . . 116
7.27 Cohesive damage distribution in the fibre-matrix (green colouring) and matrix-matrix (red colouring) element interfaces, plotted in the deformed configuration at the peak response and at the end of the simulation (scale factor of 10), for an *allCZM* + *intCZM* RVE model with TRI6 continuum elements, employing two distinct values of the PPR cohesive strength ($\sigma_{n/t}$): 15 and 30 MPa. . . . . 117
7.28 Cohesive damage distribution in the fibre-matrix (green colouring) and matrix-matrix (red colouring) interfaces, plotted in the deformed configuration at the peak response and at the end of the simulation (scale factor of 10), for an *PF* + *intCZM* RVE model with TRI6 continuum elements, employing two distinct values of the PPR cohesive strength, $\sigma_{n/t}$, 45 and 60 MPa. . . . . 118

# List of Tables


5.1 Elastic material properties of the fibre, adopted in the comparison study of the current and legacy versions of the cohesive insertion script, adapted from a glass fibre found in Melro et al. (2013b). . . . 62
5.2 Elastic material properties of the matrix, adopted in the comparison study of the current and legacy versions of the cohesive insertion script, adapted from an epoxy matrix found in Melro et al. (2013a). . . . 62
5.3 Cohesive zone model material properties for the cohesive elements, adopted in the comparison study of the current and legacy versions of the cohesive insertion script. . 62
5.4 Descriptive statistics of the preprocessing runtimes extracted for 10 executions of the Python script that inserts cohesive elements in the interfaces of each RVE. Times are reported for current and legacy script versions and for TRI3 and TRI6 meshes. . . . 63

6.1 Elastic material properties of the bulk material. . . . 68
6.2 Constitutive cohesive model input parameters. . . . 68
6.3 Cohesive material properties of the PPR potential-based material. . . . 68
6.4 Elastic properties of the PF-CZM material, adopted in the parametric study of a notched rectangular plate. . . . 74
6.5 Fracture properties of the PF-CZM material, adopted in the parametric study of a notched rectangular plate. . . . 75
6.6 Fracture properties of the PF-CZM material adopted in the comparison study with the AT2 fracture model, for the notched rectangular plate. . . . 76
6.7 Fracture properties of the AT2 material adopted in the comparison study with the PF-CZM fracture model, for the notched rectangular plate. . . . 76
6.9 Cohesive zone model material properties for the cohesive elements, adopted in comparison study between the CZM and PF models, for the perforated cantilever beam. . 80
6.10 Material properties of the PF-CZM material, adopted in comparison study between the CZM and PF models, for the perforated cantilever beam. . . . 81

7.1 Elastic material properties of the fibre, adopted in the mesh convergence study, adapted from a glass fibre found in Melro et al. (2013b). . . . 87
7.2 Elastic and fracture properties of the matrix, for a PF-CZM material, adopted in the mesh convergence study, adapted from an epoxy matrix found in Melro et al. (2013a). 88
7.3 Mesh sizes adopted in the convergence study. . . . 88
7.4 Cohesive zone model material properties for the interface cohesive elements, adopted in the initial simulations in the microstructure study, for a quadratic meshed RVE. . . 93
7.5 Cohesive zone model material properties for the cohesive elements, adopted in the parametric studies of the composite microstructure *PF* + *intCZM* RVE. . . . 99
7.6 Cohesive zone model material properties for the matrix-matrix cohesive elements, adopted in the parametric study of an *allCZM* + *intCZM* RVE model, for a linear meshed RVE. . . . 112

7.7 Cohesive zone model material properties for the fibre-matrix interface cohesive elements, adopted in the parametric study of an *allCZM* + *intCZM* RVE model, for a linear meshed RVE. . . . . 112
7.8 Summary of the comparison between the hybrid configuration (*PF* + *intCZM*) and the fully cohesive zone modelling approach (*allCZM* + *intCZM*) for composite RVE analysis. 115

# List of Symbols

**Acronyms and abbreviations**

| | |
|---|---|
| BC | Boundary condition |
| CFRT | Continuous Fibre-Reinforced Thermoplastic |
| CMSP | Coupled Multi-Scale Problem |
| CPU | Central Processing Unit (processor) |
| CZM | Cohesive Zone Model |
| DoF | Degree of freedom |
| FEM | Finite Element Method |
| MSP | Micro-Scale Problem |
| OPP | Object-Oriented Programming |
| PF | Phase-field |
| RAM | Random Access Memory |
| RVE | Representative Volume Element |

**General Convention**

| | |
|---|---|
| $(\bullet)_0$ | Variable defined in the reference configuration |
| $\mathbf{a}, \mathbf{A}$ | Higher-order tensors |
| $\boldsymbol{A}$ | Second-order tensors |
| $\boldsymbol{a}$ | Vectors |
| $\mathbf{a}, \mathbf{A}$ | Finite elements related arrays (vectors and matrices) |
| $\mathscr{A}$ | Spaces, generic functions |
| $a, A$ | Scalar values |

**Variables**

| | |
|---|---|
| $\mathbf{A}$ | Material tangent modulus in matrix format |
| $\mathbf{a}$ | Spatial tangent modulus in matrix format |
| $\mathbf{A}$ | Material tangent modulus $\partial \boldsymbol{P} / \partial \boldsymbol{F}$ |

| | |
|---|---|
| $\mathbf{a}$ | Spatial tangent modulus |
| $\boldsymbol{\lambda}$ | Lagrange multiplier vector |
| $\boldsymbol{\sigma}$ | Cauchy stress tensor |
| $\boldsymbol{\tau}$ | Kirchhoff stress tensor |
| $\boldsymbol{\theta}$ | Macroscopic set of internal variables |
| $\boldsymbol{\lambda}$ | Nodal Lagrange multiplier vector |
| $\boldsymbol{\varphi}$ | Deformation mapping function |
| $\boldsymbol{\xi}$ | Coordinates in element natural space |
| $\boldsymbol{B}$ | Left Cauchy-Green strain tensor |
| $\boldsymbol{b}$ | External volume force vector in the current configuration |
| $\boldsymbol{C}$ | Right Cauchy-Green strain tensor |
| $\boldsymbol{E}, \boldsymbol{\varepsilon}$ | Strain tensors |
| $\boldsymbol{E}_i$ | Eulerian principal directions |
| $\boldsymbol{e}_i$ | Lagrangian principal directions |
| $\boldsymbol{g}$ | Gap function |
| $\boldsymbol{I}$ | Second-order identity tensor |
| $\boldsymbol{J}$ | Second-order moment of volume, Jacobian matrix |
| $\boldsymbol{N}$ | Unit outward normal vector in the reference configuration |
| $\boldsymbol{n}$ | Unit outward normal vector in the current configuration |
| $\boldsymbol{P}$ | First Piola-Kirchhoff stress tensor |
| $\boldsymbol{R}_0$ | Double traction tensor in the reference configuration |
| $\boldsymbol{r}_0$ | Double tractions in the reference configuration |
| $\boldsymbol{S}$ | Second Piola-Kirchhoff stress tensor |
| $\boldsymbol{s}$ | Deviatoric stress tensor |
| $\boldsymbol{s}_0$ | External line forces in the reference configuration |
| $\boldsymbol{t}$ | External traction vector in the current configuration |
| $\boldsymbol{U}$ | Right stretch tensor |
| $\boldsymbol{u}$ | Displacement vector |
| $\boldsymbol{V}$ | Left stretch tensor |
| $\boldsymbol{v}$ | Velocity vector |
| $\boldsymbol{X}$ | Macroscopic material coordinate |

| | |
|---|---|
| $\boldsymbol{x}$ | Macroscopic spatial coordinate |
| $\boldsymbol{F}$ | Deformation gradient |
| $\Delta\mathbf{u}$ | Nodal iterative displacement vector |
| $\tilde{\boldsymbol{u}}$ | Displacement fluctuation vector |
| $\tilde{\mathbf{u}}$ | Nodal displacement fluctuation vector |
| $\epsilon_{\text{tol}}$ | Convergence tolerance |
| $\mathbf{H}_F$ | Consistent tangent $\mathsf{H}_F$ in matrix format |
| $\mathsf{Q}$ | Higher-order stress tensor |
| $\boldsymbol{L}$ | Lagrange multiplier enforcing the first-order minimal constraint |
| $\mathsf{M}$ | Lagrange multiplier enforcing the second-order minimal constraint |
| $\{\mathbf{I}\}$ | Identity tensor in vector format |
| $\mathbf{B}$ | Discrete symmetric gradient operator matrix |
| $\mathbf{b}$ | External volume force nodal vector |
| $\mathbf{C}$ | Constraint matrix |
| $\mathbf{D}$ | Coordinates matrix |
| $\mathbf{F}$ | Deformation gradient in vector format |
| $\mathbf{f}^{\text{ext}}$ | Nodal external force vector |
| $\mathbf{f}^{\text{int}}$ | Nodal internal force vector |
| $\mathbf{G}$ | Discrete gradient operator matrix |
| $\mathbf{I}$ | Identity matrix |
| $\mathbf{k}$ | Stiffness sub-matrix |
| $\mathbf{K}_e$ | Element stiffness matrix |
| $\mathbf{K}_T$ | Global tangent stiffness matrix |
| $\mathbf{L}$ | Lagrange multiplier $\boldsymbol{L}$ in vector format |
| $\mathbf{M}$ | Lagrange multiplier $\mathsf{M}$ in vector format |
| $\mathbf{N}, \mathbf{N}^u$ | Shape function matrix |
| $\mathbf{N}^\lambda$ | Lagrange multiplier interpolation function matrix |
| $\mathbf{P}$ | First Piola-Kirchhoff stress tensor in vector format |
| $\mathbf{Q}$ | Higher-order stress in vector format |
| $\mathbf{R}$ | Rotation tensor |
| $\mathbf{r}$ | Nodal residual vector |

| | |
|---|---|
| $\mathbf{T}$ | Transformation matrix |
| $\mathbf{t}$ | External traction nodal vector |
| $\mathbf{u}$ | Nodal displacement vector |
| $\mathbf{V}$ | Second-order coordinates matrix |
| $\mathcal{V}$ | Space of admissible virtual displacements |
| $\mu, \lambda$ | Lamé parameters |
| $\nu$ | Poisson's ratio |
| $\Omega$ | Domain |
| $\Omega^d$ | Discretised domain |
| $\partial\Omega, \Gamma$ | Domain boundary |
| $\rho$ | Mass density |
| $\sigma_y$ | Yield stress |
| $\sigma_{y0}$ | Initial yield stress |
| $\boldsymbol{\sigma}$ | Vector representation of $\boldsymbol{\sigma}$ |
| $\delta\boldsymbol{u}$ | Virtual displacements vector |
| $\delta\mathbf{u}$ | Nodal virtual displacements vector |
| $\delta\boldsymbol{\Delta}$ | Virtual separation vector |
| $E$ | Young's modulus, Parallel efficiency |
| $f$ | Void volume fraction |
| $G$ | Shear modulus |
| $H$ | Hardening modulus |
| $J$ | Determinant of the deformation gradient (Jacobian of deformation) |
| $J_p$ | Determinant of the Jacobian of the transformation mapping |
| $K$ | Bulk modulus |
| $l$ | Characteristic length |
| $l_{RVE}$ | RVE length |
| $N_i^\lambda$ | Lagrange multiplier interpolation functions related to the node $i$ |
| $n_e$ | Number of elements |
| $N_i, N_i^u, H_i$ | Shape functions related to the node $i$ |
| $n_n$ | Number of nodes |
| $n_p$ | Number of points |

$p$ Hydrostatic pressure

$S$ Speedup

$s_{RVE}$ RVE size

$t$ Time variable

$V$ Volume

$w_{gp}$ Gaussian quadrature weight value

**Operators**

$(\bullet)^S$ Symmetric of $(\bullet)$: $(\bullet)^S = 1/2(\bullet + \bullet^T)$

$(\bullet)^T$ Transpose of $(\bullet)$: $\boldsymbol{A}^T = A_{ji}\boldsymbol{e}_i \otimes \boldsymbol{e}_j$, $\mathbf{A}^T = A_{ikj}\boldsymbol{e}_i \otimes \boldsymbol{e}_j \otimes \boldsymbol{e}_k$

$(\bullet)^{-1}$ Inverse of $(\bullet)$

: Double contraction: $\boldsymbol{A} : \boldsymbol{B} = A_{ij}B_{ij}$, $\mathbf{A} : \boldsymbol{B} = \mathsf{A}_{ijk}B_{jk}\boldsymbol{e}_k$

$\mathsf{A}$ Finite element assembly operator

$\cdot$ Single contraction, dot product: $\boldsymbol{A} \cdot \boldsymbol{v} = A_{ij}v_j\boldsymbol{e}_i$, $\boldsymbol{A} \cdot \boldsymbol{B} = A_{ij}B_{jk}\boldsymbol{e}_i \otimes \boldsymbol{e}_k$, $\mathbf{A} \cdot \boldsymbol{v} = \mathsf{A}_{ijk}v_k\boldsymbol{e}_i \otimes \boldsymbol{e}_j$

$\delta_{ij}$ Kronecker delta

$\mathrm{div}(\bullet)$ Divergence of $(\bullet)$

$\mathrm{div}^n(\bullet)$ Normal divergence of $(\bullet)$

$\mathrm{div}^t(\bullet)$ Tangential divergence of $(\bullet)$

$\mathrm{div}_X(\bullet)$ Material divergence of $(\bullet)$ (macro-scale)

$\mathrm{div}_x(\bullet)$ Spatial divergence of $(\bullet)$ (macro-scale)

$\dot{(\bullet)}$ Temporal derivative $\partial \bullet / \partial t$

$\nabla(\bullet)$ Gradient of $(\bullet)$

$\nabla^s(\bullet)$ Symmetric gradient of $(\bullet)$

$\nabla^t(\bullet)$ Tangential gradient of $(\bullet)$: $\nabla^t(\bullet) = \nabla(\bullet) \cdot (\boldsymbol{I} - \boldsymbol{N} \otimes \boldsymbol{N})$

$\nabla_X(\bullet)$ Material gradient of $(\bullet)$ (macro-scale)

$\nabla_x(\bullet)$ Spatial gradient of $(\bullet)$ (macro-scale)

$\|\bullet\|$ Norm or jump of $(\bullet)$

$\otimes$ Tensor Product

$\partial(\bullet)/\partial(*)$ Partial derivative of $(\bullet)$ with respect to $(*)$

$D_0(\bullet)$ Normal gradient of $(\bullet)$: $D_0(\bullet) = \nabla(\bullet) \cdot \boldsymbol{N}$

$\mathrm{tr}(\bullet)$ Trace of $(\bullet)$

# Chapter 1

# Introduction

## 1.1 Context

Over recent years, the prediction and mitigation of failure in engineering structures has become an increasingly active research field and a critical issue in high-performance industries such as the aeronautic, aerospace and automotive sectors. Modern lightweight composite designs are driven by microstructural optimisation, where design choices that enhance the macroscopic mechanical properties yield highly nonlinear, heterogeneous microstructures in which the underlying micro-scale fracture mechanisms (e.g., matrix cracking and fibre–matrix debonding) control the global response (Gonçalves (2024)). As a result, continuum models, in isolation, are insufficient to reproduce the complex damage processes that occur in fibre-reinforced polymers (FRPs).

Multiscale modelling approaches bridge this gap by solving statistically representative samples at the micro-scale (e.g., an RVE) and employing homogenisation techniques to obtain realistic macroscopic constitutive relations. Scale-bridging strategies have been successfully employed in composites (Elmasry et al. (2023)), dual-phase steels (Rodrigues Lopes et al. (2023)), and also metamaterials (dos Santos et al. (2024)). Although a multi-scale approach is feasible, this work will focus exclusively on micro-scale models with homogenisation performed manually rather than through a fully coupled multi-scale framework.

To model material fracture, a wide range of numerical strategies can be employed. These include approaches that represent crack as a smeared zone (continuum damage mechanics and the phase-field method), as well as methods that explicitly model cracks as discrete discontinuities, such as the Extended Finite Element Method (XFEM), or Cohesive Zone Models. First proposed by Barenblatt (1962), Dugdale (1960), cohesive zone models represent fracture by inserting zero-thickness cohesive elements governed by a traction-separation law, while the bulk continua retains described by the classic stress-strain relation. Due to its discrete approach to fracture, cohesive zone models naturally capture initiation, propagation and the coalescence of cracks, in particular when their location is known a priori (e.g., fibre-matrix debonding).

An alternative approach introduce by Kachanov (1958) is continuum damage mechanics, which incorporates internal state variables into the constitutive material model of the bulk to simulate material degradation. A scalar field variable is often used to represent implicitly the crack geometry, circumventing the incorporation of discontinuities in the model. Local continuum damage models suffer from pathological mesh dependence under softening and require ad hoc enrichment to represent crack nucleation, kinking or branching (Gonçalves (2024)). Addressing some of these issues, the phase-field approach is an energy-based regularisation technique, first derived as a variational approximation of Griffith's theory of brittle fracture (Francfort and Marigo (1998)). That is, phase-field regularises sharp cracks into a smooth field which varies between an undamaged and fully damaged state over a length-scale parameter. This nonlocal formulation is thermodynamically consistent, mitigates strain localisation and naturally handles complex crack topologies. Recent efforts

have extended the phase-field approach to fracture to incorporate the material strength as a model parameter, leading to the development of the phase field - cohesive zone model (Navidtehrani et al. (2021), Wu (2017)). This approach embeds a traction-separation law within the energy functional. As a result, it is suitable for simulating fracture where the crack is not known a priori, such as bulk fracture (e.g., matrix cracking).

## 1.2 Sustainable development

This work meets several Sustainable Development Goals, by promoting greener, more efficient composite manufacturing processes and by providing numerical tools that reduce material experimental testing phases. In particular, the outcomes of this Master's Dissertation support wider and more informed use of fibre-reinforced polymers and facilitate the adoption of thermoplastic composites in aeronautical applications and other transportation sectors. Continuous fibre-reinforced thermoplastics (CFRTs) offer intrinsic advantages in sustainable and cleaner manufacturing processes. Owning to their chemical nature, thermoplastics can be more easily recycled than traditional thermoset polymer solutions, while contributing to a greener industrialisation. These materials do not requires refrigeration prior to production of components and reduce energy costs by offering out-of-autoclave manufacturing alternatives. The use of more automatised and flexible production techniques enabled by thermoplastic technologies can also shorten cycle times, improve workplace safety and productivity, and facilitate industrial scaling.

Within this context, high-fidelity numerical tools, such as the the micro-scale fracture models discussed in this work, further reduce the experimental campaign needed in the certification of high-performance aeronautical components, by minimising material waste and promoting more agile production phases. Furthermore, this dissertation can also contribute to accelerating technology transfer, since the numerical framework can be used to feed novel statistical tools to generate design allowables, such as digital twins. All these aspects would guarantee more sustainable production patterns and industrialization processes in compliance with the SGDs 9 and 12.

Finally, the maturing of computational methods for the failure prediction of CFRT also meets the sustainable goals of SDG 13. By enabling optimised, lightweight structural designs, these can lower the carbon footprint of key transportation industries, such as aeronautical, automotive and the railway industries, without compromising the mechanical performance of the parts.

## 1.3 Main objective

This Master's Dissertation aims to compare and combine the two damage frameworks, cohesive zone model and phase-field fracture, in the context of representative volume elements (RVEs) loaded under large deformations. Computational homogenisation is extensively employed to relay the micro-scale simulations with the global fracture response of composite RVEs, while tracking crack initiation, propagation paths, and the stress-strain behaviour. Within this framework, damage evolution can be either matrix-dominated or interface-dominated, depending on the interplay the two modelling strategies. By systematically varying the fracture material properties associated with each model, the aim is to examine how the combined framework governs the effective fracture response of fibre-reinforced polymers and to identify the dominant micro-scale failure mechanisms.

## 1.4 Computational framework

The present work was carried out within the computational framework `LINKS` (*Large Strain Implicit Non-linear Analysis of Solids Linking Scales*). `LINKS` is an in-house Fortran program, continuously

developed by the research group, CM2S (Computational Multi-scale Modelling of Solids and Structures). The LINKS framework supports large strain analysis of hyperelastic and elasto-plastic solids, as well as user-defined damage models.

The finite element meshes used throughout this Master's Dissertation have been provided by CM2S and generated using GMMD, an in-house tool for computational RVE generation (Vila-Chã et al. (2021)), and Gmsh (Geuzaine and Remacle (2009)). The input files are generated using custom Python scripts, which were further developed and refined in the scope of this dissertation.

## 1.5 Dissertation layout

This dissertation is structured into several chapters, each addressing a fundamental aspect of the work.

**Chapter 2**

This Chapter details the continuum mechanics framework and thermodynamic principles under finite deformations, supporting both damage models. It introduces the kinematics of deformation, strain and stress measures, constitutive theory, and the finite element implementation of quasi-static, large strain, solid mechanics.

**Chapter 3**

In this Chapter, the cohesive zone model used to simulate interfacial fracture are presented. The general formulation and numerical implementation is reviewed. In this work, the CZM employs the Park-Paulino-Roesler (PPR) potential-based cohesive model, due to is chosen due to its ability to independently set material properties in the normal and tangential directions.

**Chapter 4**

The phase-field approach to fracture is discussed in this Chapter. The variational derivation of the model is shown, the governing equations of the coupled problem are derived, with a final Section presenting the finite element implementation strategies.

**Chapter 5**

This Chapter documents the preprocessing routine implemented in Python that automatically pre-inserts zero-thickness cohesive elements along material interfaces. This routine expands the effectiveness of a legacy script, by including new features and testing its improved performance with selected benchmark examples.

**Chapter 6**

Several numerical applications are presented in this Chapter to thoroughly assess the impact of the material properties of the fracture models on the fracture response of macro-scale models. This Chapter includes parametric studies conducted on each separate model, followed by a direct comparison of both modelling approaches.

**Chapter 7**

An extension of the analysis is presented in this Chapter, by applying and comparing both CZM and PF models to representative volume elements of fibre-reinforced polymers. In addition to a mesh sensitivity study, parametric studies are performed, with a particular focus on analysing crack patterns and the homogenised stress-strain behaviour at the micro-scale.

**Chapter 8**

The final Chapter summarises the key findings, discusses limitations encountered throughout the work, and defines directions for future improvements.

## 1.6 Contributions

Attending the motivation and main goals of this dissertation presented previously, the main findings and original contributions are detailed as follows:

- Design of an automated mesh-processing script for robust insertion of cohesive elements, achieving up to 37 times more efficiency than the legacy version. The script efficiently prepares input files with a text-based format compatible with the in-house solver `LINKS`;
- Comprehensive numerical comparison between damage models, cohesive zone model with interface elements, and the phase-field fracture approach, in fibre-reinforced polymers. The interplay and resulting crack evolutions is also discussed and reported.

This dissertation's work further contributes to the current state-of-the-art by integrating the two complementary fracture frameworks into unified mechanical models, demonstrating their applicability to realistic composite microstructures.

# Chapter 2

# Continuum mechanics and the finite element method

This chapter reviews the fundamental concepts governing the mechanical behaviour of first-order continua, under finite deformations. Sections 2.1 to 2.5 provide an overview over the main principles of continuum mechanics, starting with kinematics of deformation, force and stress measures, the fundamental conservation principles, and ending with the general constitutive theory. In addition, the numerical procedures associated with the application of large strain *Finite Element Method* (FEM) to quasi-static nonlinear solid mechanics are described throughout Sections 2.6 to 2.8. The following Sections are based on the references by de Souza Neto et al. (2008) and Bonet and Wood (2008).

## 2.1 Kinematics of deformation

### 2.1.1 Motion

Let a body $\mathscr{B}$ occupy an open region $\Omega$ of the three-dimensional (3D) Euclidean space $\mathscr{E}$ with a regular boundary $\partial\Omega$ in the reference configuration, which is subjected to a deformation, as depicted by Figure 2.1.

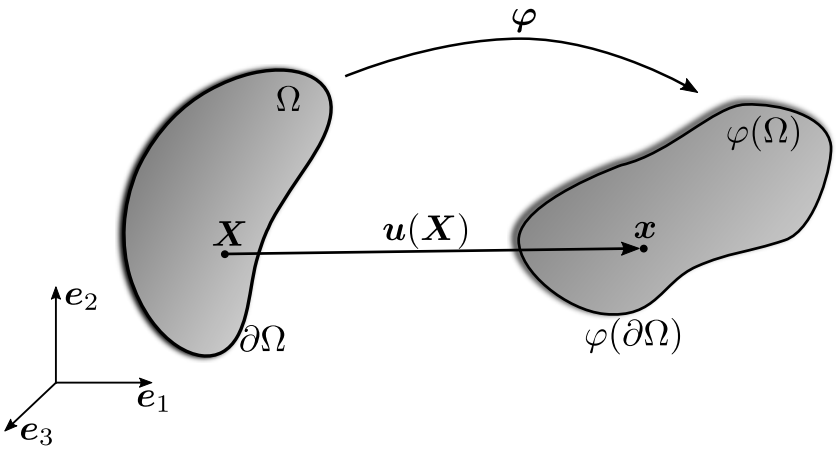


Figure 2.1: Generic deformation of a tri-dimensional body. Taken from Rodrigues Lopes et al. (2018).

The deformation map, or motion, is defined as a smooth univocal function denoted by

$$\boldsymbol{\varphi} : \Omega \rightarrow \mathscr{E}, \tag{2.1}$$

such that it takes the position of a given material particle, $\boldsymbol{X}$, from the reference configuration, and places it in the deformed configuration of $\mathscr{B}$,

$$\boldsymbol{x} = \boldsymbol{\varphi}(\boldsymbol{X}). \tag{2.2}$$

The deformed region of $\mathscr{E}$ occupied by $\mathscr{B}$ is given by $\boldsymbol{\varphi}(\Omega)$. The displacement field is a vector written as

$$\boldsymbol{u} = \boldsymbol{\varphi}(\boldsymbol{X}) - \boldsymbol{X}. \tag{2.3}$$

Therefore, the current position can be rewritten as

$$\boldsymbol{x} = \boldsymbol{X} + \boldsymbol{u}(\boldsymbol{X}). \tag{2.4}$$

The motion, or time-dependent deformation of a given body, $\mathscr{B}$, can be expressed as

$$\boldsymbol{\varphi} : \Omega \times \mathscr{R} \rightarrow \mathscr{E}, \tag{2.5}$$

where for each instance $t$, the deformation of $\mathscr{B}$ is given as $\boldsymbol{\varphi}_t$.

The position of a point in the deformed configuration, at time $t$,

$$\boldsymbol{x}(t) = \boldsymbol{\varphi}(\boldsymbol{X}, t), \tag{2.6}$$

is given as a function of each material point, $\boldsymbol{X}$, of $\mathscr{B}$. The displacement field of motion for this material particle can be given as:

$$\boldsymbol{u} = \boldsymbol{\varphi}(\boldsymbol{X}, t) - \boldsymbol{X}. \tag{2.7}$$

Therefore, the current position can also be given as a function of the displacement field as

$$\boldsymbol{x}(t) = \boldsymbol{X} + \boldsymbol{u}(\boldsymbol{X}, t). \tag{2.8}$$

For the inverse of the deformation map, the reference configuration can be recovered from the current position of a material particle

$$\boldsymbol{X} = \boldsymbol{\varphi}^{-1}(\boldsymbol{x}), \tag{2.9}$$

such that it can be rewritten as

$$\boldsymbol{X} = \boldsymbol{x} - \boldsymbol{u}\left(\boldsymbol{\varphi}^{-1}(\boldsymbol{x}, t), t\right). \tag{2.10}$$

Equation (2.6) represents any time-dependent deformation, whether deformations that change the shape of the body, or those that preserve the relative positions between all material particles of $\mathscr{B}$. The latter, referred to as rigid-body motion, is any combination of a translation and a rotation.

Additionally, at a given time, $t$, the velocity of a material particle $\boldsymbol{X}$ is given as the derivative of its deformed position with respect to time. Thus, the velocity field can be computed, in the material description, as

$$\boldsymbol{v}(\boldsymbol{X}, t) = \dot{\boldsymbol{u}}(\boldsymbol{X}, t) = \frac{\partial \boldsymbol{\varphi}(\boldsymbol{X}, t)}{\partial t}, \tag{2.11}$$

and, in the spatial description, as

$$\boldsymbol{v}(\boldsymbol{x}, t) \equiv \dot{\boldsymbol{u}}\left(\boldsymbol{\varphi}(\boldsymbol{x}, t), t\right) = \frac{\partial \boldsymbol{\varphi}\left(\boldsymbol{\varphi}(\boldsymbol{x}, t), t\right)}{\partial t}. \tag{2.12}$$

### 2.1.2 Material and spatial descriptions

The material or Lagrangian description of motion of a body $\mathscr{B}$ represents its time-dependent deformation, with respect to the undeformed configuration. In contrast, the spatial or Eulerian description expresses the kinematic variables as functions of the deformed configuration. Only once the gradient and divergence operators have been rigorously defined in both descriptions for a generic vectorial and tensor fields, it is possible to introduce the deformation gradient $\boldsymbol{F}$, and then derive the various strain tensors, as well as to formulate consistent constitutive and equilibrium equations in continuum mechanics.

Let $\alpha$ be a generic field, whose representation in the material and spatial configurations is given, respectively, as

$$\boldsymbol{\alpha}_m(\boldsymbol{X},t) = \alpha\left(\boldsymbol{\varphi}(\boldsymbol{X},t),t\right), \tag{2.13}$$

$$\boldsymbol{\alpha}_s(\boldsymbol{x},t) = \alpha\left(\boldsymbol{\varphi}^{-1}(\boldsymbol{x},t),t\right). \tag{2.14}$$

The material gradient is given as the derivative of the material field with respect to $\boldsymbol{X}$, such that

$$\nabla_{\boldsymbol{X}}\alpha = \frac{\partial}{\partial \boldsymbol{X}}\alpha_m(\boldsymbol{X},t). \tag{2.15}$$

Similarly, the spatial gradient is the derivative of the spatial field with respect to $\boldsymbol{x}$,

$$\nabla_{\boldsymbol{x}}\alpha = \frac{\partial}{\partial \boldsymbol{x}}\alpha_m(\boldsymbol{x},t). \tag{2.16}$$

For a generic tensor field, $\boldsymbol{A}$, the divergence can be expressed in the material, or spatial configuration, such that

$$\mathrm{div}_{\boldsymbol{X}}(\boldsymbol{A})_i = \frac{\partial A_{ij}}{\partial X_j}, \tag{2.17}$$

$$\mathrm{div}_{\boldsymbol{x}}(\boldsymbol{A})_i = \frac{\partial A_{ij}}{\partial x_j}. \tag{2.18}$$

### 2.1.3 Deformation gradient

At a given time, $t$, the *deformation gradient* associated with a motion $\boldsymbol{\varphi}$ is expressed as the second-order tensor which maps the reference configuration of a material particle to its deformed configuration, and expressed as

$$\boldsymbol{F}(\boldsymbol{X},t) = \nabla_{\boldsymbol{X}}(\boldsymbol{\varphi}(\boldsymbol{X},t)) = \frac{\partial \boldsymbol{x}_t}{\partial \boldsymbol{X}}, \tag{2.19}$$

which can be rewritten with respect to the displacement field as

$$\boldsymbol{F} = \boldsymbol{I} + \nabla_{\boldsymbol{X}}(\boldsymbol{u}), \tag{2.20}$$

where $\boldsymbol{I}$ is the second-order identity tensor.

According to the spatial description, the deformation gradient can be written as

$$\boldsymbol{F}(\boldsymbol{x},t) = [\nabla_{\boldsymbol{x}}\boldsymbol{\varphi}^{-1}(\boldsymbol{x},t)]^{-1} = [\boldsymbol{I} - \nabla_{\boldsymbol{x}}\boldsymbol{u}]^{-1}. \tag{2.21}$$

Relation (2.20) allows obtaining the expression of the deformation gradient in cartesian coordinates,

$$F_{ij} = \frac{\partial x_i}{\partial X_j} = \delta_{ij} + \frac{\partial u_i}{\partial X_j}. \tag{2.22}$$

### 2.1.4 Isochoric and volumetric decomposition of the deformation gradient

Let $\mathrm{d}V$ and $\mathrm{d}v$ be the infinitesimal volume of a body $\mathscr{B}$ in the reference and deformed configurations, respectively. The volume change ratio is given, locally, as the determinant of the deformation gradient tensor, such that

$$J \equiv \frac{\mathrm{d}v}{\mathrm{d}V} = \det \boldsymbol{F}. \tag{2.23}$$

Therefore, the change in volume of an infinitesimal element, $\mathrm{d}V$, in the deformed body $\mathscr{B}$, is given as

$$\mathrm{d}v = J\mathrm{d}V, \tag{2.24}$$

When $J = 0$, the infinitesimal volume, $\mathrm{d}V$, has collapsed into a material particle, $\mathrm{d}v = 0$, which is not a physically acceptable assumption. To ensure the body does not penetrate itself, the deformation map, $\boldsymbol{\varphi}$, must be a one-to-one mapping. Since the determinant of the deformation gradient is $J = 1$, at the reference configuration ($\boldsymbol{F} = \boldsymbol{I}$), $J < 0$ cannot be reached, without violating the previous assumption that $J = 0$ (de Souza Neto et al. (2008)). Thus, for any deformed configuration, the determinant must respect

$$J > 0. \tag{2.25}$$

Following the previous definition, a deformation can be locally split into an *isochoric* (or *volume-preserving*) deformation, $\boldsymbol{F}_{\mathrm{iso}}$, and a purely *volumetric* deformation, $\boldsymbol{F}_{\mathrm{vol}}$, such that

$$\boldsymbol{F} = \boldsymbol{F}_{\mathrm{iso}}\boldsymbol{F}_{\mathrm{vol}} = \boldsymbol{F}_{\mathrm{vol}}\boldsymbol{F}_{\mathrm{iso}}. \tag{2.26}$$

For a purely volumetric deformation, only change in volume is present, such that its deformation gradient is a spherical tensor of the form

$$\boldsymbol{F}_{\mathrm{vol}} = \alpha \boldsymbol{I}, \tag{2.27}$$

where $\alpha$ is the contraction or expansion ratio.

The determinant of a volumetric deformation expresses its local ratio of volume change

$$J = \det \boldsymbol{F}_{\mathrm{vol}} = \det(\alpha \boldsymbol{I}) = \alpha^3. \tag{2.28}$$

The volumetric component can thus be given as

$$\boldsymbol{F}_{\mathrm{vol}} \equiv J^{1/3}\boldsymbol{I}. \tag{2.29}$$

For a purely isochoric deformation, the volume of the deformed body remains unchanged, with $J = 1$. To satisfy Equation (2.26), the corresponding isochoric component is

$$\boldsymbol{F}_{\mathrm{iso}} \equiv J^{-1/3}\boldsymbol{F}. \tag{2.30}$$

### 2.1.5 Polar decomposition of the deformation gradient

A *polar decomposition* can also be applied to the deformation gradient, such that

$$\boldsymbol{F} = \boldsymbol{R}\boldsymbol{U} = \boldsymbol{V}\boldsymbol{R}, \tag{2.31}$$

where the local rotation tensor, $\boldsymbol{R}$, is the proper orthogonal tensor that must satisfy

$$\boldsymbol{R}\boldsymbol{R}^T = \boldsymbol{I}, \tag{2.32}$$

$$\det \boldsymbol{R} = 1. \tag{2.33}$$

The *left* and *right stretch tensors*, $\boldsymbol{V}$ and $\boldsymbol{U}$ respectively, are symmetric positive definite tensors, related as

$$\boldsymbol{V} = \boldsymbol{R}\boldsymbol{U}\boldsymbol{R}^T. \tag{2.34}$$

The spectral decomposition of the stretch tensors is given as

$$\boldsymbol{U} = \sum_{i=1}^{3} \lambda_i \boldsymbol{E}_i \otimes \boldsymbol{E}_i, \tag{2.35}$$

$$\boldsymbol{V} = \sum_{i=1}^{3} \lambda_i \boldsymbol{e}_i \otimes \boldsymbol{e}_i, \tag{2.36}$$

where the eigenvalues, $\lambda_i$, denote the principal stretches, and the eigenvectors, $\boldsymbol{E}_i$ and $\boldsymbol{e}_i$, define the Lagrangian and Eulerian principal directions, respectively, such that

$$\boldsymbol{E}_i = \boldsymbol{R}\boldsymbol{e}_i. \tag{2.37}$$

## 2.2 Strain measures

In the context of continuum mechanics, several strain tensors can be defined based upon the definition of the deformation gradient, such as the *Cauchy-Green*, the *Green-Lagrange*, the *Lagrangian*, and the *Eulerian* strain tensors.

The right and left Cauchy-Green strain tensors are, respectively, given as

$$\boldsymbol{C} = \boldsymbol{U}^2 = \boldsymbol{F}^T\boldsymbol{F}, \tag{2.38}$$

$$\boldsymbol{b} = \boldsymbol{V}^2 = \boldsymbol{F}\boldsymbol{F}^T. \tag{2.39}$$

The strain tensors from the Lagrangian family can thus be defined as

$$\boldsymbol{E}^{(m)} = \begin{cases} \dfrac{1}{m}\left(\boldsymbol{U}^m - \boldsymbol{I}\right), & m \neq 0 \\ \ln \boldsymbol{U}, & m = 0 \end{cases}, \tag{2.40}$$

Particular instances of Lagrangian strain tensors include the Biot ($m = 1$), Hencky ($m = 0$), Almansi ($m = -2$), and Green-Lagrange ($m = 2$) strain tensors, with the latter defined as

$$\boldsymbol{E}^{(2)} = \frac{1}{2}(\boldsymbol{C} - \boldsymbol{I}) = \frac{1}{2}(\nabla_{\boldsymbol{X}}\boldsymbol{u} + (\nabla_{\boldsymbol{X}}\boldsymbol{u})^T + (\nabla_{\boldsymbol{X}}\boldsymbol{u})^T\nabla_{\boldsymbol{X}}\boldsymbol{u}). \tag{2.41}$$

The Eulerian strain tensors can be similarly expressed with respect to the left stretch tensor as

$$\boldsymbol{\varepsilon}^{(m)} = \begin{cases} \dfrac{1}{m}(\boldsymbol{V}^m - \boldsymbol{I}), & m \neq 0 \\ \ln \boldsymbol{V}, & m = 0 \end{cases}, \tag{2.42}$$

where the relation between the two strain tensor families is given as

$$\boldsymbol{\varepsilon}^{(m)} = \boldsymbol{R}\boldsymbol{E}^{(m)}\boldsymbol{R}^T. \tag{2.43}$$

For a large strain spatial formulation, the Eulerian logarithmic (or Hencky) strain tensor

$$\boldsymbol{\varepsilon}^{(0)} = \ln \boldsymbol{V} = \sum_{i=1}^{3} \ln \lambda_i \boldsymbol{E}_i \otimes \boldsymbol{E}_i \tag{2.44}$$

is the strain measure implemented in `LINKS` and employed in this Master's Dissertation.

The Cauchy-Green strain tensors can be given with respect to the displacement field, such that

$$\boldsymbol{C} = \boldsymbol{I} + \nabla_{\boldsymbol{X}}\boldsymbol{u} + (\nabla_{\boldsymbol{X}}\boldsymbol{u})^T + (\nabla_{\boldsymbol{X}}\boldsymbol{u})^T\nabla_{\boldsymbol{X}}\boldsymbol{u}, \tag{2.45}$$

$$\boldsymbol{b} = \boldsymbol{I} + \nabla_{\boldsymbol{X}}\boldsymbol{u} + (\nabla_{\boldsymbol{X}}\boldsymbol{u})^T + \nabla_{\boldsymbol{X}}\boldsymbol{u}(\nabla_{\boldsymbol{X}}\boldsymbol{u})^T, \tag{2.46}$$

Considering a sufficiently small displacement gradient, such that the second terms in Equations (2.45) and (2.46) can be neglected, the following holds true

$$\boldsymbol{C} \approx \boldsymbol{b} \approx \boldsymbol{I} + \nabla_{\boldsymbol{X}} \boldsymbol{u} + (\nabla_{\boldsymbol{X}} \boldsymbol{u})^T. \tag{2.47}$$

It follows that the Green-Lagrange strain tensor can be approximated as

$$\boldsymbol{E}^{(2)} \approx \boldsymbol{\varepsilon}^{(2)} \approx \frac{1}{2}(\nabla_{\boldsymbol{X}} \boldsymbol{u} + (\nabla_{\boldsymbol{X}} \boldsymbol{u})^T). \tag{2.48}$$

Therefore, under small deformations, the infinitesimal strain tensor is the same for the material and spatial configurations, given as a linear functional of $\boldsymbol{u}$, such that

$$\boldsymbol{\varepsilon} \equiv \nabla^s \boldsymbol{u} = \frac{1}{2}\left(\nabla \boldsymbol{u} + (\nabla \boldsymbol{u})^T\right). \tag{2.49}$$

In fact, all Lagrangian and Eulerian strain tensors can be approximated to the infinitesimal strain tensor, such that

$$\boldsymbol{E}^{(m)} \approx \boldsymbol{\varepsilon}^{(m)} \approx \boldsymbol{\varepsilon} \tag{2.50}$$

Analogously to the isochoric and volumetric decomposition of the deformation gradient, the infinitesimal strain tensor can be expressed as

$$\boldsymbol{\varepsilon} = \boldsymbol{\varepsilon}_{\text{dev}} + \boldsymbol{\varepsilon}_{\text{vol}}. \tag{2.51}$$

The volumetric strain component is expressed as

$$\boldsymbol{\varepsilon}_{\text{vol}} \equiv \frac{1}{3}\varepsilon_{\text{vol}} \boldsymbol{I} \tag{2.52}$$

with the scalar invariant defined as

$$\varepsilon_{\text{vol}} \equiv \text{tr}\, \boldsymbol{\varepsilon} = \text{tr}\, \nabla^s \boldsymbol{u} = \text{tr}\, \nabla \boldsymbol{u}. \tag{2.53}$$

On the other hand, the isochoric or deviatoric strain component, also referred to as *strain deviator*, can be computed as

$$\boldsymbol{\varepsilon}_{\text{dev}} \equiv \boldsymbol{\varepsilon} - \boldsymbol{\varepsilon}_{\text{vol}}. \tag{2.54}$$

The spectral decomposition of the strain tensor is given as:

$$\boldsymbol{\varepsilon} = \sum_{i=1}^{n} \varepsilon_i \boldsymbol{e}_i \otimes \boldsymbol{e}_i \tag{2.55}$$

where $\varepsilon_i$ are the eigenvalues of the strain tensor, and $\boldsymbol{e}_i$ are the corresponding eigenvectors.

## 2.3 Forces and stress measures

A continuum body may be subjected to forces which may cause its deformation. When applied in the interior of the body, these forces are referred to as *body* or *volume forces* and with units of force per unit mass (or volume). *Boundary forces* are external forces applied to the boundary or surface of the body, with units of force per unit area. *Interior forces* reflect the internal interactions between adjacent parts of a body, transmitted across the surface that separates them. In addition to boundary forces, interior forces are also known as *surface forces*, with units of force per unit area.

### 2.3.1 The Cauchy stress tensor

The description of surface forces is based upon the *Cauchy's axiom* and the *Cauchy stress vector*. The axiom states that a surface force exerted at a point $\boldsymbol{x}$ on any oriented surface, $\mathscr{S}$, of a body $\mathscr{B}$, depends only on $\mathscr{S}$ through its normal vector, $\boldsymbol{n}$. Thus, the traction vector is given by

$$\boldsymbol{t}(\boldsymbol{x}, \boldsymbol{n}, t), \tag{2.56}$$

which represents the force exerted on the surrounding boundary of $\mathscr{B}$, should $\mathscr{S}$ belong to the boundary of $\mathscr{B}$.

The Cauchy stress tensor, $\boldsymbol{\sigma}$, is a spatial second order tensor defined from the quantities previously presented, such that

$$\boldsymbol{t}(\boldsymbol{x}, \boldsymbol{n}, t) = \boldsymbol{\sigma}(\boldsymbol{x}, t) \cdot \boldsymbol{n}, \tag{2.57}$$

where $\boldsymbol{t}$ is the surface traction, and $\boldsymbol{n}$ is the unit outward vector normal to the corresponding surface. The traction vector, $\boldsymbol{t}$, has units of force per unit of *deformed* area.

The Cauchy stress tensor is a symmetric tensor defined in the deformed configuration of the body, such that

$$\boldsymbol{\sigma} = \boldsymbol{\sigma}^T. \tag{2.58}$$

The cartesian components of the Cauchy stress tensor are defined as

$$\sigma_{ij} = (\boldsymbol{\sigma}\boldsymbol{e}_i) \cdot \boldsymbol{e}_j, \tag{2.59}$$

where $\boldsymbol{\sigma}\boldsymbol{e}_i$ is the force vector per unit area exerted on a surface whose normal unit vector is $\boldsymbol{e}_i$, and $\boldsymbol{e}_j$ is the direction in which the force is projected to obtain the component of the Cauchy stress tensor.

### 2.3.2 Deviatoric and hydrostatic stress components

The stress tensor can be split into the sum of a *spherical* component, associated with the uniform traction/compression of the solid, and a *traceless* component, associated with the solid distortion, such that

$$\boldsymbol{\sigma} = \boldsymbol{s} + p\boldsymbol{I}. \tag{2.60}$$

For a three-dimensional stress state, the *hydrostatic pressure* or *mean stress* is given as the invariant

$$p \equiv \frac{1}{3} I_1(\boldsymbol{\sigma}) = \frac{1}{3} \operatorname{tr} \boldsymbol{\sigma}. \tag{2.61}$$

The *hydrostatic* or *spherical stress tensor* translates a uniform traction or compression of a continuum body, expressed as

$$\boldsymbol{\sigma}_{\text{vol}} = p\boldsymbol{I} = \frac{1}{3}(\boldsymbol{I} \otimes \boldsymbol{I}) : \boldsymbol{\sigma} = \frac{1}{3} tr(\boldsymbol{\sigma})\boldsymbol{I}. \tag{2.62}$$

The *deviatoric stress* or *stress deviator* measures pure distortion and is given as

$$\boldsymbol{s} \equiv \boldsymbol{\sigma} - p\boldsymbol{I} = \mathbf{I}_{\text{dev}} : \boldsymbol{\sigma}, \tag{2.63}$$

where $\mathbf{I}_{\text{dev}}$ is the fourth-order traceless deviatoric projection tensor

$$\mathbf{I}_{\text{dev}} = \mathbf{I} - \frac{1}{3}\boldsymbol{I} \otimes \boldsymbol{I}. \tag{2.64}$$

### 2.3.3 First Piola-Kirchhoff stress tensor

The *First Piola-Kirchhoff stress* tensor is a two-point stress tensor that relates the current force to the deformed area, defined as

$$\boldsymbol{P} \equiv J\boldsymbol{\sigma}\boldsymbol{F}^{-T}. \tag{2.65}$$

In contrast with its Cauchy stress tensor, the First Piola-Kirchhoff stress tensor can be asymmetric and is associated with the material counterpart $\boldsymbol{t}_0$ of $\boldsymbol{t}$, which measures the surface force acting on a surface per unit of *reference* or *undeformed* area. The two quantities can be related as

$$\boldsymbol{t}_0 = \frac{\mathrm{d}a}{\mathrm{d}a_0}\boldsymbol{t}, \tag{2.66}$$

where $\mathrm{d}a$ and $\mathrm{d}a_0$ represent the infinitesimal area of a surface normal to $\boldsymbol{n}$ and $\boldsymbol{n_0}$, respectively.

### 2.3.4 Second Piola-Kirchhoff stress tensor

The *Second Piola-Kirchhoff stress* tensor is a material symmetric stress tensor defined by

$$\boldsymbol{S} \equiv J\boldsymbol{F}^{-1}\boldsymbol{\sigma}\boldsymbol{F}^{-T}, \tag{2.67}$$

which acts as conjugate to the Green-Lagrange strain tensor, $\boldsymbol{E}^{(2)}$.

Relating the First and Second Piola-Kirchhoff stress tensors yields the following relation

$$\boldsymbol{S} = \boldsymbol{F}^{-1}\boldsymbol{P}. \tag{2.68}$$

### 2.3.5 Kirchhoff stress tensor

The *Kirchhoff stress* tensor is a spatial stress tensor defined as

$$\boldsymbol{\tau} \equiv J\boldsymbol{\sigma}. \tag{2.69}$$

## 2.4 Fundamental conservation principles

To fully characterise the mechanical behaviour of a continuum body, it is necessary to establish the fundamental governing laws that relate the strain and stress measures previously introduced. Alongside the mechanical variables, it is necessary to introduce scalar fields for temperature ($\theta$), specific internal energy ($e$), specific entropy ($s$), and density of heat production ($r$), which are defined over $\mathscr{B}$. In addition, the vector fields $\boldsymbol{q}$ and $\boldsymbol{b}$ represent, respectively, the heat flux and body forces per unit volume.

### 2.4.1 Conservation of mass

The principle of conservation of mass states that the mass of a body $\mathscr{B}$ remains constant over time and during motion. Naturally, the mass expressed in the reference configuration must be equal to the mass expressed in the current configuration, such that

$$m_0(\Omega_0) = m(\Omega), \tag{2.70}$$

where $m_0$ and $m$ are the mass of the body in the material and spatial descriptions, respectively.

Additionally, consider a continuous distribution of mass along the body

$$m_0 = \int_{\Omega} \rho_0 \mathrm{d}V \tag{2.71}$$

$$m = \int_{\boldsymbol{\varphi}(\Omega)} \rho \mathrm{d}v, \tag{2.72}$$

where $\rho_0$ and $\rho$ are the density, or volumic mass, in the material and spatial descriptions, respectively.

By making use of the volume change ratio $J$ introduced in Equation (2.23), the mass conservation principle can be reformulated as

$$\int_\Omega \rho_0 \mathrm{d}V = \int_\Omega \rho J \mathrm{d}V \tag{2.73}$$

$$\Leftrightarrow \int_\Omega (\rho_0 - J\rho)\mathrm{d}V = 0. \tag{2.74}$$

For the previous Equation to hold true for all domain $\Omega$, the following must be satisfied point-wise

$$\rho_0 - J\rho = 0, \tag{2.75}$$

which is referred to as the material form of principle of the conservation of mass.

In the spatial description, the principle of conservation of mass can be expressed as:

$$\dot{m}\left(\boldsymbol{\varphi}(\Omega)\right) = \frac{\mathrm{d}}{\mathrm{d}t}\int_{\boldsymbol{\varphi}(\Omega)} \rho \mathrm{d}v = 0 \tag{2.76}$$

$$\Rightarrow \dot{\rho} + \rho \operatorname{div}_{\boldsymbol{x}} \dot{\boldsymbol{u}} = 0, \tag{2.77}$$

where $\dot{\rho}$ is the time derivative of the mass per unit volume in the deformed configuration.

### 2.4.2 Momentum balance

For the deformed configuration, the strong (point-wise, or differential) statement of the conservation of linear momentum for $\mathscr{B}$ states that

$$\operatorname{div}_{\boldsymbol{x}} \boldsymbol{\sigma} + \boldsymbol{b} = \rho \ddot{\boldsymbol{u}}, \quad \text{in } \boldsymbol{\varphi}(\Omega) \tag{2.78}$$

$$\boldsymbol{\sigma}\boldsymbol{n} = \boldsymbol{t}, \quad \text{in } \boldsymbol{\varphi}(\partial\Omega) \tag{2.79}$$

where $\boldsymbol{b}$ denotes the external body force per unit volume, $\boldsymbol{t}$ is the external traction vector acting on the boundary of the domain, in the deformed configuration, with $\boldsymbol{n}$ as its outward normal vector, and $\operatorname{div}_{\boldsymbol{x}}\boldsymbol{\sigma}$ or $\nabla_{\boldsymbol{x}}\cdot\boldsymbol{\sigma}$ is the spatial divergence of the Cauchy stress tensor. Equation (2.78) is referred to as Cauchy's equation of motion.

### 2.4.3 First law of thermodynamics

The first principle of thermodynamics postulates the conservation of energy

$$\rho\dot{e} = \boldsymbol{\sigma} : \boldsymbol{D} + \rho r - \operatorname{div}_{\boldsymbol{x}} \boldsymbol{q}, \tag{2.80}$$

where $\boldsymbol{\sigma} : \boldsymbol{D}$ represents the stress power per unit volume in the spatial description, $\boldsymbol{D} = \nabla_{\boldsymbol{x}}\boldsymbol{v}$ is the *stretch rate tensor*, $\dot{e}$ is the first derivative of the specific internal energy with respect to time, $r$ is the density of heat production, and $\boldsymbol{q}$ is the heat flux.

### 2.4.4 Second law of thermodynamics

The second law of thermodynamics translates the irreversibility of the production of entropy, which cannot decrease over time, written as

$$\rho\dot{s} + \operatorname{div}_{\boldsymbol{x}}\left(\frac{\boldsymbol{q}}{\theta}\right) - \frac{\rho r}{\theta} \geq 0. \tag{2.81}$$

### 2.4.5 Clausius-Duhem inequality

Combining the first two laws of thermodynamics applied to continuum mechanics, the following inequality is obtained

$$\rho \dot{s} + \operatorname{div}_{\boldsymbol{x}}\left(\frac{\boldsymbol{q}}{\theta}\right) - \frac{1}{\theta}\left(\rho \dot{e} - \boldsymbol{\sigma} : \boldsymbol{D} + \operatorname{div}_{\boldsymbol{x}} \boldsymbol{q}\right) \geq 0. \tag{2.82}$$

The *Helmholtz free energy per unit mass*, or *specific free energy*, is given

$$\psi = e - \theta s. \tag{2.83}$$

Employing the Gauss or divergence theorem, one gets

$$\operatorname{div}_{\boldsymbol{x}}\left(\frac{\boldsymbol{q}}{\theta}\right) = \frac{1}{\theta}\operatorname{div}_{\boldsymbol{x}}(\boldsymbol{q}) - \frac{1}{\theta^2}\boldsymbol{q} \cdot \nabla_{\boldsymbol{x}}\theta. \tag{2.84}$$

Introducing Equations (2.83) and (2.84) into the thermodynamics inequality yields the Clausius-Duhem inequality

$$\boldsymbol{\sigma} : \boldsymbol{D} - \rho(\dot{\psi} + s\dot{\theta}) - \frac{1}{\theta}\boldsymbol{q} \cdot \boldsymbol{g} \geq 0, \tag{2.85}$$

where the temperature field gradient (or heat flux) is given as $\boldsymbol{g} = \nabla_{\boldsymbol{x}}\theta$, and the left-side of the Equation represents the dissipation per unit deformed volume, always greater than or equal to zero.

Rewriting the inequality for the dissipation per unit reference volume,

$$\boldsymbol{\tau} : \boldsymbol{D} - \rho_0(\dot{\psi} + s\dot{\theta}) - \frac{J}{\theta}\boldsymbol{q} \cdot \boldsymbol{g} \geq 0. \tag{2.86}$$

## 2.5 Constitutive theory

A *constitutive model* defines the physical behaviour of a given material for a continuum body. More specifically, the formulation presented here uses the definition of internal variables related to a thermodynamic state.

### 2.5.1 Thermodynamics with internal variables

*Thermodynamics with internal variables* is used to establish the constitutive equations. The main hypothesis states that *the thermodynamic state of a thermodynamical process, defined by $\boldsymbol{\sigma}$, $\psi$, $s$ and $\boldsymbol{q}$ at a given material point $\boldsymbol{X}$, is completely defined by a finite number of state variables.* Only the *instantaneous* value of the state variable, not their past history, is sufficient to define the thermodynamic state.

For any instance $t$, let the thermodynamic state of a point be defined by a set of state variables

$$\{\boldsymbol{F}, \theta, \boldsymbol{g}, \boldsymbol{\alpha}\} \tag{2.87}$$

where $\boldsymbol{F}$, $\theta$, and $\boldsymbol{g}$ are the instantaneous value of the deformation gradient, the temperature and the spatial temperature gradient, respectively, and

$$\boldsymbol{\alpha} = \{\alpha_k\} \tag{2.88}$$

is the set of *internal variables*, associated with internal dissipative mechanisms (de Souza Neto et al. (2008)).

The free energy function introduced in Section 2.4.5 can be defined as a function of the state variables with the exception of the temperature gradient, since it would contradict the second law of thermodynamics (Coleman and Gurtin (1967)), such that

$$\psi = \psi(\boldsymbol{F}, \theta, \boldsymbol{\alpha}), \tag{2.89}$$

with its derivative with respect to time given as

$$\dot{\psi} = \frac{\partial \psi}{\partial \boldsymbol{F}} : \dot{\boldsymbol{F}} + \frac{\partial \psi}{\partial \theta}\dot{\theta} + \sum_{k=1}^{n} \frac{\partial \psi}{\partial \alpha_k}\dot{\alpha}_k, \tag{2.90}$$

and where $n$ is the number of internal variables.

The Clausius-Duhem inequality can now be expressed in the deformed configuration as

$$\left(\boldsymbol{\sigma}\boldsymbol{F}^{-T} - \rho\frac{\partial \psi}{\partial \boldsymbol{F}}\right) : \dot{\boldsymbol{F}} - \rho\left(s + \frac{\partial \psi}{\partial \theta}\right)\dot{\theta} - \rho\sum_{k=1}^{n}\frac{\partial \psi}{\partial \alpha_k}\dot{\alpha}_k - \frac{1}{\theta}\boldsymbol{q}\cdot\boldsymbol{g} \geq 0. \tag{2.91}$$

Rewriting the inequality in the reference configuration yields

$$\left(\boldsymbol{P} - \rho_0\frac{\partial \psi}{\partial \boldsymbol{F}}\right) : \dot{\boldsymbol{F}} - \rho_0\left(s + \frac{\partial \psi}{\partial \theta}\right)\dot{\theta} - \rho_0\sum_{k=1}^{n}\frac{\partial \psi}{\partial \alpha_k}\dot{\alpha}_k - \frac{J}{\theta}\boldsymbol{q}\cdot\boldsymbol{g} \geq 0. \tag{2.92}$$

To satisfy the principle of thermodynamic determinism, Equation (2.92) must hold for any thermokinetic process, associated with a pair of functions $\{\dot{\boldsymbol{F}}(t), \dot{\theta}(t)\}$, such that one arrives at the following constitutive equations

$$\boldsymbol{P} = \rho_0\frac{\partial \psi}{\partial \boldsymbol{F}}, \quad s = -\frac{\partial \psi}{\partial \theta}. \tag{2.93}$$

In terms of the Cauchy and Kirchhoff stress tensors,

$$\boldsymbol{\sigma} = \frac{1}{J}\rho_0\frac{\partial \psi}{\partial \boldsymbol{F}}\boldsymbol{F}^T, \quad \boldsymbol{P} = \rho_0\frac{\partial \psi}{\partial \boldsymbol{F}}\boldsymbol{F}^T. \tag{2.94}$$

### 2.5.2 The constitutive initial value problem

When considering the internal variable approach, the generic form of the constitutive problem can be formulated as the fundamental mechanical initial value problem stated in the material configuration as follows (de Souza Neto et al. (2008)).

**Problem 2.1** (**The material constitutive initial value problem**). *Given the initial values of the internal variables $\boldsymbol{\alpha}(t_0)$ and the history of the deformation gradient,*

$$\boldsymbol{F}(t), \quad t \in [t_0, t_f], \tag{2.95}$$

*find the functions $\boldsymbol{P}(t)$ and $\boldsymbol{\alpha}(t)$, for the first Piola-Kirchhoff stress and the set of internal variables, such that the constitutive equations*

$$\begin{cases} \boldsymbol{P}(t) = \rho_0\dfrac{\partial \psi}{\partial \boldsymbol{F}}\Big|_t, \\ \psi = \psi(\boldsymbol{F}, \boldsymbol{\alpha}), \\ \dot{\boldsymbol{\alpha}} = f(\boldsymbol{F}(t), \boldsymbol{\alpha}(t)), \end{cases} \tag{2.96}$$

*are satisfied for every $t \in [t_0, t_f]$.*

Reformulating the problem in the spatial description yields:

**Problem 2.2** (**The spatial constitutive initial value problem**). *Given the initial values of the internal variables* $\boldsymbol{\alpha}(t_0)$ *and the history of the deformation gradient,*

$$\boldsymbol{F}(t), \quad t \in [t_0, t_f], \tag{2.97}$$

*find the functions* $\boldsymbol{\sigma}(t)$ *and* $\boldsymbol{\alpha}(t)$*, for the Cauchy stress tensor and the set of internal variables, such that the constitutive equations*

$$\begin{cases} \boldsymbol{\sigma}(t) = \rho \dfrac{\partial \psi}{\partial \boldsymbol{F}}\Big|_t \boldsymbol{F}^T, \\ \psi = \psi(\boldsymbol{F}, \boldsymbol{\alpha}), \\ \dot{\boldsymbol{\alpha}} = f(\boldsymbol{F}(t), \boldsymbol{\alpha}(t)), \end{cases} \tag{2.98}$$

*are satisfied for every* $t \in [t_0, t_f]$.

## 2.6 Weak equilibrium equations

The strong form of the equilibrium equations, in the deformed configuration, ensures the equilibrium of linear moment at every material point of the continuum body (see Equations (2.78) and (2.79)). To solve these differential equations, the exact solution solution must be obtained, which can be challenging for most engineering problems. For numerical implementation, it is convenient to reformulate the linear momentum equilibrium as a set of integral equations, which must be satisfied over the body domain, instead of pointwise. These are referred to as the weak or global form of equilibrium equations.

The weak form can be obtained from an energy formulation, or directly from the strong form, by applying the *Principle of Virtual Work* (PVW). The Principle of Virtual Work postulates that the virtual work produced by a system of forces at equilibrium, subjected to virtual displacements, $\delta \boldsymbol{u}$, is null, for arbitrary kinematically admissible displacement fields, $\boldsymbol{u}$.

Recall the body $\mathscr{B}$, from Section 2.1, which occupies the domain $\Omega \subset \mathscr{E}$ with boundary $\partial\Omega$ in the reference configuration, subjected to body forces per unit volume, $\boldsymbol{b}$, on its interior and surface tractions, $\boldsymbol{t}$, in its boundary.

### 2.6.1 Spatial description

In the Eulerian description, the total energy is given as

$$\Pi(\boldsymbol{u}) = \int_{\boldsymbol{\varphi}(\Omega)} \psi(\boldsymbol{u}) \mathrm{d}v - \int_{\boldsymbol{\varphi}(\Omega)} \boldsymbol{b} \cdot \boldsymbol{u} \mathrm{d}v - \int_{\boldsymbol{\varphi}(\partial\Omega)} \boldsymbol{t} \cdot \boldsymbol{u} \mathrm{d}a + \int_{\boldsymbol{\varphi}(\Omega)} \rho \ddot{\boldsymbol{u}} \cdot \boldsymbol{u} \mathrm{d}v. \tag{2.99}$$

Per the PVW, the mechanical virtual work is null, such that the following holds true,

$$\delta\Pi(\boldsymbol{u}, \delta\boldsymbol{u}) = \delta\Pi_{\text{int}}(\boldsymbol{u}, \delta\boldsymbol{u}) + \delta\Pi_{\text{ext}}(\boldsymbol{u}, \delta\boldsymbol{u}) + \delta\Pi_{\text{kin}}(\boldsymbol{u}, \delta\boldsymbol{u}) = 0, \quad \forall \delta\boldsymbol{u} \in \mathscr{V}, \tag{2.100}$$

where the internal virtual work is given as

$$\delta\Pi_{\text{int}}(\boldsymbol{u}, \delta\boldsymbol{u}) = \int_{\boldsymbol{\varphi}(\Omega)} [\boldsymbol{\sigma} : \nabla_{\boldsymbol{x}} \delta\boldsymbol{u}] \, \mathrm{d}v, \tag{2.101}$$

the virtual work due to external forces is given as

$$\delta\Pi_{\text{ext}}(\boldsymbol{u}, \delta\boldsymbol{u}) = -\int_{\boldsymbol{\varphi}(\Omega)} \boldsymbol{b} \cdot \delta\boldsymbol{u} \mathrm{d}v - \int_{\boldsymbol{\varphi}(\partial\Omega)} \boldsymbol{t} \cdot \delta\boldsymbol{u} \mathrm{d}a, \tag{2.102}$$

and the kinetic virtual work is given as

$$\delta\Pi_{\text{kin}}(\boldsymbol{u}, \delta\boldsymbol{u}) = \int_{\boldsymbol{\varphi}(\Omega)} \rho \ddot{\boldsymbol{u}} \cdot \delta\boldsymbol{u} \mathrm{d}v. \tag{2.103}$$

In the spatial description, the weak form of the momentum balance is

$$\int_{\boldsymbol{\varphi}(\Omega)} \left[\boldsymbol{\sigma} : \nabla_{\boldsymbol{x}} \delta \boldsymbol{u} - (\boldsymbol{b} - \rho \ddot{\boldsymbol{u}}) \cdot \delta \boldsymbol{u}\right] \mathrm{d}v - \int_{\boldsymbol{\varphi}(\partial\Omega)} \boldsymbol{t} \cdot \delta \boldsymbol{u} \mathrm{d}a = 0, \quad \forall \delta \boldsymbol{u} \in \mathcal{V}. \tag{2.104}$$

Neglecting the contribution from dynamic effects yields the variational equilibrium statement in the quasi-static configuration

$$\int_{\boldsymbol{\varphi}(\Omega)} [\boldsymbol{\sigma} : \nabla_{\boldsymbol{x}} \delta \boldsymbol{u} - \boldsymbol{b} \cdot \delta \boldsymbol{u}] \, \mathrm{d}v - \int_{\boldsymbol{\varphi}(\partial\Omega)} \boldsymbol{t} \cdot \delta \boldsymbol{u} \mathrm{d}a = 0, \quad \forall \delta \boldsymbol{u} \in \mathcal{V}. \tag{2.105}$$

The solution spaces $\mathcal{U}$ and $\mathcal{V}$ for the displacement and virtual displacement fields, respectively, are defined as

$$\mathcal{U}^i \equiv \{\boldsymbol{u} \in \left[H^1(\Omega^i)\right]^d | \boldsymbol{u}^i = \bar{\boldsymbol{u}}^i \text{ in } \gamma_u^i\}, \tag{2.106}$$

$$\mathcal{V}^i \equiv \{\delta \boldsymbol{u} \in \left[H^1(\Omega^i)\right]^d | \delta \boldsymbol{u}^i = \boldsymbol{0} \text{ in } \gamma_u^i\}, \tag{2.107}$$

where $\mathcal{U}^i$ satisfies the Dirichlet boundary conditions, $\left[H^1(\Omega^i)\right]$ represents the n-dimensional Sobolev functional space over $\Omega^i$, containing all square integrable first-order derivatives in the current configuration (Carneiro (2021)). For simplicity, the following is considered

$$\boldsymbol{u} \equiv \boldsymbol{u}^s \times \boldsymbol{u}^m, \tag{2.108}$$

$$\delta \boldsymbol{u} \equiv \delta \boldsymbol{u}^s \times \delta \boldsymbol{u}^m, \tag{2.109}$$

$$\mathcal{U} \equiv \mathcal{U}^s \times \mathcal{U}^m, \tag{2.110}$$

$$\mathcal{V} \equiv \mathcal{V}^s \times \mathcal{V}^m. \tag{2.111}$$

### 2.6.2 Equivalence between weak and strong equilibrium statements

For a quasi-static framework, this Section derives the strong momentum balance statement expressed in the spatial description from its weak form, with the opposite derivation achieved by performing the same steps in reverse.

For a sufficiently smooth stress field $\boldsymbol{\sigma}$, the Principle of Virtual Work (Equation (2.105)) is equivalent to the strong momentum balance statement (Equations (2.78) and (2.79)). For a sufficiently regular and symmetric stress field, the chain rule is given as

$$\boldsymbol{\sigma} : \nabla_{\boldsymbol{x}}(\delta \boldsymbol{u}) = \mathrm{div}_{\boldsymbol{x}}(\boldsymbol{\sigma} \delta \boldsymbol{u}) - (\mathrm{div}_{\boldsymbol{x}} \boldsymbol{\sigma}) \cdot \delta \boldsymbol{u}. \tag{2.112}$$

Substituting Equation (2.112) into Equation (2.105) yields

$$\int_{\boldsymbol{\varphi}(\Omega)} [\mathrm{div}_{\boldsymbol{x}}(\boldsymbol{\sigma} \delta \boldsymbol{u}) - (\mathrm{div}_{\boldsymbol{x}} \boldsymbol{\sigma} + \boldsymbol{b}) \cdot \delta \boldsymbol{u}] \, \mathrm{d}v - \int_{\boldsymbol{\varphi}(\partial\Omega)} \boldsymbol{t} \cdot \delta \boldsymbol{u} \mathrm{d}a = 0, \quad \forall \delta \boldsymbol{u} \in \mathcal{V}. \tag{2.113}$$

The Gauss or divergence theorem states that

$$\int_{\boldsymbol{\varphi}(\Omega)} \mathrm{div}_{\boldsymbol{x}}(\boldsymbol{\sigma} \delta \boldsymbol{u}) \mathrm{d}v = \int_{\boldsymbol{\varphi}(\partial\Omega)} \boldsymbol{\sigma} \delta \boldsymbol{u} \cdot \boldsymbol{n} \mathrm{d}v. \tag{2.114}$$

Since the Cauchy stress tensor is symmetric, $\boldsymbol{\sigma} \delta \boldsymbol{u} \cdot \boldsymbol{n} = \boldsymbol{\sigma} \boldsymbol{n} \cdot \delta \boldsymbol{u}$, Equation (2.113) becomes

$$\int_{\boldsymbol{\varphi}(\Omega)} (\mathrm{div}_{\boldsymbol{x}} \boldsymbol{\sigma} + \boldsymbol{b}) \cdot \delta \boldsymbol{u} \mathrm{d}v + \int_{\boldsymbol{\varphi}(\partial\Omega)} (\boldsymbol{t} - \boldsymbol{\sigma} \boldsymbol{n}) \cdot \delta \boldsymbol{u} \mathrm{d}a = 0, \quad \forall \delta \boldsymbol{u} \in \mathcal{V}. \tag{2.115}$$

From the fundamental theorem of variational calculus, each term inside brackets must vanish within the respective domain, such that

$$\mathrm{div}_{\boldsymbol{x}} \boldsymbol{\sigma} + \boldsymbol{b} = \boldsymbol{0}, \quad \text{in } \boldsymbol{\varphi}(\Omega), \tag{2.116}$$

$$\boldsymbol{t} - \boldsymbol{\sigma} \cdot \boldsymbol{n} = \boldsymbol{0}, \quad \text{on } \boldsymbol{\varphi}(\partial\Omega), \tag{2.117}$$

where the latter Equation is the *Cauchy's theorem*.

## 2.7 The quasi-static initial boundary value problem

The general formulation of the constitutive initial value problem was presented in Section 2.5.2. Taking into consideration the weak form equilibrium statements stated in Section 2.6, the initial boundary value problem for a quasi-static framework can be obtained, under finite deformations.

Reintroducing the body $\mathscr{B}$ of Section 2.1, the history of prescribed body forces in its interior is given as

$$\boldsymbol{b}(\boldsymbol{x},t), \quad t\in[t_0,t_f]. \tag{2.118}$$

The following boundary conditions are also imposed.

- Natural boundary condition. The history of prescribed tractions forces acting on a material point $\boldsymbol{X}$ on the boundary $\partial\Omega_t$, in the reference configuration, is given as

$$\boldsymbol{t}(\boldsymbol{x},t), \quad t\in[t_0,t_f]. \tag{2.119}$$

- Essential boundary condition. The prescribed displacement field, $\bar{\boldsymbol{u}}$, over the boundary $\partial\Omega_u$, in the reference configuration, is given as

$$\bar{\boldsymbol{\varphi}}(\boldsymbol{X},t)=\boldsymbol{X}+\bar{\boldsymbol{u}}(\boldsymbol{X},t), \quad t\in[t_0,t_f]. \tag{2.120}$$

  As stated in de Souza Neto et al. (2008), it is assumed that $\partial\Omega_t\cap\partial\Omega_u=\varnothing$ to simplify the problem. Therefore, the set of *kinematically admissible displacements* of $\mathscr{B}$, which satisfy the essential boundary condition, is given as

$$\mathscr{K}=\{\boldsymbol{u}:\Omega\times\mathscr{R}\rightarrow\mathscr{U}\,|\,\boldsymbol{u}(\boldsymbol{X},t)=\bar{\boldsymbol{u}}(\boldsymbol{X},t),t\in[t_0,t_f],\boldsymbol{X}\in\partial\Omega_u\}. \tag{2.121}$$

The body $\mathscr{B}$ is assumed to be constituted of a generic material, characterised by a set of internal variables, known at the initial time instance $t_0$, given as

$$\boldsymbol{\alpha}(\boldsymbol{X},t)=\boldsymbol{\alpha}_0(\boldsymbol{X}) \tag{2.122}$$

In the spatial description, the fundamental quasi-static initial boundary value problem is stated as follows (de Souza Neto et al. (2008)).

**Problem 2.3** (**The spatial quasi-static initial boundary value problem**). *Find a kinematically admissible displacement function, $\boldsymbol{u}\in\mathscr{K}$, such that, for all $t\in[t_0,t_f]$, the virtual work equation is satisfied*

$$\int_{\boldsymbol{\varphi}(\Omega,t)}[\boldsymbol{\sigma}(t):\nabla_{\boldsymbol{x}}\delta\boldsymbol{u}-\boldsymbol{b}(t)\cdot\delta\boldsymbol{u}]\,dv-\int_{\boldsymbol{\varphi}(\partial\Omega_t,t)}\boldsymbol{t}(t)\cdot\delta\boldsymbol{u}\,da=0, \quad \forall\delta\boldsymbol{u}\in\mathscr{V}_t. \tag{2.123}$$

*The space of virtual displacements at time t is defined by*

$$\mathscr{V}_t=\left\{\delta\boldsymbol{u}:\boldsymbol{\varphi}(\Omega,t)\rightarrow\mathscr{U}\,|\,\delta\boldsymbol{u}=\boldsymbol{0}\ on\ \boldsymbol{\varphi}(\partial\Omega_u,t)\right\}, \tag{2.124}$$

*and, at each point of $\mathscr{B}$, the Cauchy stress is given by*

$$\boldsymbol{\sigma}(t)=\frac{1}{J(t)}\boldsymbol{P}(t)\boldsymbol{F}(t)^T, \tag{2.125}$$

*where $\boldsymbol{P}(t)$ is the solution of constitutive initial value problem (Problem 2.1) with prescribed deformation gradient*

$$\boldsymbol{F}(t)=\nabla_{\boldsymbol{X}}\boldsymbol{\varphi}(\boldsymbol{X},t)=\boldsymbol{I}+\nabla_{\boldsymbol{X}}\boldsymbol{u}(\boldsymbol{X},t). \tag{2.126}$$

## 2.8 Finite Element Method

The Finite Element Method provides a numerical solution to the weak form of the quasi-static initial boundary value problem, as stated in general form in Section 2.7. Temporal discretisation converts the time-continuum constitutive equations into incremental ones. Spatial discretisation divides the domain into finite elements, where interpolation functions translate the weak statement in terms of nodal values. Thus, the displacement-based Finite Element Method provides a set of incremental, algebraic equations which can be solved numerically, such as by the Newton-Raphson iterative scheme.

### 2.8.1 Domain spatial discretisation

Let a given body $\mathscr{B}$ be defined by a spatial domain, $\Omega$, approximated to a discretised solid domain, $\Omega^d$, given as the set of all non-overlapping element subdomains, such that

$$\Omega \approx \Omega^d = \bigcup_{e=1}^{n_e} \Omega^e, \tag{2.127}$$

where $n_e$ is the total number of finite elements which occupy the region $\Omega^e$.

Each element, $e$, is defined by a set of $n_n$ nodes and *shape*, or *interpolation*, functions, which must comply with

$$N_i^e(\boldsymbol{x}_i) = 1, \tag{2.128}$$

$$N_i^e(\boldsymbol{x}_j) = 0, \quad \text{for } i \neq j. \tag{2.129}$$

Each nodal value for a generic vectorial field is interpolated inside the element from their nodal values using shape functions, such that

$$\boldsymbol{a}(\boldsymbol{x}) \equiv \sum_{i=1}^{n_n} N_i^e(\boldsymbol{x})\mathbf{a}_i, \quad \boldsymbol{x} \in \Omega^e, \tag{2.130}$$

where $\mathbf{a}_i$ represents the nodal value, and $N_i^e(\boldsymbol{x})$ denotes the shape function value for node $i$ of element $e$. Similarly, each nodal value for a generic vectorial field can also be interpolated using global shape functions, such that

$$\boldsymbol{a}(\boldsymbol{x}) = \sum_{i=1}^{n_p} N_i(\boldsymbol{x})\mathbf{a}_i, \quad \boldsymbol{x} \in \Omega^d, \tag{2.131}$$

where $n_p < n_n \cdot n_e$ is the total number of nodes over the discretised domain $\Omega^d$.

The values of a generic vectorial field for each nodal point in the entire domain are written as

$$\mathbf{a} = \begin{Bmatrix} \mathbf{a}_1 \\ \mathbf{a}_2 \\ \vdots \\ \mathbf{a}_{n_p} \end{Bmatrix}. \tag{2.132}$$

The global shape functions for a generic element may be stored as a *global interpolation matrix* given as

$$\mathbf{N}(\boldsymbol{x}) = \begin{bmatrix} \text{diag}[N_1(\boldsymbol{x})] & \text{diag}[N_2(\boldsymbol{x})] & \dots & \text{diag}[N_{n_p}(\boldsymbol{x})] \end{bmatrix}, \tag{2.133}$$

where the diagonal matrix has dimensions $n_{\text{DoF}} \times n_{\text{DoF}}$ is written as

$$\text{diag}[N_i(\boldsymbol{x})] = \begin{bmatrix} N_i(\boldsymbol{x}) & 0 & \dots & 0 \\ 0 & N_i(\boldsymbol{x}) & \dots & 0 \\ \vdots & \vdots & \ddots & \vdots \\ 0 & 0 & \dots & N_i(\boldsymbol{x}) \end{bmatrix}_{n_{\text{DoF}} \times n_{\text{DoF}}}. \tag{2.134}$$

Therefore, the generic vectorial field is given as

$$\boldsymbol{a}(\boldsymbol{x}) = \mathbf{N}(\boldsymbol{x})\mathbf{a}. \tag{2.135}$$

For two-dimensional (2D) elements, the global shape functions become

$$\mathbf{N}(\boldsymbol{x}) = \left[\begin{array}{cc|cc|c|cc} N_1(\boldsymbol{x}) & 0 & N_2(\boldsymbol{x}) & 0 & \cdots & N_{n_p}(\boldsymbol{x}) & 0 \\ 0 & N_1(\boldsymbol{x}) & 0 & N_2(\boldsymbol{x}) & & 0 & N_{n_p}(\boldsymbol{x}) \end{array}\right]. \tag{2.136}$$

The global discrete symmetric gradient operator (or strain-displacement matrix) for a 2D problem is given as

$$\mathbf{B} = \left[\begin{array}{cc|cc|c|cc} \frac{\partial N_1}{\partial x} & 0 & \frac{\partial N_2}{\partial x} & 0 & \cdots & \frac{\partial N_{n_p}}{\partial x} & 0 \\ 0 & \frac{\partial N_1}{\partial y} & 0 & \frac{\partial N_2}{\partial y} & & 0 & \frac{\partial N_{n_p}}{\partial y} \\ \frac{\partial N_1}{\partial y} & \frac{\partial N_1}{\partial x} & \frac{\partial N_2}{\partial y} & \frac{\partial N_2}{\partial x} & & \frac{\partial N_{n_p}}{\partial y} & \frac{\partial N_{n_p}}{\partial x} \end{array}\right]. \tag{2.137}$$

The global finite element asymmetric gradient operator for a 2D problem is similarly given as

$$\mathbf{G} = \left[\begin{array}{cc|cc|c|cc} \frac{\partial N_1}{\partial x} & 0 & \frac{\partial N_2}{\partial x} & 0 & \cdots & \frac{\partial N_{n_p}}{\partial x} & 0 \\ 0 & \frac{\partial N_1}{\partial x} & 0 & \frac{\partial N_2}{\partial x} & & 0 & \frac{\partial N_{n_p}}{\partial x} \\ \frac{\partial N_1}{\partial y} & 0 & \frac{\partial N_2}{\partial y} & 0 & & \frac{\partial N_{n_p}}{\partial y} & 0 \\ 0 & \frac{\partial N_1}{\partial y} & 0 & \frac{\partial N_2}{\partial y} & & 0 & \frac{\partial N_{n_p}}{\partial y} \end{array}\right]. \tag{2.138}$$

### 2.8.2 Discretisation of the equilibrium equations

With the definition of a generic discretised vectorial field of Equation (2.135), the discretised weak statement can be obtained from Equation (2.105)

$$\int_{\boldsymbol{\varphi}(\Omega^d)} [\boldsymbol{\sigma} : \nabla_{\boldsymbol{x}} \mathbf{N}\delta\mathbf{u} - \boldsymbol{b}\cdot\mathbf{N}\delta\mathbf{u}]\,\mathrm{d}v - \int_{\boldsymbol{\varphi}(\partial\Omega^d)} \boldsymbol{t}\cdot\mathbf{N}\delta\mathbf{u}\mathrm{d}a = 0, \quad \forall\delta\mathbf{u}\in\mathcal{V}^d, \tag{2.139}$$

with the inertia effects neglected, and where $\mathcal{V}^d$ denotes the discretised virtual displacement space. The Equation above can be rewritten as

$$\int_{\boldsymbol{\varphi}(\Omega^d)} \left[\boldsymbol{\sigma}^T\mathbf{B}\delta\mathbf{u} - \mathbf{N}^T\boldsymbol{b}\cdot\delta\mathbf{u}\right]\mathrm{d}v - \int_{\boldsymbol{\varphi}(\partial\Omega^d)} \mathbf{N}^T\boldsymbol{t}\cdot\delta\mathbf{u}\mathrm{d}a = 0, \quad \forall\delta\mathbf{u}\in\mathcal{V}^d, \tag{2.140}$$

where $\boldsymbol{\sigma}$ represents the vector representation of the Cauchy stress tensor. Finally, the discretised spatial weak equilibrium equation is now given as

$$\left\{\int_{\boldsymbol{\varphi}(\Omega^d)} \left[\mathbf{B}^T\boldsymbol{\sigma} - \mathbf{N}^T\boldsymbol{b}\right]\mathrm{d}v - \int_{\boldsymbol{\varphi}(\partial\Omega^d)} \mathbf{N}^T\boldsymbol{t}\mathrm{d}a\right\}^T \delta\mathbf{u} = 0, \quad \forall\delta\mathbf{u}\in\mathcal{V}^d. \tag{2.141}$$

The relation above can be reformulated to provide the finite element discrete boundary value problem

$$\mathbf{f}^{\mathrm{int}}(\mathbf{u}) - \mathbf{f}^{\mathrm{ext}} = \mathbf{0}, \tag{2.142}$$

where the nodal internal and external force vectors are, respectively,

$$\mathbf{f}^{\mathrm{int}} = \int_{\boldsymbol{\varphi}(\Omega^d)} \mathbf{B}^T\boldsymbol{\sigma}\mathrm{d}v = \mathop{\mathsf{A}}_{e=1}^{n_e} \mathbf{f}_e^{\mathrm{int}}, \tag{2.143}$$

$$\mathbf{f}^{\mathrm{ext}} = \int_{\boldsymbol{\varphi}(\Omega^d)} \mathbf{N}^T\boldsymbol{b}\mathrm{d}v + \int_{\boldsymbol{\varphi}(\partial\Omega^d)} \mathbf{N}^T\boldsymbol{t}\mathrm{d}a = \mathop{\mathsf{A}}_{e=1}^{n_e} \mathbf{f}_e^{\mathrm{ext}}. \tag{2.144}$$

The corresponding element force vectors are given as

$$\mathbf{f}_e^{\text{int}} = \int_{\boldsymbol{\varphi}(\Omega^e)} (\mathbf{B}^e)^T \boldsymbol{\sigma} \mathrm{d}v, \tag{2.145}$$

$$\mathbf{f}_e^{\text{ext}} = \int_{\boldsymbol{\varphi}(\Omega^e)} (\mathbf{N}^e)^T \boldsymbol{b} \mathrm{d}v + \int_{\boldsymbol{\varphi}(\partial\Omega^e)} (\mathbf{N}^e)^T \boldsymbol{t} \mathrm{d}a, \tag{2.146}$$

where $(\cdot)^e$ denotes the elemental counterpart to the globally defined operators **N**, **B** and **G**.

### 2.8.3 Time discretisation

Most engineering problems are characterised by path-dependent constitutive models, i.e., the material state of the continuum body is defined by its current deformation and its deformation history. As mentioned in Section 2.5, internal variables depict the intrinsic information about a material state. Time, or *pseudo-time*, discretisation over a domain $[t_0, t_f]$ attempts to incrementally solve the quasi-static initial boundary value problem, using an implicit or explicit time integration scheme.

The Cauchy stress tensor is given as

$$\boldsymbol{\sigma}_{n+1} = \hat{\boldsymbol{\sigma}}(\boldsymbol{F}_{n+1}, \boldsymbol{\alpha}_n), \tag{2.147}$$

where $\hat{\boldsymbol{\sigma}}$ is the incremental constitutive functional, $n$ denotes the time-discrete increment number, $\boldsymbol{\alpha}_n$ represents the set of internal variables at time $t_n$, and $\boldsymbol{F}_n$ is the deformation gradient at time $t_n$.

For infinitesimal deformations, the approximate incremental constitutive functions are given with respect to the infinitesimal strain tensor, such that

$$\boldsymbol{\sigma}_{n+1} = \hat{\boldsymbol{\sigma}}(\boldsymbol{\varepsilon}_{n+1}, \boldsymbol{\alpha}_n), \tag{2.148}$$

$$\boldsymbol{\alpha}_{n+1} = \hat{\boldsymbol{\alpha}}(\boldsymbol{\varepsilon}_{n+1}, \boldsymbol{\alpha}_n). \tag{2.149}$$

The incremental boundary value problem can be expressed in the following problem (de Souza Neto et al. (2008)).

**Problem 2.4** (**The incremental quasi-static initial boundary value problem**). *Given the set $\boldsymbol{\alpha}_n$ of internal variables at time $t_n$, find a displacement field $\boldsymbol{u}_{n+1} \in \mathcal{K}_{n+1}$ such that*

$$\int_{\boldsymbol{\varphi}(\Omega)} [\hat{\boldsymbol{\sigma}}(\boldsymbol{F}_{n+1}, \boldsymbol{\alpha}_n) : \nabla_{\boldsymbol{x}} \delta\boldsymbol{u} - \boldsymbol{b}_{n+1} \cdot \delta\boldsymbol{u}]\, dv - \int_{\boldsymbol{\varphi}(\partial\Omega)} \boldsymbol{t}_{n+1} \cdot \delta\boldsymbol{u} da = 0, \quad \forall \delta\boldsymbol{u} \in \mathcal{V}, \tag{2.150}$$

*for any $\delta\boldsymbol{u} \in \mathcal{V}$, where $\boldsymbol{b}_{n+1}$ and $\boldsymbol{t}_{n+1}$ are the body force and surface traction fields prescribed at time $t_{n+1}$.*

### 2.8.4 Incremental finite element solution

Discretizing the equilibrium Equation (2.150), the residual is given as

$$\mathbf{r}(\mathbf{u}_{n+1}) \equiv \mathbf{f}^{\text{int}}(\mathbf{u}_{n+1}) - \mathbf{f}_{n+1}^{\text{ext}} = \mathbf{0}, \tag{2.151}$$

which must be solved for the nodal displacement vector $\mathbf{u}_{n+1}$ to ensure the residual vanishes.

Recalling Equations (2.143) and (2.144), the internal and external force vectors are assembled from their element counterparts, such that

$$\mathbf{f}_{e,n+1}^{\text{int}} = \int_{\boldsymbol{\varphi}(\Omega^e)} (\mathbf{B}^e)^T \hat{\boldsymbol{\sigma}}(\boldsymbol{F}_{n+1}, \boldsymbol{\alpha}_n) \mathrm{d}v \tag{2.152}$$

$$\mathbf{f}_{e,n+1}^{\text{ext}} = \int_{\boldsymbol{\varphi}(\Omega^e)} (\mathbf{N}^e)^T \boldsymbol{b}_{n+1} \mathrm{d}v + \int_{\boldsymbol{\varphi}(\partial\Omega^e)} (\mathbf{N}^e)^T \boldsymbol{t}_{n+1} \mathrm{d}a. \tag{2.153}$$

To solve the non-linear Equation (2.151), the iterative Newton-Raphson scheme is employed, as it provides a quadratic convergence rate. For each iteration, the linearised virtual work in the spatial description, is discretised as

$$\left\{\int_{\boldsymbol{\varphi}(\Omega^d)} \mathbf{G})^T \mathbf{a}\mathbf{G}\mathrm{d}v\right\}\Delta\mathbf{u}\cdot\delta\mathbf{u} = -\left\{\int_{\boldsymbol{\varphi}(\Omega^d)}\left[\mathbf{B}^T\boldsymbol{\sigma} - \mathbf{N}^T\boldsymbol{b}\mathrm{d}v\right] - \int_{\boldsymbol{\varphi}(\partial\Omega^d)}\mathbf{N}^T\boldsymbol{t}\mathrm{d}a\right\}\cdot\delta\mathbf{u}, \quad \forall\delta\mathbf{u}\in\mathcal{V}, \tag{2.154}$$

where $\mathbf{a}$ is the spatial tangent modulus.

The above equation must hold true for any admissible virtual displacement $\delta\mathbf{u}$, such that

$$\left\{\int_{\boldsymbol{\varphi}(\Omega^d)} \mathbf{G}^T\mathbf{a}\mathbf{G}\mathrm{d}v\right\}\Delta\mathbf{u} = -\left\{\int_{\boldsymbol{\varphi}(\Omega^d)}\left[\mathbf{B}^T\boldsymbol{\sigma} - \mathbf{N}^T\boldsymbol{b}\mathrm{d}v\right] - \int_{\boldsymbol{\varphi}(\partial\Omega^d)}\mathbf{N}^T\boldsymbol{t}\mathrm{d}a\right\}, \tag{2.155}$$

where $\mathbf{G}$ is the global discrete spatial gradient operator.

For the increment $n+1$, the initial guess for the displacement vector is the last converged value,

$$\mathbf{u}_{n+1}^{(0)} = \mathbf{u}_n, \tag{2.156}$$

and for each Newton-Raphson iteration $j$, within the same time increment $n+1$, $\Delta\mathbf{u}^{(k)}$ is added as a Newton correction to the global displacement, such that

$$\mathbf{u}_{n+1}^{(j)} = \mathbf{u}_n^{(j-1)} + \Delta\mathbf{u}^{(j)}, \tag{2.157}$$

where $\Delta\mathbf{u}^{(j)}$ is obtained by solving

$$\mathbf{K}_T^{(j-1)}\Delta\mathbf{u}^{(j)} = -\mathbf{r}\left(\mathbf{u}_{n+1}^{(j-1)}\right), \tag{2.158}$$

the residual (or out-of-balance force) vector is given as

$$\mathbf{r}^{j-1} \equiv \mathbf{f}^{\mathrm{int}}\left(\mathbf{u}_{n+1}^{(k-1)}\right) - \mathbf{f}_{n+1}^{\mathrm{ext}}, \tag{2.159}$$

and the global tangent stiffness matrix is written as

$$\mathbf{K}_T^{(j-1)} = \int_{\boldsymbol{\varphi}(\Omega^d)} \mathbf{G}^T\mathbf{a}\mathbf{G}\mathrm{d}v = \left.\frac{\partial\mathbf{r}}{\partial\mathbf{u}_{n+1}}\right|_{\mathbf{u}_{n+1}^{(j-1)}}. \tag{2.160}$$

The global stiffness matrix is given as the assembly of its elemental counterparts

$$\mathbf{K}_T = \bigwedge_{e=1}^{n_e}\mathbf{K}_e. \tag{2.161}$$

The Newton-Raphson iterations are repeated until after iteration $m$, when the following convergence criteria is satisfied

$$\left|\frac{\mathbf{r}^{(m)}}{\mathbf{f}_{n+1}^{\mathrm{ext}}}\right| \leq \epsilon_{\mathrm{tol}}, \tag{2.162}$$

where $\epsilon_{\mathrm{tol}}$ is a sufficiently small specified equilibrium convergence tolerance, such that $\mathbf{u}_{n+1} = \mathbf{u}_{n+1}^{(m)}$.

### 2.8.5 Gaussian quadrature

The integral of a generic quantity $\boldsymbol{a}$ is given as the sum over a finite number of integration points $n_{gp}$, such that

$$\int_\Omega \boldsymbol{a}(\boldsymbol{x})\mathrm{d}v = \sum_{gp=1}^{n_{gp}} \boldsymbol{a}(\boldsymbol{\xi}_{gp})\, w_{gp} J_{gp}, \tag{2.163}$$

where $\boldsymbol{\xi}_{gp}$ are the coordinates of the Gauss integration points points, defined a priori in the natural coordinate system, with $w_{gp}$ as the corresponding weight, and

$$J_{gp} = \det\left[\frac{\partial \boldsymbol{x}}{\partial \boldsymbol{\xi}}\right] \tag{2.164}$$

is the determinant of the Jacobian that maps the physical to natural space.

For continuum elements, it is common to numerically integrate the internal force vector and the stiffness tangent matrix using *Gaussian quadrature* (Vieira de Carvalho (2023)). Using the Gaussian quadrature, a polynomial of order $2n+1$ is integrated exactly for at least $n$ function evaluations (Ramm (1983)).

# Chapter 3

# Cohesive zone model for fracture

This Chapter explores the topic of *Cohesive Zone Models* (CZM), starting with a brief introduction to the cohesive zone model in Section 3.1, followed by the general formulation of the boundary value problem with cohesive elements in Section 3.3. Additionally, an overview of the constitutive model is provided in Section 3.3.4, where the potential-based approach for the formulation of thermodynamically consistent constitutive equations is established, detailing all terms related to cohesive zone models. The formulations presented in this Chapter are primarily based on the work by Vieira de Carvalho (2023) and Park and Paulino (2012). For more in-depth references, the interested reader is referred to Mosler and Scheider (2011), Needleman (1987), Park and Paulino (2011), Park et al. (2009), Turon et al. (2007).

## 3.1 Introduction to the cohesive zone model

Fracture is often the cause of failure in engineering materials, solids and structures. Ever since Griffith's seminal work in 1921, *fracture mechanics* has been established has a relevant field of research within solid mechanics. Understanding the failure mechanisms that arise during fracture, such as cracks, shear bands or delaminations, is thus essential for accurate material modelling and for predicting how and why components ultimately fail.

To address the issue of material separation, several numerical approaches may be followed, such as those which simulate the crack as a smeared zone (*continuum damage mechanics* and the *phase-field* method, discussed later in Chapter 4), or those that simulate the crack as a discrete entity, such as the *Extended Finite Element Method* (XFEM), or Cohesive Zone Models.

Introduced by Dugdale (1960) and Barenblatt (1962), CZMs address the stress singularity which occurs at the crack tip in linear elastic fracture mechanics by simulating a nonlinear explicit fracture process zone, on the finite element mesh, ahead of the physical crack tip (Park and Paulino (2012)). In a CZM-based continuum approach, the solid is split into two or more sections. The continuum elements are defined by a stress-strain relation, independent of the chosen constitutive model, while the cohesive elements are inserted in predefined crack paths, and are governed by a *traction-separation law* (TSL), described with respect to the current configuration. In contrast with smeared crack approaches, the elastic response of the model only depends on the properties of the bulk material, neglecting the contribution from the cohesive elements, once the stress associated with the separation of the interface reaches a certain threshold.

Implementing CZM allows handling crack initiation, branching, propagation, and coalescence, if the most likely crack locations are known a priori when formulating the problem, such as the case of fibre-matrix cracking in composite materials. Due to its discrete approach to fracture, the failure zone has null thickness, and is represented as a line in 2D problems, and as a surface in 3D problems. Thus the resulting length-scale is infinitely smaller than that of overall model (Mosler and Scheider (2011)).

Although CZMs bridge the gap between continuum models, and fracture mechanics, some aspects need to be considered, such as the dependence of the crack path on the discretised mesh. In contrast with XFEM, proposed by Moës et al. (1999), which used discontinuous shape functions, and are thus mesh-agnostic, CZMs require knowledge a priori of the crack paths, unless adaptative remeshing techniques are employed (Vieira de Carvalho (2023)).

## 3.2 On the use of CZMs to model interface and bulk fracture

As noted above, a known limitation of intrinsic cohesive zone formulations is the need to define possible crack paths a priori. Two approaches may be employed to overcome address this issue. The first is an extrinsic (adaptative) strategy where bulk continuum elements are split and cohesive elements are inserted on-the-fly once a given fracture criterion is met (see Marusich and Ortiz (1995), Ortiz and Pandolfi (1999)). Implementation generally requires defining a crack-growth criteria (e.g., reaching a critical stress or a critical strain at a critical distance from the crack tip), and a crack-tracking logic to identify the crack front and update the element connectivities and manage node duplication. Adaptive remeshing techniques allow for crack branching and crack kinking (Ortiz and Pandolfi (1999)), but introduce additional implementation complexity.

The second is an intrinsic approach, where zero-thickness cohesive elements are pre-inserted between adjacent continuum elements across the entire domain (or within large pre-selected regions of interest). In this formulation, the mesh already contains the potential fracture surfaces required to represent intra-material (bulk) cracking, and therefore avoids on-the-fly topology changes. This approach is well established in the literature (e.g., Infuso et al. (2014), Xu and Needleman (1994)). Although new cohesive interface elements must be defined a priori along the boundaries of the bulk elements, the location and propagation path of the possible cracks remain unrestricted in the sense that cracks may originate from pre-existing defects or nucleate as new and propagate along new arbitrary paths (Xu and Needleman (1994)). This removes the need for adaptive remeshing and renumbering of nodes and elements at each time step. A limitation is the required initial linear branch in the traction-separation law, which may introduce artificial compliance (Infuso et al. (2014))

Some authors, such as Aduloju and Truster (2019), Paggi and Wriggers (2012), Shahzamanian et al. (2023), detail strategies to implement the pre-insertion of cohesive elements, the duplication of shared nodes, the orientation of the interface normals, and the assignment of element connectivities. These authors also discuss automation steps for complex microstructures and the inclusion of boundary conditions.

## 3.3 CZM for the onset and propagation of fracture

Elaborating upon the continuous formulation presented in Chapter 2, this Section details the framework for solving the quasi-static initial boundary value problem, with the inclusion of cohesive models, by employing the Finite Element Method within an iterative scheme.

Within a finite element framework, CZMs can be implemented via cohesive surfaces (contact-based) methods, or cohesive (interface) elements. The cohesive surface approach employs a traction–separation law directly in inter-element faces (similar to the *virtual crack closure technique* (VCCT)), activating when local separation exceeds a threshold and enabling automatic crack initiation. In contrast, cohesive elements are zero-thickness elements inserted into the mesh. The CZM implementation in `LINKS` and employed in this Master's thesis is the cohesive element approach, which is discussed in this Section.

### 3.3.1 Boundary value problem

Recall the weak statement of the quasi-static initial boundary value problem, in the spatial description, stated in Equation (2.105). Incorporating cohesive elements yields

$$\int_{\boldsymbol{\varphi}(\Omega)} [\boldsymbol{\sigma} : \nabla_{\boldsymbol{x}} \delta \boldsymbol{u} - \boldsymbol{b} \delta \boldsymbol{u}] \, \mathrm{d}v - \int_{\boldsymbol{\varphi}(\partial\Omega)} \boldsymbol{t} \delta \boldsymbol{u} \mathrm{d}a + \int_{\boldsymbol{\varphi}(\Gamma)} \boldsymbol{t}_c \delta \boldsymbol{\Delta} \mathrm{d}a = 0, \quad \forall \delta \boldsymbol{u} \in \mathcal{V}. \tag{3.1}$$

with the last term due to the contribution of the cohesive elements to the internal work, computed as

$$\Pi(\boldsymbol{\Delta}) = \int_{\boldsymbol{\varphi}(\partial\Omega)} \boldsymbol{t}_c \boldsymbol{\Delta} \mathrm{d}a, \tag{3.2}$$

where $\boldsymbol{t}_c$ is the cohesive stress vector, $\boldsymbol{\Delta}$ is the separation vector, with $\delta\boldsymbol{\Delta}$ as the corresponding virtual separation vector, and $\delta\boldsymbol{u}$ is the virtual displacements associated with the space of admissible virtual displacements $\mathcal{V}$ (see Equation (2.107)). Rearranging Equation (3.1) as

$$\int_{\boldsymbol{\varphi}(\Omega)} \boldsymbol{\sigma} : \nabla_{\boldsymbol{x}} \delta \boldsymbol{u} \mathrm{d}v + \int_{\boldsymbol{\varphi}(\Gamma)} \boldsymbol{t}_c \delta \boldsymbol{\Delta} \mathrm{d}a = \int_{\boldsymbol{\varphi}(\Omega)} \boldsymbol{b} \delta \boldsymbol{u} \mathrm{d}v + \int_{\boldsymbol{\varphi}(\partial\Omega)} \boldsymbol{t} \delta \boldsymbol{u} \mathrm{d}a, \quad \forall \delta \boldsymbol{u} \in \mathcal{V} \tag{3.3}$$

allow us to identify the internal and external virtual work as the left and right hand side terms, respectively. The first term of the internal work refers to the contribution of the internal force of the bulk material acting on the deformed region $\boldsymbol{\varphi}(\Omega)$ occupied by the body $\mathscr{B}$, which is null in a cohesive element. The second term adds the effect of the internal cohesive force acting on the fracture surface $\boldsymbol{\varphi}(\Gamma)$ delimited by the cohesive element, and null in a continuum element.

### 3.3.2 Finite element formulation

Following closely the implementation detailed by Park and Paulino (2012), it is possible to obtain the tangent stiffness matrix and corresponding internal force vector related to the cohesive elements.

Consider the displacement field in the global coordinate system as

$$\boldsymbol{u}(\boldsymbol{X}) = \mathbf{N}\mathbf{u}, \tag{3.4}$$

where $\boldsymbol{u}$ is the global displacement field, $\mathbf{N}$ is the global interpolation matrix defined in Equation (2.133), and $\mathbf{u}$ are the global nodal displacements, in the global coordinate system.

Similarly, the nodal displacements in the local coordinate system, $\underline{\mathbf{u}}$, are given as

$$\underline{\mathbf{u}} = \mathbf{R}\mathbf{u}, \tag{3.5}$$

where $\mathbf{R}$ is the rotation matrix.

With that in mind, the nodal separation vector in the local coordinate system is expressed as

$$\underline{\boldsymbol{\Delta}} = \mathbf{L}\underline{\mathbf{u}}, \tag{3.6}$$

where $\mathbf{L}$ is the local displacement-separation matrix.

Similarly to the displacement field, the separation vector along a cohesive surface element in the local coordinate system

$$\boldsymbol{\Delta}(\underline{\boldsymbol{x}}) = \mathbf{N}\underline{\boldsymbol{\Delta}} \tag{3.7}$$

can also be interpolated from the local nodal separation vector $\underline{\boldsymbol{\Delta}}$ using the shape functions.

In alternative, the separation vector in local coordinates can be written as

$$\boldsymbol{\Delta}(\underline{\boldsymbol{x}}) = \mathbf{N}\mathbf{L}\mathbf{R}\mathbf{u}, \tag{3.8}$$

where $\mathbf{B}_c \equiv \mathbf{NLR}$ is the global displacement-separation matrix which also expresses the relation between the virtual separation vector and the nodal virtual displacement vector as

$$\delta\boldsymbol{\Delta} = \mathbf{B_c}\delta\mathbf{u}. \tag{3.9}$$

With cohesive elements, the spatially discretised weak statement of Equation (3.1) becomes

$$\left\{\int_{\varphi(\Omega^d)} \left[\mathbf{B}^T\boldsymbol{\sigma} - \mathbf{N}^T\boldsymbol{b}\right] \mathrm{d}v - \int_{\varphi(\partial\Omega^d)} \mathbf{N}^T\boldsymbol{t}\mathrm{d}a + \int_{\boldsymbol{\varphi}(\Gamma^d)} \mathbf{B}_c^T\boldsymbol{t_c}\mathrm{d}a\right\}^T \delta\mathbf{u} = 0, \quad \forall\delta\mathbf{u} \in \mathcal{V}^d. \tag{3.10}$$

The nodal cohesive force vector is given as

$$\mathbf{f}^{\mathrm{coh}} \equiv \int_{\boldsymbol{\varphi}(\Gamma^d)} \mathbf{B}_c^T\boldsymbol{t_c}\mathrm{d}a, \tag{3.11}$$

with the stiffness matrix given as the gradient of the internal force vector, such that

$$\mathbf{K}^{\mathrm{coh}} \equiv \frac{\partial\mathbf{f}^{\mathrm{coh}}}{\partial\mathbf{u}} = \int_{\boldsymbol{\varphi}(\Gamma^d)} \mathbf{B}_c^T\frac{\partial\boldsymbol{t}_c}{\partial\boldsymbol{\Delta}}\frac{\partial\boldsymbol{\Delta}}{\partial\mathbf{u}}\mathrm{d}a = \int_{\boldsymbol{\varphi}(\Gamma^d)} \mathbf{B}_c^T\frac{\partial\boldsymbol{t}_c}{\partial\boldsymbol{\Delta}}\mathbf{B}_c\mathrm{d}a. \tag{3.12}$$

Finally, the cohesive force vector and stiffness tangent matrix are assembled from their respective element counterparts

$$\mathbf{f}^{\mathrm{coh}} = \mathop{\mathsf{A}}_{e=1}^{n_e} \mathbf{f}_e^{\mathrm{coh}} = \mathop{\mathsf{A}}_{e=1}^{n_e} \int_{\boldsymbol{\varphi}(\Gamma^e)} \left(\mathbf{B}_c^e\right)^T\boldsymbol{t_c}\mathrm{d}a \tag{3.13}$$

$$\mathbf{K}^{\mathrm{coh}} \equiv \frac{\partial\mathbf{f}^{\mathrm{coh}}}{\partial\mathbf{u}} = \mathop{\mathsf{A}}_{e=1}^{n_e} \int_{\boldsymbol{\varphi}(\Gamma^e)} \left(\mathbf{B}_c^e\right)^T\frac{\partial\boldsymbol{t}_c}{\partial\boldsymbol{\Delta}}\mathbf{B}_c^e\mathrm{d}a, \tag{3.14}$$

with the element displacement-separation matrix given as

$$\mathbf{B}_c^e \equiv \mathbf{N}^e\mathbf{L}^e\mathbf{R}^e \tag{3.15}$$

where $\boldsymbol{t}_c$ and $\partial\boldsymbol{t}_c/\partial\boldsymbol{\Delta}$ are obtained from a cohesive zone model (e.g., PPR potential-based).

### 3.3.3 Kinematics of the interface model

The global displacement-separation matrix $\mathbf{B}_c$ for two and three-dimensional cohesive elements, is obtained from the rotation matrix $\mathbf{R}$, the global shape functions matrix $\mathbf{N}$ and the local displacement-separation matrix $\mathbf{L}$, as described above.

For each type of cohesive element, whether linear or quadratic, in 2D or 3D, stores all its degrees of freedom in $\mathbf{u}^e$. For instance, a 2D linear cohesive element resembles a quadrilateral linear continuum element, composed of four nodes, with two degrees of freedom per node (Figure 3.1a). The 2D quadratic cohesive element, on the other hand, is a six-node quadrilateral element (Figure 3.1b), linear in the normal direction, but possesses an additional mid-edge node in the tangential direction. Figure 3.1 presents three-dimensional cohesive elements, with three degrees of freedom per node (Figures 3.1c to 3.1f).

Additionally, only the cohesive elements contribute to the global cohesive force vector $\mathbf{f}^{\mathrm{coh}}$ and cohesive stiffness matrix $\mathbf{K}^{\mathrm{coh}}$. In contrast with continuum elements, whose internal forces and stiffness matrices are integrated over the dimension of the problem, these quantities are integrated over a domain one dimension lower. For example, in a two-dimensional cohesive element, the cohesive force and stiffness matrix are integrated over a line (e.g., the middle line) (Vieira de Carvalho (2023)). The justification resides in the traction continuity requirement, such that the interface geometry with respect to the deformed configuration has to be taken as the average of both sides (Mosler and Scheider (2011)).

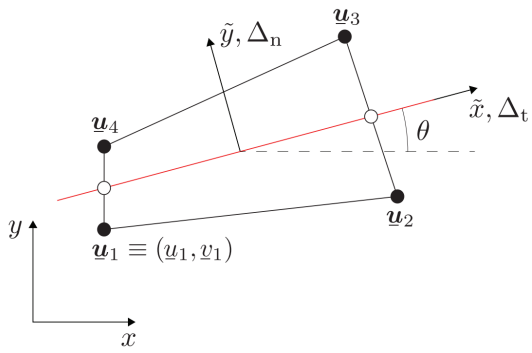


(a) Two dimensional 4 node linear element

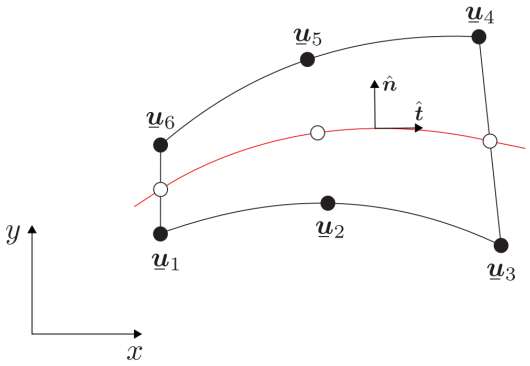


(b) Two dimensional 6 node quadratic element

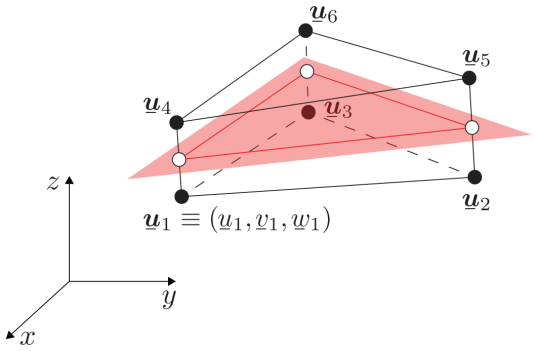


(c) Three dimensional 6 node linear element.

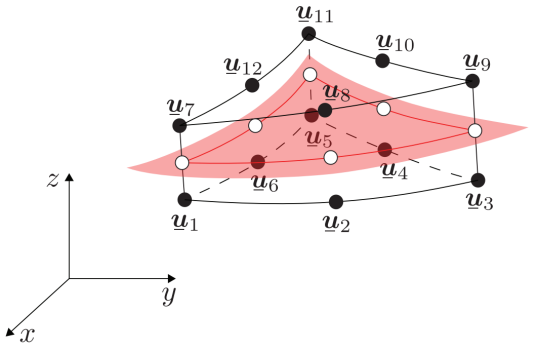


(d) Three dimensional 12 node quadratic element

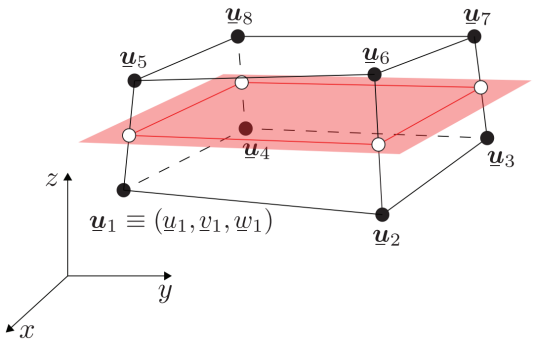


(e) Three dimensional 8 node linear element

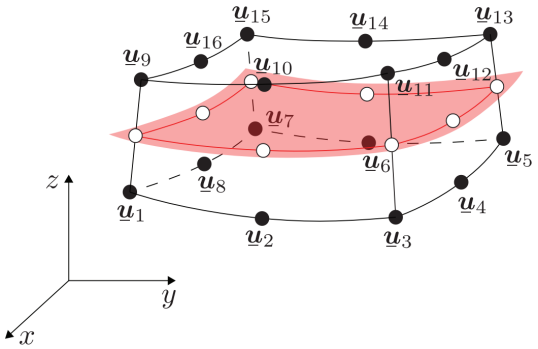


(f) Three dimensional 16 node quadratic element

Figure 3.1: Schematic representation of six cohesive elements with respective node displacements defined in the local coordinate system. The white circles in the middle lines/planes represent the position of the middle plane nodes. Taken from Vieira de Carvalho (2023).

Consider the element coordinates in the deformed configuration (global coordinates) stored in the vector $\mathbf{x}^e$, given for a three-dimensional element as

$$\mathbf{x}^e \equiv \left(x_1^1, x_2^1, x_3^1, ..., x_1^{n_n}, x_2^{n_n}, x_3^{n_n}\right), \tag{3.16}$$

where $n_n$ expresses the number of nodes of the corresponding cohesive element, with the order of the nodes is defined in a counter-clockwise direction.

Similarly, the coordinates of the middle plane/line nodes are linearly interpolated from their corresponding node pairs as

$$\mathbf{x}^m = \frac{1}{2}\overset{+}{\mathbf{L}}{}^e \mathbf{x}^e, \tag{3.17}$$

with $\overset{+}{\mathbf{L}}{}^e$ defining the matrix with the absolute values of $\mathbf{L}^e$, such that $\overset{+}{L}{}^e_{ij} = |L^e_{ij}|$

Since the integration domain of cohesive variables (e.g., global cohesive vector and the cohesive stiffness matrix) is in a space one dimension lower than that of the remaining simulation, the shape functions also are associated with that lower dimensional space. For example, for a two-dimensional linear cohesive element, the shape functions are those of a one-dimensional linear isoparametric element, such that

$$\mathbf{N}^e = \left[\begin{array}{cc|cc} N_1 & 0 & N_2 & 0 \\ 0 & N_1 & 0 & N_2 \end{array}\right]. \tag{3.18}$$

The shape functions are equal to those of a one-dimensional linear isoparametric element, such that

$$\begin{cases} N_1 = \dfrac{1-\xi}{2} \\ N_2 = \dfrac{1+\xi}{2} \end{cases}. \tag{3.19}$$

Another example is a two-dimensional quadratic cohesive element, the shape functions are those of a one-dimensional quadratic isoparametric element, such that

$$\mathbf{N} = \left[\begin{array}{cc|cc|cc} N_1 & 0 & N_2 & 0 & N_3 & 0 \\ 0 & N_1 & 0 & N_2 & 0 & N_3 \end{array}\right]. \tag{3.20}$$

For this case, the shape functions are equal to those of a one-dimensional quadratic isoparametric element, such that

$$\begin{cases} N_1 = -\dfrac{1}{2}\xi(1-\xi) \\ N_2 = (1-\xi)(1+\xi) \\ N_3 = \dfrac{1}{2}\xi(1+\xi) \end{cases}. \tag{3.21}$$

For the two-dimensional case, the shape functions are defined in the natural coordinate system, $\xi$. For the three-dimensional case, an additional axis is considered $(\xi, \eta)$.

The rotation matrix

$$\mathbf{R}^e = \text{diag}\,[\boldsymbol{\Theta}] \tag{3.22}$$

has dimensions $n^e_{\text{DoF}} \times n^e_{\text{DoF}}$, where $n^e_{\text{DoF}}$ is the number of degrees of freedom of the corresponding cohesive element, and, for two-dimensional cohesive elements, $\boldsymbol{\Theta}$ is given as

$$\boldsymbol{\Theta} = \left[\begin{array}{c} \hat{\boldsymbol{t}} \\ \hat{\boldsymbol{n}} \end{array}\right], \quad \hat{\boldsymbol{x}} = \mathbf{N}^e(\xi)\mathbf{x}^m, \tag{3.23}$$

with $\hat{\boldsymbol{x}}$ as the coordinates of a generic point within the middle line. The unit local coordinate vectors, $\hat{\boldsymbol{t}}$ and $\hat{\boldsymbol{n}}$, can be expressed as

$$\hat{\boldsymbol{t}} = \frac{1}{\left\| \frac{\mathrm{d}\hat{\mathbf{x}}^m}{\mathrm{d}\xi} \right\|} \frac{\mathrm{d}\hat{\boldsymbol{x}}^m}{\mathrm{d}\xi}, \quad \hat{\boldsymbol{n}}\hat{\boldsymbol{t}} = 0, \tag{3.24}$$

where

$$\frac{\mathrm{d}\hat{\boldsymbol{x}}^m}{\mathrm{d}\xi} = \begin{bmatrix} \dfrac{\mathrm{d}N_1}{\mathrm{d}\xi} & 0 & \dfrac{\mathrm{d}N_2}{\mathrm{d}\xi} & 0 \\ 0 & \dfrac{\mathrm{d}N_1}{\mathrm{d}\xi} & 0 & \dfrac{\mathrm{d}N_2}{\mathrm{d}\xi} \end{bmatrix} \begin{bmatrix} (x_1^1)^m \\ (x_2^1)^m \\ (x_1^2)^m \\ (x_2^2)^m \end{bmatrix}, \tag{3.25}$$

for a two-dimensional linear cohesive element, with the corresponding rotation matrix with dimension $8 \times 8$, or alternatively

$$\frac{\mathrm{d}\hat{\boldsymbol{x}}^m}{\mathrm{d}\xi} = \begin{bmatrix} \dfrac{\mathrm{d}N_1}{\mathrm{d}\xi} & 0 & \dfrac{\mathrm{d}N_2}{\mathrm{d}\xi} & 0 & \dfrac{\mathrm{d}N_3}{\mathrm{d}\xi} & 0 \\ 0 & \dfrac{\mathrm{d}N_1}{\mathrm{d}\xi} & 0 & \dfrac{\mathrm{d}N_2}{\mathrm{d}\xi} & 0 & \dfrac{\mathrm{d}N_3}{\mathrm{d}\xi} \end{bmatrix} \begin{bmatrix} (x_1^1)^m \\ (x_2^1)^m \\ (x_1^2)^m \\ (x_2^2)^m \\ (x_1^3)^m \\ (x_2^3)^m \end{bmatrix}, \tag{3.26}$$

for a two-dimensional quadratic cohesive element , with the corresponding rotation matrix with dimensions $12 \times 12$.

For three-dimensional six-node linear cohesive elements:

$$\boldsymbol{\Theta} = \begin{bmatrix} \hat{\boldsymbol{t}}_\xi \\ \hat{\boldsymbol{t}}_\eta \\ \hat{\boldsymbol{n}} \end{bmatrix}, \quad \hat{\boldsymbol{x}} = \mathbf{N}^e(\xi,\eta)\mathbf{x}^m, \tag{3.27}$$

with $\hat{\boldsymbol{x}}$ as the coordinates of a generic point within the middle plane. The unit local coordinate vectors, $\hat{\boldsymbol{t}}_\xi$, $\hat{\boldsymbol{t}}_\eta$ and $\hat{\boldsymbol{n}}$, formally defined as

$$\hat{\boldsymbol{t}}_\xi = \frac{1}{\left\| \frac{\partial \hat{\boldsymbol{x}}^m}{\partial \xi} \right\|} \frac{\partial \hat{\boldsymbol{x}}^m}{\partial \xi}, \quad \hat{\boldsymbol{t}}_\xi = \frac{1}{\left\| \frac{\partial \hat{\boldsymbol{x}}^m}{\partial \eta} \right\|} \frac{\partial \hat{\boldsymbol{x}}^m}{\partial \eta}, \quad \hat{\boldsymbol{n}} = \hat{\boldsymbol{t}}_\xi \times \hat{\boldsymbol{t}}_\eta, \tag{3.28}$$

where

$$\frac{\partial \hat{\boldsymbol{x}}^m}{\partial \xi} = \begin{bmatrix} \dfrac{\partial N_1}{\partial \xi} & 0 & 0 & \dfrac{\partial N_2}{\partial \xi} & 0 & 0 & \dfrac{\partial N_3}{\partial \xi} & 0 & 0 \\ 0 & 0 & \dfrac{\partial N_1}{\partial \xi} & 0 & 0 & \dfrac{\partial N_2}{\partial \xi} & 0 & 0 & \dfrac{\partial N_3}{\partial \xi} \end{bmatrix} \begin{bmatrix} (x_1^1)^m \\ (x_2^1)^m \\ (x_3^1)^m \\ (x_1^2)^m \\ (x_2^2)^m \\ (x_3^2)^m \\ (x_1^3)^m \\ (x_2^3)^m \\ (x_3^3)^m \end{bmatrix}, \tag{3.29}$$

$$\frac{\partial \hat{\boldsymbol{x}}^m}{\partial \eta} = \begin{bmatrix} \dfrac{\partial N_1}{\partial \eta} & 0 & 0 & \dfrac{\partial N_2}{\partial \eta} & 0 & 0 & \dfrac{\partial N_3}{\partial \eta} & 0 & 0 \\ 0 & 0 & \dfrac{\partial N_1}{\partial \eta} & 0 & 0 & \dfrac{\partial N_2}{\partial \eta} & 0 & 0 & \dfrac{\partial N_3}{\partial \eta} \end{bmatrix} \begin{bmatrix} (x_1^1)^m \\ (x_2^1)^m \\ (x_3^1)^m \\ (x_1^2)^m \\ (x_2^2)^m \\ (x_3^2)^m \\ (x_1^3)^m \\ (x_2^3)^m \\ (x_3^3)^m \end{bmatrix}, \tag{3.30}$$

with a corresponding $18 \times 18$ rotation matrix.

Since the rotation matrix is only a function of the derivatives of the shape functions, it is constant for a two-dimensional linear (4-node) cohesive element (Vieira de Carvalho (2023)), and given

as

$$\mathbf{R}^e = \begin{bmatrix} \boldsymbol{\Theta} & \mathbf{0} & \mathbf{0} & \mathbf{0} \\ \mathbf{0} & \boldsymbol{\Theta} & \mathbf{0} & \mathbf{0} \\ \mathbf{0} & \mathbf{0} & \boldsymbol{\Theta} & \mathbf{0} \\ \mathbf{0} & \mathbf{0} & \mathbf{0} & \boldsymbol{\Theta} \end{bmatrix}, \tag{3.31}$$

where the two-dimensional transformation matrix expressed as

$$\boldsymbol{\Theta} = \begin{bmatrix} \cos\theta & \sin\theta \\ -\sin\theta & \cos\theta \end{bmatrix}, \tag{3.32}$$

with $\theta$ defined in the Euclidean plane, between the positive x-axis and the point $(x,y)$, i.e., between the global coordinates and the local coordinates of a the point $(x,y)$. This angle can be computed as a function of the vector that defines the middle of the element, $\boldsymbol{m} \equiv (m_1, m_2)$, such that

$$\theta = \tan^{-1}\left(\frac{m_2}{m_1}\right) \in [-\pi, \pi]. \tag{3.33}$$

In addition, the element nodal displacements in the local coordinate system are given as

$$\underline{\mathbf{u}}^e \equiv (\underline{\mathbf{u}}^1, ..., \underline{\mathbf{u}}^{n_n}), \tag{3.34}$$

with $\underline{\mathbf{u}}^i \equiv (\underline{u}_1^i, \underline{u}_2^i)$ or $\underline{\mathbf{u}}^i \equiv (\underline{u}_1^i, \underline{u}_2^i, \underline{u}_3^i)$, for a two- or three-dimensional element, respectively.

Similarly, the separation vector of the middle plane of the cohesive element is

$$\underline{\boldsymbol{\Delta}} \equiv (\underline{\boldsymbol{\Delta}}^1, ..., \underline{\boldsymbol{\Delta}}^{n_m}), \tag{3.35}$$

with $\underline{\boldsymbol{\Delta}}^i \equiv (\underline{\Delta}_1^i, \underline{\Delta}_2^i) = (\underline{\Delta}_t^i, \underline{\Delta}_n^i)$ or $\underline{\boldsymbol{\Delta}}^i \equiv (\underline{\Delta}_1^i, \underline{\Delta}_2^i, \underline{\Delta}_3^i) = (\underline{\Delta}_{t,\xi}^i, \underline{\Delta}_{t,\eta}^i, \underline{\Delta}_n^i)$, for a two- or three-dimensional element, respectively. The number of nodes in the middle plane is equal to half of the total number of nodes of the cohesive element, such that

$$n_m = \frac{n_n}{2}. \tag{3.36}$$

The local displacement-separation matrix $\mathbf{L}^e$ has dimensions $n_{\text{DoF}}^m \times n_{\text{DoF}}^e$, where $n_{\text{DoF}}^m$ and $n_{\text{DoF}}^e$ are the number of degrees of freedom of the middle line/plane and of the entire cohesive element, respectively. For a two-dimensional linear cohesive element, it is given as

$$\mathbf{L}^e = \begin{bmatrix} -1 & 0 & 0 & 0 & 0 & 0 & 1 & 0 \\ 0 & -1 & 0 & 0 & 0 & 0 & 0 & 1 \\ 0 & 0 & -1 & 0 & 1 & 0 & 0 & 0 \\ 0 & 0 & 0 & -1 & 0 & 1 & 0 & 0 \end{bmatrix}. \tag{3.37}$$

The gap, or separation, vector can finally be interpolated from its nodal counterparts as

$$\boldsymbol{\Delta} = \mathbf{N}^e \underline{\boldsymbol{\Delta}}. \tag{3.38}$$

For interface elements, large stress gradients over the element and coupling between the degrees of freedom introduced by Gaussian quadrature can lead to an oscillatory type of response. Using Newton-Cotes or Lobatto integration schemes does not create the same issues (Schellekens and Borst, de (1993), Vieira de Carvalho (2023)). As a result, the following quantities are calculated using Newton-Cotes quadrature in the cohesive elements.

Using Equations (3.13) and (3.14), the global internal force vector and stiffness tangent matrix are assembled by their element counterparts as

$$\mathbf{f}_e^{\text{coh}} = \sum_{ip=1}^{n_{ip}} \left(\mathbf{B}_{c,ip}^e\right)^T \boldsymbol{t_c}(\boldsymbol{\Delta}_{ip})\, w_{ip} J_{ip}, \tag{3.39}$$

$$\mathbf{K}_e^{\text{coh}} = \sum_{ip=1}^{n_{ip}} \left(\mathbf{B}_{c,ip}^e\right)^T \left.\frac{\partial \boldsymbol{t}_c(\boldsymbol{\Delta})}{\partial \boldsymbol{\Delta}}\right|_{\boldsymbol{\Delta}=\boldsymbol{\Delta}_{ip}} \mathbf{B}_{c,ip}^e\, w_{ip} J_{ip}, \tag{3.40}$$

where *ip* indicates an integration point with the respective weight $w_{ip}$, and the Jacobian of the transformation between the natural and local coordinate systems, for two-dimensional cohesive elements, is given as

$$J \equiv \|\boldsymbol{t}\| = \left\| \frac{\mathrm{d}\boldsymbol{x}^m}{\mathrm{d}\xi} \right\|, \tag{3.41}$$

and, for three-dimensional cohesive elements, is given as

$$J \equiv \|\boldsymbol{n}\| = \left\| \frac{\partial \boldsymbol{x}^m}{\partial \xi} \times \frac{\partial \boldsymbol{x}^m}{\partial \eta} \right\|. \tag{3.42}$$

An increase in the number of integration points, which improves the accuracy of the stiffness matrix and of the residual force vector, decreases the robustness of the solution algorithm. Therefore, it leads to a reduction of the average increment size. It is also incompatible with a coarser mesh (Crisfield and Alfano (2001), Vieira de Carvalho (2023)).

### 3.3.4 Constitutive cohesive model

To obtain the internal force vector (Equation (3.39)) and the stiffness tangent matrix (Equation (3.40)) for a cohesive element, it is necessary to first define the traction vector $\boldsymbol{t}_c$ as a function of the displacement jump $\boldsymbol{\Delta}$, via Traction Separation Law.

Before discussing the relation between the traction and the material separation, it is important to consider the three distinct modes of fracture (represented in Figure 3.2), associated with different fracture energies, which impact the formulation of the constitutive model. Mode I, referred to as opening or tensile mode, corresponds with the tensile stress normal to the crack plane. Mode II is the sliding or in-plane shear mode, where the in-pane shear stress acts tangential to the crack plane and perpendicular to the crack front (first tangential direction). For Mode III, also known as tearing or anti-plane shear mode, the out-of-plane shear stress is acting tangential to the crack plane and the crack front (second tangential direction).

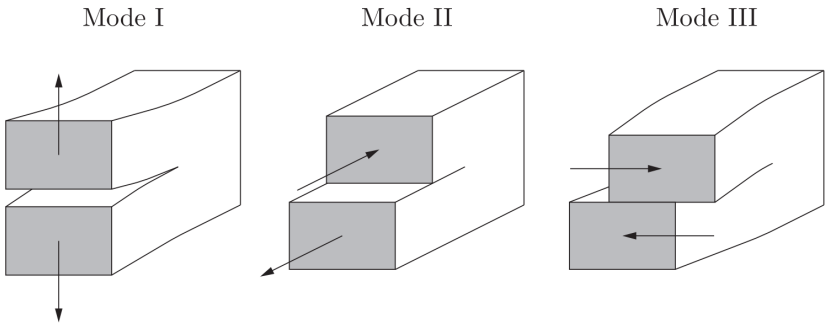


Figure 3.2: Schematic representation of the three modes of fracture. Taken from Vieira de Carvalho (2023).

In a cohesive zone framework, crack growth can be split into four stages: an initial elastic response; crack initiation marked by the onset of separation at the cohesive interface; softening domain where tractions degrade according to a traction-separation law; and ending with complete cohesive failure where the traction of the interface vanishes. More specifically, crack initiation converts pre-existing flaws (e.g., voids, microcracks, fibre-matrix weak interfaces) into an active crack through local damage in the fracture process zone around the crack tip. Crack propagation corresponds to the evolution of the crack post damage onset, governed by the energy release and the chosen traction law. Fracture initiation depends on the strength of the interface material, e.g., maximum stress the interface element can withstand or the peak stress in the traction-separation law. Once the crack front forms, fracture propagation depends on the fracture toughness of the interface

material. If the area under the traction-gap function, i.e., the energy release rate, equals the fracture toughness, complete failure occurs, where the cohesive stresses are null and a new crack surface is formed (Vieira de Carvalho (2023)).

#### Pure mode loading

For loading under pure mode (I, II or III), fracture initiation occurs when the traction equals the maximum traction of a given mode, such that

$$t_i = \sigma_{\max_i}. \tag{3.43}$$

Fracture propagation occurs when the energy release rate $\bar{\phi}_i$ equals the fracture toughness $\phi_i$ for a given mode, such that

$$\bar{\phi}_i = \phi_i. \tag{3.44}$$

#### Mixed mode loading

Cohesive laws which consider mixed mode fracture can be divided into those derived from potential functions and those which are not (discussed in the following Sections 3.3.4 and 3.3.4), and between "uncoupled" and "coupled".

For uncoupled mixed mode traction-separation laws, the normal cohesive stresses are only a function of the normal crack opening, while the shear cohesive stresses depend only on the tangential crack openings. Coupling effects between distinct loading modes are considered and introduced via failure criteria. As is the case for multiaxial loadings, a scalar function of the tractions and energy release rates, for the different modes of fracture, can be defined. A criterion for predicting the initiation of cracks may consider the interaction of the traction components, such as the one proposed by Ye (1988). Models which consider the interaction between the energy release rates can be used to predict the propagation of cracks.

In coupled cohesive laws, the normal and shear tractions depend each on both the normal and tangential material separations. Thus, no additional failure criteria are established to account for interaction between the modes of fracture (Goutianos et al. (2021)).

#### Traction-separation laws

As mentioned previously, a traction-gap function relates the relative displacement, or separation $\boldsymbol{\Delta}$ at the interface, with the traction force vector $\boldsymbol{t}_c$ acting ahead of the physical crack tip.

The formulation of a TSL involves two key material parameters: the maximum strength; and the separation at failure. From these, the dissipated energy per cohesive element is obtained, as well as the shape of the traction-separation law. Several TSLs have been proposed in the literature, such as polynomial (Needleman (1987)), piecewise linear (Tvergaard and Hutchinson (1992)), exponential (Xu and Needleman (1993)), perfectly plastic (Cui and Wisnom (1993)), and bilinear (Camanho et al. (2003)).

Cohesive models can be implemented in a finite element framework using two main strategies: extrinsic and intrinsic. Following an extrinsic approach means assuming an initial rigid response, similar to the behaviour of the physical model of the interface, after which the cohesive element is inserted. This approach may result in numerical challenges in a finite element implementation, due to the use of adaptative remeshing techniques (Vieira de Carvalho (2023)). In alternative, an intrinsic approach can be followed, which considers an initial elastic regime before damage onset and inserts cohesive elements between the continuum elements before the beginning of the analysis, as long as the possible crack paths are known a priori. Despite enabling smoother numerical implementation, this method can introduce artificial compliance, particularly when the density of the cohesive elements is high. To reduce the impact of artificial stiffness, the elastic phase of the

TSL should not significantly alter the behaviour of the material before damage onset. This can be achieved by assigning a sufficiently high stiffness to the cohesive elements, effectively modelling them as a series of springs inserted in the continuum medium. However, using excessively high stiffness values may lead to convergence issues and oscillation of the cohesive stresses inside the cohesive fracture zone (Long et al. (2019)).

To ensure the effective elastic properties of a composite are not affected by the cohesive surface, the through-the-thickness Young's modulus the material $E_3$ must satisfy the following condition

$$E_3 \ll Kt, \tag{3.45}$$

where $K$ is the interface stiffness which relates the resulting tractions at the interface with the opening displacement $\Delta$. In addition, $K$ acts as the initial slope of the traction-separation law (Turon et al. (2007)), given by

$$K = \alpha \frac{E_3}{t}, \tag{3.46}$$

with the optimal value of $\alpha = 50$, the loss of stiffness due to the presence of the interface is less than 2%. This applies even for zero-thickness cohesive elements (Turon et al. (2007)).

Finally, cohesive constitutive models may be categorised as nonpotential-based or potential-based, depending on whether a potential function governs the relationship between the tractions and displacement jumps.

#### Nonpotential-based models

Nonpotential-based cohesive models are defined in an case-specific manner, with the traction vector given as

$$\boldsymbol{t}_c = \boldsymbol{t}_c(\boldsymbol{\Delta}). \tag{3.47}$$

These cohesive models are easier to develop, since the stiffness matrix does not need to be symmetric. Although nonpotential-based cohesive models can capture the physical fracture behaviour for known path problems (e.g., mode I fracture), the same does not hold true for arbitrary mixed mode loading conditions, since they do not account for all possible separation paths. Because these models are not derived from a potential, the dissipation might be non-vanishing, even for elastic loadings. Additionally, non-potential based models may provide non-physical cohesive interactions, e.g., positive stiffness in a softening zone (Park et al. (2009)).

#### Potential-based model

Potential-based cohesive models derive the traction-separation relation across the fracture surface from a scalar potential function, ensuring thermodynamic consistency (Mosler and Scheider (2011)). In essence, a potential function is associated with physical field quantities, such as the strain-energy in the case of continuum mechanics, so that the stresses and stiffnesses naturally follows from its derivatives.

There are two main approaches proposed for deriving a potential-based TSL: the one proposed by Needleman (1987) and later expanded by Xu and Needleman (1993); and the one based on a stored Helmholtz energy.

In Park et al. (2009), the authors derive the TSL from a store Helmholtz energy potential. The potential approach has its roots in atomistic pair potentials which describe the particle debonding process as a function of an atomic distance $l$, such as the Lennard-Jones potential. At large separations, the interaction forces are attractive, whereas at short distance these become repulsive, leading to a distinct energy minimum at the equilibrium bond length. For this approach, the interaction force is given as the first derivative of the potential energy, with the area under the curve corresponding to the work needed to dissociate an interaction (Vieira de Carvalho (2023)).

To ensure the macroscopic fracture energy potential captures the characteristic of the atomistic interactions, multi-scale techniques may be employed. For more information on this topic, the reader is referred to Tadmor et al. (1996), which proposed a quasi-static continuum method, and Gao and Klein (1998) which introduced the virtual bond model.

Within this theoretical framework, the first derivative of a fracture energy potential $\Psi$ with respect to a given displacement jump $\boldsymbol{\Delta}$ corresponds to the cohesive interactions, while the second derivative of a fracture energy potential corresponds to the material tangent stiffness, such that

$$\boldsymbol{t}_c = \frac{\partial \Psi}{\partial \boldsymbol{\Delta}}, \quad \Psi = \Psi(\boldsymbol{\Delta}). \tag{3.48}$$

Some cohesive laws simplify mixed-mode behaviour by considering the traction as a function of a combined or effective displacement. Because these formulations reduce the problem to one dimension, they inherently assumed an equal fracture energy for every loading mode. In reality, most materials fracture differently under opening, sliding or tearing loads. In other words, these TSLs cannot capture the anisotropic fracture response of the material, with distinct fracture energies for modes I, II and III (Park et al. (2009), Vieira de Carvalho (2023)). Consider, for example, a one-dimensional scalar potential given as

$$\Psi = \delta_n \int_0^{\lambda} \sigma(\lambda') \mathrm{d}\lambda', \tag{3.49}$$

with the mode-mixity considered by an effective displacement written as

$$\lambda = \sqrt{\left(\frac{\Delta_n}{\delta_n}\right)^2 + \left(\frac{\Delta_t}{\delta_t}\right)^2} \tag{3.50}$$

with $\Delta_n$ and $\Delta_t$ as normal and tangential separations over the fractured surface, respectively, and $\delta_n$ and $\delta_t$ as characteristic length-scales related to the fracture energy and the cohesive strength (Park et al. (2009), Tvergaard and Hutchinson (1993)).

In alternative, several potential functions have been proposed which model the fracture behaviour as a function of both normal and tangential separation. These include a polynomial cubic-linear potential (Needleman (1987)), an exponential-exponential cohesive law (Xu and Needleman (1993)), and the polynomial-polynomial proposed by Park et al. (2009), which is discussed in greater detail in the following Section.

More specifically, Needleman (1987) specified a polynomial functional-based potential, whose constitutive relation is given as

$$\phi(u_n, u_t, u_b) = -\int_0^{u} [t_n \mathrm{d}u_n + t_t \mathrm{d}u_t + t_b \mathrm{d}u_b], \tag{3.51}$$

where the tractions $t_n$, $t_t$, and $t_b$ are dependent on the displacements $u_n$, $u_t$, and $u_b$, with $\delta$ as the characteristic length. As the interface separation $(u_i/\delta)$ increases, the magnitude of the tractions $(t_i)$ increase until a maximum value is reached. From that instance, the traction drops to zero and separation occurs, i.e., $u_i = \delta$. When $u_n > \phi$, the potential function used equals the work of separation, i.e, given as the area below the curve of traction-separation relation. Since a potential approach is followed, the expression for work of separation is independent of the path.

#### PPR (Park-Paulino-Roesler) potential-based model

As mentioned previously, dissertation focuses more extensively on the Park-Paulino-Roesler cohesive formulation, as it is the sole cohesive zone model implemented within `LINKS`. Originally proposed by Park et al. (2009), the PPR framework employs a unified potential-based description, capable of both intrinsic and extrinsic cohesive zone models. Its traction-separation relationship

is expressed as a polynomial function of both normal, $\Delta_n$, and tangential, $\Delta_t$, separations, capable of having distinct properties for modes I and II. Furthermore, the model parameters correspond to well-known macroscopic fracture properties, summarised as

- **Fracture toughness** - $\phi_n$ and $\phi_t$.
- **Cohesive strength** - $\sigma_{\max}$ and $\tau_{\max}$.
- **Initial slope indicator** - $\lambda_n$ and $\lambda_t$. These parameter provides the ratio of the critical crack opening width to the final crack opening, thus defining the initial stiffness response.
- **Shape parameters** - $\alpha$ and $\beta$. In addition to the initial slope indicators, these parameters provide control over the elastic and softening domains.

The potential of the mixed-mode cohesive fracture is given as

$$\begin{aligned}\Psi(\Delta_n,\Delta_t) =& \min(\phi_n,\phi_t) + \left[\Gamma_n\left(1-\frac{\Delta_n}{\delta_n}\right)^{\alpha}\left(\frac{m}{\alpha}+\frac{\Delta_n}{\delta_n}\right)^{m} + \langle\phi_n-\phi_t\rangle\right] \\ &\times\left[\Gamma_t\left(1-\frac{|\Delta_t|}{\delta_t}\right)^{\beta}\left(\frac{n}{\beta}+\frac{|\Delta_t|}{\delta_t}\right)^{n} + \langle\phi_t-\phi_n\rangle\right],\end{aligned} \tag{3.52}$$

where $\delta_n$ and $\delta_t$ denote the final crack opening widths, in the normal and tangential directions, respectively, $\Gamma_n$ and $\Gamma_t$ are energy constants, and $m$ and $n$ are non-dimensional parameters, later derived.

By taking the gradient, or first derivative, of the PPR potential, the traction vector is obtained as

$$\begin{aligned}t_n(\Delta_n,\Delta_t) \equiv& \frac{\partial\Psi(\Delta_n,\Delta_t)}{\partial\Delta_n} \\ =& \frac{\Gamma_n}{\delta_n}\left[m\left(1-\frac{\Delta_n}{\delta_n}\right)^{\alpha}\left(\frac{m}{\alpha}+\frac{\Delta_n}{\delta_n}\right)^{m-1} - \alpha\left(1-\frac{\Delta_n}{\delta_n}\right)^{\alpha-1}\left(\frac{m}{\alpha}+\frac{\Delta_n}{\delta_n}\right)^{m}\right] \\ &\times\left[\Gamma_t\left(1-\frac{|\Delta_t|}{\delta_t}\right)^{\beta}\left(\frac{n}{\beta}+\frac{|\Delta_t|}{\delta_t}\right)^{n} + \langle\phi_t-\phi_n\rangle\right],\end{aligned} \tag{3.53}$$

$$\begin{aligned}t_t(\Delta_n,\Delta_t) \equiv& \frac{\partial\Psi(\Delta_n,\Delta_t)}{\partial\Delta_t} \\ =& \frac{\Gamma_t}{\delta_t}\left[n\left(1-\frac{|\Delta_t|}{\delta_t}\right)^{\beta}\left(\frac{n}{\beta}+\frac{|\Delta_t|}{\delta_t}\right)^{n-1} - \beta\left(1-\frac{|\Delta_t|}{\delta_t}\right)^{\beta-1}\left(\frac{n}{\beta}+\frac{|\Delta_t|}{\delta_t}\right)^{n}\right] \\ &\times\left[\Gamma_n\left(1-\frac{\Delta_n}{\delta_n}\right)^{\alpha}\left(\frac{m}{\alpha}+\frac{\Delta_n}{\delta_n}\right)^{m} + \langle\phi_n-\phi_t\rangle\right]\frac{\Delta_t}{|\Delta_t|}.\end{aligned} \tag{3.54}$$

The potential function presented in Equation (3.52) has the following fracture boundary conditions detailed in Vieira de Carvalho (2023),

- The softening domain of the TSL is characterised by a pair of final crack opening widths, $\delta_n$ and $\delta_t$, and a pair of conjugate final crack opening widths, $\bar{\delta}_n$ and $\bar{\delta}_t$. The former depend only on the material properties of the respective fracture mode, while the latter consider mode-mixity and accounts for materials with distinct fracture energies. Because the conjugate final openings adjust the normal and tangential limits when both modes interact, complete normal separation occurs when either the normal separation $\Delta_n$ reaches the normal final crack opening width $\delta_n$, or the tangential separation $\Delta_t$ reaches the tangential conjugate final crack opening width $\bar{\delta}_t$, such that

$$t_n(\delta_n,\Delta_t) = 0, \quad t_n(\Delta_n,\bar{\delta}_t) = 0. \tag{3.55}$$

- Similarly, complete tangential separation occurs when either the tangential separation $\Delta_t$ reaches the tangential final crack opening width $\delta_t$, or the normal separation $\Delta_n$ reaches the normal conjugate final crack opening width $\bar{\delta}_n$, such that

$$t_t(\Delta_n,\delta_t) = 0, \quad t_t(\bar{\delta}_n,\Delta_t) = 0. \tag{3.56}$$

- Under pure normal or tangential loads, the propagation of a crack must dissipate energy equal to the fracture energy. I.e., the area under the traction-separation functions until the respective final crack opening corresponds to the respective fracture mode toughness, such that

$$\Phi_n = \int_0^{\delta_n} t_n(\Delta_n, 0)\mathrm{d}\Delta_n, \quad \Phi_t = \int_0^{\delta_t} t_t(0, \Delta_t)\mathrm{d}\Delta_t. \tag{3.57}$$

- The traction-separation functions have their maximum when the separation reaches a critical opening width, $\delta_{n_c}$ or $\delta_{t_c}$, such that

$$\left.\frac{\partial t_n(\Delta_n, \Delta_t)}{\partial \Delta_n}\right|_{\Delta_n = \delta_{n_c}} = 0, \quad \left.\frac{\partial t_t(\Delta_n, \Delta_t)}{\partial \Delta_t}\right|_{\Delta_t = \delta_{t_c}} = 0. \tag{3.58}$$

- Under pure normal or tangential loads, the maximum tractions correspond to the respective fracture mode cohesive strengths, such that

$$t_n(\delta_{n_c}, 0) = \sigma_{\max}, \quad t_t(0, \delta_{t_c}) = \tau_{\max}. \tag{3.59}$$

In addition, the symmetric and anti-symmetric conditions (Vieira de Carvalho (2023)) are given as

$$t_n(\Delta_n, \Delta_t) = t_n(\Delta_n, -\Delta_t), \quad t_t(\Delta_n, \Delta_t) = -t_t(\Delta_n, -\Delta_t). \tag{3.60}$$

The tangential traction at null tangential separation is defined in the limit sense as

$$\lim_{\Delta_t \to 0^+} t_t(\Delta_n, \Delta_t) = 0, \quad \lim_{\Delta_t \to 0^-} t_t(\Delta_n, \Delta_t) = 0. \tag{3.61}$$

To satisfy the previous boundary conditions, it is necessary to define all the unknown parameters in Equation (3.52). Given the boundary condition related to the fracture energies (Equation (3.57)), the energy constants are obtained as

$$\Gamma_n = (-\phi_n)\frac{\langle \phi_n - \phi_t \rangle}{\phi_n - \phi_t}\left(\frac{\alpha}{m}\right)^m, \quad \Gamma_t = (-\phi_t)\frac{\langle \phi_t - \phi_n \rangle}{\phi_t - \phi_n}\left(\frac{\beta}{n}\right)^n. \tag{3.62}$$

In the particular case of equal fracture energies ($\phi_n = \phi_t$), the energy constants are given as

$$\Gamma_n = -\phi_n\left(\frac{\alpha}{m}\right)^m, \quad \Gamma_t = \left(\frac{\beta}{n}\right)^n. \tag{3.63}$$

Using Equation (3.58), the non-dimensional parameters, $m$ and $n$, can be computed as

$$m = \frac{\alpha(\alpha-1)\lambda_n^2}{1-\alpha\lambda_n^2}, \quad m = \frac{\beta(\beta-1)\lambda_t^2}{1-\beta\lambda_t^2}, \tag{3.64}$$

where the initial slope indicators equate the ratio between the critical crack opening width to the final crack width, such that

$$\lambda_n = \frac{\delta_{n_c}}{\delta_n}, \quad \lambda_t = \frac{\delta_{t_c}}{\delta_t}. \tag{3.65}$$

As mentioned previously, a lower values of $\lambda$ correspond to a higher initial stiffness, which decreases the artificial compliance of the intrinsic cohesive elements in the analysis. Nonetheless, numerical issues may occur if the value is too low (Vieira de Carvalho (2023)).

The characteristic lengths are the normal and tangential final crack opening widths

$$\delta_n = \frac{\phi_n}{\sigma_{\max}}\alpha\lambda_n(1-\lambda_n)^{\alpha-1}\left(\frac{\alpha}{m}+1\right)\left(\frac{\alpha}{m}\lambda_n+1\right)^{m-1}, \tag{3.66}$$

$$\delta_t = \frac{\phi_t}{\tau_{\max}}\beta\lambda_t(1-\lambda_t)^{\beta-1}\left(\frac{\beta}{n}+1\right)\left(\frac{\beta}{n}\lambda_t+1\right)^{n-1}. \tag{3.67}$$

To compute the conjugate final crack opening widths, it is convenient to solve the following nonlinear equations for $\Delta_t$ and $\Delta_n$ to obtain the tangential and normal conjugate crack opening widths, respectively,

$$f_t(\Delta_t) = \Gamma_t \left(1 - \frac{|\Delta_t|}{\delta_t}\right)^{\beta} \left(\frac{n}{\beta} + \frac{|\Delta_t|}{\delta_t}\right)^{n} + \langle \phi_t - \phi_n \rangle = 0 \tag{3.68}$$

$$f_n(\Delta_n) = \Gamma_n \left(1 - \frac{\Delta_n}{\delta_n}\right)^{\alpha} \left(\frac{m}{\alpha} + \frac{\Delta_n}{\delta_n}\right)^{m} + \langle \phi_n - \phi_t \rangle = 0. \tag{3.69}$$

The aforementioned nonlinear functions allows us to define the normal softening region as $0 \leq \Delta_n \leq \delta_n$ and $-\bar{\delta}_t \leq \Delta_t \leq \bar{\delta}_t$, while the tangential softening region is defined as $0 \leq \Delta_n \leq \bar{\delta}_n$ and $-\delta_t \leq \Delta_t \leq \delta_t$. According to Park and Paulino (2012), the normal softening region may be alternatively computed as $0 \leq \Delta_n \leq \delta_n$, $-\delta_t \leq \Delta_t \leq \delta_t$, and $t_n(\Delta_n, \Delta_t) \geq 0$, while the tangential softening region is defined as $0 \leq \Delta_n \leq \delta_n$, $-\delta_t \leq \Delta_t \leq \delta_t$, and $t_t(\Delta_n, \Delta_t) \geq 0$.

Finally, the shape parameters $\alpha$ and $\beta$ are introduced to characterise the material softening response, such as brittle, plateau, and quasi-brittle. Setting the shape parameters as $\alpha = \beta = 2$ defines a linear softening law. For the same fracture toughness, lower values of these material parameters yield a more concave softening response, while increasing them provides a more convex softening response.

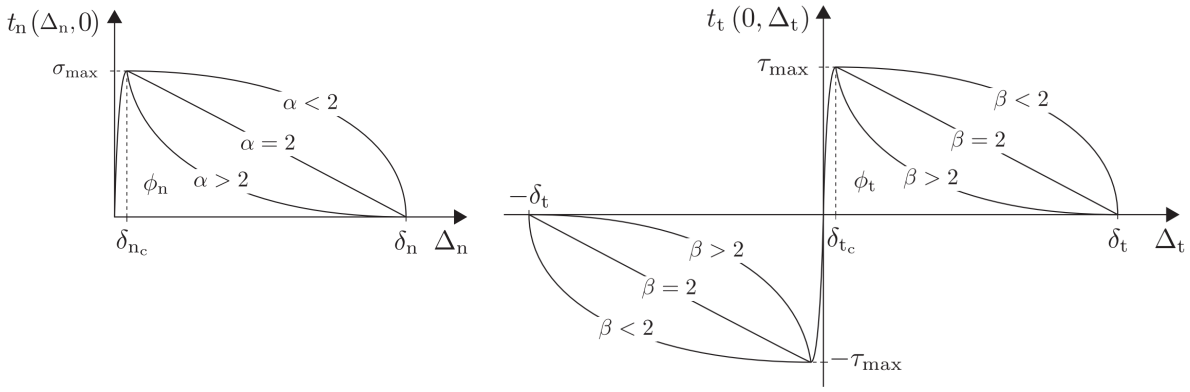


(a) Normal shape parameter, $\alpha$

(b) Normal shape parameter, $\beta$

Figure 3.3: Schematic representation of the PPR cohesive zone model (traction-separation curves) for different values of the normal and tangential shape parameter, $\alpha$ and $\beta$, respectively. Taken from Vieira de Carvalho (2023).

### Unloading/reloading model

The previous Sections address the loading response of the cohesive elements, in which the displacement jump increases. Once the crack opening reaches the critical value, the cohesive elements unload, ceasing to transmit the stresses between the adjacent bulk material elements, and the crack propagation occurs. However, a structure may also be subjected to unloading, due to a decrease in the displacement jump in a given material direction. This can arise not only from global unloading of the structure, but also from local phenomena, such crack branching or the existence of multiple cracks (Vieira de Carvalho (2023)).

To address this issue, material unloading may be implemented as ductile unloading and cleavage unloading. The former resembles the unloading/reloading relationship characteristic of elasto-plastic materials, in which the stiffness of the elastic domain remains constant. The latter implements a linear-to-origin unloading/reloading relationship. First introduced by Camacho and Ortiz (1996), this cohesive law is initially rigid linear, but with decreasing elastic stiffness as the material damage increases.

If the unloading/reloading response is handled with the coupled method, the internal variable created to store the loading history is given as

$$\eta(\Delta_n, \Delta_t) = \sqrt{\Delta_n^2 + \Delta_t^2}, \tag{3.70}$$

where $\eta$ is compared at each load step with the maximum stored value

$$\eta_{\max} = \eta\left(\Delta_{n_{\max}}, \Delta_{t_{\max}}\right). \tag{3.71}$$

If the current value of the internal variable exceeds its historical maximum, the cohesive element remains in the softening domain; otherwise, the element follows the unloading/reloading path (Vieira de Carvalho (2023)).

For the uncoupled method, the internal variables created to store the loading history are given as

$$\eta_{n_{\max}} = \Delta_{n_{\max}}, \quad \eta_{t_{\max}} = |\Delta_t|_{\max}. \tag{3.72}$$

Inside the elastic domain, the fracture process is reversible and so these internal variables are not updated. If $\Delta_n > \delta_{n_c}$ and $\Delta_n > \eta_{n_{\max}}$, the internal value is updated to match the current normal separation, with the normal traction computed via traction-separation law. Conversely, if $\Delta_n > \delta_{n_c}$ and $\Delta_n < \eta_{n_{\max}}$, the element follows the unloading/reloading relation for the normal direction. The same logic applies in the tangential direction, but with the absolute value of the tangential separation $|\Delta_t|$ (Vieira de Carvalho (2023)).

In the LINKS implementation, the unloading/reloading relation follows a uncoupled cleavage model, independent of the PPR potential. The normal and tangential tractions during unloading/reloading are expressed as

$$t_n^u(\Delta_n, \Delta_t) = t_n\left(\eta_{n_{\max}}, \Delta_t\right)\left(\frac{\Delta_n}{\eta_{n_{\max}}}\right)^{\alpha_u}, \tag{3.73}$$

$$t_t^u(\Delta_n, \Delta_t) = t_t\left(\Delta_n, \eta_{t_{\max}}\right)\left(\frac{|\Delta_t|}{\eta_{t_{\max}}}\right)^{\beta_u}\frac{\Delta_t}{|\Delta_t|}, \tag{3.74}$$

where $\eta_{n_{\max}}$ and $\eta_{t_{\max}}$ are the maximum normal and tangential separation in a loading history, respectively. In the particular case of a linear-to-origin traction-separation relation, the additional shape parameters are set as $\alpha_u = \beta_u = 1$ (Vieira de Carvalho (2023)).

### Contact

Even after failure, computation contact mechanics must be verified to prevent a negative normal displacement jump.Once a cohesive element has completely collapsed, adjacent continuum elements cannot penetrate each other. To achieve this, a penalty parameter, $\alpha_p$, is introduced to enforce $\Delta_n \geq 0$, such that

$$t_n = \alpha_p \Delta_n, \quad \text{for } \Delta_n < 0. \tag{3.75}$$

Here, $\alpha_p$ represents the interface stiffness in the normal direction at zero separation, defined as

$$\alpha_p = \left.\frac{\partial^2 \Psi(\Delta_n, \Delta_t)}{\partial \Delta_n^2}\right|_{\Delta_n = \Delta_t = 0}. \tag{3.76}$$

Choosing a larger $\alpha_p$ reduces interpenetrations of the continuum elements, but can also degrade the convergence performance in the simulation.

**Output damage variable**

The PPR-potential based cohesive model as formulated by Park et al. (2009) does not consider a damage variable. However, as noted by Vieira de Carvalho (2023), for visually representing the damaged state of the cohesive elements in the finite element mesh, it is useful to introduce a post-processing scalar variable. For the normal and tangential directions, the damage variables are, respectively, given as

$$D_n = \frac{\bar{\phi}_n}{\phi_n^{\text{eff}}} \in [0,1], \tag{3.77}$$

$$D_t = \frac{\bar{\phi}_t}{\phi_t^{\text{eff}}} \in [0,1], \tag{3.78}$$

where $\phi_n^{\text{eff}}$, $\phi_t^{\text{eff}}$ are the normal and tangential effective fracture toughness, and $\bar{\phi}_n$ and $\bar{\phi}_t$ are the energy release rates for each direction (area under the traction-separation curve). Each output damage variable

More specifically, the present work focuses on a variable, $D_{\text{total}}$, which combines the effects of the normal and tangential directions, written as

$$D_{\text{total}} = \zeta D_n + (1-\xi) D_t, \tag{3.79}$$

where $\zeta$ is the weight factor given as

$$\zeta = \frac{\bar{\phi}_n}{\bar{\phi}_n + \bar{\phi}_t}. \tag{3.80}$$

It can be inferred that, under normal loading conditions, $\zeta = 1$, $\phi_n^{\text{eff}} = \phi_n$, $D_t = 0$ and $D_{\text{total}} = D_n$. Similarly, under tangential loading conditions, $\zeta = 0$, $\phi_t^{\text{eff}} = \phi_t$, $D_n = 0$ and $D_{\text{total}} = D_t$.

# Chapter 4

# Phase-Field

In this Chapter, *continuum damage models* (CDM) and smeared fracture mechanics are briefly discussed (Section 4.1). Section 4.2 presents a generalised formulation of the *phase-field* (PF) models utilised in the context of this Master's Dissertation. In Section 4.3, the weak form of the governing equations is derived, followed by a discussion of their finite element implementation. The three particularised formulations of the phase-field model are addressed in Section 4.4.

## 4.1 Introduction to fracture and continuum damage

Continuum damage mechanics, first proposed by Kachanov (1958) to model creep damage in metals, is a macroscopic failure theory that incorporates internal state variables into the constitutive model of the bulk material to account for material degradation and implicitly model cracks.

Since then, CDM formulations have been extended for many materials (metals, composites, concrete), using scalar (or tensorial) damage variables. In most cases, a scalar $D$ ($0 \leq D \leq 1$) is defined which represents the fraction of lost load-bearing area, and evolves with loading. As a result, the load-bearing capacity of the material, in the form of its macroscopic properties, is greatly reduced, without the need to simulate explicit discontinuities in the displacement field. The implicit handing of cracking reduces the geometrical complexity of the problem, precluding the need for remeshing or crack-tracking algorithms, which are computationally burdensome.

Local continuum damage models suffer from *pathological mesh dependency* when softening is encountered. In particular, strain localisation neglects size effects, which may cause the computed stress-strain response to be mesh-dependent. In addition, the standard *crack-band* regularisation forces damage to smear over an element, so varying mesh or orientation can change the results. For instance, a mesh size smaller than the physical process zone may result in the incorrect values for the damage zone width and resulting stresses (Song et al. (2011)). Moreover, most CDM laws compute the damage at each integration point based only on local stress-strain measures, without accounting for the interactions with neighbouring material points. In composites, this can fail to capture the failure mechanisms, such as cracking and delamination of the coupled matrix. By definition, CDMs use a continuous damage field, so they are not able to capture sharp crack discontinuities, thus ad hoc criteria or enrichment schemes are used to predict crack nucleation, kinking or branching (Gonçalves (2024)).

*Nonlocal* approaches in CDM have been developed to address some of these limitations. Among these, phase-field fracture was formulated by Francfort et al. as a variational approximation for the Griffith's theory of brittle fracture (Francfort and Marigo (1998)), expressed as a differential energy balance. In this approach, sharp cracks are regularised into diffuse zones of damage through a spatially continuous auxiliary phase-field variable $\phi$ which transitions smoothly from zero (undamaged) to unity (fully cracked). Alongside its gradient, the phase-field characterises the fracture state within a localised crack band, whose width is described by a small length-scale parameter which

governs the gradient penalty on $\phi$ (Wu (2024)). By regularising sharp discontinuities in the displacement field, phase-field mitigates strain localisation and alleviates the mesh-dependence pathology, while also remaining thermodynamically consistent (Navidtehrani et al. (2021)). As a result, the PF formulation can be implemented using similar numerical strategies to those already developed for gradient-enhanced CDM (Frémond and Nedjar (1996), Lorentz and Andrieux (1999)), while also naturally accommodating complex crack geometries through an energy-based formulation.

The two most common phase-field formulations are the so-called AT2 and AT1 models. The AT2 model was the first phase-field formulation that resulted from the regularisation for the variational approach to fracture (Bourdin et al. (2000), Miehe et al. (2010)). The AT1 model includes an elastic phase in the damage response (Mesgarnejad et al. (2015), Pham et al. (2011)). Both the AT1 and AT2 phase-field models treat the length-scale as a material parameter inherently dependent on the fracture toughness of the material. For a vanishing length-scale, both PF models recover the sharp crack solutions of LEFM for brittle materials. However, their application for models with a substantial softening behaviour is not advisable (Wu (2024)).

*Phase field - cohesive zone models* (PF-CZM) are a recent effort to enrich existing PF formulations with an additional criteria for crack nucleation, based on the strength of the material (Wu (2017), Wu and Nguyen (2018)). In PF-CZM, the crack propagation is governed by a traction-separation law embedded within the phase-field energy functional, making it suitable for modelling both brittle and quasi-brittle fracture without a predefined crack path. Crucially, PF-CZM decouples the length-scale parameter from the remaining material parameters (e.g., strength and fracture energy), enabling an independent calibration of the model. In addition, by selecting appropriate parameters for the characteristics functions of the PF-CZM model, common cohesive zone softening laws, such as linear or exponential TSLs, could be recovered or closely approximated, even for complex fracture problems (Wu (2024)).

## 4.2 A generalised formulation for phase-field fracture

For an arbitrary constitutive model, the generalised phase-field fracture model is formulated in this Section, and then particularised for the AT1, AT2, and PF-CZM models. Note that an Eulerian description of the phase-field balance is implemented in `LINKS`.

### 4.2.1 Kinematics

For an arbitrary constitutive crack density function and an arbitrary fracture driving force, consider a pre-cracked elastic homogeneous body occupying an arbitrary domain $\Omega \subset \mathbb{R}^n$ with the dimension $n \in [1,2,3]$, and having an arbitrary external domain $\partial\Omega \subset \mathbb{R}^{n-1}$ with an outward unit normal $\boldsymbol{n}$ (Navidtehrani et al. (2021)). Let $\Gamma$ be the crack surface of the body, where the displacement field $\boldsymbol{u}$, introduced in Section 2.1.1, is discontinuous (Figure 4.1).

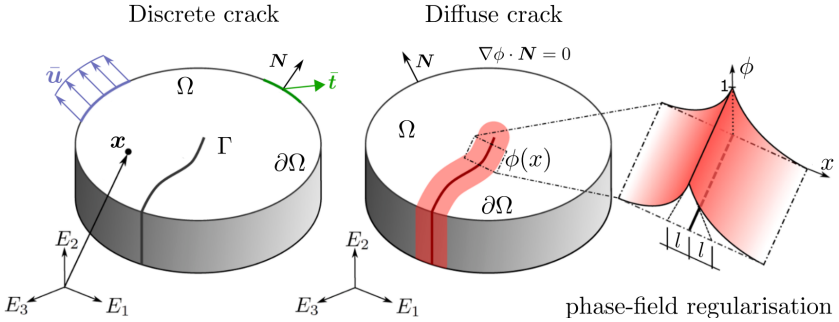


Figure 4.1: Schematic representation of an arbitrary body with a discrete or a diffuse crack. Taken from Gonçalves (2024).

Any point $\boldsymbol{x} \in \boldsymbol{\varphi}(\Omega)$, in the deformed configuration, is affected by the displacement field $\boldsymbol{u}$ and the irreversible scalar damage phase-field variable $\phi$. This continuous variable $\phi \in [0;1]$ smoothly captures the transition from undamaged material (in its intact state) for $\phi = 0$, to fully damaged (or broken) states for $\phi = 1$, with intermediate values corresponding to partially fractured material states. This allows the model to capture the nucleation and growth of cracks. In fact, the cracks are not explicitly modelled as sharp discontinuous, but in a regularised diffuse manner, over a localised crack band whose smearing is controlled by a phase-field length-scale parameter, $l$ (Navidtehrani et al. (2021)).

### 4.2.2 Differential form of the Griffith thermodynamic balance

Phase-field models may be derived from the Griffith thermodynamic balance. By imposing thermodynamic irreversibility, the crack growth occurs only if the total energy of the solid decreases or stays constant over time (Griffith (1921)). Therefore, the Griffith principle allows us to obtain the local (differential) minimum for the total energy of the body $\Pi$, with respect to the increment of the crack area ($\mathrm{d}A$),

$$\frac{\mathrm{d}\Pi}{\mathrm{d}A} = \frac{\mathrm{d}\Psi_0}{\mathrm{d}A} + \frac{\mathrm{d}W_c}{\mathrm{d}A} - \frac{\mathrm{d}W_{\text{ext}}}{\mathrm{d}A}, \tag{4.1}$$

where $\Psi_0$ is the internal/stored strain energy due to elastic deformation, $W_{\text{ext}}$ is the work due to all external forces, and $W_c$ is the work necessary to generate a crack surface. Thus, the Griffith's critical energy release rate (Griffith energy) can be identified as

$$G_c = \frac{\mathrm{d}W_c}{\mathrm{d}A}, \tag{4.2}$$

a quantity often referred to as the fracture toughness of a material.

### 4.2.3 Variational form of the Griffith thermodynamic balance

Francfort and Marigo (1998) managed to restructure Griffith's differential approach to fracture mechanics into a variational integral approach of quasi-static crack evolution, introducing the energy functional

$$\Pi(\boldsymbol{u}) = \int_{\boldsymbol{\varphi}(\Omega)} \psi_0(\boldsymbol{u})\mathrm{d}v + \int_{\boldsymbol{\varphi}(\Gamma)} G_c \mathrm{d}a - W_{\text{ext}}(\boldsymbol{u}), \tag{4.3}$$

where the term

$$\int_{\boldsymbol{\varphi}(\Omega)} \psi_0(\boldsymbol{u})\mathrm{d}v \tag{4.4}$$

is the accumulated elastic strain energy of the damaged body, the term

$$\Phi = \int_{\boldsymbol{\varphi}(\Gamma)} G_c \mathrm{d}a \tag{4.5}$$

is the fracture energy over a discontinuous surface $\Gamma$, also called the dissipated energy associated with the creation of new material surfaces, and the work of the external forces is thus given as

$$W_{\text{ext}}(\boldsymbol{u}) = \int_{\boldsymbol{\varphi}(\Omega)} \boldsymbol{b}\cdot\boldsymbol{u}\mathrm{d}v + \int_{\boldsymbol{\varphi}(\partial\Omega)} \boldsymbol{t}\cdot\boldsymbol{u}\mathrm{d}a. \tag{4.6}$$

### 4.2.4 Crack surface density function

For an arbitrary crack path, the fracture or dissipated energy over a discontinuous surface can be approximated in a damaged zone of finite width (Macías et al. (2023)), such that

$$\Phi = \int_{\boldsymbol{\varphi}(\Gamma)} G_c \mathrm{d}a \approx \int_{\boldsymbol{\varphi}(\Omega)} G_c \gamma(\phi, \nabla_{\boldsymbol{x}}\phi)\mathrm{d}v, \quad \text{for } l \to 0, \tag{4.7}$$

where $\gamma(\phi, \nabla_{\boldsymbol{x}}\phi)$ is the crack surface density functional written as

$$\gamma\left(\phi, \nabla_{\boldsymbol{x}}\phi\right) = \frac{1}{4c_w}\left(\frac{w(\phi)}{l} + l|\nabla_{\boldsymbol{x}}\phi|^2\right). \tag{4.8}$$

For the AT1 and AT2 formulations, the $\Gamma$-convergence of the phase-field model to the Griffith (1921) fracture model requires the length-scale parameter to be set as small as possible. Briefly, the $\Gamma$-convergence, as explained by Braides (2002), is a variational notion of convergence for a family of regularised phase-field energy functionals $\Pi_l(\boldsymbol{u}, \phi)$, such that $\Pi_l(\boldsymbol{u}, \phi)$ converges to the sharp crack Griffith functional $\Pi(\boldsymbol{u})$ as $l \to 0$. Any minimiser $(\boldsymbol{u}, \phi)$ of $\Pi(\boldsymbol{u}, \phi)$ is also a minimiser of $\Pi(\boldsymbol{u})$, with the same corresponding minimum values.

However, Borden et al. (2012) pointed out that infinitesimal values could lead to an infinite stress for crack nucleation, which is not physically realistic. To address this issue, some authors, such as Borden et al. (2012), Bourdin et al. (2014), Kuhn et al. (2015), Pham and Marigo (2013), have proposed calibrating the length-scale parameter to physical values by using mathematical expressions which relate the length-scale parameter to the material characteristic length (Quintanas-Corominas et al. (2019)),

$$l_c = \frac{G_c E}{\sigma_c^2}. \tag{4.9}$$

For PF-CZM, it is necessary to ensure the $\Gamma$-convergence of the phase-field model to the a cohesive zone model, such as Barenblatt (1959) or Dugdale (1960), which occurs for a vanishing length-scale parameter.

### 4.2.5 Geometric crack function

Equation (4.7) translates the regularisation of the surface energy (Marigo et al. (2016)), with the regularised term divided into a local ($\phi$ dependent) and nonlocal ($\nabla_{\boldsymbol{x}}\phi$ dependent) contributions, such that

$$\int_{\boldsymbol{\varphi}(\Omega)} G_c \gamma\left(\phi, \nabla_{\boldsymbol{x}}\phi\right) \mathrm{d}v = \frac{G_c}{4c_w} \int_{\boldsymbol{\varphi}(\Omega)} \left(\frac{w(\phi)}{l} + l|\nabla_{\boldsymbol{x}}\phi|^2\right) \mathrm{d}v. \tag{4.10}$$

From the equation above, the regularised fracture energy density can be expressed as

$$\varphi\left(\phi, \nabla_{\boldsymbol{x}}\phi\right) = G_c \gamma\left(\phi, \nabla_{\boldsymbol{x}}\phi\right) = G_c \frac{1}{4c_w l}\left(w(\phi) + l|\nabla_{\boldsymbol{x}}\phi|^2\right), \tag{4.11}$$

where $l$ is the phase-field length-scale, $c_w$ is the scaling constant, and $w(\phi)$ is the geometric crack function, which defines the spatial distribution of the damage variable $\phi(\boldsymbol{x})$ in the domain $\Omega$ and must fulfil the following boundary conditions

$$w(\phi) \geq 0, \quad w(0) = 0, \quad w(1) = 1, \quad w'(\phi) \geq 0 \text{ for } 0 \leq \phi \leq 1. \tag{4.12}$$

The boundary conditions state that no dissipated energy exists ($w = 0$) when the material is undamaged ($\phi = 0$), and the local dissipation must be at its maximum ($w = 1$) when the material damage is the highest ($\phi = 1$). The final requirement prevents healing of the crack ($w' < 0$), ensuring thermodynamic consistency (Macías et al. (2023)). As a result of these conditions, the crack path is *bullet*-shaped, shown in Figure 4.2 for several expressions of the geometric rack function.

The scaling constant is a normalisation parameter that guarantees the same dissipation energy, regardless of the phase-field formulation, and given as

$$c_w = \int_0^1 \sqrt{w(\zeta)}\, d\zeta. \tag{4.13}$$

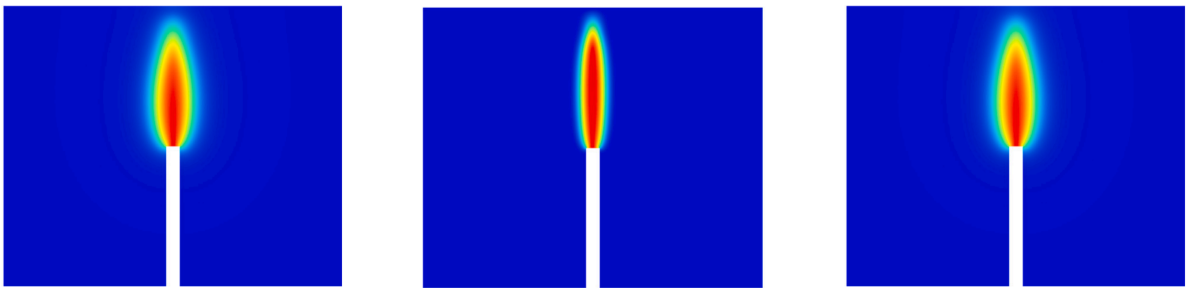

(a) $w(\phi) = 2\phi - \phi^2$ (b) $w(\phi) = \phi(1-\phi)$ (c) $w(\phi) = \phi^2(1-\phi)^2$

Figure 4.2: Crack profiles for various geometric crack functions. Taken from Wu (2024).

### 4.2.6 Energy degradation function

For a continuum damage model, the strain energy of the body must decrease with the increase of the damage variable, such that

$$\int_{\boldsymbol{\varphi}(\Omega)} \psi_0(\boldsymbol{u}) \mathrm{d}v \approx \int_{\boldsymbol{\varphi}(\Omega)} \psi(\boldsymbol{u},\phi) \mathrm{d}v = \int_{\boldsymbol{\varphi}(\Omega)} [g(\phi)\psi_0^+(\boldsymbol{u}) + \psi_0^-(\boldsymbol{u})] \mathrm{d}v, \tag{4.14}$$

where $g(\phi)$ is the energetic degradation function, $\psi_0^+(\boldsymbol{u})$ and $\psi_0^-(\boldsymbol{u})$ are the positive and negative contributions to the strain energy, respectively. The energy split avoids fracture under compressive loadings, and is discussed in greater detail in Appendix A.

Most PF models incorporate two characteristic functions dependent on the phase-field variable: the geometric crack function $w(\phi)$ previously introduced, and the energy degradation function $g(\phi)$, which is responsible for determining how the stress and the crack driving force are influenced by the variation of the phase-field variable (Wu (2024)). The boundary conditions of the degradation function can be written as

$$g(0) = 1, \quad g(1) = 0, \quad g' \leq 0 \text{ for } 0 \leq \phi \leq 1. \tag{4.15}$$

These equations state that all the external work is stored as strain energy ($g = 1$) for an undamaged material ($\phi = 0$), while a completely damaged one ($\phi = 1$) loses all its load-carrying capacity ($g = 0$). Moreover, the evolution of the damage cannot increase the internal energy ($g' > 0$) (Macías et al. (2023)). As damage increases, the degradation function $g(\phi)$ causes a reduction in the elastic strain energy density, reflecting the gradual loss of stiffness in the cracked material (Navidtehrani et al. (2021)).

### 4.2.7 Total internal energy density

For quasi-static fracture, the total energy of the solid can now be approximated as

$$\Pi(\boldsymbol{u}) \approx \Pi(\boldsymbol{u},\phi) = \int_{\boldsymbol{\varphi}(\Omega)} \psi(\boldsymbol{u},\phi) \mathrm{d}v + \int_{\boldsymbol{\varphi}(\Omega)} G_c \gamma(\phi, \nabla_{\boldsymbol{x}}\phi) \mathrm{d}v - W_{\text{ext}}(\boldsymbol{u}), \tag{4.16}$$

where $\psi(\boldsymbol{u},\phi)$ is the degraded internal energy density.

Alternatively, for a generalised version of the constitutive theory, the total energy at time $t$ of a solid is the sum of its strain energy and the potential energy of all external forces, such that

$$\Pi(\boldsymbol{u},\phi) = \int_{\boldsymbol{\varphi}(\Omega)} \overline{W}_{\text{int}}(\boldsymbol{u},\phi,\nabla_{\boldsymbol{x}}\phi) \mathrm{d}v - W_{\text{ext}}(\boldsymbol{u}), \tag{4.17}$$

where the total strain/potential energy density of the solid is written as

$$\overline{W}_{\text{int}}(\boldsymbol{u},\phi,\nabla_{\boldsymbol{x}}\phi) = \psi(\boldsymbol{u}, g(\phi)) + \varphi(\phi, \nabla_{\boldsymbol{x}}\phi). \tag{4.18}$$

### 4.2.8 Principle of virtual work and balance of forces

For the coupled deformation-fracture system, it is necessary to derive the balance equations using the principle of virtual work (see Equation (2.105)). To achieve this, Equation (4.6) is introduced in Equation (4.16), such that

$$\Pi(\boldsymbol{u},\phi) = \int_{\boldsymbol{\varphi}(\Omega)} \psi(\boldsymbol{u},\phi)\mathrm{d}v + \int_{\boldsymbol{\varphi}(\Omega)} G_c\gamma(\phi,\nabla_{\boldsymbol{x}}\phi)\mathrm{d}v - \int_{\boldsymbol{\varphi}(\Omega)} \boldsymbol{b}\cdot\boldsymbol{u}\mathrm{d}v - \int_{\boldsymbol{\varphi}(\partial\Omega)} \boldsymbol{t}\cdot\boldsymbol{u}\mathrm{d}a. \tag{4.19}$$

The displacement field and the crack phase-field are the stationary functions of the total energy functional, i.e., the variables to which the functional corresponds to a minimum value (Macías et al. (2023)). Applying the PVW to the variation of $\Pi(\boldsymbol{u},\phi)$ with respect to $\boldsymbol{u}$ and $\phi$ yields the quasi-static version of the weak statement in the spatial description,

$$\begin{aligned}\delta\Pi(\boldsymbol{u},\phi) = &\int_{\boldsymbol{\varphi}(\Omega)} \left(\frac{\partial\psi(\boldsymbol{u},\phi)}{\partial\boldsymbol{\varepsilon}(\boldsymbol{u})} : \delta\boldsymbol{\varepsilon} + \frac{\partial\psi(\boldsymbol{u},\phi)}{\partial\phi}\delta\phi\right)\mathrm{d}v \\ &+ G_c\int_{\boldsymbol{\varphi}(\Omega)} \left(\frac{\partial\gamma(\phi,\nabla_{\boldsymbol{x}}\phi)}{\partial\phi}\delta\phi + \frac{\partial\gamma(\phi,\nabla_{\boldsymbol{x}}\phi)}{\partial\nabla_{\boldsymbol{x}}\phi}\cdot\delta(\nabla_{\boldsymbol{x}}\phi)\right)\mathrm{d}v \\ &- \int_{\boldsymbol{\varphi}(\Omega)} \boldsymbol{b}\cdot\delta\boldsymbol{u}\mathrm{d}v - \int_{\boldsymbol{\varphi}(\partial\Omega)} \boldsymbol{t}\cdot\delta\boldsymbol{u}\mathrm{d}a,\end{aligned} \tag{4.20}$$

where the following definitions are employed

$$\delta\boldsymbol{\varepsilon} = \nabla_{\boldsymbol{x}}\delta\boldsymbol{u}, \tag{4.21}$$

and

$$\delta\psi(\boldsymbol{u},\phi) = \frac{\partial\psi(\boldsymbol{u},\phi)}{\partial\boldsymbol{\varepsilon}(\boldsymbol{u})} : \delta\boldsymbol{\varepsilon} + \frac{\partial\psi(\boldsymbol{u},\phi)}{\partial\phi}\delta\phi. \tag{4.22}$$

Similarly to Section 2.6.2, the strong statement can be obtained from the weak statement by applying the divergence theorem to the variation of $\Pi(\boldsymbol{u},\phi)$, such that

$$\delta\Pi(\boldsymbol{u},\phi) = -\int_{\boldsymbol{\varphi}(\Omega)} \left[\mathrm{div}_{\boldsymbol{x}}\left(\frac{\partial\psi(\boldsymbol{u},\phi)}{\partial\boldsymbol{\varepsilon}(\boldsymbol{u})}\right) + \boldsymbol{b}\right]\cdot\delta\boldsymbol{u}\mathrm{d}v + \int_{\boldsymbol{\varphi}(\partial\Omega)} \left[\left(\frac{\partial\psi(\boldsymbol{u},\phi)}{\partial\boldsymbol{\varepsilon}(\boldsymbol{u})}\right)\cdot\boldsymbol{n} - \boldsymbol{t}\right]\cdot\delta\boldsymbol{u}\mathrm{d}a \tag{4.23}$$

$$+ \int_{\boldsymbol{\varphi}(\Omega)} \left[\frac{\partial\psi(\boldsymbol{u},\phi)}{\partial\phi} + G_c\left(\frac{\partial\gamma}{\partial\phi} - \mathrm{div}_{\boldsymbol{x}}\left(\frac{\partial\gamma}{\partial\nabla_{\boldsymbol{x}}\phi}\right)\right)\right]\delta\phi\mathrm{d}v + \int_{\boldsymbol{\varphi}(\Gamma)} G_c\left(\frac{\partial\gamma}{\partial\nabla_{\boldsymbol{x}}\phi}\cdot\boldsymbol{n}\right)\delta\phi\mathrm{d}a, \tag{4.24}$$

where $\boldsymbol{n}$ is the outward unit normal vector of the boundary $\Gamma$.

To determine $\boldsymbol{u}$ and $\phi$, the Euler-Lagrange equation must be fulfilled, such that

$$\mathrm{div}_{\boldsymbol{x}}\left(\frac{\partial\psi(\boldsymbol{u},\phi)}{\partial\boldsymbol{\varepsilon}(\boldsymbol{u})}\right) + \boldsymbol{b} = \boldsymbol{0}, \quad \text{in } \boldsymbol{\varphi}(\Omega) \tag{4.25}$$

$$\frac{\partial\psi(\boldsymbol{u},\phi)}{\partial\phi} + G_c\left(\frac{\partial\gamma(\phi,\nabla_{\boldsymbol{x}}\phi)}{\partial\phi} - \mathrm{div}_{\boldsymbol{x}}\left(\frac{\partial\gamma(\phi,\nabla_{\boldsymbol{x}}\phi)}{\partial\nabla_{\boldsymbol{x}}\phi}\right)\right) = 0, \quad \text{in } \boldsymbol{\varphi}(\Omega), \tag{4.26}$$

with the boundary conditions

$$\frac{\partial\psi(\boldsymbol{u},\phi)}{\partial\boldsymbol{\varepsilon}(\boldsymbol{u})}\cdot\boldsymbol{n} = \boldsymbol{t}, \quad \text{on } \boldsymbol{\varphi}(\partial\Omega), \tag{4.27}$$

$$\nabla_{\boldsymbol{x}}\phi\cdot\boldsymbol{n} = \boldsymbol{0}, \quad \text{on } \boldsymbol{\varphi}(\Gamma). \tag{4.28}$$

In addition, the variational, or functional, derivate is

$$\delta_\phi\gamma = \frac{\partial\gamma}{\partial\phi} - \mathrm{div}_{\boldsymbol{x}}\frac{\partial\gamma}{\partial\nabla_{\boldsymbol{x}}\phi}, \tag{4.29}$$

which allows us to write the crack resistance as $\delta_\phi \gamma G_c$ and the energetic crack driving force as

$$Y = -\frac{\partial \psi(\boldsymbol{u},\phi)}{\partial \phi} = -\frac{\partial \psi(\boldsymbol{u},\phi)}{\partial g(\phi)}\frac{\partial g(\phi)}{\partial \phi} = -g'(\phi)\psi^+(\boldsymbol{u}), \tag{4.30}$$

and the partial derivatives of the crack surface density function given as

$$\frac{\partial \gamma}{\partial \nabla_{\boldsymbol{x}}\phi} = \frac{l}{2c_w}|\nabla_{\boldsymbol{x}}\phi|, \tag{4.31}$$

$$\frac{\partial \gamma}{\partial \phi} = \frac{1}{4c_w l}\frac{\partial w(\phi)}{\partial \phi}. \tag{4.32}$$

### 4.2.9 Damage irreversibility

To ensure damage is irreversible (i.e., $\dot{\phi} \geq 0$), a local history field variable, $\mathscr{H}$, is introduced, which must fulfil the Karush-Kuhn-Tucker (KKT) conditions,

$$\psi_0^+ - \mathscr{H} \leq 0, \quad \dot{\mathscr{H}} \geq 0, \quad \dot{\mathscr{H}}(\psi_0^+ - \mathscr{H}) = 0. \tag{4.33}$$

The history-dependent strain energy density has several formulations. For instance, for the current time $t$, over a total time $\tau$, the history field variable can be formulated as

$$\mathscr{H} = \max_{t\in[0,\tau]}\psi_0^+(t). \tag{4.34}$$

The total potential energy of the solid formulated in Equation (4.18) can be rewritten as

$$\overline{W}_{\text{int}} = g(\phi)\mathscr{H} + \frac{G_c}{4c_w}\left(\frac{1}{l}w(\phi) + l|\nabla_{\boldsymbol{x}}\phi|^2\right). \tag{4.35}$$

## 4.3 Weak statement of the phase-field model and finite element discretisation

To incorporate fracture in the formulation, a scalar stress-like quality $\omega$ is introduced as the work conjugate to the phase-field variable $\phi$. Additionally, the phase-field microstress vector $\boldsymbol{\xi}$ is defined as the work conjugate to the gradient of the phase-field $\nabla_{\boldsymbol{x}}\phi$.

In the absence of body forces, the weak momentum balance statement is derived in the spatial description, for a quasi-static configuration (see Equation (4.20)) through the application of the principal of virtual work, such that

$$\int_{\boldsymbol{\varphi}(\Omega)} \left[\boldsymbol{\sigma}^* : \delta\boldsymbol{\varepsilon} + \omega\delta\phi + \boldsymbol{\xi}\cdot\delta(\nabla_{\boldsymbol{x}}\phi)\right] \mathrm{d}v - \int_{\boldsymbol{\varphi}(\partial\Omega)} \boldsymbol{t}\cdot\delta\boldsymbol{u}\,\mathrm{d}a = 0, \quad \forall\delta\boldsymbol{u}\in\mathscr{V}, \tag{4.36}$$

where $\boldsymbol{\sigma}^*$ is damaged Cauchy stress tensor given as

$$\boldsymbol{\sigma}^*(\boldsymbol{u},\phi) = \frac{\partial \psi(\boldsymbol{u},\phi)}{\partial \boldsymbol{\varepsilon}(\boldsymbol{u})}. \tag{4.37}$$

Equation (4.36) holds for an arbitrary domain $\Omega$, and for any kinematically admissible variations of the virtual quantities (Navidtehrani et al. (2021)).

The local force balance equations in $\boldsymbol{\varphi}(\Omega)$ can be rewritten as

$$\mathrm{div}_{\boldsymbol{x}}\,\boldsymbol{\sigma}^* = 0, \tag{4.38}$$

$$\mathrm{div}_{\boldsymbol{x}}\,\boldsymbol{\xi} - w = 0, \tag{4.39}$$

with the natural boundary conditions on $\boldsymbol{\varphi}(\partial\Omega)$ given as

$$\boldsymbol{\sigma}^* \cdot \boldsymbol{n} = \boldsymbol{t}, \tag{4.40}$$

$$\boldsymbol{\xi} \cdot \boldsymbol{n} = 0. \tag{4.41}$$

Accordingly, the micro-stress scalar ($\omega$) and the micro-stress vector ($\boldsymbol{\xi}$) are derived in a generalised way, such that

$$\omega = \frac{\partial \overline{W}_{\text{int}}}{\partial \phi} = g'(\phi)\mathscr{H} + \frac{G_c}{4c_w l} w'(\phi), \tag{4.42}$$

$$\boldsymbol{\xi} = \frac{\partial \overline{W}_{\text{int}}}{\partial \nabla_{\boldsymbol{x}} \phi} = \frac{G_c l}{2c_w} \nabla_{\boldsymbol{x}} \phi. \tag{4.43}$$

Replacing the micro-stress values into the phase-field local force balance (Equation (4.38)), it is possible to obtain the phase-field evolution law as

$$\frac{G_c}{2c_w}\left(\frac{w'(\phi)}{2l} - l\nabla^2\phi\right) + g'(\phi)\mathscr{H} = 0. \tag{4.44}$$

### 4.3.1 Finite element discretisation of the phase-field equation

Adapting the weak balance statement for phase-field models (Equation (4.36)) with the expressions for the micro-stresses, $\omega$ and $\boldsymbol{\xi}$ from Equations (4.42) and (4.43), respectively,

$$\begin{aligned}\int_{\boldsymbol{\varphi}(\Omega)} \left[\boldsymbol{\sigma}^* : \delta\boldsymbol{\varepsilon} + \left(g'(\phi)\mathscr{H} + \frac{G_c}{4c_w l} w'(\phi)\right)\delta\phi + \left(\frac{G_c l}{2c_w}\nabla_{\boldsymbol{x}}\phi\right)\cdot\nabla_{\boldsymbol{x}}(\delta\phi)\right] \mathrm{d}v \\ - \int_{\boldsymbol{\varphi}(\partial\Omega)} \boldsymbol{t}\cdot\delta\boldsymbol{u}\,\mathrm{d}a = 0, \quad \forall\delta\boldsymbol{u}\in\mathscr{V}.\end{aligned} \tag{4.45}$$

In order to de-couple the weak form of equilibrium into the mechanical and phase-field problem, it is possible to write the weak form of momentum balance as

$$\int_{\boldsymbol{\varphi}(\Omega)} \boldsymbol{\sigma}^* : \delta\boldsymbol{\varepsilon}\,\mathrm{d}v = \int_{\boldsymbol{\varphi}(\partial\Omega)} \boldsymbol{t}\cdot\delta\boldsymbol{u}\,\mathrm{d}a, \tag{4.46}$$

and the weak form of the phase-field balance is given as

$$\int_{\boldsymbol{\varphi}(\Omega)} \left[\left(g'(\phi)\mathscr{H} + \frac{G_c}{4c_w l} w'(\phi)\right)\delta\phi + \left(\frac{G_c l}{2c_w}\nabla_{\boldsymbol{x}}\phi\right)\cdot\nabla(\delta\phi)\right] \mathrm{d}v = 0. \tag{4.47}$$

Once the weak form statements of momentum and phase-field balance have been defined, it is necessary to discretise in finite elements the coupled problem.

Similarly to the discretisation explained in Section 2.8 and recalling Equation (2.135), the discretised version of the phase-field is given as the interpolation of nodal phase-field vectors,

$$\phi(\boldsymbol{x}) = \mathbf{N}_\phi(\boldsymbol{x})\Phi, \tag{4.48}$$

where $\mathbf{N}_\phi$ is the global phase-field interpolation function, and $\Phi$ is the global phase-field nodal vector written as

$$\Phi = \begin{Bmatrix} \phi_1 \\ \phi_2 \\ \vdots \\ \phi_j \\ \vdots \\ \phi_{n_p} \end{Bmatrix}, \tag{4.49}$$

where $\phi_j$ is the nonlocal damage at node $j = 1, ..., n_p$. In addition, the virtual phase-field $\delta\phi$ is also discretised with $\mathbf{N}_\phi$.

The displacement field can also be interpolated as in Section 2.8.1, such that

$$\boldsymbol{u}(\boldsymbol{x}) = \mathbf{N}(\boldsymbol{x})\mathbf{u}, \tag{4.50}$$

where $\mathbf{N}$ is the global displacement interpolation function, and $\mathbf{u}$ is the global vector of nodal displacements, written as

$$\mathbf{u} = \begin{Bmatrix} \mathbf{u}_1 \\ \mathbf{u}_2 \\ \vdots \\ \mathbf{u}_j \\ \vdots \\ \mathbf{u}_{n_p} \end{Bmatrix}. \tag{4.51}$$

Equations (4.46) and (4.47) can now be discretised. The discretised balance equation is given as

$$\int_{\boldsymbol{\varphi}(\Omega)} \mathbf{B}^T \boldsymbol{\sigma}^* \mathrm{d}v = \int_{\boldsymbol{\varphi}(\partial\Omega)} \mathbf{N}^T \boldsymbol{t} \mathrm{d}a, \tag{4.52}$$

where $\mathbf{B}$ is the global discrete symmetric gradient operator, defined in Equation (2.137).

Substituting the expression for the damaged Cauchy stress tensor:

$$\int_{\boldsymbol{\varphi}(\Omega)} g(\phi)\mathbf{B}^T \boldsymbol{\sigma} \mathrm{d}v = \int_{\boldsymbol{\varphi}(\partial\Omega)} \mathbf{N}^T \boldsymbol{t} \mathrm{d}a \tag{4.53}$$

The discretised phase-field is:

$$\int_{\boldsymbol{\varphi}(\Omega)} \left( \left(g'(\phi)\mathscr{H}\right)\mathbf{N}_\phi^T + \frac{G_c}{4c_w l} w'(\phi)\mathbf{N}_\phi^T \phi + \frac{G_c l}{2c_w} (\nabla(\mathbf{N}_\phi))^T \nabla_{\boldsymbol{x}} \phi \right) \mathrm{d}v = 0 \tag{4.54}$$

Equations (4.53) and (4.54) lead to space-discrete time-continuous mechanical and phase-field residuals, which, respectively, are given at every time instant $t$ as

$$\mathbf{r}_u = \mathbf{f}_u^{\text{int}} + \mathbf{f}_u^{\text{ext}} = \mathbf{0}, \tag{4.55}$$

$$\mathbf{r}_\phi = \mathbf{f}_\phi^{\text{int}} + \mathbf{f}_\phi^{\text{ext}} = \mathbf{0}, \tag{4.56}$$

with the force vectors given as

$$\mathbf{f}_u^{\text{int}} = \int_{\boldsymbol{\varphi}(\Omega)} \mathbf{B}^T \boldsymbol{\sigma}^* \mathrm{d}v, \tag{4.57}$$

$$\mathbf{f}_u^{\text{ext}} = \int_{\boldsymbol{\varphi}(\partial\Omega)} \mathbf{N}^T \boldsymbol{t} \mathrm{d}a, \tag{4.58}$$

$$\mathbf{f}_\phi^{\text{int}} = \int_{\boldsymbol{\varphi}(\Omega)} \frac{G_c l}{2c_w} (\nabla(\mathbf{N}_\phi))^T \nabla_{\boldsymbol{x}} \phi \mathrm{d}v, \tag{4.59}$$

$$\mathbf{f}_\phi^{\text{ext}} = \int_{\boldsymbol{\varphi}(\Omega)} \left( g'(\phi)\mathscr{H} + \frac{G_c}{4c_w l} w'(\phi)\phi \right) \mathbf{N}_\phi^T \mathrm{d}v. \tag{4.60}$$

Time discretisation of the mechanical and phase-field residuals leads to a fully discrete coupled problem for a pseudo-time increment $t_{n+1} \in [t_0, t_f]$, such that:

$$\mathbf{r}_u^{n+1}(\mathbf{u}_{n+1}, \phi_{n+1}) = \mathbf{0}, \tag{4.61}$$

$$\mathbf{r}_\phi^{n+1}(\mathbf{u}_{n+1}, \phi_{n+1}) = \mathbf{0}. \tag{4.62}$$

The systems of equations can be solved using the Newton-Raphson scheme, obtaining the displacement $\Delta\mathbf{u}_{n+1}$ and phase-field variable $\Delta\phi_{n+1}$, such that

$$\begin{bmatrix} \mathbf{K}_{uu} & \mathbf{K}_{u\phi} \\ \mathbf{K}_{\phi u} & \mathbf{K}_{\phi\phi} \end{bmatrix}_{n+1}^{i} \begin{bmatrix} \delta\mathbf{u} \\ \delta\phi \end{bmatrix}_{n+1}^{i+1} = -\begin{bmatrix} \mathbf{r}_u \\ \mathbf{r}_\phi \end{bmatrix}_{n+1}^{i}. \tag{4.63}$$

where $\mathbf{r}_u$ is the mechanical residual and $\mathbf{r}_\phi$ is the phase-field residual, obtained by time discretisation of the finite element equations (4.53) and (4.54). The superscripts $i$ and $i+1$ are the solution scheme iterations. Note that using a history-dependent variable $\mathscr{H}$ to enforce damage irreversibility yields a non-symmetric tangent matrix (Wu et al. (2020)).

There are several options for solving coupled system of nonlinear algebraic equations, such as operator splitting, fractional-step method, staggered/partitioned solution schemes, and monolithic solution schemes. Monolithic method is a common approach, consisting in solving simultaneously the coupled system of solutions to find the incremental solutions for the displacement and phase-field at time $t_{n+1}$, respecting exactly the coupling conditions. This solution method is not dependent on the size of the time step increment, but the total potential energy functional is non-convex, which may lead to convergence issues. When used together with implicit time-integration, monolithic methods provide unconditional stability (Kristensen et al. (2021), Wu and Huang (2020)).

An alternative is employing an alternating minimisation, or staggered, solution scheme, by freezing the displacements and solving the phase-field balance law, and then freezing the phase-field variable and solving the linear momentum balance. A drawback is the dependence on the time step increment size (Macías et al. (2023)). This solution scheme allows de-coupling the nonlinear system of equations of the mechanical and phase-field problems (Gonçalves (2024)), such that

$$\begin{bmatrix} \mathbf{K}_{uu} & \mathbf{0} \\ \mathbf{0} & \mathbf{K}_{\phi\phi} \end{bmatrix}_{n+1}^{i} \begin{bmatrix} \delta\mathbf{u} \\ \delta\phi \end{bmatrix}_{n+1}^{i+1} = -\begin{bmatrix} \mathbf{r}_u \\ \mathbf{r}_\phi \end{bmatrix}_{n+1}^{i} \tag{4.64}$$

The coupling stiffness components ($\mathbf{K}_{\phi u}$ and $\mathbf{K}_{u\phi}$) are not considered in an explicit way. Only the stiffness matrices for each isolated problem is of importance ($\mathbf{K}_{uu}$ and $\mathbf{K}_{\phi\phi}$). The phase-field residual $\mathbf{r}_\phi$ is obtained using equation (4.47). For a pseudo-time increment and for the $k$-th iteration of the Newton-Raphson scheme, the phase-field residual is given as

$$\mathbf{r}_\phi^{k-1} = \left[\int_{\boldsymbol{\varphi}(\Omega)} \left(g'(\phi)\mathscr{H} + \frac{G_c}{4c_w l} w'(\phi)\phi\right)\mathbf{N}_\phi^T \mathrm{d}v + \int_{\boldsymbol{\varphi}(\Omega)} \frac{G_c l}{2c_w} (\nabla(\mathbf{N}_\phi))^T \nabla_{\boldsymbol{x}}\phi \mathrm{d}v\right]^{k-1}. \tag{4.65}$$

The phase-field tangent stiffness matrix is written as

$$\mathbf{K}_{\phi\phi} = \left[\int_{\boldsymbol{\varphi}(\Omega)} \left(g'(\phi)\mathscr{H} + \frac{G_c}{4c_w l} w'(\phi)\phi\right)\mathbf{N}_\phi^T\mathbf{N}_\phi \mathrm{d}v + \int_{\boldsymbol{\varphi}(\Omega)} \frac{G_c l}{2c_w} (\nabla(\mathbf{N}_\phi))^T \nabla_{\boldsymbol{x}}\phi\mathbf{N}_\phi \mathrm{d}v\right]^{k-1}. \tag{4.66}$$

## 4.4 Phase-field formulations of interest

Phase-field formulations are defined by the geometric crack function $w(\phi)$, its normalisation parameter $c_w$, and the specific degradation function $g(\phi)$.

### 4.4.1 Hyperelastic constitutive model

This work adopts the Hencky hyperelastic material model, which incorporates the logarithmic tensor as the strain measure and defines the elastic energy potential as shown in Equation 4.69. Within this framework, the logarithmic strain tensor is defined as

$$\boldsymbol{\varepsilon} = \ln \boldsymbol{V} = \ln\left(\boldsymbol{F}\boldsymbol{R}^T\right) \tag{4.67}$$

Its work conjugate is the Cauchy stress tensor,

$$\boldsymbol{\sigma} = \mathbf{E}_0 : \boldsymbol{\varepsilon}, \tag{4.68}$$

where $\mathbf{E}_0$ is the fourth-order isotropic elasticity tensor.

Several definitions for the elastic strain energy, $\psi_0$, are used in the phase-field formulations presented in the next Sections.

### 4.4.2 AT1 phase-field model

The AT1 model employs a linear crack geometric function and a quadratic degradation law. In `LINKS` (Gonçalves (2024)), the fracture driving force, or undamaged free-energy density, is defined as

$$\psi_0(\boldsymbol{\varepsilon}) = \frac{1}{2}\boldsymbol{\sigma} : \boldsymbol{\varepsilon} = \frac{1}{2}\boldsymbol{\varepsilon} : \mathbf{E}_0 : \boldsymbol{\varepsilon} = \frac{1}{2}\lambda \,\mathrm{tr}^2(\boldsymbol{\varepsilon}) + \mu \,\mathrm{tr}\left(\boldsymbol{\varepsilon}^2\right), \tag{4.69}$$

where $\mathbf{E}_0$ is the undamaged elastic stiffness tensor. For an isotropic elastic undamaged material, the Lamé constants and the bulk modulus $\kappa$ are given as a function of the Young's modulus $E$, the Poisson's ratio $\nu$ and the number of space dimensions $n$ (e.g., 3), such that

$$\lambda = \frac{E\nu}{(1+\nu)[1-(n-1)\nu]}, \tag{4.70}$$

$$\mu = \frac{E}{2(1+\nu)}, \tag{4.71}$$

$$\kappa = \lambda + \frac{2\mu}{n} = \frac{E}{n[1-(n-1)\nu]}. \tag{4.72}$$

No energy decomposition of $\psi_0$ is applied for either the AT1 or AT2 models in this work. Instead, the history-dependent maximum strain energy can be rewritten as

$$\mathscr{H} = \max_{t\in[0,\tau]}\left[\frac{1}{2}\lambda \,\mathrm{tr}^2(\boldsymbol{\varepsilon}) + \mu \,\mathrm{tr}\left(\boldsymbol{\varepsilon}^2\right)\right]. \tag{4.73}$$

The degraded energy density is given simply as

$$\psi = g(\phi)\left(\frac{1}{2}\lambda \,\mathrm{tr}^2(\boldsymbol{\varepsilon}) + \mu \,\mathrm{tr}\left(\boldsymbol{\varepsilon}^2\right)\right). \tag{4.74}$$

Therefore, the damaged Cauchy stress tensor can be identified as

$$\boldsymbol{\sigma}^* = g(\phi)\boldsymbol{\sigma}. \tag{4.75}$$

The AT1 model employs the quadratic degradation function

$$g(\phi) = (1-\phi)^2 + k, \tag{4.76}$$

where $k$ is a small positive constant, introduced to prevent ill-conditioning when $\phi = 1$ (Navidtehrani et al. (2021)).

For the AT1 model, the geometric crack function is linear and defined as

$$w(\phi) = \phi, \quad c_w = \frac{2}{3}. \tag{4.77}$$

In addition, there is a minimum value for the fracture driving force for $\phi = 0$, obtained by solving (4.44) for $\phi = 0$, such that

$$\mathscr{H}_{\min} = \frac{3G_c}{16l}. \tag{4.78}$$

The AT1 model presents a linear-elastic behaviour prior to the maximum stress, with the phase-field material parameters used to control indirectly the material strength $\sigma_m$, which can be obtained from Equations (4.25) and (4.26), such that

$$\sigma_m = \sqrt{\frac{3EG_c}{8l}}. \tag{4.79}$$

### 4.4.3 AT2 phase-field model

The AT2 model shares the same functional definitions as AT1, namely: the undamaged elastic energy (Equation 4.69), the history field (Equation 4.73); the degraded energy density (Equation 4.74); the damaged stress tensor (Equation 4.75); and the quadratic degradation function (Equation 4.76).

However, the AT2 model employs a quadratic geometric crack function,

$$w(\phi) = \phi^2, \quad c_w = \frac{1}{2}. \tag{4.80}$$

Due to $w'(\phi = 0) = 0$, this implies a vanishing threshold for damage, and enforces a non-linear elastic behaviour prior to reaching the material strength $\sigma_m$ (Macías et al. (2023), Navidtehrani et al. (2021)).

The AT2 model also employs the phase-field material parameters to control indirectly the material strength $\sigma_m$, written as

$$\sigma_m = \frac{3}{16}\sqrt{\frac{3EG_c}{l}}. \tag{4.81}$$

It follows from Equations (4.79) and (4.81) that increasing the stiffness of the material increases the material strength. Therefore, for incompressible materials ($E \to \infty$), the material is simulated as infinitely strong ($\sigma_m \to \infty$), which is not physically realistic. In addition, phase-field models for brittle fracture (e.g., AT1 and AT2) require the decomposition of the elastic strain energy density to capture fracture for multi-axial stress states (Vicentini et al. (2024)). Further details on the specific energy decompositions can be found in Appendix A.

### 4.4.4 PF-CZM phase-field model

In this work, the PF-CZM model is the primary fracture formulation employed for the parametric studies in Chapter 6. In contrast with the AT1 and AT2 models, this formulation introduces a cohesive law within the diffuse crack representation of phase-field formulations and models the material strength explicitly.

By default, the driving force for fracture for PF-CZM is split into tensile and compressive components based on the principal stresses as follows

$$\psi_0^+(\boldsymbol{\sigma}) = \frac{\langle\sigma_1\rangle_+^2}{2E}, \tag{4.82}$$

$$\psi_0^-(\boldsymbol{\sigma}) = \frac{1}{2E}[\sigma_1\langle\sigma_1\rangle_- + \sigma_2^2 + \sigma_3^2 - 2\nu(\sigma_2\sigma_3 + \sigma_1\sigma_3 + \sigma_1\sigma_2)], \tag{4.83}$$

where $\sigma_i$ are the principal stresses, and $\langle\cdot\rangle_\pm$ denote the positive and negative parts. In this context, $\sigma_1$ represents the maximum principal (undamaged) stress. Unlike variationally consistent phase-field models, the PF-CZM formulation adopts a hybrid approach which simplifies the numerical implementation, i.e., it considers the energy split exclusively in the phase-field balance law and not in the linear momentum balance (Navidtehrani et al. (2021)).

The PF-CZM model employs a rational degradation function, given as

$$g(\phi) = \frac{(1-\phi)^d}{(1-\phi)^d + a\phi(1+b\phi)}, \tag{4.84}$$

with

$$a = \frac{4EG_c}{\pi l\sigma_m^2}, \tag{4.85}$$

where $E$ is the Young's modulus, and $\sigma_m$ is the tensile strength of the material. In contrast with the AT1 and AT2 fracture models, PF-CZM can model the material strength $\sigma_m$ explicitly. The softening

law defines the constants $b$ and $d$. For a linear softening law, $b = -0.5$ and $d = 2$, while for an exponential softening law, $b = 2^{5/3} - 3$ and $d = 2.5$.

For the PF-CZM model, the geometric crack function is quadratic, such that

$$w(\phi) = 2\phi - \phi^2, \quad c_w = \frac{\pi}{4}. \tag{4.86}$$

Similarly to AT1 model, PF-CZM has a minimum value for the fracture driving force for $\phi = 0$, obtained by solving (4.44) for $\phi = 0$, such that

$$\mathscr{H}_{\min} = \frac{2G_c}{\pi a l} = \frac{\sigma_m^2}{2E}. \tag{4.87}$$

The choice of characteristic functions in the PF-CZM model ensures that the energy-based crack propagation depends on strength criteria, thus addressing one of the main limitation of the AT1 and AT2 PF models (Lopez-Pamies et al. (2025)).

**Remark 1.** *For a hybrid isotropic/anisotropic phase-field damage model, the stress is obtained from an isotropic constitutive relation and scaled by the degradation function $g(\phi)$, while the phase-field is governed by an anisotropic evolution law (Wu and Nguyen (2018)). The free energy is given as $g(\phi)\psi_0(\boldsymbol{\varepsilon})$ where $\psi_0$ is the undamaged strain energy.*

*In other words, the energy split between a tensile and compressive contribution is only applied to the phase-field balance (fracture driving force), and not the balance of linear momentum, simplifying the implementation.*

*By contrast, the variationally consistent approach also decomposes the derivative of the free energy density with respect the strain tensor (the stress tensor). As a result, only the stress and stiffness active components are multiplied by the degradation function $g(\phi)$. While this approach is physically more realistic and provides more accuracy (e.g., in the presence of micro-crack closure-reopening (MCR) effects), it also demands higher computational power. For the case of monotonic tensile crack propagation, such as the examples analysed in this dissertation, the gain in accuracy is negligible.*

# Chapter 5

# Preprocessing routine for cohesive element insertion

## 5.1 Problem statement

A dedicated preprocessing routine was implemented in Python to generate two-dimensional meshes with zero-thickness cohesive elements inserted between continuum elements. The Python script automates the nontrivial topology changes required to simulate interfacial and intra-material fracture within the text-based input format compatible with the in-house FEM solver (`LINKS`). The preprocessing routine must comply with the following requisites:

- Read and register the input FEM mesh topology (e.g., node coordinates and element connectivities) and model parameters;
- Insert cohesive elements along material interfaces (e.g., fibre-matrix interfaces in RVEs) or across the entire domain;
- Preserve or prescribe the required boundary conditions, uniform tension/compression and first-order periodicity;
- Write a text-based output file compatible with the solver.

The preprocessing routine must perform modifications of the mesh topology efficiently and accurately, while being robust with respect to mixed finite element types and/or large mesh sizes.

Several open-source finite element mesh generators and pre/post-processing packages are available, such as `Gmsh` (Geuzaine and Remacle (2009)), Netgen (Schöberl (1997)) and Calculix (Dhondt and Wittig (1998)). However, without custom scripting, these tools do not provide a native feature to insert zero-thickness cohesive elements into an existing mesh while simultaneously preserving or prescribing the required boundary conditions and exporting a suitably formatted FEM output file that is compatible with the in-house solver `LINKS`. For these reasons, a custom script routine that operates directly on the target solver input format is preferable.

An existing legacy Python script for cohesive element insertion was available but presents some limitations that preclude it from its use in its current state for this dissertation objectives. In particular, the legacy implementation is unable to correctly handle mixed meshes (a non-negligible issue since a primary RVE mesh generator, GMMD, can produce meshes with different element types), is only able to insert cohesive elements at interfaces between different materials (e.g., fibre-matrix) and cannot pre-insert cohesive interfaces across the entire domain (or within selected materials) to simulate bulk fracture (Section 3.2).

Section 5.2 details the main architecture of the new version of the preprocessing routine. A brief description of the legacy implementation script which serves as the basis for the new features

is detailed in Section 5.3. Finally, Section 5.4 outlines a benchmark validation example employed to compare the processing times of both versions of the script.

## 5.2 Software architecture

The cohesive element insertion algorithm is implemented in an object-oriented Python module. The main class represents the mesh model and encapsulates attributes that store node coordinates, element connectivities, material identifiers, boundary conditions, incrementation details, as well as all relevant metadata. Core methods handle the main steps of the workflow of cohesive element insertion, such as connectivity searches, group assignments and file input/output. Auxiliary methods handle periodic pairs generation and additional user configurations.

The modular design, or object-oriented programming (OPP), is chosen to cleanly separate computationally intensive tasks (e.g., element/node searches and manipulation) from file I/O, to allow for efficient in-memory Python operations using hashed lookups and NumPy array vectorised operations, and to facilitate extension to complementary features, such as the optional insertion of intra-material cohesive elements, or the imposition of boundary conditions.

### 5.2.1 Implementation workflow

This in-house Python module generates interfacial and periodic zero-thickness cohesive elements once the initial two-dimensional meshed model is provided. The high-level workflow is controlled by the main method `insert_cohesive_elements`, which selects a sequence of steps depending on the chosen insertion procedure: along material interfaces; or across the entire finite element domain. Finally, it preserves or prescribes the requested boundary conditions. In summary, the script must follow these steps (see also Comprido Nascimento et al. (2023), Costa Amaro et al. (2023)):

- Register the input FEM mesh topology, model parameters, and boundary condition type in adequate in-memory Python data structures;
- Determine the insertion mode:
  - **Interface-CZM model**: if only selected inter-material interfaces are considered;
    1. Identify continuum elements adjacent to the relevant interfaces, and respective facets;
    2. Create new nodes and zero-thickness cohesive elements at relevant facets;
    3. Update connectivities of the continuum elements.
  - **All-CZM model**: if all material pairs are considered:
    1. Duplicate all nodes;
    2. Update connectivities of the continuum elements;
    3. Connect zero-thickness cohesive elements at every possible facet.
- Preserve or prescribe required boundary conditions (e.g., periodic, uniform displacements);
- Write a text-based FEM output file compatible with the in-house solver `LINKS`.

### 5.2.2 Enforcement of periodic boundary conditions

The generation of cohesive elements may disrupt strict periodic displacement constraints, by altering node numbering and by introducing new cohesive elements that intercept with prescribed boundaries. To enforce periodic boundary conditions to RVEs after cohesive element insertion (see Section 7.1.2), such as the ones needed for Chapter 7, an optional preprocessing routine is added to the Python module, which performs the following tasks:

- Identify master-slave node pairs on selected RVE edges;
- Update or reassign those master-slave pairs after node duplication so that periodicity is preserved in the output file;
- Optionally generate periodic zero-thickness cohesive elements at the RVE edges which are explicitly linked to the opposite edges.

## 5.3 Legacy implementation

This Section offers a brief description of the legacy version of the Python script, whose implementation is described in great detail in Comprido Nascimento et al. (2023), Costa Amaro et al. (2023). The same workflow of Section 5.2.1 is followed, the key differences being the implementation strategy and data handling.

Similarly to the structure presented in Section 5.2, the legacy code reads a text-based FEM input file, detects all interfaces between different materials, inserts the cohesive elements at those interfaces (by duplicating and renumbering nodes), modifies the continuum element connectivities to reflect the new node ids, and finally writes the modified mesh to a text-based FEM output file compatible with the in-house `LINKS` solver.

In contrast with the current script, the legacy implementation keeps the model information in the text-based output file and frequently scans and updates the file after each modification of the model parameters and/or mesh. Concretely, the script performs many line scans, text parsing operations and small reads/writes, while searching for node or element information. Every file read/write involves file I/O (system calls, buffering and parsing overhead), and is expected to add substantial latency when compared with the current script. Conversely, the current implementation retains mesh information in indexed in-memory Python structures (dictionaries, lists, tuples and NumPy arrays), performing hashed lookups or vectorised operations, and writing a single text-based output file at the end. The higher Ram usage is associated with lower Python interpreter overhead and fewer disk operations. An advantage of the legacy script storing information systematically thus lies in its increased robustness to system crashes, where progress is only partially lost.

## 5.4 Benchmark validation example

The code architecture of the Python module responsible for inserting cohesive elements along material interfaces has been presented in the previous Section. To validate the methodology and implementation, two benchmark microstructural (RVEs) models are processed: one with linear three-node triangular (TRI3) elements and another with quadratic six-node triangular (TRI6) elements. Performance and accuracy of the current version of the cohesive element insertion script is compared with the legacy implementation by Comprido Nascimento et al. (2023), Costa Amaro et al. (2023) (Section 5.3).

The properties assigned to the cohesive elements are reported in Table 5.3. The cohesive elements have identical properties in the normal and tangential directions, with a penalty factor of 0.1 to prevent element inter-penetrability. The isotropic elastic properties of the RVE constituents (epoxy matrix and glass fibres) are provided in Tables 5.1 and 5.2, respectively.

A medium-sized squared composite representative volume element (RVE) with a length of 0.05 mm was generated generated using GMMD (Vila-Chã et al. (2021)). The RVE is composed of an epoxy matrix containing glass fibres with 0.01 mm of diameter to achieve a volume fraction of 0.6, and subjected to a prescribed global deformation gradient of

$$\boldsymbol{F} = \begin{bmatrix} 1.01 & 0.00 \\ 0.00 & 1.00 \end{bmatrix}. \tag{5.1}$$

Table 5.1: Elastic material properties of the fibre, adopted in the comparison study of the current and legacy versions of the cohesive insertion script, adapted from a glass fibre found in Melro et al. (2013b).

| $\rho$ / tonne·mm$^{-3}$ | $E$ / MPa | $\nu$ / - |
|---|---|---|
| $7.8 \cdot 10^{-9}$ | $74 \cdot 10^{3}$ | 0.2 |

Table 5.2: Elastic material properties of the matrix, adopted in the comparison study of the current and legacy versions of the cohesive insertion script, adapted from an epoxy matrix found in Melro et al. (2013a).

| $\rho$ / tonne·mm$^{-3}$ | $E$ / MPa | $\nu$ / - |
|---|---|---|
| $7.8 \cdot 10^{-9}$ | $3.76 \cdot 10^{3}$ | 0.39 |

Two mesh configurations are considered: a linear triangular (TRI3) mesh, and a quadratic triangular (TRI6) mesh. Each mesh contains 671606 triangular continuum elements, with the TRI3 mesh with 333660 nodes and the TRI6 mesh with 1332619 nodes. Both the current and legacy Python scripts were executed independently ten times per mesh to record insertion times.

Table 5.3: Cohesive zone model material properties for the cohesive elements, adopted in the comparison study of the current and legacy versions of the cohesive insertion script.

| $\phi_n$ / MPa·mm | $\phi_t$ / MPa·mm | $\sigma_n$ / MPa | $\sigma_t$ / MPa | $\alpha$ / - | $\beta$ / - | $\lambda_n$ / - | $\lambda_t$ / - |
|---|---|---|---|---|---|---|---|
| 10 | 10 | 50 | 50 | 1.5 | 1.5 | 0.1 | 0.1 |

It can be noted that the new version of the cohesive script is able to accommodate mixed meshes, i.e., meshes with more than one element type[1]. Furthermore, all input-file keywords, or simulation parameters, are correctly parsed by both versions of the script.

Table 5.4 summarises mean runtimes, standard deviations, and coefficients of variation (ratio of standard deviation to mean value) for each combination of mesh and version of the code. As can be observed, the current routine reduces the total processing time by factors of approximately 37 and 21, for TRI3 or TRI6 meshes, respectively. This is expected due the suboptimal data-storage scheme of the legacy code (see Section 5.3).

In addition, Figure 5.1 compares the mean values for each execution of the scripts, while Figure 5.2 presents boxplot distributions of the ten trial runtimes. It can be inferred that the current version presents a more spread distribution of its runtimes. Although the current routine achieves substantially shorter insertion times, the average runtime renders it more sensitive to minor system fluctuations, e.g., transient memory spikes or background tasks. For example, a variation of 0.75 seconds corresponds to a deviation of 5%. In contrast, the legacy version's longer runtimes reduces the relative impact of these spurious effects, yielding tighter boxplot distributions.

The post-insertion RVEs are analysed in `LINKS` using both scripts outputs, with the reaction curves and deformed configurations being indistinguishable, as seen in Figures 5.3 and 5.4, respectively. As a result, the current implementation of the cohesive element insertion methodology detailed in Comprido Nascimento et al. (2023), Costa Amaro et al. (2023) is considered valid for the purposes of RVE generation.

[1] Previous attempts to run the run the legacy script on meshes combining TRI3 and QUAD4 (or QUAD4-FBAR) elements failed, so no direct comparison with the current version was possible.

Table 5.4: Descriptive statistics of the preprocessing runtimes extracted for 10 executions of the Python script that inserts cohesive elements in the interfaces of each RVE. Times are reported for current and legacy script versions and for TRI3 and TRI6 meshes.

| | Tri3 mesh | | Tri6 mesh | |
|---|---|---|---|---|
| Version | current | legacy | current | legacy |
| Mean / s | 14.805 | 545.793 | 24.511 | 533.551 |
| Standard deviation / s | 0.289 | 2.795 | 0.219 | 4.980 |
| Coefficient of variation / % | 1.950 | 0.512 | 0.894 | 0.933 |

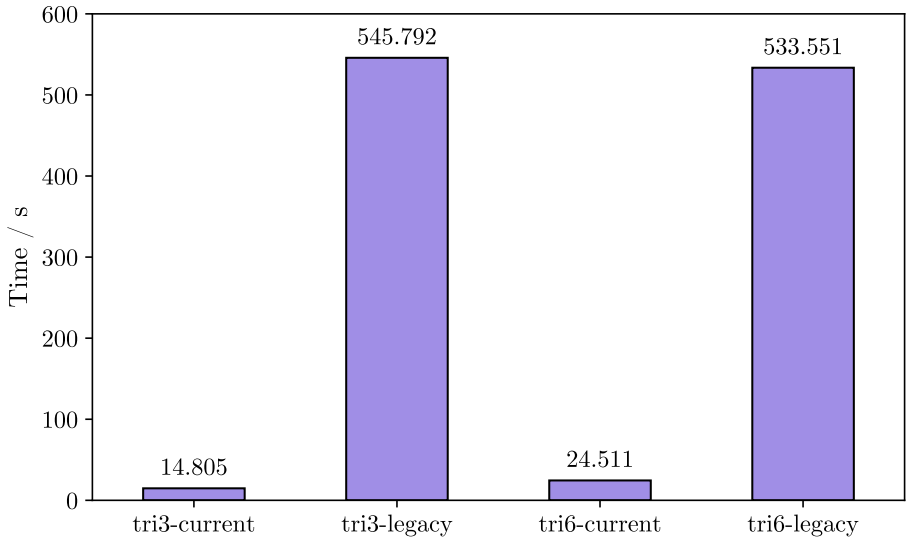


Figure 5.1: Mean runtime per execution (ten trials) for each script version and mesh type.

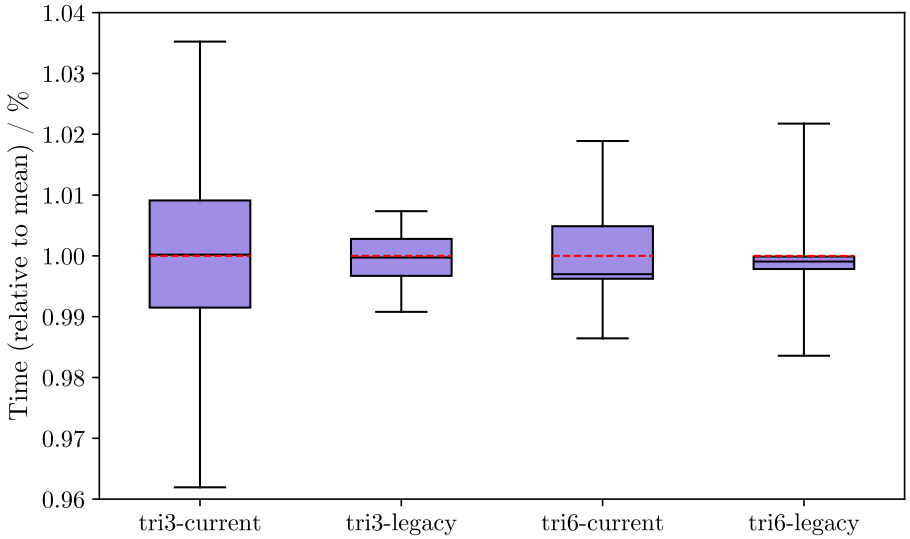


Figure 5.2: Boxplot distributions of the ten trial runtimes for each script version and mesh type.

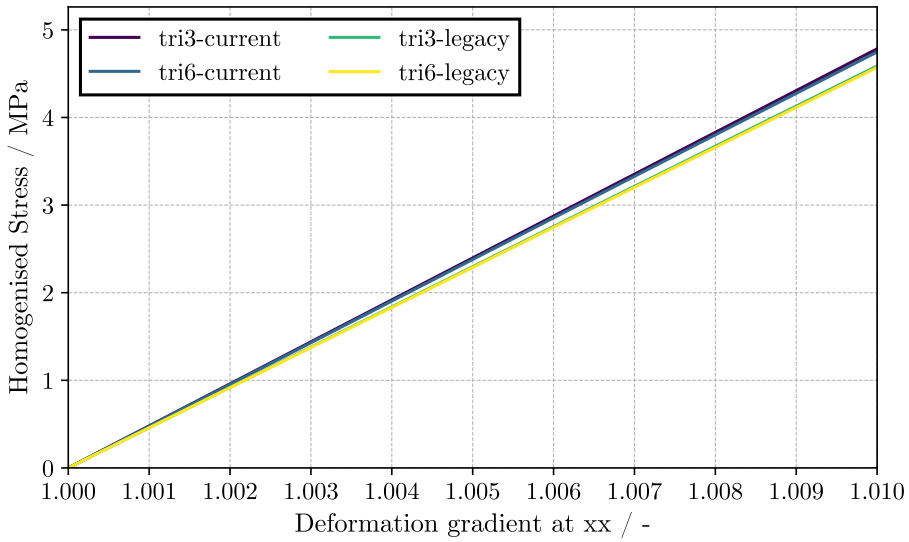


Figure 5.3: Homogenised stress against prescribed deformation gradient component $\boldsymbol{F}_{xx}$, for each script version and mesh type.

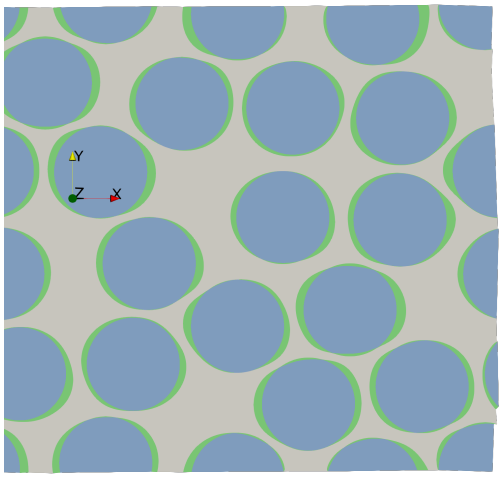

(a) TRI3 mesh, processed with the current script version.

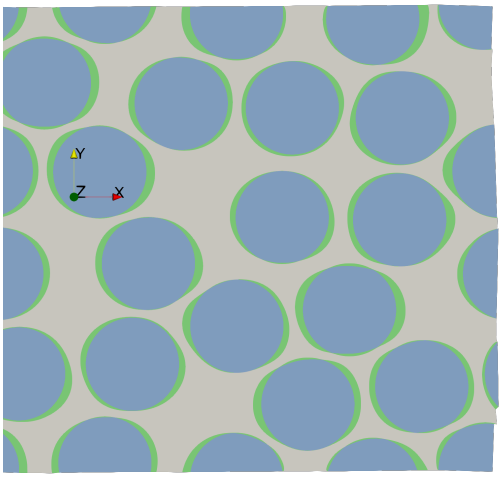

(b) TRI6 mesh, processed with the current script version.

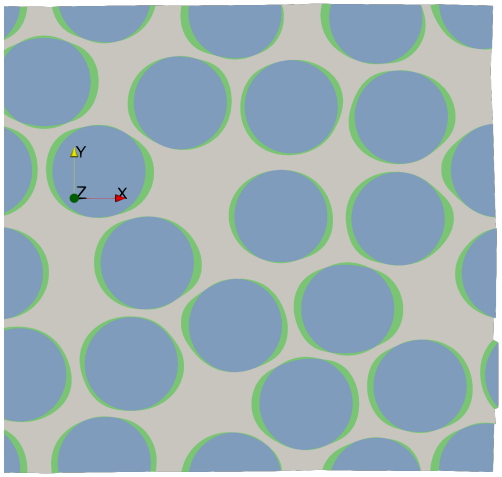

(c) TRI3 mesh, processed with the legacy script version.

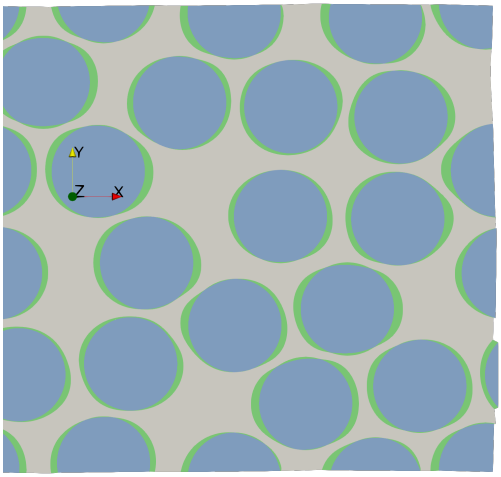

(d) TRI6 mesh, processed with the legacy script version.

Figure 5.4: Deformed configurations (scale factor of 10) of the RVEs after preprocessing.

# Chapter 6

# Numerical applications in fracture mechanics

This Chapter reports several numerical applications and benchmarks implemented in the finite element software LINKS to evaluate the cohesive zone model and the phase-field fracture approach previously introduced in Chapters 3 and 4, respectively. Section 6.1 investigates the impact of the material properties of the CZM in the fracture behaviour of selected macro-scale models. Section 6.2 presents several benchmark examples to assess the impact of phase-field material properties in the mechanical response. Section 6.3 then compares two phase-field formulations (AT2 and PF-CZM), and, finally, Section 6.4 closes this Chapter with a direct comparison between the phase-field and cohesive zone model approaches.

## 6.1 Influence of the cohesive material properties

In order to perform a parametric study of the eight fracture properties associated with the fracture of a model with cohesive elements, a simple two-dimensional mesh (0.1 m × 0.1 m) is selected, with two continuum linear three-node triangular (TRI3) elements, separated by a cohesive 4-node quadrangular (COH2D4) element along the diagonal direction (see Figure 6.1).

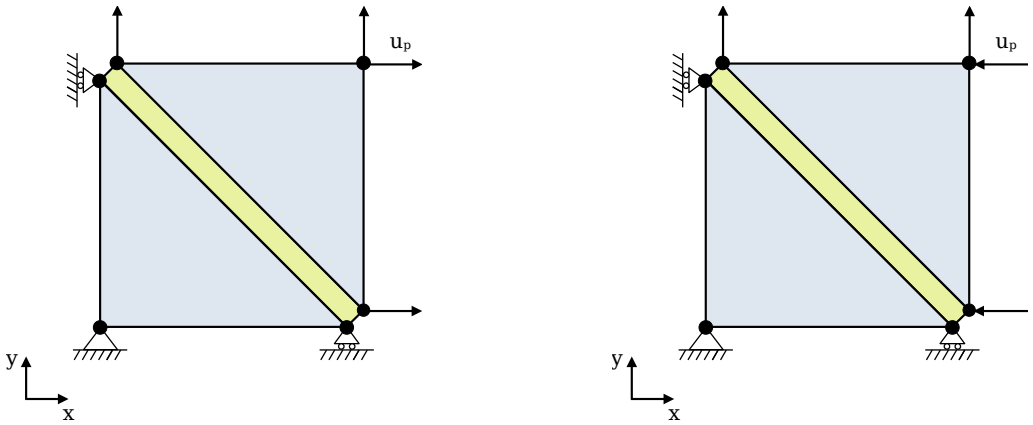


(a) Mode 1 - two-dimensional

(b) Mode 2 - two-dimensional

Figure 6.1: Schematic representation of the two-dimensional patch test presented in Park and Paulino (2012) and employed in the cohesive zone model benchmark. The COH2D4 cohesive element is in light green, with zero thickness at the beginning of the analyses, while the two TRI3 continuum elements are in light blue.

The load cases were selected to reflect the three distinct modes of fracture presented previously

in Section 3.3.4. For the mode I benchmark test, the structure is elongated under a displacement up to $7.5 \cdot 10^{-5}$ m at the top and right edge nodes, as depicted in Figure 6.1a. Regarding the mode II numerical application, the same mesh is elongated and compressed simultaneously in the top and right edge nodes, up to the same prescribed displacement. In order to simulate mixed-mode fracture, the mesh is elongated in the y-direction in the top edge nodes, for the same prescribed displacement. The overall type of loading is expected to be directly linked to the corresponding material properties, such that mode I, or opening mode, of fracture is to be associated with just the normal fracture properties of the cohesive element, while the mode II, or shearing mode, will be supported by the tangential properties of the cohesive element.

The mode II model is identical to a patch test proposed by Park and Paulino (2012) and examined by Vieira de Carvalho (2023). Thus, the same elastic properties found in those references are used for the bulk material present in the continuum elements, as presented in Table 6.1.

Table 6.1: Elastic material properties of the bulk material.

| $E$ / Pa | $\nu$ / - |
|---|---|
| $32 \cdot 10^9$ | 0.3 |

In addition, a PPR potential-based material was selected for the cohesive element, with a null density since the meshed body is statically loaded, an irreversible traction separation law, and a penalty factor of 1 to prevent inter-penetrability of the continuum elements, which is not expected due to the opening and/or tangential loads applied. The characteristic parameters in the PPR potential (Table 6.2) were distinguished between the normal, $(\cdot)_n$, and tangential, $(\cdot)_t$, directions: fracture toughness $\phi$, cohesive strength $\sigma$, the shape parameters ($\alpha$ for normal direction, and $\beta$ for tangential direction), and the initial slope parameter $\lambda$. A parametric study is performed by varying these properties individually. The reference value, and the maximum and minimum bounds for each property can be seen in Table 6.3, with the material properties varying linearly between the two bounds.

Table 6.2: Constitutive cohesive model input parameters.

| **Notation** | **Designation** |
|---|---|
| $\phi_n$ | Normal fracture energy. |
| $\phi_t$ | Tangential fracture energy. |
| $\sigma_n$ | Normal cohesive strength. |
| $\sigma_t$ | Tangential cohesive strength. |
| $\lambda_n$ | Normal initial slope indicator. |
| $\lambda_t$ | Tangential initial slope indicator. |
| $\alpha$ | Normal shape parameter. |
| $\beta$ | Tangential shape parameter. |
| $\alpha_p$ | Contact penalty factor. |
| - | Unloading type: irreversible or reversible. |

Table 6.3: Cohesive material properties of the PPR potential-based material.

| | $\phi_n$ / Pa·m | $\phi_t$ / Pa·m | $\sigma_n$ / Pa | $\sigma_t$ / Pa | $\alpha$ / - | $\beta$ / - | $\lambda_n$ / - | $\lambda_t$ / - |
|---|---|---|---|---|---|---|---|---|
| Reference | 100 | 200 | $4 \cdot 10^6$ | $3 \cdot 10^6$ | 2 | 2 | 0.005 | 0.005 |
| Minimum | 10 | 20 | $1 \cdot 10^6$ | $1.5 \cdot 10^4$ | 1.005 | 1.0001 | $5 \cdot 10^{-5}$ | $5 \cdot 10^{-5}$ |
| Maximum | 300 | 600 | $7 \cdot 10^6$ | $6 \cdot 10^6$ | 5 | 5 | 0.5 | 0.5 |

For each fracture mode (I, II, and mixed), each of the eight material properties listed in Table

6.3 was varied linearly across ten equally spaced values between a minimum and maximum range, while the penalty factor, $\alpha_p$, remained at its reference value of 1. The resulting deformed configurations for modes I, II and mixed are shown in Figure 6.2. In addition, the force-displacement curves are compared in Figures 6.3, 6.4 and 6.5, for modes I, II, and mixed, respectively. The total vertical reaction forces were computed as the sum of the reaction forces at the upper-edge nodes. The reference response, obtained with the reference CZM PPR potential-based material properties, is highlighted in red in all subfigures for comparison.

For the reference response, mode I attains a higher peak force of 657.495 kN at a smaller critical displacement of $1.2 \cdot 10^{-5}$ m, whereas Mode II reaches only 299.562 kN at $9 \cdot 10^{-6}$ m. This contrast stems from the fact that, for the reference values, the normal fracture toughness exceeds its tangential counterpart while the normal cohesive strength is lower than its tangential counterpart. As expected, for mode I, varying the tangential direction properties has no perceptible effect on the force-displacement response, i.e., the curves remain coincident with the reference (Figures 6.4-1. 6.4-3, 6.4-5 and 6.4-7). Similarly, the material properties in the normal direction do not have an impact in the response of the model, for mode II (Figures 6.4-2. 6.4-4, 6.4-6 and 6.4-8).

As anticipated, increasing the fracture toughness without changing the cohesive strength causes the final crack opening to increase (see Figures 6.3-1 and 6.4-2). In fact, once complete failure occurs for mode I and II, the predicted theoretical value for the dissipated, or cohesive, energy must be equal to the length of the cohesive element multiplied by the fracture toughness of the corresponding mode, such that

$$\Pi_{\text{coh}} = \sqrt{2} \cdot 0.1 \phi_i, \quad \text{for } i = n, t, \tag{6.1}$$

given in S.I. units of Joule/m. For modes I and II, the reference value is 14.14 J/m and 28.28 J/m, respectively.

Conversely, for mode I and II, as the fracture toughness is held constant, an increase in the respective cohesive strength leads to a stronger interface, with a higher peak load capacity: 101.58 kN up to 689.19 kN. However, it also reduces the final crack opening width, for a given fracture toughness (see Figures 6.3-3 6.4-4).

The choice for $\alpha = \beta = 2$ for the reference model corresponds a PPR potential function with an order of two, such that its gradient decreases linearly with the crack opening, resulting in a linear softening law. For values of the shape parameters greater than 2, the softening response of the traction-separation law is convex for the corresponding mode of fracture, which is characteristic of quasi-brittle materials with a more gradual loss of its load bearing capacity. Furthermore, as predicted by Equations (3.66) and (3.67), an increase in the shape parameters leads to an increase of the corresponding final crack opening widths. For a fixed initial slope indicator, an increase in $\alpha$ and $\beta$ also results in greater values of the critical opening widths. Conversely, values below 2 for the shape parameters yield a more concave softening curve, which, for values close to 1, approaches a plateau-type response. In this case, the reaction force remains at its maximum after the peak response until it suddenly drops to 0 (see Figures 6.3-5 and 6.4-6).

The initial slope parameters, $\lambda_n$ and $\lambda_t$ express the ratio between the critical crack opening width to the final crack opening width, as presented in Equation (3.65). For instance, the reference value of 0.005 yields an elastic domain corresponding to 0.5% of the total cohesive model response. Decreasing these parameters leads to a decrease of the artificial compliance introduced by the cohesive element, and, conversely, to an increase in the initial elastic stiffness for each corresponding fracture mode, as can be seen in Figure 6.3-7 for $\lambda_n$, and Figure 6.4-8 for $\lambda_t$.

In the mode II fracture models, two cases failed before complete loading. The simulation with $\alpha = 1.005$ ended abruptly at a prescribed displacement of $3.540 \cdot 10^{-5}$ m (Figure 6.4-5). In this case, the value of normal shape parameter approaches 1, which produces a near discontinuous drop in the normal stiffness which may compromise the simulation convergence. In addition, in Figure 6.4-7, the curve for $\lambda_n = 5 \cdot 10^{-5}$ matches the reference initial elastic response, but starts oscillating between the reaction-force value and zero. Due to the very low value of the normal initial

slope indicator, the normal elastic branch has a very steep branch which may overly restrain the normal opening so that, when the cracks opens tangentially under mode II, the numerical solver switches back and forth between a fully uncracked state (with zero opening) and a cracked state, which causes the simulation to terminate for a prescribed displacement of $3.539{\cdot}10^{-5}$ m in Figure 6.4-7.

As seen in Figure 6.5, the mixed mode response corresponds, in general, to a combination of the effects previously seen for mode I, and II, with some key distinctions. For the reference mixed-mode response, the maximum reaction force is 657.50 kN, higher than modes I and II, due to the combined effect from both material properties (normal and tangential).

When the normal cohesive strength is set at its two highest values (6333333 and 7000000 Pa), simulations terminated abruptly. Since the fracture toughness is not simultaneously increased with an increase in strength, the interface is too brittle to dissipate all the energy and the solver can not converge past the peak response (see Figure 6.5-3). In addition, the impact of tangential shape parameter, $\beta$, is negligible, while the change in the softening law for $\alpha$ is more noticeable. Despite these differences, the impact of both shape parameters is still much smaller than the impact of each individual shape parameter in the respective mode of fracture.

As expected, the impact of the variation of the initial slope indicators resulted in a similar impact in the mechanical response of model, as the maximum and minimum bounds for the values are the same for both properties (Figures 6.5-7 and 6.5-8). Finally, at the lowest tested value of 42.222 Pa·m for the tangential toughness, the simulation ends early for a prescribed displacement of $1.895{\cdot}10^{-5}$ m, since the interface can dissipate the energy from the combined loading.

To conclude, the parametric study of the eight cohesive properties in the PPR cohesive zone model for a benchmark example provides a flexible framework for simulating mode I, mode II and mixed mode fracture. This potential-based approach offers the possibility to adjust cohesive laws to specific material and loading conditions. Therefore, this study demonstrates that careful selection of CZM parameters is crucial for achieving both numerical stability and physically realistic predictions.

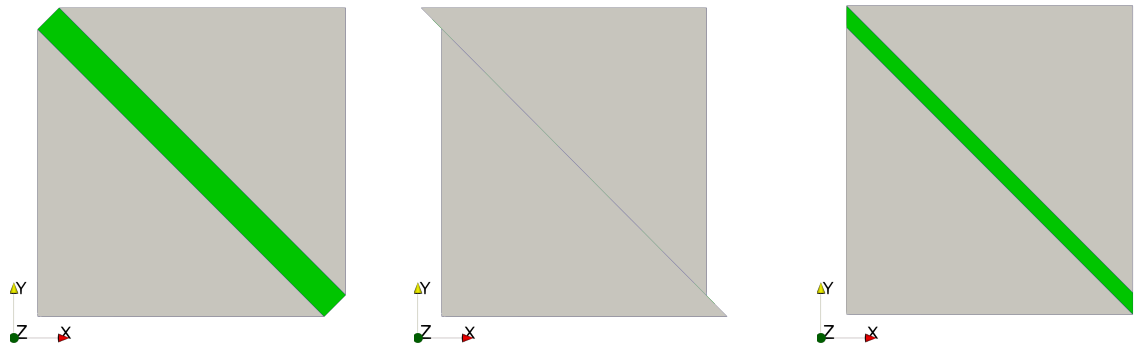


(a) Mode 1 - two-dimensional (b) Mode 2 - two-dimensional (c) Mixed mode - two-dimensional

Figure 6.2: Deformed configuration at the final prescribed displacement of $7.5 \cdot 10^{-5}$ m, for a scale factor of 100.

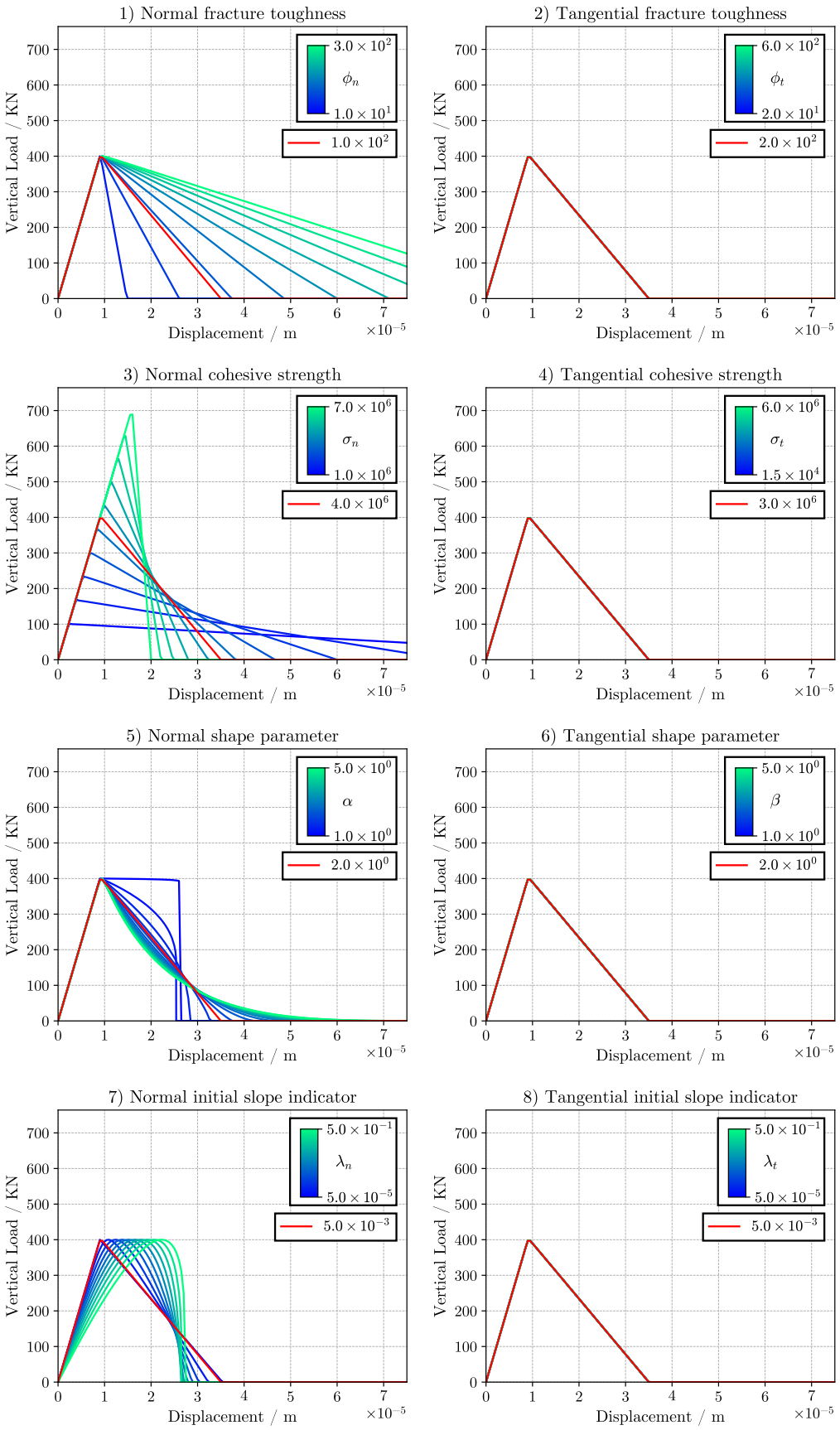


Figure 6.3: Results for the two-element mesh, for mode I fracture, varying the values of the PPR cohesive properties. Vertical reaction force against displacement.

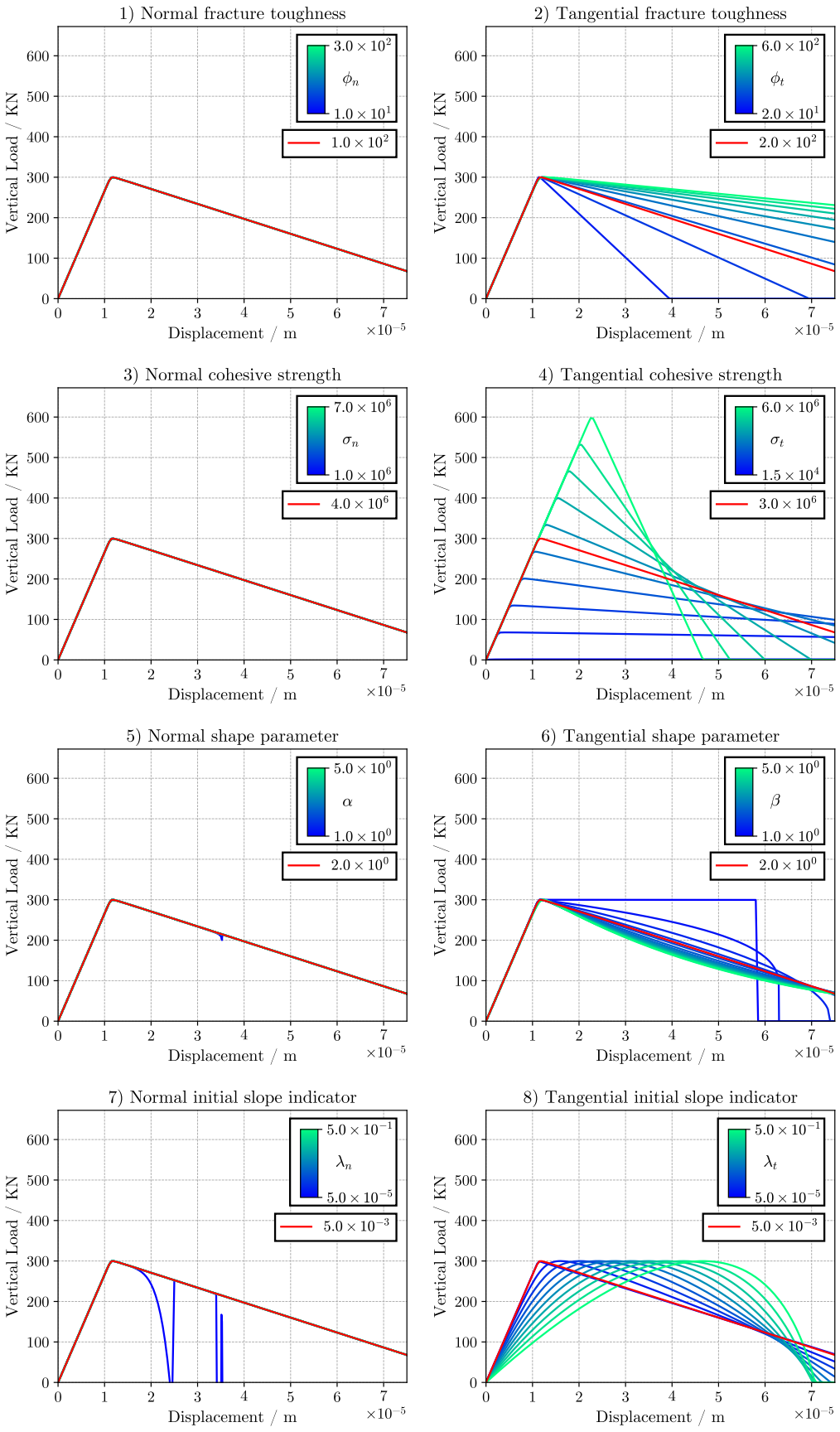


Figure 6.4: Results for the two-element mesh, for mode II fracture, varying the values of the PPR cohesive properties. Vertical reaction force against displacement.

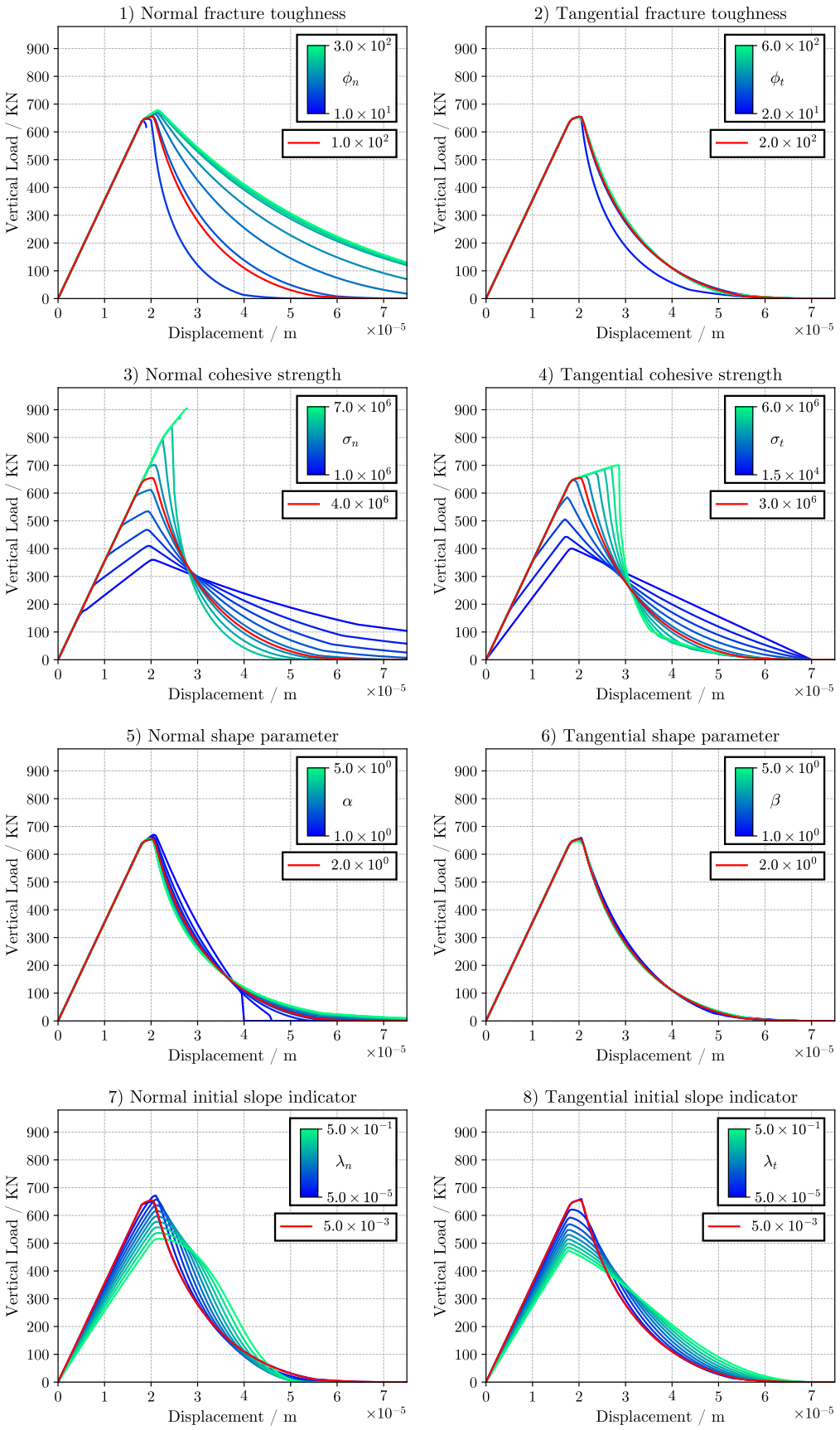


Figure 6.5: Results for the two-element mesh, for mixed-mode fracture, varying the values of the PPR cohesive properties. Vertical reaction force against displacement.

## 6.2 Influence of the PF-CZM fracture material properties

This Section evaluates the impact of the material properties associated with the PF-CZM fracture model on the mechanical response of a quarter of a rectangular plate (10 mm × 15 mm) with a central circular hole (radius of 2 mm). The plate was subjected to a tensile load, by prescribing a vertical displacement of 0.4 mm at the upper side of the plate. As shown in Figure 6.6a, the test piece is simply supported on its right and bottom edge nodes, as well as having a symmetry boundary condition in its left edge. Figure 6.6b shows the finite element discretisation, for a total of 216 2nd-order, 8-node quadrilateral (QUAD8) elements with four Gauss points and 715 nodes, with a higher mesh refinement near the open hole to better capture the stress concentration.

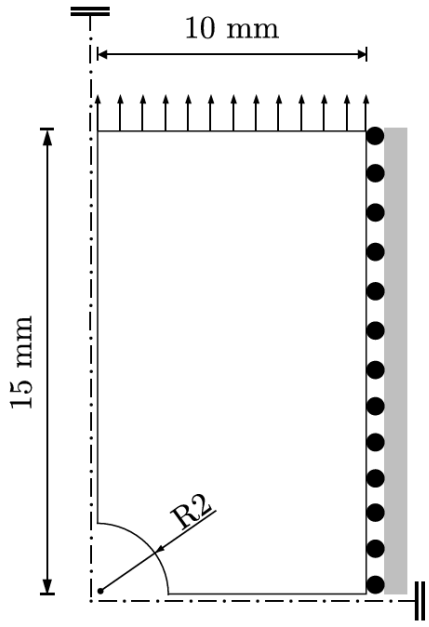


(a) Schematic representation.

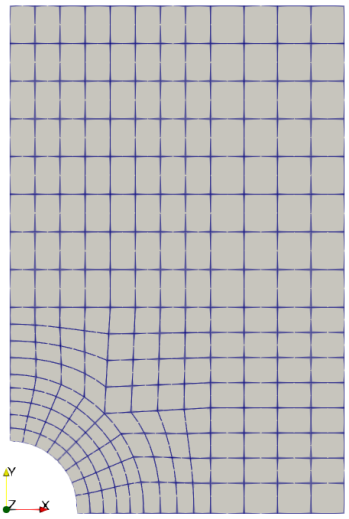

(b) Finite element mesh with 216 QUAD8 elements and 715 nodes.

Figure 6.6: A quarter of a rectangular plate with a central circular hole, under tensile load. Taken from Gonçalves (2024).

The elastic properties are displayed in Table 6.4. For the properties describing the facture behaviour of the phase-field problem, a parametric study was conducted by varying each property separately, between a maximum and minimum bound, while the remaining properties are set at their nominal, or reference, values (see Table 6.5). The reference softening law chosen for the parametric study is linear ($b = -0.5$ and $d = 2$), which is then compared with an exponential softening law ($b = 2^{5/3} - 3$ and $d = 2.5$). All simulations are performed using 1000 increments, with a pseudo-time step of 0.001 and a convergence tolerance of $1 \cdot 10^{-6}$ for the discretisation of the mechanical problem, the phase-field problem, and the coupling scheme. A vertical displacement of 0.4 mm is applied to the nodes at the upper edge of the plate.

Table 6.4: Elastic properties of the PF-CZM material, adopted in the parametric study of a notched rectangular plate.

| $E$ / MPa | $\nu$ / - |
|---|---|
| $210 \cdot 10^3$ | 0.3 |

Figure 6.7 depicts the phase-field distribution obtained for a load factor of 0.418. The size of the typical QUAD8 element in the refined region around the circular hole is 0.4 mm. The crack nucleates

Table 6.5: Fracture properties of the PF-CZM material, adopted in the parametric study of a notched rectangular plate.

| | $G_c$ / MPa·mm | $l$ / mm | $\sigma_m$ / MPa |
|---|---|---|---|
| Reference | 5 | 0.01 | 1000 |
| Minimum | 1 | 0.0005 | 500 |
| Maximum | 10 | 0.02 | 2000 |

at the bottom of the plate, near the circular hole, propagating in a straight line until reaching the right edge, perpendicular to the loading direction.

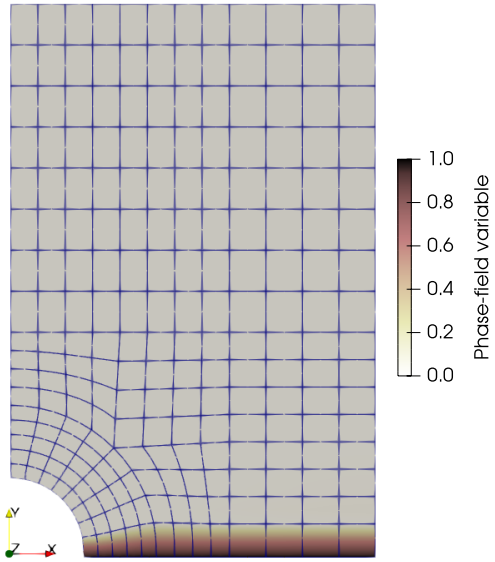


Figure 6.7: Phase-field distribution (plotted in the deformed configuration) corresponding to a model with reference PF-CZM material properties, for a load factor of 0.418 (or a prescribed displacement of 0.1672 mm).

Figure 6.8 depicts the vertical reaction forces recorded at the nodes with the prescribed displacement, and then plotted, with the reference curve in red. As expected, the PF-CZM curves show a linear-elastic behaviour up to the maximum reaction force, where fracture properties have no impact on the response of the plate. Additionally, the force-displacement curves show differences in the post-peak behaviour.

When increasing the fracture toughness above its reference value, the total fracture energy absorbed increases, while the peak-response rises slightly (see Figure 6.8-1). Conversely, reducing the fracture toughness by the same amount causes a significant reduction in the maximum load. In extreme cases, this mismatch can lead to a premature peak-load, effectively reducing the model strength below its assigned value and may even lead to an abrupt end to the simulation.

It is therefore critical that the fracture parameters, in particular $G_c$ and $\sigma_m$, must be compatible. If the fracture toughness is too low for the same fracture strength, the model is not able to dissipate the additional elastic energy. In practice, the softening branch is too steep and the force-displacement curve exhibits a steep load drop that may induce a snap-through/-back behaviour, which the solver cannot solve under displacement control.

In this work, the phase-field length-scale parameter, $l$, is treated purely as a numerical regularisation parameter of the sharp crack, which governs the width of localised crack band (the region where the phase-field variable goes from 1 to 0). In this numerical studies, the value of the length-scale $l$ must be consistent with the mesh, ensuring that $l$ is at least five times larger than the mesh size (Bian et al. (2024), Navidtehrani et al. (2021)). As a result, since the size of the finite elements

along the potential crack propagation path (bottom edge) exceeds $5l$, the coarse mesh cannot fully resolve the diffuse crack band, leading to a size effect. Decreasing $l$ introduces artificial effects which influence the global response of the model. Specifically, the artificial fracture toughness and the peak load response increase, with the post-peak softening branch less steep (Figure 6.8-2).

**Remark 2.** *Some researches relate the phase-field length-scale with physical quantities, instead of mesh density. This perspective occurs not only in brittle PF formulations (e.g., AT1 and AT2), where $l$ is related to the material strength $\sigma_m$ ( see Section 4.2.4), but in more general attempts to connect macroscopic fracture behaviour to nanoscale material properties. For example, Molnár and Barthel (2024) proposes to relate $l$ directly to the nanoscopic fracture mechanisms in amorphous solids, e.g. glass.*

As shown in Figure 6.8-3, when increasing the fracture strength $\sigma_m$, the peak response of the global force-displacement curve increases, while the total fracture energy increases as well: from 370 Joules to 615 Joules. These energy values were obtained by numerically integrating the under under each force-displacement curve with the trapezoidal rule in Python. However, if the fracture strength is too high for the values of the fracture toughness and length-scale chosen, then the simulation ends abruptly.

Finally, in Figure 6.8-4, both curves, linear ($b = -0.5$ and $d = 2$) and exponential ($b = 2^{5/3} - 3$ and $d = 2.5$), show an identical linear-elastic behaviour, with the post-peak response reflecting the corresponding softening law chosen for the simulations.

## 6.3 Comparison between AT2 and PF-CZM fracture models

This Section compares the classical AT2 model with the previously assessed PF-CZM model. Although the AT1 phase-field model, with its linear-elastic regime, reproduces more faithfully the PF-CZM response, AT2 is selected for its widespread use in academia and its capacity to highlight the differences with the PF-CZM model in the following numerical example. In particular, the goal is to study the impact of the fracture toughness material parameter in the AT2 model, and seek the value of $G_c$ that most closely reproduces the PF-CZM mechanical response.

For this numerical application, the same meshed plate with a central circular hole is employed (Figure 6.6). To establish a direct comparison with the AT2 model, a linear softening law is chosen for the PF-CZM model with phase-field material properties shown in Table 6.6.

The same elastic material properties from Table 6.4 are adopted, with the AT2 material properties seen in Table 6.7. Similarly to what was done in the PF-CZM parametric study (Section 6.2), the fracture toughness $G_c$ is varied, while the remaining phase-field variable ($l$) remained constant.

Table 6.6: Fracture properties of the PF-CZM material adopted in the comparison study with the AT2 fracture model, for the notched rectangular plate.

| $G_c$ / GPa | $l$ / mm | $\sigma_m$ / MPa |
|---|---|---|
| 5 | 0.02 | 2000 |

Table 6.7: Fracture properties of the AT2 material adopted in the comparison study with the PF-CZM fracture model, for the notched rectangular plate.

| | $G_c$ / GPa | $l$ / mm |
|---|---|---|
| Minimum | 1 | 0.02 |
| Maximum | 5 | |

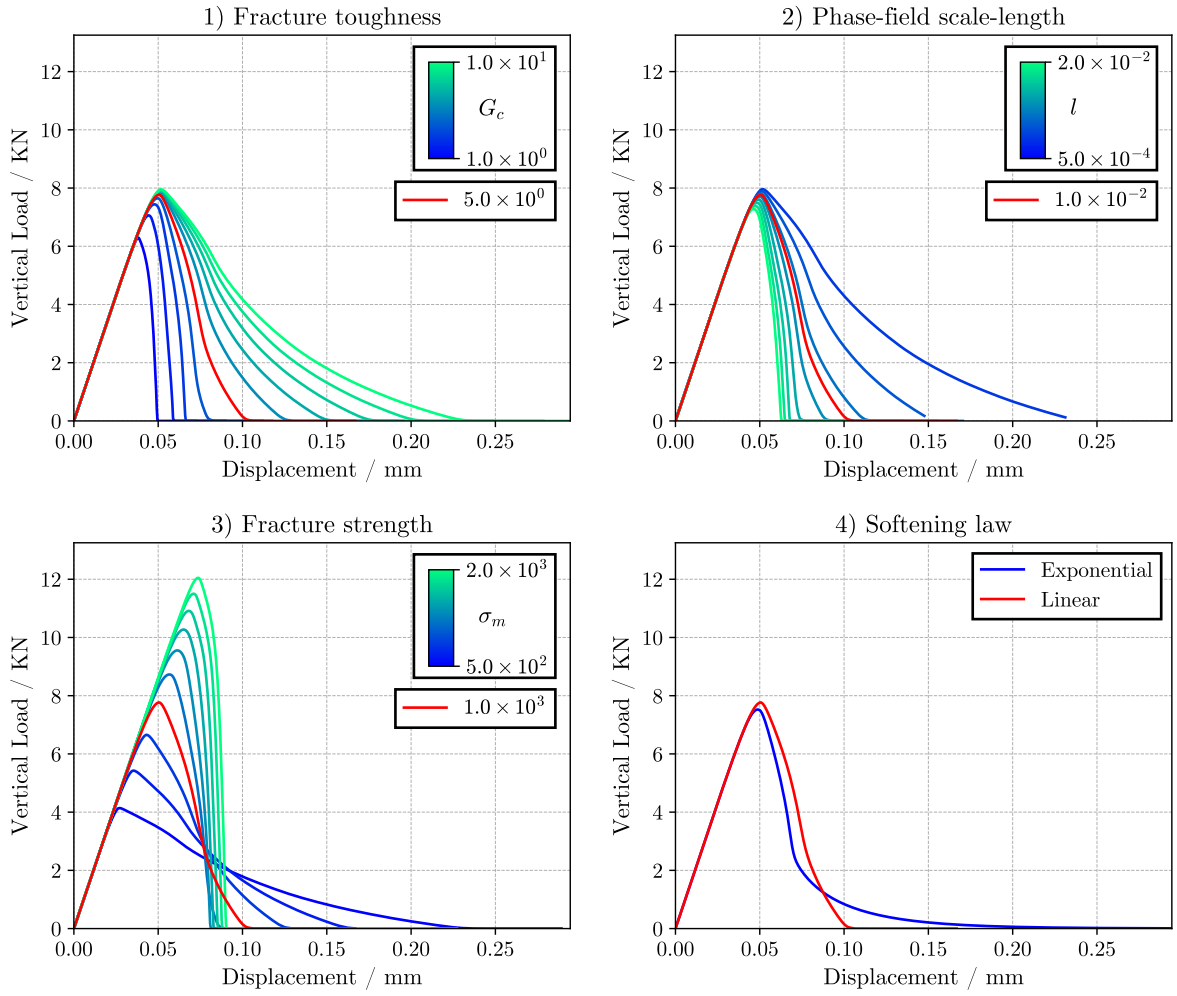


Figure 6.8: Vertical reaction force curves with the PF-CZM model for the plate with central circular hole, for a linear softening law and varying the values of the fracture properties.

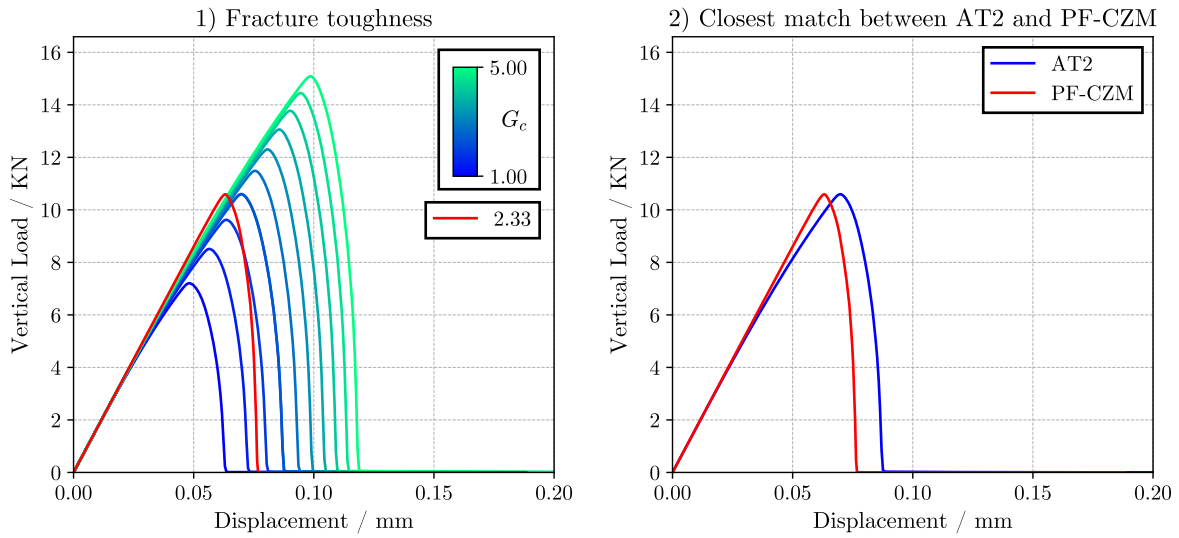


Figure 6.9: Vertical reaction force curves with the AT2 and PF-CZM models for the plate with central circular hole, varying the values of the fracture toughness. The PF-CZM simulation with $G_c = 2.33$ MPa·mm produces a peak load that matches that of the AT2 model.

For the AT2 phase-field model, an identical phase-field distribution to the one obtained for the PF-CZM model seen in Figure 6.7, so it is not reproduced here. Figure 6.9 depicts the vertical forces measured at the nodes at the upper edge, and plotted against the prescribed displacement.

In contrast with PF-CZM, the AT2 curves show a non-linear behaviour before the maximum reaction force is reached (see Figure 6.9-2). The peak response itself increases with an increasing fracture toughness, since in brittle phase-field models (AT1 and AT2), the material strength is defined indirectly from the coupling between $G_c$ and the length-scale $l$. Therefore, raising $G_c$ leads to an increase in the amount of strain energy the material absorbs, thus increasing the critical load. By contrast, PF-CZM prescribes the fracture strength explicitly, thus any change in $G_c$ must be reflected in the post-peak softening response. In the AT2 model, neither $l$ nor $G_c$ have a direct influence in the post-peak behaviour, since fracture is always brittle. Figure 6.9-1 shows a similar post-peak behaviour, for the same phase-field length (Gonçalves (2024)).

By calibrating the fracture toughness $G_c$ of the AT2 model to match the maximum vertical reaction force to the PF-CZM model, a value of 2.330 MPa·mm is obtained. Using Equation 4.81, the theoretical value for the fracture toughness is $G_c = 3.61$ MPa·mm.

## 6.4 Comparison between the cohesive zone model and the phase-field fracture model

In this Section, a comparison study between the cohesive zone model presented in Chapter 3 and the phase-field fracture model is performed, with the goal of comparing three models: a model with cohesive elements inserted in the probable crack path (*interface-CZM*); a model with a PF-CZM material for the continuum elements; and a model with cohesive elements inserted between all continuum elements (*all-CZM*). The numerical study is based on the previous work developed in Vieira de Carvalho (2023), for a spatially discretized perforated beam, subjected to opening loads along the right-most edge (see Figure 6.10). Because of the high release of energy, the simulation is dynamic, as in Vieira de Carvalho (2023).

The perforated plate is elongated in the y-direction, for a maximum prescribed displacement of 0.0001 mm at the left edge, until complete failure is obtained. Considering the boundary condi-

tions, symmetry of the perforated cantilever beam and the type of loading, it is expected that the nodes at the center line are subjected to mode I fracture (Figure 6.10). A previous meshed model employed in Vieira de Carvalho (2023) is repurposed (Figure 6.11), with quadratic 6-node triangular (TRI6) continuum elements, with three Gauss points. In the center line (between each pair of consecutive perforated holes), quadratic 6-node cohesive (COH2D6) elements were inserted, using a three-point Newton-Cotes quadrature.

To incorporate a PF-CZM material model, the perforated plate is remeshed as in Figure 6.12, with the PF-CZM material discretised with TRI6 elements. For the model with COH2D6 cohesive elements inserted everywhere, the same mesh is used. Here, the Python script detailed in Chapter 5 is used.

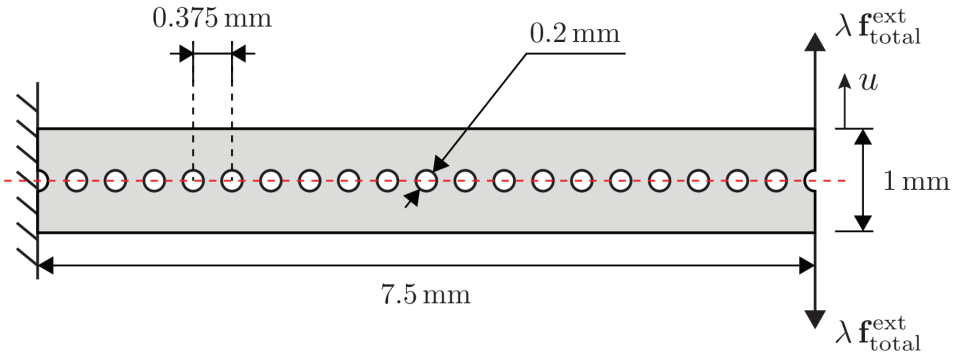


Figure 6.10: Schematic representation of the perforated cantilever beam subjected to mode I fracture presented in Verhoosel et al. (2009). The red dashed line represents the plane where the interface elements are placed. Taken from Vieira de Carvalho (2023).

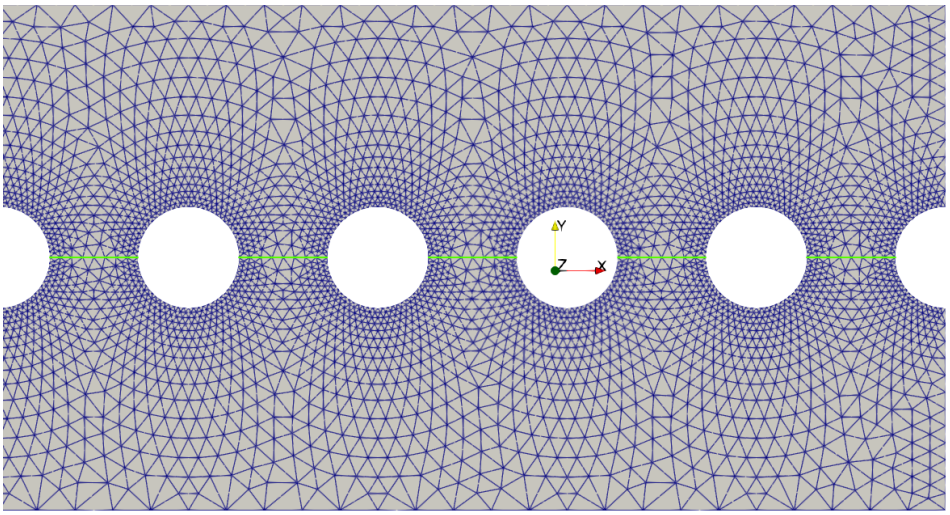

Figure 6.11: Finite element mesh for the perforated cantilever beam with zero-thickness cohesive elements inserted in the centre line (highlighted in green colour). The mesh has 26320 TRI6 elements, 160 COH2D6 elements, and 54490 nodes.

For the cohesive elements simulation, the properties of the bulk material are presented in Table 6.8. The cohesive elements have a null density, with identical properties in the normal and tangential directions (see Table 6.9) since the PF-CZM model implemented in `LINKS` assumes the same fracture properties regardless of the direction of the loading. A penalty factor of 1 is selected to

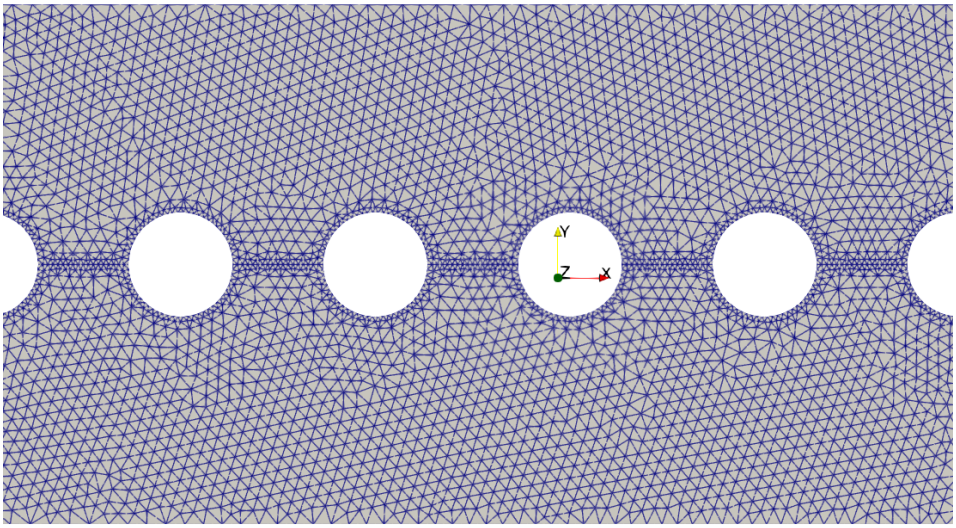

Figure 6.12: Finite element mesh for the perforated cantilever beam with 28968 TRI6 elements and 59618 nodes. Zero-thickness cohesive elements are inserted in every interface between continuum elements. The mesh has 28968 TRI6 elements, 42602 COH2D6 elements, and 173808 nodes.

prevent element inter-penetrability, which is sufficient for a plate loaded under mode I fracture. [1]

To fully compare the damage models, the fracture properties of the cohesive elements are the same in the normal and tangential directions, since the phase-field model implemented in `LINKS` does not distinguish between the two material directions. Additionally, since mode I fracture is simulated, the tangential material properties are not expected to significantly contribute to the mechanical response of the perforate plate. The properties of the PF-CZM model can be seen in Table 6.10, for a linear softening law and considering value of the length-scale, $l$, between 0.02 and 0.1.

Table 6.8: Elastic material properties of the continuum elements (bulk material), adopted in comparison study between the CZM and PF models, for the perforated cantilever beam.

| $\rho$ / tonne·mm$^{-3}$ | $E$ / MPa | $\nu$ / - |
|---|---|---|
| $940 \cdot 10^{-9}$ | 100 | 0.3 |

Table 6.9: Cohesive zone model material properties for the cohesive elements, adopted in comparison study between the CZM and PF models, for the perforated cantilever beam.

| $\phi_n$ / MPa·mm | $\phi_t$ / MPa·mm | $\sigma_n$ / MPa | $\sigma_t$ / MPa | $\alpha$ / - | $\beta$ / - | $\lambda_n$ / - | $\lambda_t$ / - |
|---|---|---|---|---|---|---|---|
| $2.5 \cdot 10^{-3}$ | $2.5 \cdot 10^{-3}$ | 1 | 1 | 2 | 2 | 0.01 | 0.01 |

The vertical reaction forces are extracted for the right edge of the plate and measured at the prescribed nodes. The forces are plotted against time in Figure 6.13, for 4 discretisation refinements, and compared with a reference model *interface-CZM* shown in red. As expected, the phase-field models has a higher sensitivity to time discretisation than the cohesive zone model, which results from the staggered coupling scheme employed to solve the coupled mechanical and phase-field equations, as discussed in Gonçalves (2024). In particular, reducing the time increment factor from 1 down to 0.1 dramatically improves the phase-field model's agreement with the cohesive element benchmark (Figure 6.13-3). With large increments, the staggered solution cannot follow the sudden load drops during softening and deviates strongly from the reference (Figure 6.13-1). Smaller incre-

[1] Higher values were tested, but provided minimal gains with additional computational cost.

Table 6.10: Material properties of the PF-CZM material, adopted in comparison study between the CZM and PF models, for the perforated cantilever beam.

| $\rho$ / tonne·mm$^{-3}$ | $E$ / MPa | $\nu$ / - | $G_c$ / MPa·mm | $\sigma_m$ / MPa |
|---|---|---|---|---|
| $940 \cdot 10^{-9}$ | 100 | 0.3 | $2.5 \cdot 10^{-3}$ | 1 |

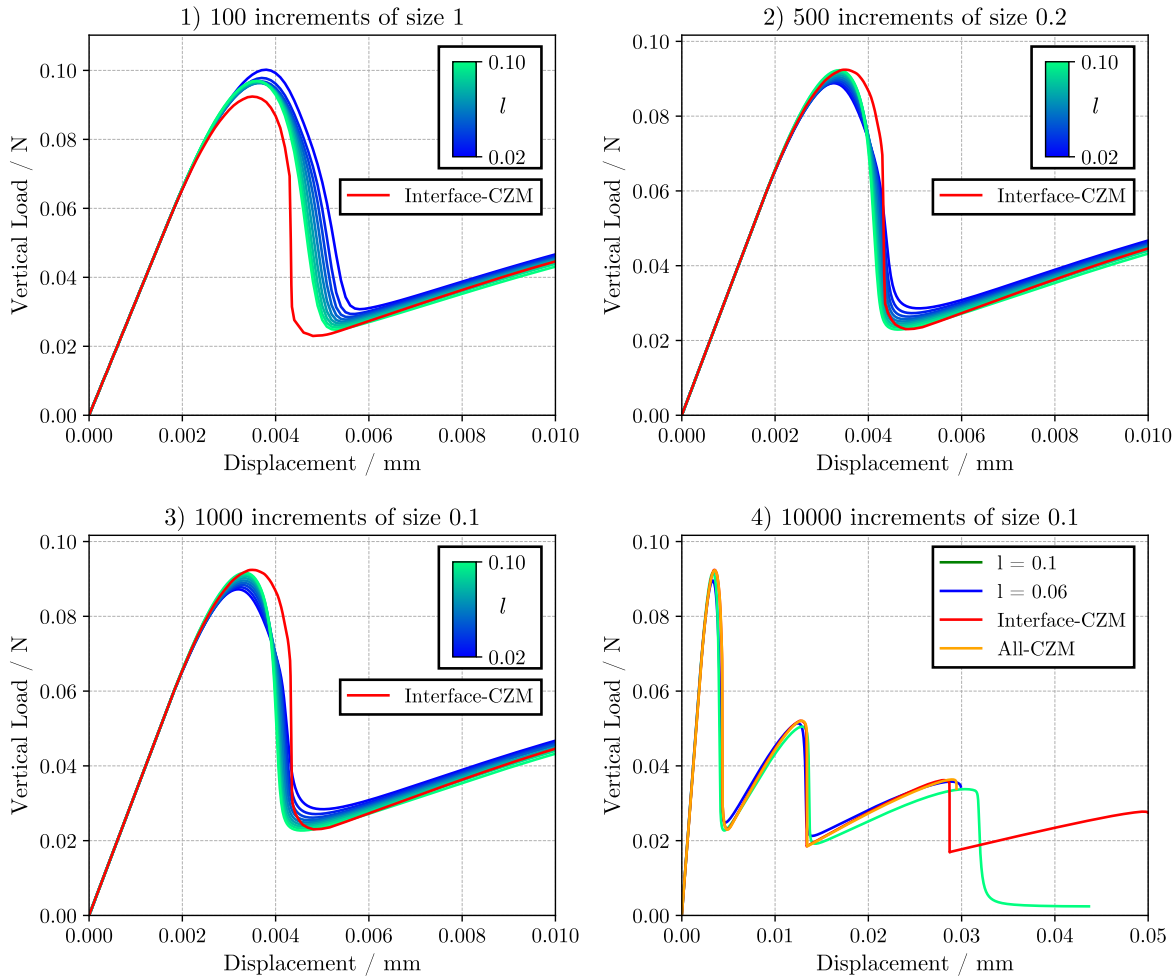


Figure 6.13: Vertical reaction force curves with the PF-CZM model for the perforated plate: varying the values of the phase-field length-scale (subfigures 1, 2, 3); and running the simulation until the complete failure (subfigure 4). The model with cohesive elements in the center plate line is shown in red, for comparison. Subfigure 4 also presents in yellow the model with cohesive elements inserted everywhere.

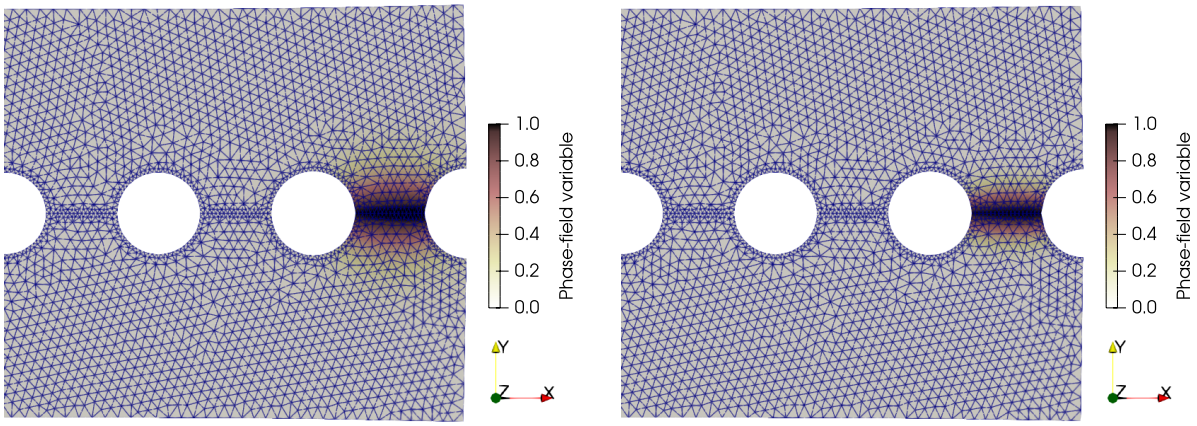


(a) Length-scale 0.10 at 10 s.




(b) Length-scale 0.06 at 10 s.

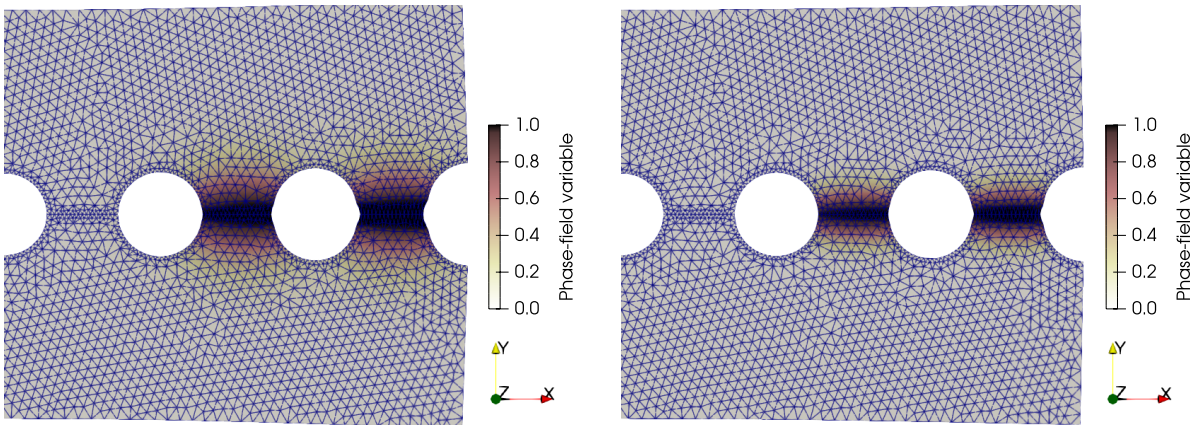


(c) Length-scale 0.10 at 25 s.




(d) Length-scale 0.06 at 25 s.

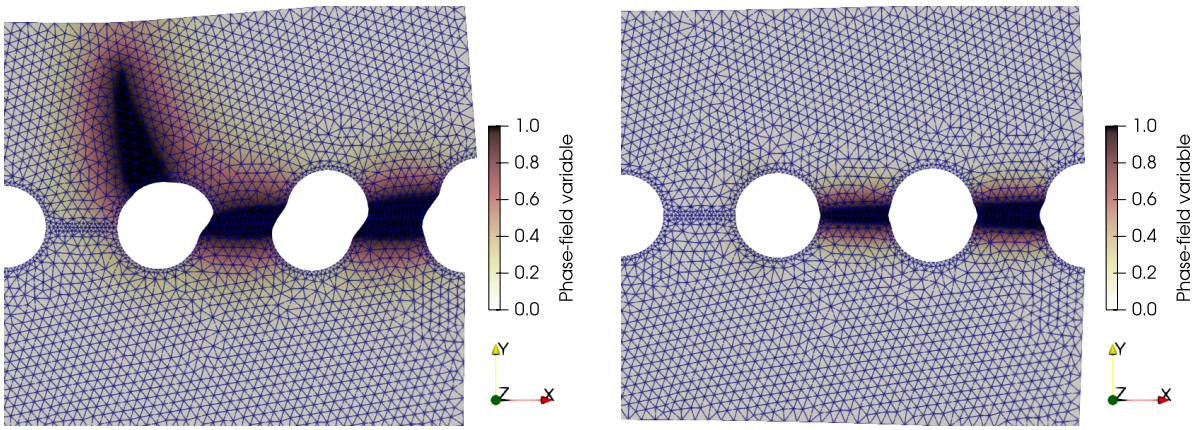


(e) Length-scale 0.10 at 40 s.




(f) Length-scale 0.06 at 40 s.

Figure 6.14: Phase-field distributions (plotted in the deformed configuration) for two length-scales ($l = 0.10$ left, $l = 0.06$ right) at three time instants.

ments capture crack propagation more faithfully and stabilize the post-peak response. However, convergence of the phase-field force-displacement curve towards the reference cohesive response was observed when using 10000 increments (Figure 6.13-4).

Figure 6.14 shows the distribution of the phase-field variable obtained for the simulations with the PF-CZM material and a length-scale of 0.06 and 0.1, for three distinct time instances.

The values for the material properties governing the fracture behaviour, $G_c$ and $\sigma_m$, must be compatible, as discussed in Section 6.2. It should be noted that the simulations were initially run with high values of the fracture strength, $\sigma_m = 100$ MPa, for a fracture toughness of $G_c = 2.5 \cdot 10^{-3}$ MPa·mm, which resulted in abrupt ends to the analyses.

For the phase-field simulation with a length-scale of 0.1, the crack path, after fracturing two holes, branched towards the top edge, ending abruptly the simulation, which is referred to as crack kinking (Figure 6.14e). Note that $l = 0.1$ is a sufficiently high value for the crack path to be selected despite the presence of a bifurcation. Thus, any slight asymmetry of the model with respect to the centre line may cause a deviation from the ideal and projected crack path (see Figure 6.12).

The phase-field simulation with a length-scale of 0.06 ended abruptly, after cracking only two perforated holes (6.13-4). This failure is due to a negative Jacobian determinant of an element in the right edge of the plate. This issue reflects a limitation of the current implementation in `LINKS`, where fully undamaged elements are not removed from the analysis. In contrast, the CZM implementation successfully handles such scenarios related to negative Jacobians. Even though there was a physically possible crack path, the mesh was not able to dissipate all the energy of the meshed specimen. This is an disadvantage compared to a cohesive element approach, where the contribution of the cohesive elements ends once a crack is formed. The phase-field elements are not removed after full failure (when $\phi = 1$).

Figure 6.13-4 the simulation with cohesive elements inserted everywhere ended abruptly, contrasting with model with cohesive elements only between the perforated holes. It should be noted that when cohesive elements are inserted only along a predefined interface, the crack path is known a priori. In this case, the solver follows the traction-separation law along those elements, so no competing crack paths exist for energy minimisation and the simulation advances smoothly to full separation. In contrast, for cohesive elements inserted everywhere, any edge between adjacent elements denotes a potential crack path. The solver then assesses locally a damage initiation criteria (stress- or energy-based) for each potential cohesive interface, which determines which set of cohesive interfaces is activated first. This leads to a path-selection ambiguity and allows the possibility for the localised damage bands to switch from one region to another, making it harder for equilibrium to be reached. In addition, small numerical perturbations or mesh irregularities may cause a localised snap-through due to a sudden release of strain energy, once the third perforated hole is reached.

This behaviour highlights a limitation observed when running the phase-field simulations: none of the phase-field models tests was able to complete the full separation of the perforated cantilever beam without a sudden end of the solver. A similar result is found for *all-CZM*, due to the presence of multiple energetically equivalent crack paths. However, for a length-scale parameter of 0.1, the phase-field simulation was able to select a crack path, although not the expected one, and proceed until the end of the simulation. For $l < 0.1$, the simulations eventually failed.

# Chapter 7

# Micro-scale analysis of damage in FRPs

This Chapter introduces the conceptual background of micro-scale models in the context of composite Representative Volume Elements (RVEs) (Section 7.1). The numerical application of these concepts is introduced in Section 7.2 with the objective of observing the interplay between distinct fracture models: cohesive zone model and phase-field fracture.

## 7.1 Introduction to micro-scale models

Over the past few years, the potential failure in engineering structures has become an increasingly active research field and a critical concern in some industries (aeronautics, aerospace, automotive). Modern high-performance and lightweight composite structures are engineering trough microstructural optimisation. As a result, the very design strategies which improve the macroscopic mechanical properties may lead to nonlinear, heterogeneous microstructures in which the underlying physical fracture mechanisms govern the macroscopic behaviour of FRPs (Gonçalves (2024)).

Macroscopic continuum models are insufficient, by themselves, to fully replicate the microstructural behaviour. Multi-scale approaches bridge this gap by solving a statistically representative sample at a lower length-scale (RVE) and use it to inform the macro-scale constitutive behaviour. Multi-scale via *scale-bridging strategies* can be applied to composite materials (Elmasry et al. (2023)), dual-phase steels undergoing mechanically-induced martensitic transformation (Rodrigues Lopes et al. (2023), Vieira de Carvalho et al. (2022)), and metamaterials (dos Santos et al. (2024)). For more detail on multi-scale modelling strategies, the reader is referred to Rodrigues Lopes (2019).

This Chapter addresses the micro-scale modelling of composite microstructures (RVEs), in which discrete features (e.g., fibre, matrix, interfaces) are modelled at the micro-scale and the extracted variables of interest are then homogenised, or averaged, to obtain representative macroscopic quantities. The modelling approach followed combines two fracture descriptions: cohesive zone models (CZMs) and phase-field (PF) fracture. Discussed in Chapter 3, the Park-Paulino-Roesler (PPR) potential-based CZM offers a detailed representation of interfacial damage and separation (e.g., fibre-matrix debonding, laminate delamination, intergranular metallic fracture). In addition, it is possible to employ this strategy to simulate bulk fracture (see Section 3.2). Phase field (see chapter 4), provides an energy-based variational framework suitable for capturing arbitrary crack topologies in the bulk material. The coupled use of PPR cohesive formulations and PF fracture, and the corresponding variation of their material parameters, can substantially affect the interaction between matrix-dominated fracture and interface debonding-dominated fracture.

### 7.1.1 Representative volume element

In a multi-scale framework, information is systematically exchanged between two, or more, length-scales. First proposed by Hill (1965), a Representative Volume Element (RVE) is the smallest possible

volume of material which can be regarded as a homogenous continuum. In other words, the RVE represents the microstructural features in the micro-scale, by considering a typical sample of the model, such that the assumption of material continuity holds true (de Souza Neto et al. (2008)).

A representative volume element is therefore the smallest possible volume of material which statistically characterises the micro-scale properties of a composite, while also being considered an infinitesimal point at the macro-scale. The *principle of separation of scales* ensures that the size of the RVE, $l_{\text{RVE}}$, must comply with

$$l \ll l_{\text{RVE}} \ll L, \tag{7.1}$$

where $l$ is the size of the microstructural features, and $L$ is the size of the macroscopic structure.

The size of an RVE model corresponds to the quantity of microscopic features, such as the number of grains in a polycrystalline microstructure, or the number of fibres or inclusions in a reinforced polymeric RVE. As a result, an increase in the number of microscopic features generally leads to an higher convergence of its homogenised properties (Gonçalves (2024)).

Figure 7.1 displays the principle of separation of scales between the macroscopic continuum and a representative volume element, where $(\cdot)_\mu$ denotes a micro-scale quantity, such that $\phi_\mu(\Omega_\mu)$ is the deformed domain and $\partial\Omega_\mu$ is the corresponding boundary of the RVE. For further discussion on RVEs in a computational mechanics context, the interested reader is forwarded to Gitman et al. (2007).

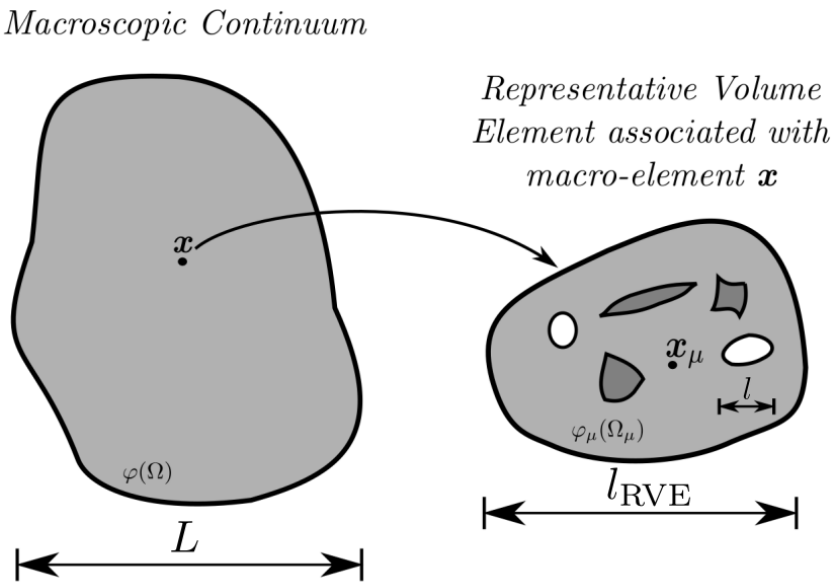


Figure 7.1: Schematic representation of the RVE concept and the principle of separation of scales. Taken from Gonçalves (2024).

### 7.1.2 Boundary conditions

Appropriate boundary conditions must be established to ensure that the response of the representative volume element accurately reflects the intended periodic microstructure of the FRPs. In the present work, this is achieved by enforcing first-order periodicity of opposite edges, while prescribing a uniaxial deformation at the top edge (uniform vertical displacement). In the text-based input files of the in-house solver `LINKS`, the analysed RVEs in the scope of this Master's Dissertation are all conform in opposite faces and analysed at a single length-scale. For two-dimensional models, periodicity is thus enforced by explicit master-slave node pairs, where each node on a given edge (master node) is associated with the opposite edge (slave node) and the corresponding degrees

of freedom are constrained accordingly: equal displacements, $\boldsymbol{u}$, and values of the phase-field variable, $\phi$, for the mechanical and phase-field coupled problem, respectively. The mortar method may be used for non-conform meshes (Rodrigues Lopes et al. (2021)). Nonetheless, as stated by Vieira de Carvalho et al. (2023), meshes with cohesive elements must be confirming to ensure a fracture patterns/discontinuities appearing on one side can develop identically on the opposite boundary.

## 7.2 Numerical applications

In this Section, numerical simulations are presented for a benchmark micro-mechanical example in order to compare and study the interaction of the two previously presented fracture models: the cohesive zone model (CZM) with cohesive elements; and the phase field - cohesive zone model (PF-CZM or PF) model.

The representative volume element (RVE) selected is of medium size ($0.05 \times 0.05$ mm), generated with GMMD (Vila-Chã et al. (2021)). The RVE is composed of a matrix and fibres with 0.01 mm of diameter, with a volume fraction of 0.6. A low proportion of fibres would otherwise lead to fracture being mostly dominated by matrix cracking, defeating the purpose of this Master's Dissertation, which hopes to study the impact of varying material properties on the fracture mechanisms, matrix-dominated and interface-dominated, encountered by RVEs.

Before comparing fracture models, a mesh convergence study is carried out, with three distinct mesh sizes (Section 7.2.1). In addition, parametric studies of the cohesive properties and the model type are performed (Sections 7.2.2, 7.2.3 and 7.2.4).

Three model versions are employed: *PF*-only model for RVEs with a matrix defined using the phase-field cohesive zone model (PF or PF-CZM) formulation presented in Chapter 4; *PF* + *intCZM* formulation for RVEs with a PF matrix coupled with PPR-potential based cohesive elements inserted between the fibre-matrix material interfaces; and *allCZM* + *intCZM* with fibre-matrix interface cohesive elements and cohesive elements inserted between the matrix continuum elements to explicitly represented intra-matrix fracture. Due to a limitation in the *Python* script developed (see Chapter 5), the current implementation erroneously inserts cohesive elements along fibre-fibre interfaces. To remove any influence of the unintended elements, high values of the cohesive strengths and corresponding fracture energies are selected (Section 7.2.4). Both *PF* and *PF* + *intCZM* models share identical properties of the phase-field matrix material, with the differentiating aspect between them being that the former allows the interface cohesive properties to be varied independently, enabling a direct comparison of the failure mechanisms.

### 7.2.1 Mesh convergence study

In order to compare the influence of mesh density and element type on the computational performance, initial microstructure simulations with a periodic *PF* RVE model are conducted, involving several distinct mesh sizes. Here, a glass-fibre-reinforced-polymer (GFRP) is considered, where the fibres are modelled as isotropic elastic materials, with their Young's modulus and Poisson's ratio presented in Table 7.1. The matrix consists of an epoxy resin, whose properties can be found in Melro et al. (2013a) and displayed in Table 7.2.

Table 7.1: Elastic material properties of the fibre, adopted in the mesh convergence study, adapted from a glass fibre found in Melro et al. (2013b).

| $E$ / MPa | $\nu$ / - |
|---|---|
| $74 \cdot 10^3$ | 0.2 |

As noted previously, GMMD was employed to generate two RVE's models with distinct finite element types: one discretised with linear elements, predominantly four-node bilinear quadran-

Table 7.2: Elastic and fracture properties of the matrix, for a PF-CZM material, adopted in the mesh convergence study, adapted from an epoxy matrix found in Melro et al. (2013a).

| $E$ / MPa | $\nu$ / - | $G_c$ / MPa·mm | $l$ / mm | $\sigma_m$ / MPa |
|---|---|---|---|---|
| $3.76 \cdot 10^3$ | 0.39 | 0.002 | 0.001 | 45 |

gular (QUAD4-FBAR) elements, with some three-node (TRI3) triangles for transition; and the other model is meshed with quadratic six-node triangular (TRI6) elements. Proposed by de Souza Neto et al. (1996), QUAD4-FBAR elements aim to reduce spurious volumetric locking or hourglass effects which occur for the standard bilinear and trilinear elements. The TRI6 model adopted a three-point triangular integration rule (sufficient for the exact integration of quadratic fields), while the QUAD4-FBAR element has four Gauss points, as its standard integration rule. The solver tolerance is $10^{-6}$ for both models, with 20 maximum Newton-Raphson iterations per increment. The number of increments is set to 1000, with a load factor of 0.001 with respect to the total vertical prescribed displacement of 0.0005 mm (1 %).

The mesh sizes can be seen in Table 7.3. To ensure a good spread of discretised models, five distinct mesh sizes are selected for the QUAD4-FBAR model, while three mesh sizes are defined for the TRI6 model, which allows for a consistent assessment of the convergence and sensitivity of both finite element formulations.

Table 7.3: Mesh sizes adopted in the convergence study.

| Mesh | Number of elements | | |
|---|---|---|---|
| | TRI3 | QUAD4-FBAR | TRI6 |
| *mesh1 - QUAD4-FBAR* | 30 | 12566 | 0 |
| *mesh2 - QUAD4-FBAR* | 32 | 19349 | 0 |
| *mesh3 - QUAD4-FBAR* | 50 | 73756 | 0 |
| *mesh4 - QUAD4-FBAR* | 70 | 149648 | 0 |
| *mesh5 - QUAD4-FBAR* | 71 | 291009 | 0 |
| *mesh1 - TRI6* | 0 | 0 | 26896 |
| *mesh2 - TRI6* | 0 | 0 | 42136 |
| *mesh3 - TRI6* | 0 | 0 | 168214 |

Figure 7.2 plots both the peak vertical reaction force and the normalised computational time per increment as a function of the number of nodes of each mesh simulated. For the QUAD4-FBAR meshes, the reaction force converges for a higher number of nodes, while for TRI6 elements the mesh exhibits a slight, although relatively constant, decrease in peak force, consistent with the expected asymptotic behaviour. Due to the higher-order interpolation of the quadratic TRI6 elements, the local stress and phase-field gradients are represented more accurately even for coarser meshes. In contrast, QUAD4-FBAR capture only constant strain inside the finite element, which may result in over predictions of the model's stiffness and thus its peak response (Zienkiewicz and Taylor (2013)). Since not all simulations completed the full prescribed displacement or load factor, the computational time is plotted as a ratio of the time per increment. Both models observed a clear increase in the time per increment as mesh size decreases.

Figures 7.3 and 7.4 display the phase-field distributions for an RVE with QUAD4-FBAR and TRI6 elements, respectively. All but the second-coarsest QUAD4-FBAR mesh reproduce a nearly identical zig-zag crack path between fibres (where the PF variables reaches unity). The coarsest meshes (*mesh1 - QUAD4-FBAR*, *mesh2 - QUAD4-FBAR*) cannot capture the fracture behaviour of the plate and fully resolve the diffuse crack band. The coarsest mesh (*mesh1 - QUAD4-FBAR*) causes an overly smeared crack path that spreads over larger elements, with a larger crack band as observed in 7.3-

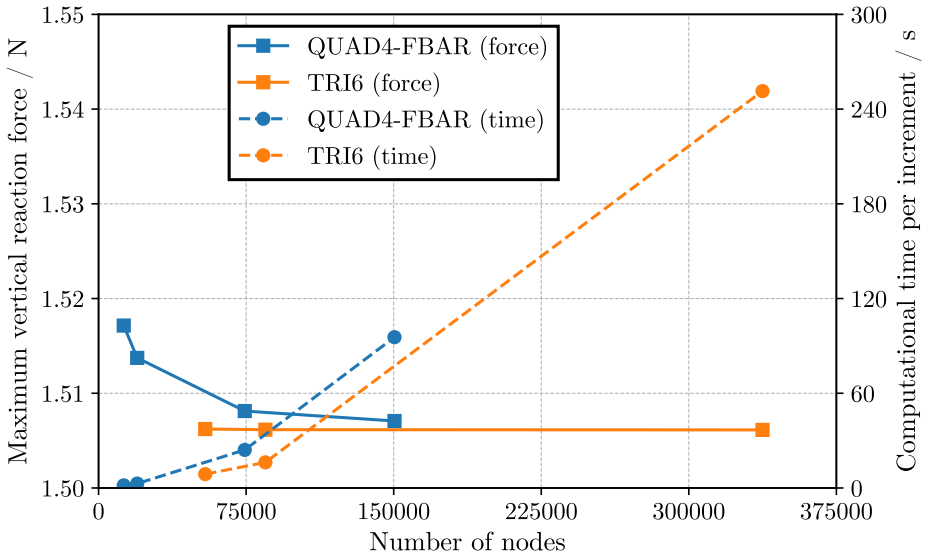


Figure 7.2: Maximum vertical reaction force (squares) and computational time per increment (circles) against the number of nodes. The QUAD4-FBAR model is in blue, while the TRI6 model is in orange.

a. Although this mesh produces a similar macroscopic crack pattern as followed by the more refined meshes, this similarity is misleading and results from numerical artifacts. The second coarsest mesh (*mesh2 - QUAD4-FBAR*) deviates further and is not refined enough to capture the phase-field distribution, showing an alternate crack trajectory, which may be due to the low number of elements when compared with much more refined models (particularly the TRI6 cases). In contrast, the more refined meshes yield mesh insensitive results, a well-established characteristic associated with phase-field models (Miehe et al. (2010), Wu (2017)).

Finally, the homogenised stress-strain curves in Figure 7.5 further corroborate these findings. The homogenised stress have been computed as the ratio of the sum of the vertical reaction forces acting on the top boundary by the lateral size of the RVE (0.05 mm) and the unit out-of-place RVE thickness. The average strain is similarly obtained by diving the prescribed vertical displacement by the RVE lateral size. As stated before, *mesh2 - QUAD4-FBAR* diverges from the expected softening branch observed in more refined cases, and *mesh1 - QUAD4-FBAR* also shows diverging reactions near the end of the simulation. In contrast, all TRI6 simulations track the expected response closely. Several simulations terminated early due to convergence issues. However, the homogenised stress in these cases had decreased to near-zero values, consistent with a fully fractured RVE.

For the following Sections comparing the mechanical response of the PF and CZM models within composite microstructures (RVEs), a mesh size is selected that best balances accuracy with computational efficiency. Accordingly, the two coarser linear QUAD4-FBAR meshes are excluded from Figures 7.2, 7.3 and 7.4, while Figure 7.2 provides a choice between models *mesh1 - tri6* and *mesh2 - tri6*. The more refined model achieves a marginally improved prediction of the peak response at only a negligible increase in the computational cost per increment. Therefore, after assessing the computational cost and accuracy of the homogenised response, the mesh chosen for subsequent analyses is the second coarsest quadratic mesh: *mesh2 - tri6*.

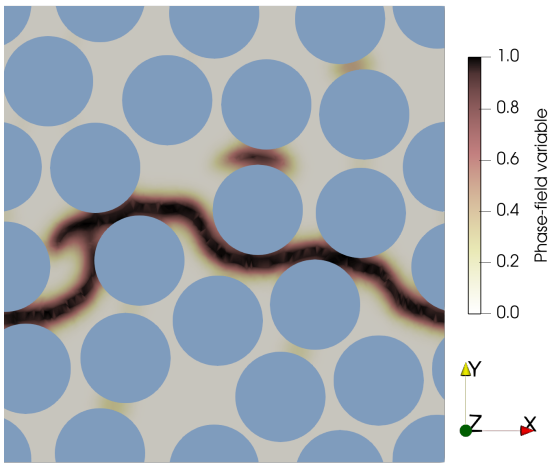


(a) RVE with 12566 QUAD4-FBAR elements and 30 TRI3 elements at 1000 increments.

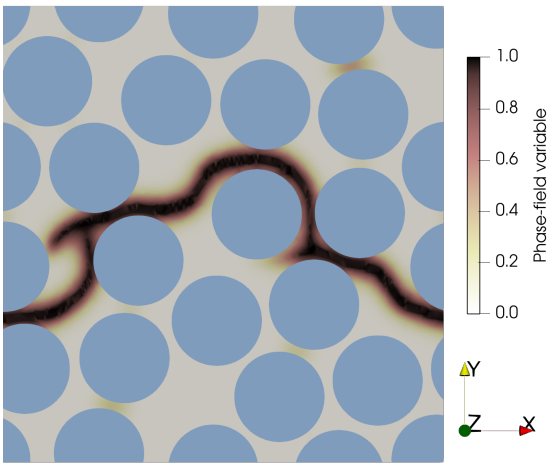


(b) RVE with 19349 QUAD4-FBAR elements and 32 TRI3 elements at 1000 increments.

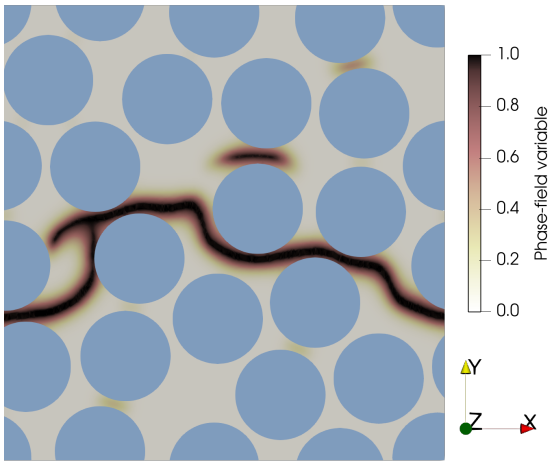


(c) RVE with 73756 QUAD4-FBAR elements and 50 TRI3 elements at 800 increments.

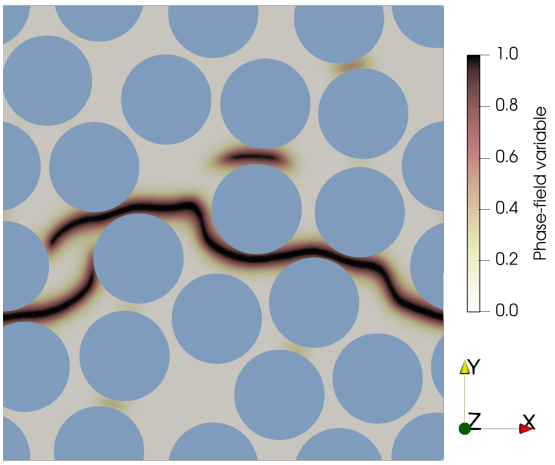


(d) RVE with 149648 QUAD4-FBAR elements and 70 TRI3 elements at 700 increments.

Figure 7.3: Phase-field distribution in the matrix, plotted in the deformed configuration at the end of the simulation (scale factor of 10), of an RVE with QUAD4-FBAR and TRI3 elements for four distinct mesh sizes.

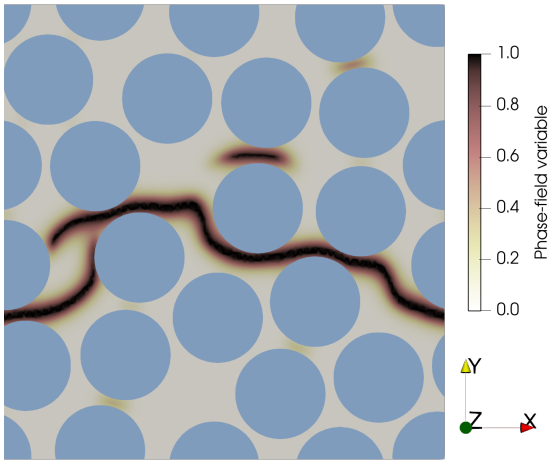


(a) RVE with 26896 TRI6 elements at 700 increments.

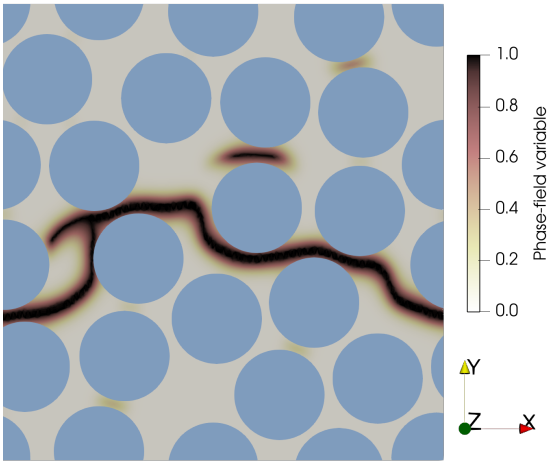


(b) RVE with 42136 TRI6 elements at 1000 increments.

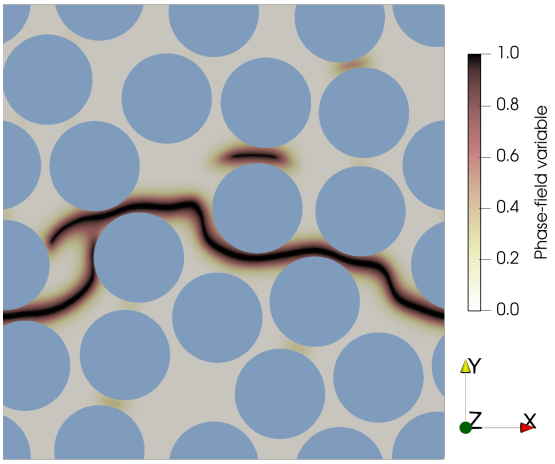


(c) RVE with 168214 TRI6 elements at 700 increments.

Figure 7.4: Phase-field distribution in the matrix, plotted in the deformed configuration at the end of the simulation (scale factor of 10), of an RVE with TRI6 elements for three distinct mesh sizes.

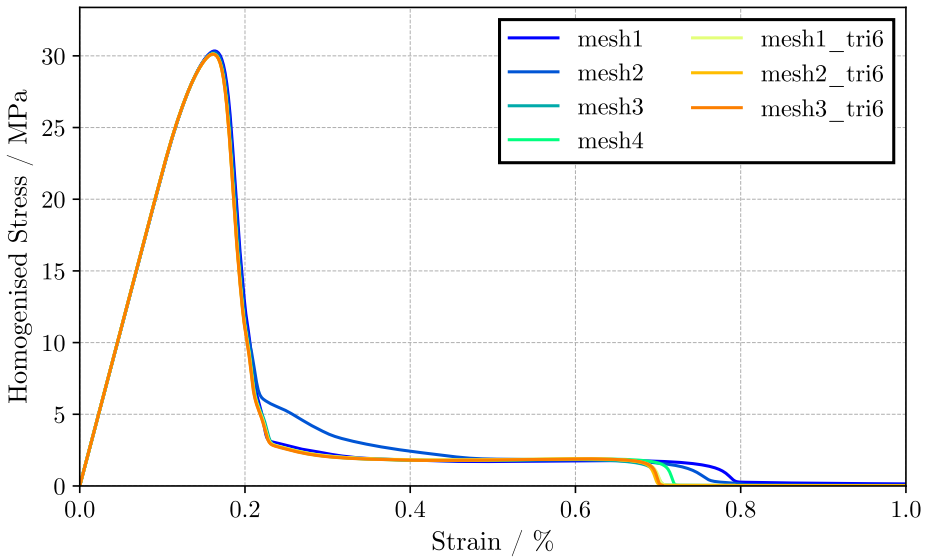


Figure 7.5: Homogenised stress-strain curves.

### 7.2.2 Initial studies with PF + intCZM FRP fracture

This study seeks to analyse the mechanical fracture response of RVEs by systematically varying material parameters for a combined cohesive model and phase-field fracture approach. To achieve this, a model is selected with a matrix simulated with phase-field cohesive zone model approach (denoted as PF henceforth), an elastic fibre and cohesive elements inserted along the material interfaces. In particular, this Section performs a parametric study of the material properties associated with the Park-Paulino-Roesler cohesive zone model presented in Chapter 3, with the reference for comparison being the phase-field only model, presented in Section 7.2.1.

The RVE has a length of 0.05 mm, with 0.01 mm fibres. The mesh selected is the *mesh2 - tri6* which performed well under the mesh convergence study of Section 7.2.1, while the mesh *mesh2 - QUAD4-FBAR* is a faster mostly accurate alternative when fast parametric studies are necessary. It has 42136 2D quadratic six-node triangular continuum (TRI6) elements with three Newton integration points, and 1587 quadratic six-node cohesive (COH2D6) elements with three Newton-Cotes integration points. As shown in Figure 7.6.

The *PF - intCZM* models were created by transforming/modifying the meshed RVEs previously created using GMMD, as detailed in Section 7.2.1, using the *Python* script for inserting cohesive elements between continuum elements, described in Chapter 5. In addition, to ensure the meshed model simulated represents the an entire composite microstructure, periodic boundary conditions are prescribed between the left and right edges of the specimen (as theoretically detailed in Section 7.1.2 and implemented in Section 5.2.2)[1]. The baseline prescribed displacement of $2 \cdot 10^{-4}$ mm (or 0.4 % of the RVE length) is further applied to the top edge nodes, while the bottom edge is fixed.

For the epoxy matrix and the glass fibres the same values for the elastic domain adopted in the previous Section are considered (Tables 7.1 and 7.2). The density properties for the fibres and matrix are extracted as average values from Shakir Abbood et al. (2021): $2.5 \cdot 10^{-9}$ and $1.3 \cdot 10^{-9}$ tonne·mm$^{-3}$, respectively. In addition the average values for the elastic properties of the glass fibres (assumed as E-glass fibres) and of the epoxy matrix found in this reference match the values suggested by Melro et al. (2013a,b). The phase-field fracture model assumes a linear softening law.

[1] A subset of RVEs lost their periodic boundary conditions defined in the corresponding input files after processing with initial versions of the *Python* script responsible for inserting cohesive elements between fibre-matrix interfaces. Nonetheless, the results do not diverge significantly from those found for periodic RVEs in Sections 7.2.3 and 7.2.4

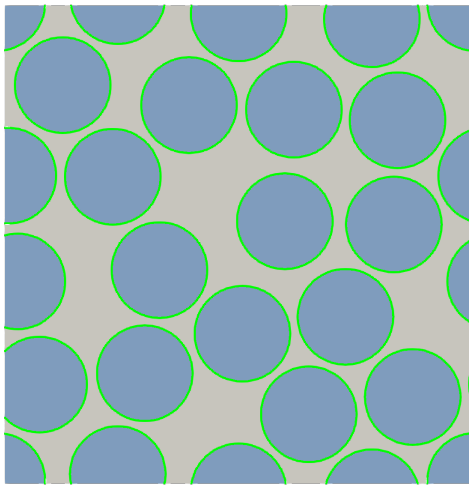

Figure 7.6: Finite element mesh for the RVE with zero-thickness cohesive elements inserted between fibre-matrix material interfaces (highlighted in green colour). The mesh has 42136 TRI6 elements, and 1587 COH2D6 elements and 87983 nodes.

### Impact of the cohesive interface strength

The first study focused on the impact of the strength of the cohesive interfaces on the overall response and failure modes of the RVE. Table 7.4 reports the cohesive the material properties chosen for the initial simulations of the *PF* + *intCZM* model. The normal and tangential properties are taken equal, as mentioned previously, with the cohesive strength set to 30, 45, and 60 MPa, to explore the model response around the fracture strength of the phase-field material.

Table 7.4: Cohesive zone model material properties for the interface cohesive elements, adopted in the initial simulations in the microstructure study, for a quadratic meshed RVE.

| | $\rho$ / tonne·mm$^{-3}$ | $\phi_{n/t}$ / MPa·mm | $\sigma_{n/t}$ / MPa | $\alpha = \beta$ / - | $\lambda_{n/t}$ / - | $\alpha_p$ |
|---|---|---|---|---|---|---|
| Reference | $1.3 \cdot 10^{-9}$ | 0.002 | 45 | 2 | 0.1 | 1 |
| Minimum | - | 0.002 | 30 | - | 0.01 | - |
| Maximum | - | 0.004 | 60 | - | 0.2 | - |

Figure 7.7 displays the homogenised stress-strain curves for these simulations[2]. The two highest values of the cohesive strength result in stress-strain curves similar to that of the *PF* meshed model, which are almost linear until the crack grown initiates. This behaviour can be explained by the fact that the *PF* + *intCZM* and *PF* models employ identical phase-field matrix material parameters, and, for higher cohesive strengths, the interface elements have a negligible contribution to the global response. When the cohesive strength equals the PF matrix fracture strength ($\sigma_{n/t} = \sigma_m = 45$ MPa), the global stress-strain curve and the residual stress most closely match the *PF* model (residual stress $\approx$ 2.5 MPa and the apparent RVE strength $\approx$ 28.5 MPa). Increasing the cohesive strength above the matrix value of 45 MPa leads to the stress-strain response deviating progressively from the *PF* solution.

Figure 7.8 shows the phase-field distributions for the RVEs with three distinct cohesive strengths. For the two highest cohesive strengths , the crack propagation is dominated by matrix (phase-field) fracture, where cohesive elements have a negligible effect, as evidenced by small normal interface

[2]Preliminary simulations were conducted without strictly prescribed periodic boundary conditions. This produced system responses and crack topologies consistent with simulations employing fully implemented periodic RVEs. Despite the apparent agreement, potentially due to a low displacement applied, periodicity must be imposed to ensure the RVE is a statistically accurate representation of the composite microstructure.

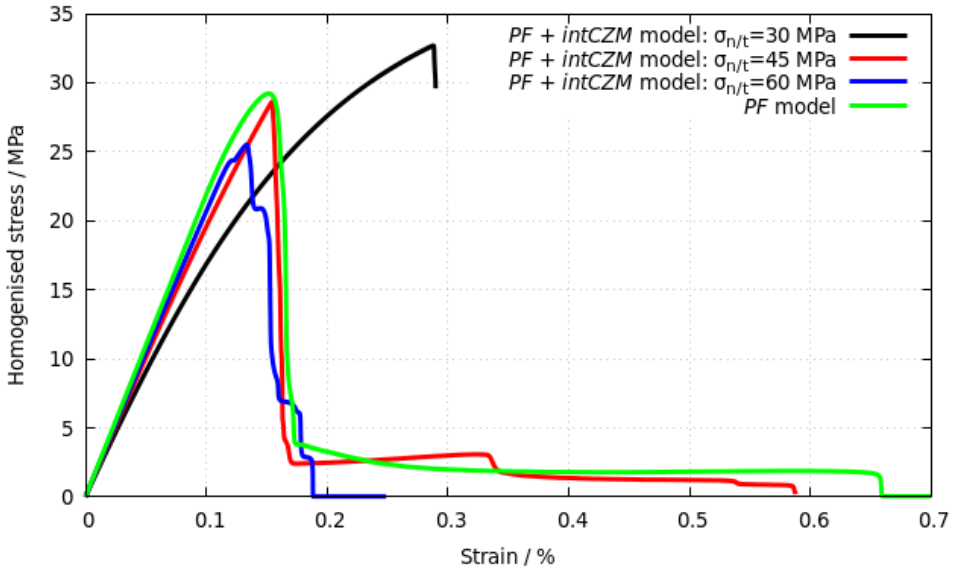


Figure 7.7: Homogenised stress-strain curves or the initial parametric study of the quadratic *PF* + *intCZM* RVE, for three distinct values of the cohesive interface strength, $\sigma_{n/t}$.

openings and low total damage variable (Figures 7.8b and 7.8c). In contrast, the RVE with the lowest cohesive strength (30 MPa) shows a more pronounced influence of the cohesive elements on the fracture response (Figure 7.8a). This simulation fails to converge shortly after the peak response, despite using the same numerical setup as two other simulations. The internal energy of the bulk/continuum material may be so large that the fracture mechanism introduced by the cohesive elements is not able to dissipate all the energy, resulting in an abrupt end to the simulation. In addition, the crack path did not fully develop since the simulation ended early when damaged nucleated between two upper left fibres. When damage began to involve the bordering interface cohesive elements, the solver failed to progress.

**Impact of the cohesive interface toughness**

Because the main objective of this work is to study the interaction between failure mechanisms (matrix cracking and fibre-matrix debonding), the focus is on improving the convergence for the cohesive stress of 30 MPa, where cohesive elements have the greatest influence but also caused the simulation to abruptly end. To identify possible numerical issues, additional simulations were performed with elastic fibres and purely elastic matrix (phase-field damage formulation deactivated) and with the cohesive elements along the interfaces only (*intCZM*). When the cohesive strength is too high for a given fracture energy, the interface may become too stiff to dissipate all the internal energy with the solver not converging. To identify a good value for the fracture energy of the PPR material in the fibre-matrix interface, for a cohesive strength of 30 MPa, several values for the fracture energy (normal and tangential) are tested: 0.002, 0.003, and 0.004 MPa·mm.

The corresponding stress-strain curves are included in Figure 7.9. The two lowest fracture energies were still not able to transverse the peak response smoothly, ending shortly after softening began. Only the *intCZM* with the highest fracture toughness (0.004 MPa·mm) managed to enter smoothly into the softening branch. These results justify increasing the fracture energy assigned to the PPR material so that it is compatible with the selected cohesive strength. The compatibility issue is less relevant for the higher cohesive strengths, where phase-field matrix cracking dominates and the cohesive elements remain largely inactive.

**Remark 3.** *To improve convergence in the low strength cases, one approach consists of reducing the increment size to provide the solver better changes of dealing numerically with the damage initia-*

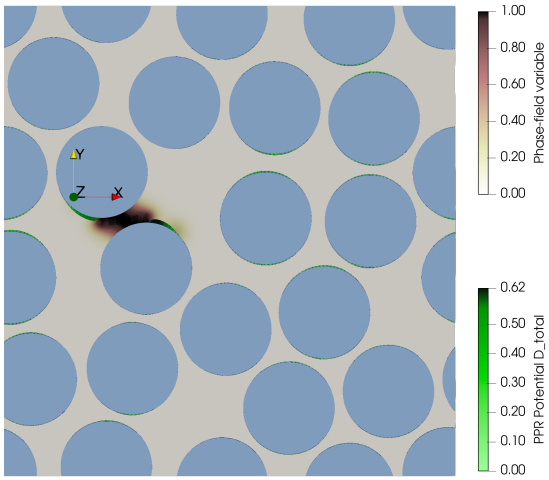


(a) RVE with $\sigma_{n/t} = 30$ MPa at a load factor of 0.724 (or a prescribed displacement of 0.290 %).

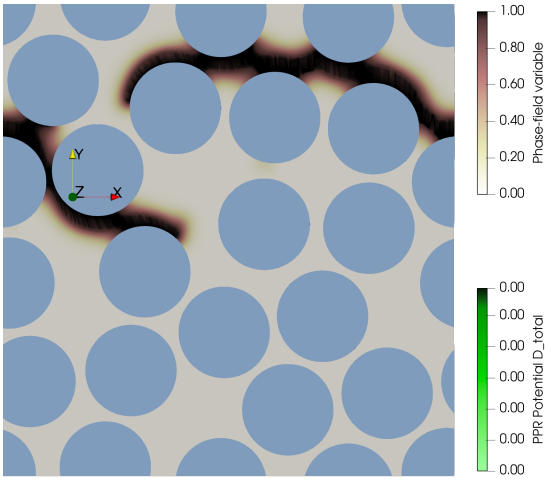


(b) RVE with $\sigma_{n/t} = 45$ MPa at a load factor of 0.826 (or a prescribed displacement of 0.330 %).

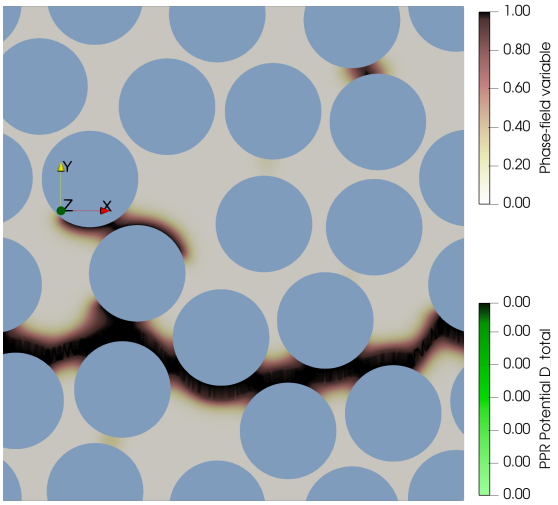


(c) RVE with $\sigma_{n/t} = 60$ MPa at a load factor of 0.62 (or a prescribed displacement of 0.248 %).

Figure 7.8: Phase-field distribution in the matrix, plotted in the deformed configuration at the end of the simulation (scale factor of 10), of an *PF + intCZM* RVE model with TRI6 continuum elements, for three distinct values of the PPR cohesive strength ($\sigma_{n/t}$): 30, 45, and 60 MPa.

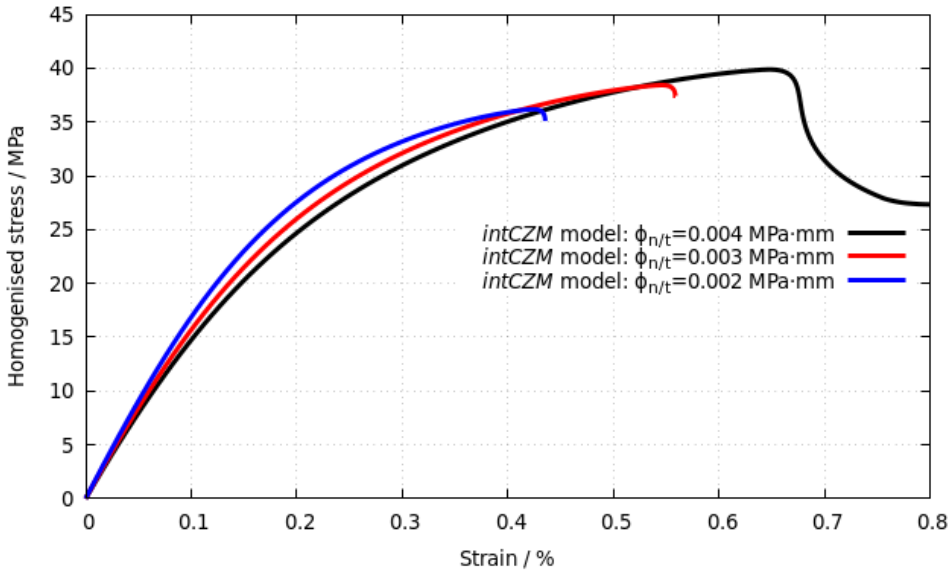


Figure 7.9: Homogenised stress-strain curves or the initial parametric study of the quadratic *intCZM* RVE, for three distinct values of the cohesive interface toughness, $\phi_{n/t}$.

*tion and propagation. In alternative, increasing the PF matrix strength from 45 to 75 MPa, while simultaneously increasing the PF fracture toughness from 0.002 to 0.003 MPa·mm to ensure compatibility between these two parameters, can make sure that matrix-dominated failure does not occur so early. Note that the value of 45 MPa found in Melro et al. (2013a) corresponds to a combined (matrix-interface) strength and therefore may not be strictly appropriate as the PF-matrix tensile strength. These mitigation strategies, although valid, were not implemented in the present work to ensure consistency across parametric comparisons.*

### Impact of the initial slope parameter

Selection of the most appropriate value for the initial stiffness parameters, $\lambda_{n/t}$, is likewise critical. Higher values introduce artificial compliance, increasing the influence of the cohesive elements on the elastic response prior to damage onset (peak response), where the elastic behaviour should be ideally governed by the elastic properties of the fibre and matrix. However, excessively low values may lead to convergence issues. To identify a value striking a balance between interface compliance and numerical stability, a small parametric study is conducted for a cohesive strength of 30 MPa, comparing four values of the initial shape parameters, as 0.01, 0.05, 0.2, and including the value of 0.1 from initial simulations.

Figure 7.10 includes the corresponding system response. As can be seen, considerable gains are observed by reducing these parameters from 0.2 until 0.05, whereas further reduction to 0.01 offers only a marginal increase in the initial stiffness. Based on these results, since $\lambda_{n/t} = 0.05$ offers a reasonable trade-off between a faithful elastic behaviour and numerical robustness, it will be used as the default for simulations with $\sigma_{n/t} \geq 30$ MPa. For higher cohesive strengths (45 or 60 MPa), the cohesive interfaces have a reduced impact on the global stress-strain response and, based on these results, no further testing is required. Note that this analysis focuses solely on the initial elastic response, thus convergence issues observed in the post-peak response for these values of $\lambda_{n/t}$ are not considered here and are addressed in the following Section.

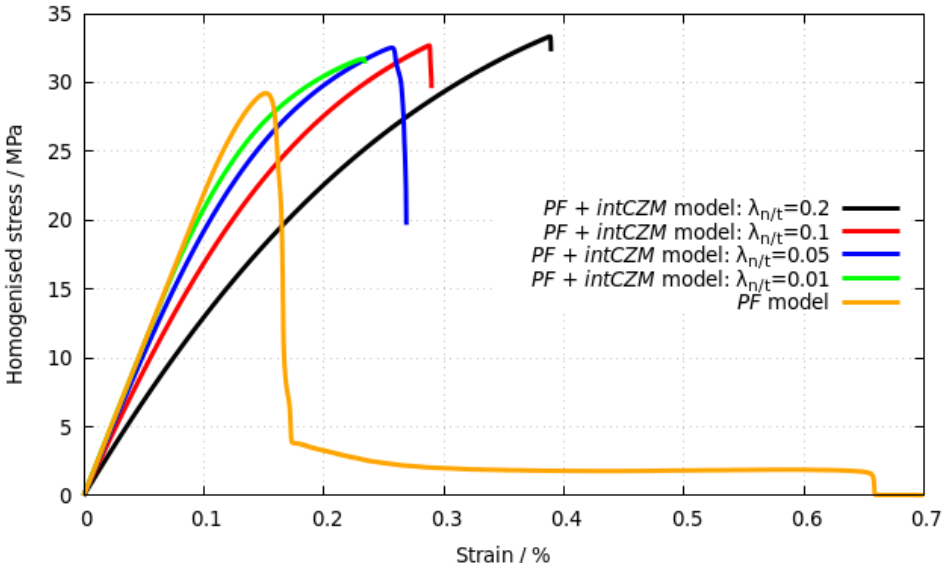


Figure 7.10: Homogenised stress-strain curves or the initial parametric study of the quadratic *PF + intCZM* RVE, for three distinct values of the cohesive initial slope indicator, $\lambda_{n/t}$.

### 7.2.3 Parametric study of FRP fracture with PF + intCZM and dynamics

As noted in Section 6.4, certain models may require inertial and viscous contributions to dissipate adequately all of the internal energy, particularly during damage initiation and propagation. To ensure simulations run until the imposed end displacement, dynamic effects are incorporated and the initial quasi-static simulations are repeated using a dynamic formulation. This consideration is particularly relevant for cohesive zone models, where their discrete nature results in sudden releases of stored elastic energy difficult to dissipate within quasi-static frameworks. Similar requirements have been found in literature for CZM implementations (see Hamitouche et al. (2008), Vieira de Carvalho (2023)).

Dynamic analyses in `LINKS` can be performed with explicit or implicit time integrations. In particular, the present simulations employ the generalised-$\alpha$ method, an implicit time integration scheme which provides numerical damping controlled by the spectral radius parameter, $\rho_\infty$. Following the parametric tests reported in Vieira de Carvalho (2023), a spectral radius of 0.7 was chosen. Values of $\rho_\infty < 1$ provide numerical damping of high frequency oscillations, with a negligible effect on the global quasi-static behaviour.

Furthermore, viscous Rayleigh damping is introduced to enhance the convergence behaviour of a dynamic simulation (Vieira de Carvalho (2023)). Increased viscous damping can help the solver react to numerical instabilities and may reduce the number of the solver iterations, potentially providing net savings in the total run time. In fact, the post-fracture behaviour is drastically reduced with the introduction of the Rayleigh damping, in the presence of cohesive elements (see Appendix C). In these dynamic simulations, the loading is applied in the form of prescribed constant velocities at the top boundary rather than an imposed displacement. For sufficiently low values of the velocity, the inertial terms are small when compared with the viscous contribution. As a result, the Rayleigh damping primarily governs the transient response. Adjusting the Rayleigh damping coefficients thus provides control over the dynamic response. For simulations with displacement control and a constant prescribed velocity, the reduction of the Rayleigh coefficients recovers the quasi-static response by minimising the inertial contribution. Hence, the objective is to select the correct parameters (spectral radius and Rayleigh damping) that best approximate the initial static response. The present parametric study focuses on the *PF + intCZM* model with a cohesive strength of 30 MPa, a fracture energy of 0.004 MPa·mm (selected from the initial parameter study as these

yield the most balanced interaction between matrix- and interface-dominated failure), an initial stiffness indicator of 0.05 to reduce the artificial compliance introduced by the cohesive elements, and the remaining properties taken as reference values from Table 7.4. To achieve fast results, due to time constraints in the dissertation and because the accuracy is not the main concern, the linear coarser mesh used in Section 7.2.1 (*mesh2 - QUAD4-FBAR*) is employed and compared with the more accurate quadratic mesh. Table 7.5 shows the material properties of the PPR potential employed in the parametric study.

**Dynamic parameters**

The first dynamic study assumes identical Rayleigh damping coefficients set between 0.01, 0.001, 0.0001 and 0.00001. Figure 7.11 reports the stress-strain curves, at the prescribed top edge of the RVE, for the four damping coefficients (7.11a) and for two cases where the cohesive elements are assigned different densities (0 or 1.3 tonne/mm$^3$, the latter identical to the epoxy matrix density). The near agreement between the quadratic and linear mesh stress-strain curves confirms that the coarser mesh is sufficiently accurate for the present study of the dynamic parameters.

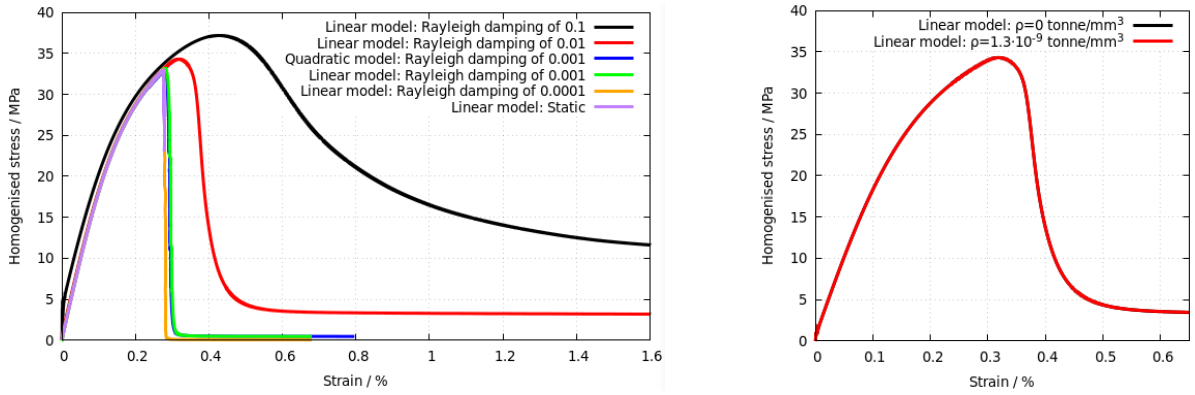


(a) Rayleigh damping variation

(b) Density variation

Figure 7.11: Homogenised stress-strain curves, for the parametric study of the dynamic parameters of the linear *PF* + *intCZM* RVE model with a cohesive interface strength of 30 MPa: Rayleigh damping (7.11a) and density (7.11b).

Three main conclusions follow. Firstly, the assigned density of the cohesive elements at the interfaces does not influence the global stress-strain response: curves for 0 and 1.3 tonne/$mm^3$ density are identical. Secondly, the Rayleigh damping increases the amplitude of the oscillations at the first few increments (see Figure 7.12). These spurious oscillations, also observed by Vieira de Carvalho (2023), arise from the initial transient activation of the inertial and viscous effects, which may excite high frequency modes. In the case of relatively stiff structures, or finite element meshes with relatively small elements (e.g., cohesive elements with an initial zero thickness), the fundamental frequency of the model may be very large, so that the high-frequency response is amplified by the Rayleigh damping (Xu et al. (2019)). Thirdly, higher values of the Rayleigh damping coefficients resulting in higher residual stresses and higher values of the RVE strength, deviating from the quasi-static response. In contrast, lower values of the Rayleigh coefficients are preferred in so much as they recover the static response., but enable modelling the post-peak region in a robust manner Therefore, the value of 0.001 is chosen due to matching the peak response (same strength) and the softening branch. The value of 0.0001 also recovers the response, but choosing a higher value is preferable since additional simulations will consider lower cohesive strengths (< 30 MPa) and adopting this slightly larger value of 0.001 provides a safer margin for cases with steeper softening branches.

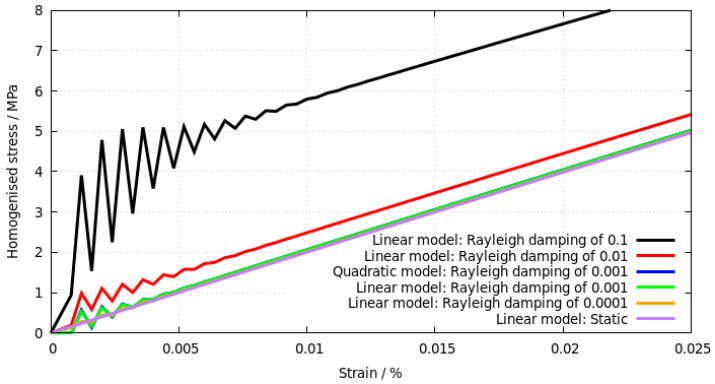


Figure 7.12: Detailed view of the homogenised stress-strain curves, for the different Rayleigh coefficients of the interface cohesive elements, for the linear *PF* + *intCZM* RVE model.

### Initial slope indicator

Since the dynamic formulation mitigates the numerical instabilities introduced by the cohesive element at the fibre-matrix interfaces, a more detailed parametric study may thus be conducted of the phase-field coupled with an interfacial cohesive-zone (*PF* + *intCZM*) model. To better explore an interface-dominated fracture behaviour, in addition to the previously examinated cases, an extra cohesive strength of 15 MPa (i.e., below the lowest tested value of 30 MPa) is included henceforth. This, in addition to the adoption of a dynamic computational framework, justifies repeating the simulations to obtain a stable post-peak system response. Table 7.5 summarises the cohesive material properties adopted, with identical normal and tangential components.

Table 7.5: Cohesive zone model material properties for the cohesive elements, adopted in the parametric studies of the composite microstructure *PF* + *intCZM* RVE.

| | $\phi_{n/t}$ / MPa·mm | $\sigma_{n/t}$ / MPa | $\alpha = \beta$ / - | $\lambda_{n/t}$ / - | $\alpha_p$ |
|---|---|---|---|---|---|
| Reference | 0.004 | 30 | 2 | 0.05 | 2 |
| Maximum | 0.005 | 60 | 15 | 0.1 | 15 |
| Minimum | 0.002 | 15 | 2 | 0.005 | 2 |

Similar to the preliminary microstructure studies, selection of the appropriate value for the initial slope indicator is critical: $\lambda_{n/t} = 0.05$ has already been selected for the cohesive strength of 30 MPa. For the lower strength of 15 MPa, an additional study is conducted using the coarser linear mesh and varying $\lambda_{n/t}$ between 0.005 and 0.1 (Table 7.5). Figure 7.13 displays the homogenised stress-strain responses for the different values of $\lambda_{n/t}$. As expected, the results for the linear and quadratic meshes are indistinguishable, following the reasoning explained before. Moreover, the value of 0.1 is inadequate since it artificially increasings the strength ($\approx$ 27.5 MPa), while the lower values yield consistent apparent strength predictions. The initial stiffness of the homogenised response is increased with a decrease in the initial slope parameter, but no significant gains are observed when reducing $\lambda_{n/t}$ below 0.01. As a result, for all subsequent simulations with a cohesive strength of 15 MPa, a value of 0.01 is chosen for $\lambda_{n/t}$.

### Cohesive strength

To understand the fracture response of a composite RVE, a series of *PF* + *intCZM* RVEs meshes tested. All models employ a baseline fracture energy of 0.004 MPa·mm, while the interfacial cohesive strength is varied between 15, 30, 45, and 60 MPa. Results are compared against the quasi-static

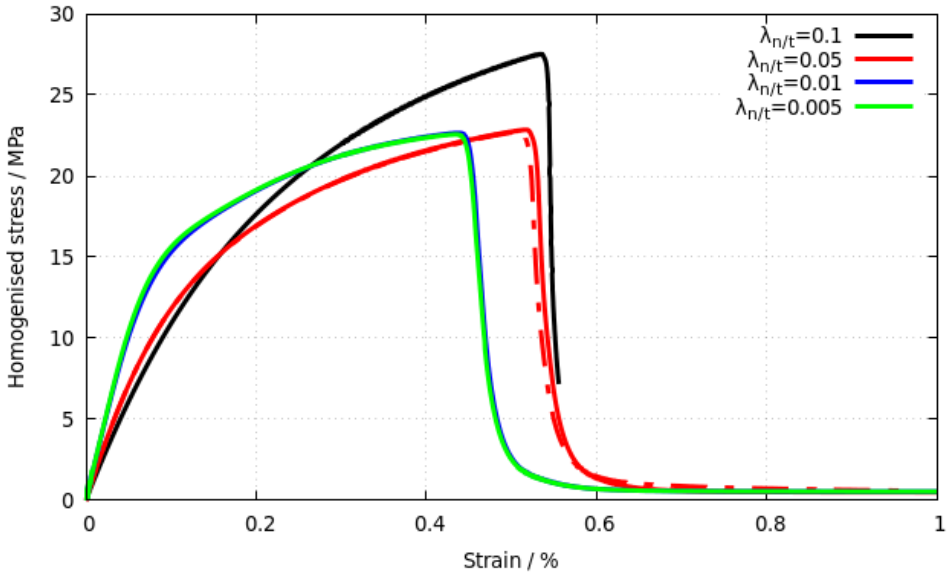


Figure 7.13: Homogenised stress-strain curves, for the different values of the initial slope indicator, $\lambda_{n/t}$, of the interface cohesive elements, for the linear *PF* + *intCZM* RVE model (full lines), in comparison with the quadratic *PF* + *intCZM* mesh (dashed line).

simulations and the reference *PF* model which lacks cohesive elements[3]. Figure 7.14 shows the homogenised stress-strain curves.

For every value of the cohesive strength, the dynamic formulation successfully circumvented the numerical instability that otherwise arise from the presence of the cohesive elements. As result, the stress-strain curves are similar between dynamic and non-dynamic formulations. Nonetheless, the dynamic versions produce a slight increase in the initial stiffness and only marginal differences in the global strength[4]. The relative difference between the peak stresses are between -1.4 to 1.7 % (see Figure 7.14). For a cohesive strength of 15, 30, 45 and 60 MPa, the apparent strength of the model is, respectively, 23, 33, 28 and 26 MPa.

Figures 7.15 and 7.16 show the phase-field distribution and the total output damage variable for the interface cohesive elements, for the distinct values of the cohesive strength. The phase-field length-scale parameter was previously chosen as $l = 0.001$, consistent with values found in literature (Macías et al. (2023)). The regularisation parameter defines the width of crack band, with larger values producing more smeared cracks, and lower values reproducing a sharper crack representation. While the crack patterns observed in this study appear relatively diffuse, lower values would required additional mesh refinement to obtain a response insensitive to $l$, substantially increasing computational costs. Thus, $l = 0.001$ was adopted as a compromise between a physically accurate representation and computational efficiency.

The increase in the cohesive strength reduces the influence of the interfacial debonding on the overall response and thus the failure mode is progressively more matrix-dominated (phase-field variable fracture). For low cohesive strength ($\sigma_{n/t} = 15$ MPa), failure is driven by interface debonding and the cohesive elements reach full separation, $D_{\text{total}} = 1$ (Figure 7.15b). The damage initiates

[3]The strength definitions differ significantly between the two fracture models and thus are not directly comparable. The phase field - cohesive zone formulation of Navidtehrani et al. (2021), Wu (2017) employs an energetic criteria linked to the principal stress $\sigma_1$ which drives the PF evolution through as embedded traction-separation law. By contrast, the PPR cohesive strength is a local threshold of the interface tractions (Park et al. (2009)).

[4]The influence of the Rayleigh damping was found to be higher in *PF*-only simulations rather than the combined *PF* + *intCZM* cases. The latter observed numerical issues in the softening branch and therefore motivated the calibration of the Rayleigh coefficients to better stabilise the response. Despite that, when matrix fracture (i.e., phase-field formulation) is the dominant failure mode, the dynamic effects and viscous damping were found to exert a greater influence on the global RVE response.

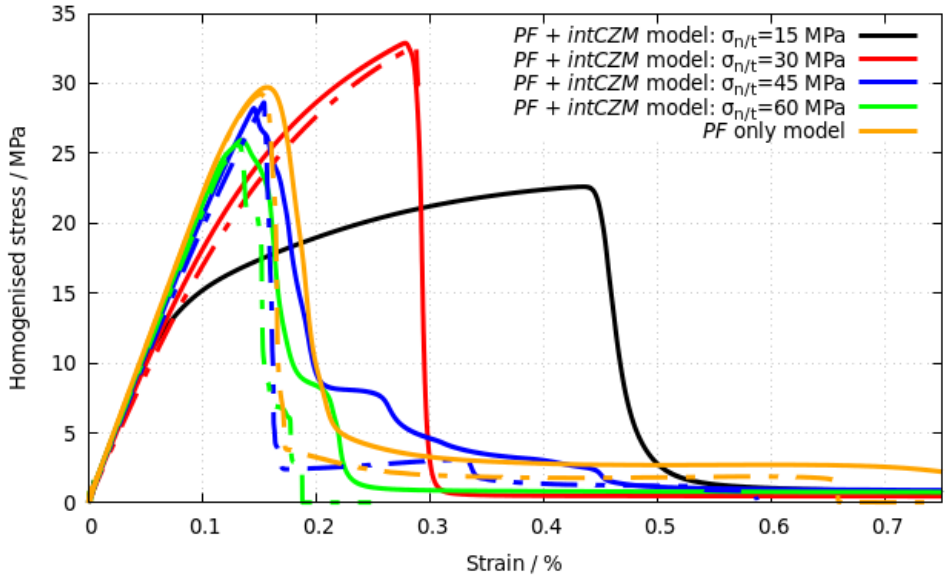


Figure 7.14: Homogenised stress-strain curves, for the parametric study of the cohesive parameters for the quadratic *PF* + *intCZM* RVE model, for different values of the cohesive strength, $\sigma_{n/t}$, of the interface cohesive elements. Full lines correspond to dynamic formulation, and dashed lines to a quasi-static formulation.

and propagates parallel to the loaded edge, at the bottom of the RVE. For $\sigma_{n/t} = 30$ MPa, damage nucleates in the matrix at the same location observed for the quasi-static simulations (between two upper left fibres) and then propagates roughly parallel to the loaded edge. In this case, the cohesive elements never reach a total damage variable of 1. Notably, for the lowest cohesive strengths, the interfaces partially unloaded past the peak response, as noticed by the reduction in the gap opening compared to the peak deformed configuration.

For the two highest cohesive strengths of 45 and 60 MPa (Figure 7.16), the phase-field variable reaches 1 in the matrix, while the cohesive elements remain undamaged (PPR potential total damage variable, $D_{\text{total}}$, is 0). The post-peak response for the simulations where the phase-field dominates exhibit a stepped softening branch: the homogenised stress decreases through a sequence of discrete drops separated by short plateaus, each step corresponding to local damage phenomena and partial load redistribution. At $\sigma_{n/t} = 45$ MPa (Figure 7.16b), the crack path is comparable to the one observed for 30 MPa (Figure 7.15b), but shows increased branching in the phase-field distribution. Atr $\sigma_{n/t} = 60$ MPa, matrix cracking initiates at the upper left region, but propagates closer to the fixed bottom edge.

The complex interaction between matrix- and interface-dominated failure modes can further justify the values of the apparent strength observed in Figure 7.14. Cohesive elements at the interfaces introduce fibre-matrix debonding as a competing failure mode that can enhance the overall RVE strength, as demonstrated for the cohesive strength of 30 MPa. This intermediate value represents a balanced fibre-matrix interaction, whereas a lower value of interface strength (15 MPa) leads to premature fibre-matrix debonding which worsens load transfer. In contrast, the RVE strength reduction at higher cohesive values (45 and 60 MPa) occurs since overly strong interfaces prevents controlled load redistribution through interface debonding which results in more brittle matrix-dominated failure.

**Fracture energy**

In addition, several *PF* + *intCZM* models are tested for cohesive strength of 30 MPa, given it showed a good balance between matrix cracking and fibre-matrix debonding. Setting the interface strength

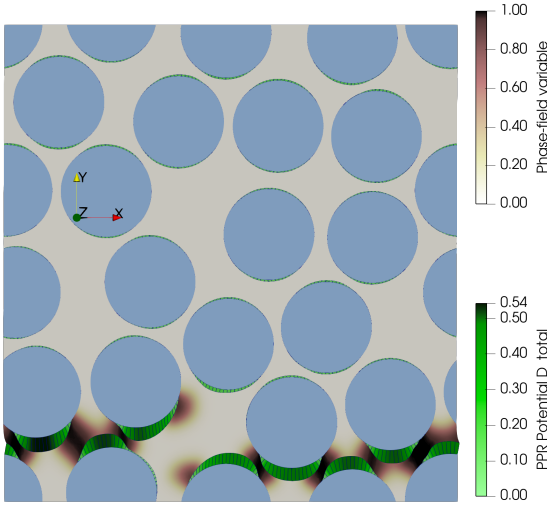


(a) RVE with $\sigma_{n/t}$ = 15 MPa at a load factor of 1.32 (or a prescribed displacement of 0.528 %).

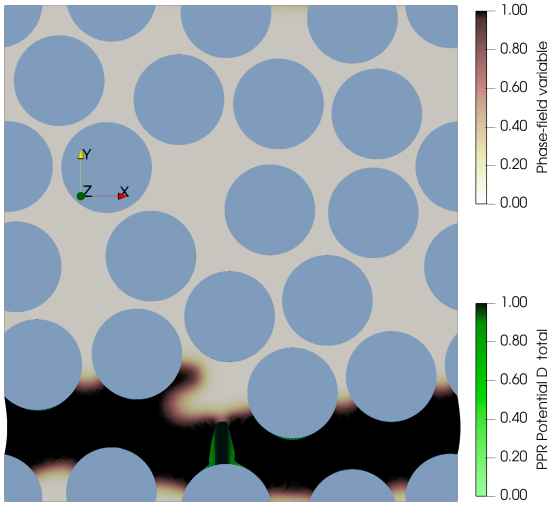


(b) RVE with $\sigma_{n/t}$ = 15 MPa at a load factor of 2.4 (or a prescribed displacement of 0.96 %).

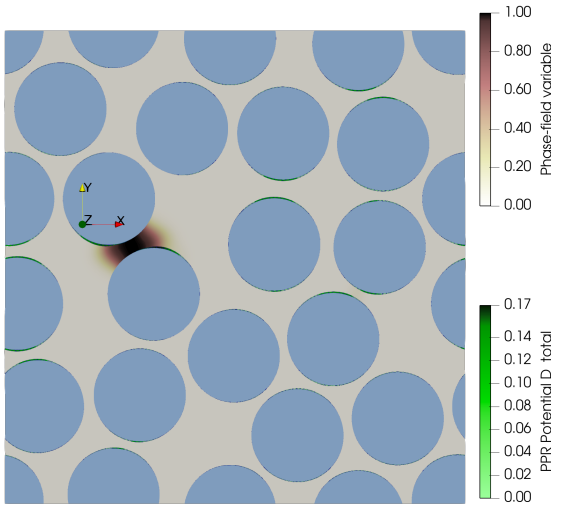


(c) RVE with $\sigma_{n/t}$ = 30 MPa at a load factor of 0.672 (or a prescribed displacement of 0.269 %).

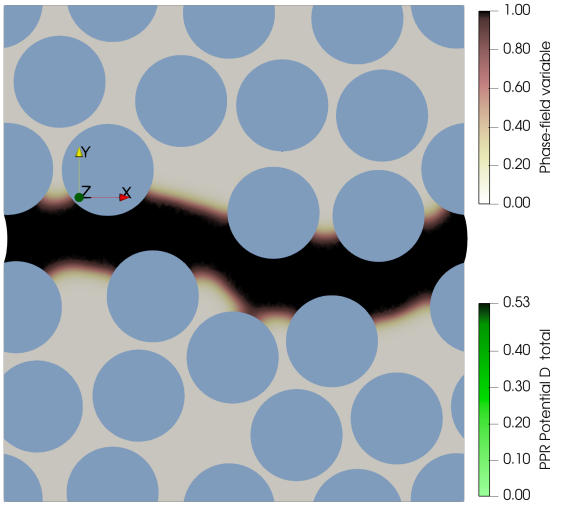


(d) RVE with $\sigma_{n/t}$ = 30 MPa at a load factor of 1.99 (or a prescribed displacement of 0.796 %).

Figure 7.15: Phase-field distribution in the matrix and cohesive damage distribution in the fibre-matrix interfaces, plotted in the deformed configuration at the peak response and at the end of the simulation (scale factor of 10), of an *PF + intCZM* RVE model with TRI6 continuum elements, employing two distinct values of the PPR cohesive strength ($\sigma_{n/t}$): 15 and 30 MPa.

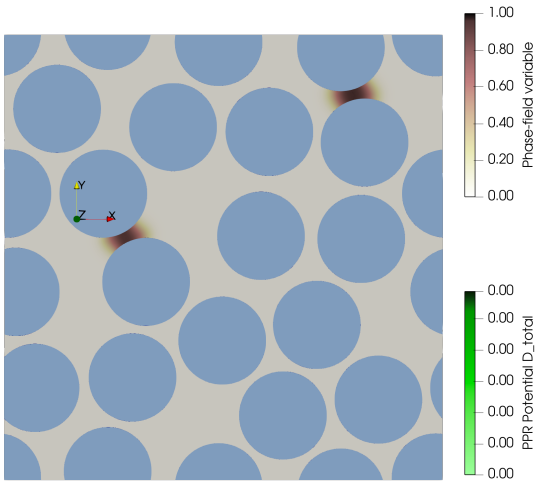


(a) RVE with $\sigma_{n/t}$ = 45 MPa at a load factor of 0.38 (or a prescribed displacement of 0.152 %).

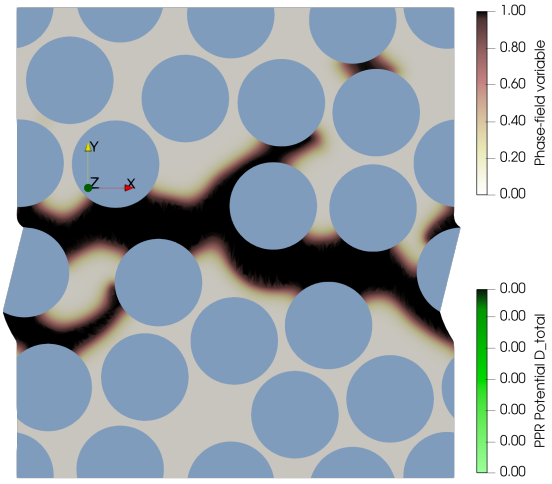


(b) RVE with $\sigma_{n/t}$ = 45 MPa at a load factor of 1.9 (or a prescribed displacement of 0.76 %).

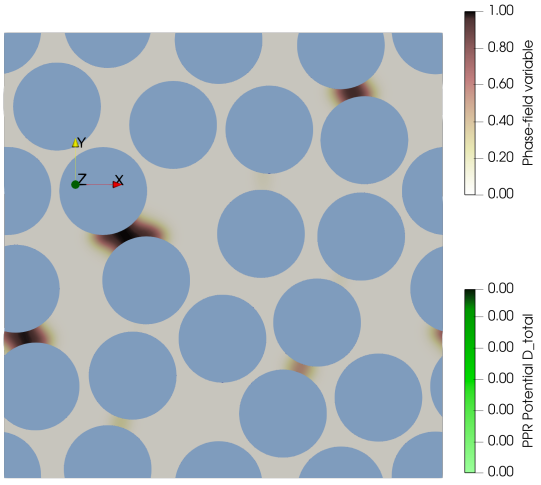


(c) RVE with $\sigma_{n/t}$ = 60 MPa at a load factor of 0.38 (or a prescribed displacement of 0.152 %).

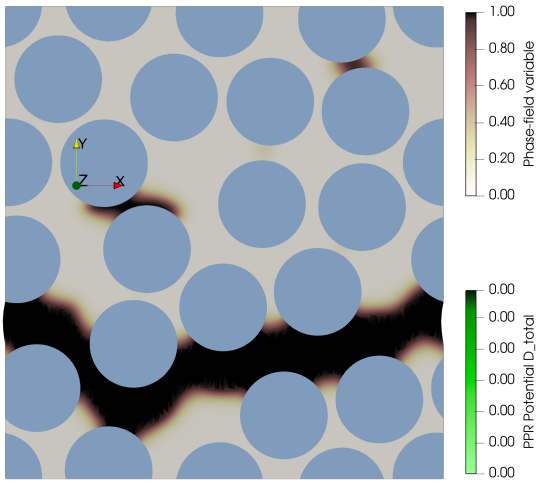


(d) RVE with $\sigma_{n/t}$ = 60 MPa at a load factor of 1.95 (or a prescribed displacement of 0.78 %).

Figure 7.16: Phase-field distribution in the matrix and cohesive damage distribution in the fibre-matrix interfaces, plotted in the deformed configuration at the peak response and at the end of the simulation (scale factor of 10), of an *PF + intCZM* RVE model with TRI6 continuum elements, employing two distinct values of the PPR cohesive strength ($\sigma_{n/t}$): 45 and 60 MPa.

constant and equal to 30 MPa, values of the interfacial fracture energy are considered: 0.002, 0.003, 0.004, and 0.005 MPa·mm. Figure 7.17 shows the stress-strain curves for these cases, which are then compared with the baseline *PF* model (in light gray). Consistent with the initial studies, variations of the fracture energy do not significantly change the global strength of the meshed model (≈ 33 MPa). However, higher values of cohesive fracture energy delay the peak response (the peak stress occurs at a larger prescribed strain), while a reduction of $\phi_{n/t}$ produces a stiffer initial response that approaches more closely the *PF* model, without cohesive elements.

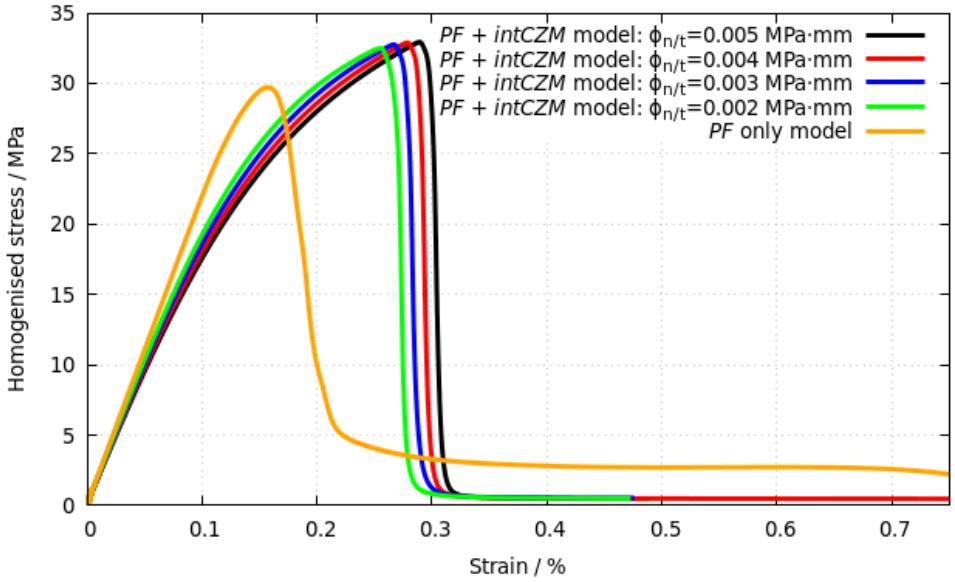


Figure 7.17: Homogenised stress-strain curves, for the parametric study of the cohesive parameters for the quadratic *PF + intCZM* RVE model, for different values of the fracture energy, $\phi n/t$, of the interface cohesive elements.

Observing the phase-field distributions of Figure 7.18, it is clear that the main matrix crack paths ($\phi \approx 1$) initiate at the same two locations (between two upper left fibres and between two right center fibres). Around the peak response, lower fracture energy of the cohesive elements along the material interfaces is associated with higher maximum values of the interface damage output variable. The exception is the case for a cohesive strength of 30 MPa and a fracture energy of 0.002 MPa·mm (Figures 7.18a and 7.18b). Here, at the end of the simulation, the cohesive elements surrounding three fibres reached $D_{\text{total}} = 1$, which can be seen by their larger normal interface gaps (visualised for a deformation scale factor of 10).

**Softening laws**

The mechanical behaviour of the RVE is studied by running simulations with different combinations of the phase-field softening branch (linear or exponential) and the PPR traction-separation law (linear or exponential). In contrast with many cohesive zone models (CZMs), the PPR cohesive model allows to reproduce user-defined softening shapes, such as concave, convex, linear or exponential, through the shape parameters, $\alpha$ and $\beta$. When $\alpha = \beta = 2$ a linear cohesive softening curve is obtained, with values greater than 2, the cohesive traction law has a convex softening curve. Muñetón-López and Giraldo-Londoño (2024) suggests setting the shape parameters to $\alpha = \beta = 15$ to reproduce an exponential traction-separation softening. This is further corroborated in Appendix B. These combinations are studied for *PF + intCZM* models with interfacial cohesive strength of 15 MPa ( and $\lambda_{n/t} = 0.01$), or 30 MPa (and $\lambda_{n/t} = 0.05$).

Figure 7.19 presents the homogenised stress-strain curves for the different combinations of the softening laws. The global response is identical for the quadratic and linear meshes. In addition,

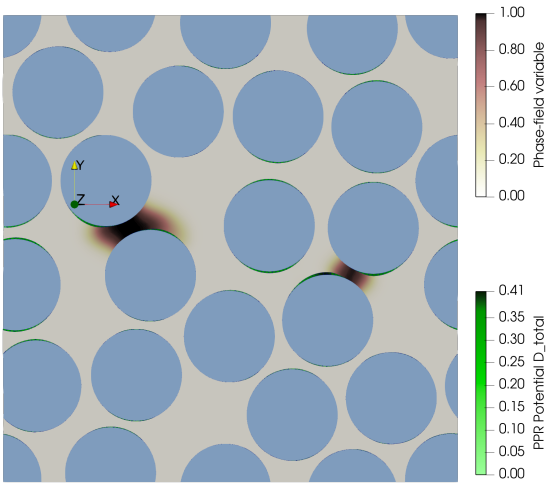


(a) RVE with $\phi_{n/t} = 0.002$ MPa·mm at a load factor of 0.667 (or a prescribed displacement of 0.267 %).

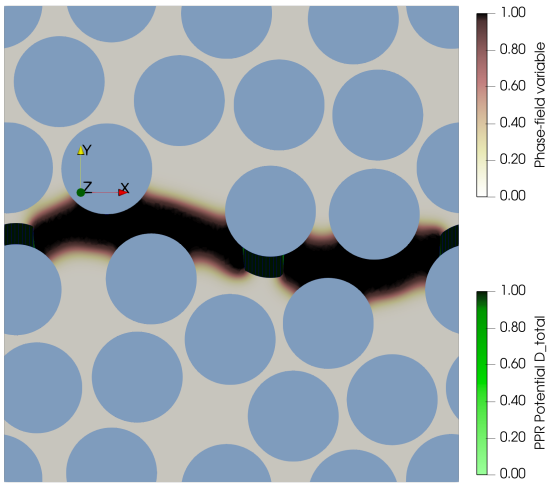


(b) RVE with $\phi_{n/t} = 0.002$ MPa·mm at a load factor of 1.177 (or a prescribed displacement of 0.741 %).

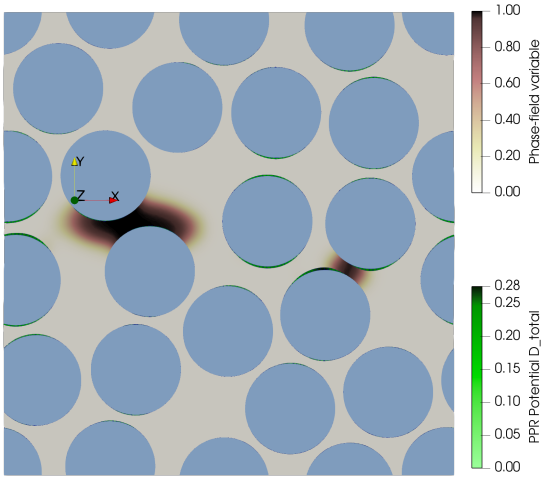


(c) RVE with $\phi_{n/t} = 0.003$ MPa·mm at a load factor of 0.697 (or a prescribed displacement of 0.279 %).

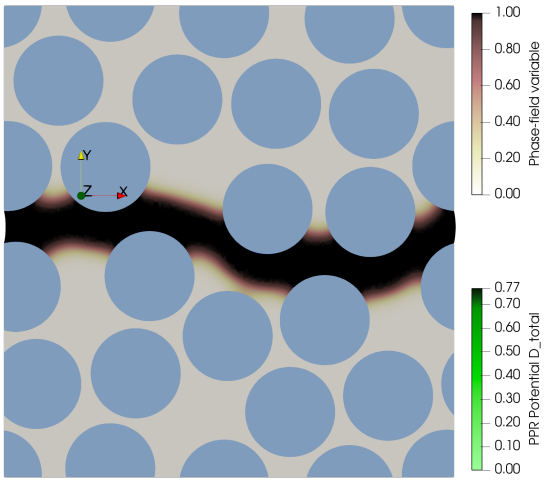


(d) RVE with $\phi_{n/t} = 0.003$ MPa·mm at a load factor of 1.177 (or a prescribed displacement of 0.471 %).

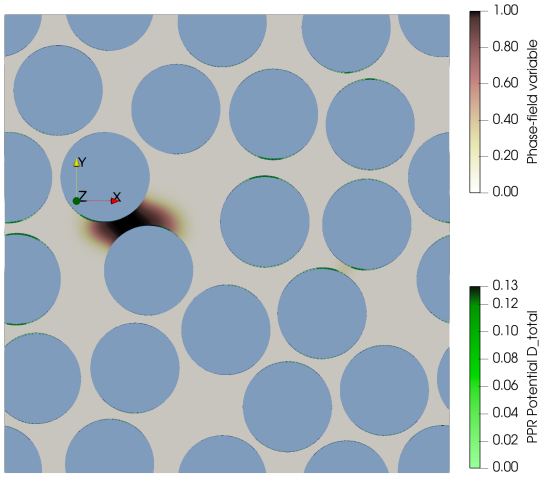


(e) RVE with $\phi_{n/t} = 0.005$ MPa·mm at a load factor of 0.742 (or a prescribed displacement of 0.471 %).

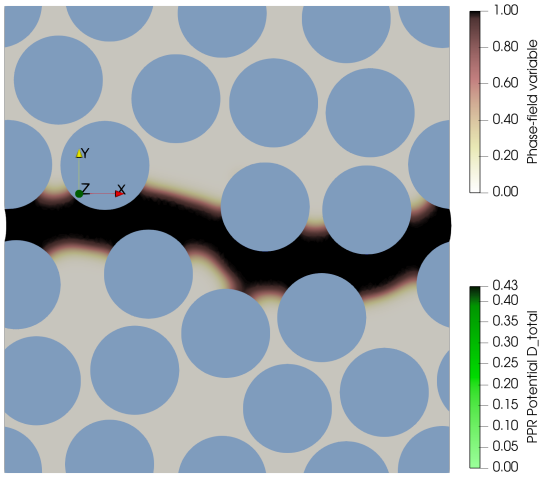


(f) RVE with $\phi_{n/t} = 0.005$ MPa·mm at a load factor of 1.222 (or a prescribed displacement of 0.489 %).

Figure 7.18: Phase-field distribution in the matrix, plotted in the deformed configuration at the peak response and at the end of the simulation (scale factor of 10), of an *PF + intCZM* RVE model with TRI6 continuum elements, for three distinct values of the PPR cohesive strength, $\phi_{n/t}$.

the different combinations of the softening parameters did not alter the peak stress for a fixed cohesive strength. When the cohesive shape parameters are fixed (2 or 15), switching from a linear to an exponential phase-field softening law produces an identical pre-peak response, but also anticipates the peak response, with the subsequent softening branch remaining similar in shape. This effect is accentuated for the lower cohesive strength of 15 MPa. Conversely, for a given phase-field softening law (linear or exponential), increasing the cohesive shape parameters from 2 to 15 delays the peak response, and introduces artificial compliance (lower initial stiffness), and yields a similar, but slightly less steep, softening branch.

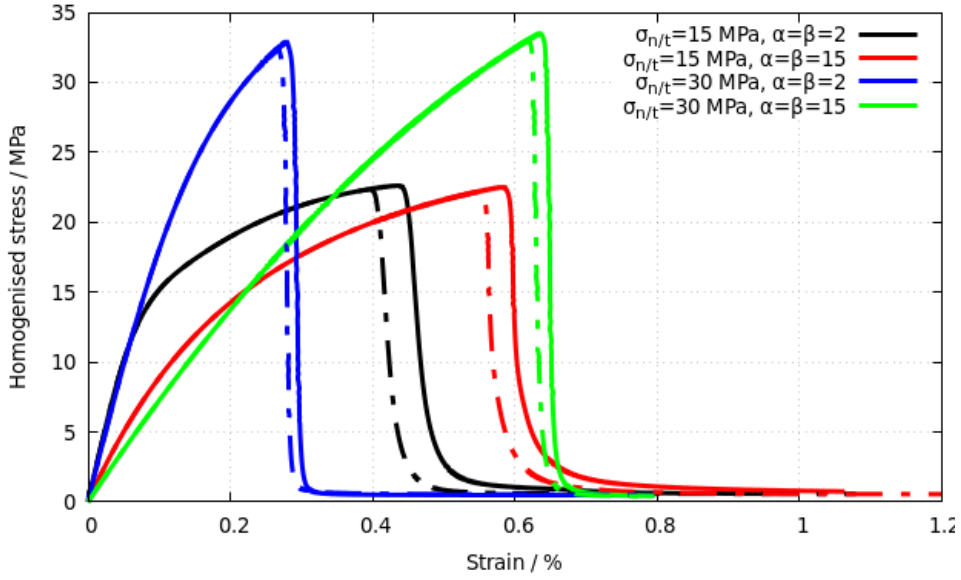


Figure 7.19: Homogenised stress-strain curves, for different values of the shape parameters $\alpha$ and $\beta$ of the interface cohesive elements, for the quadratic *PF + intCZM* RVE model. Full lines correspond a PF linear softening law, and dashed lines to a PF exponential softening law.

Comparison of the phase-field distributions and the cohesive total damage variable, $D_{\text{total}}$, in Figures 7.20 and 7.21 shows that adopting an exponential PF softening law results in a more smeared crack band and a smoother transition from $\phi = 1$ to $\phi = 0$. For cohesive strength of 15 MPa, increasing the cohesive shape parameter from 2 to 15 for the same PF softening law yields a higher final values of $D_{\text{total}}$, larger normal interface gaps and a wider phase-field crack band (compare Figures 7.15b-7.20b and Figures 7.20d-7.20f). In contrast, when the cohesive shape parameters are fixed and the PF softening law is changed from linear to exponential, the reverse trend occurs (Figures 7.15d-7.21b and Figures 7.21b-7.21f).

A similar behaviour is observed for the higher cohesive strength of 30 MPa, where setting $\alpha = \beta = 15$ produces a more sparse phase-field distribution with increased branching of the matrix crack pattern, whereas an exponential PF softening concentrates the matrix crack band parallel to the top prescribed edge and smooths the transition from $\phi = 1$ to $\phi = 0$. Overall, the results indicate that, for the *PF + intCZM* models with the lower cohesive strengths for the interface elements, (i) the PF softening law primarily controls the localisation and smear of the matrix crack band, and (ii) the cohesive shape parameters govern the degree of interfacial damage and the critical imposed displacement. In contrast, for models with higher cohesive strengths of 45 and 60 MPa of cohesive strength, the fibre-matrix debonding plays a much reduced role. As a result, in these cases, the influence of the PPR shape parameters is expected to be reduced when compared with the type of PF softening law.

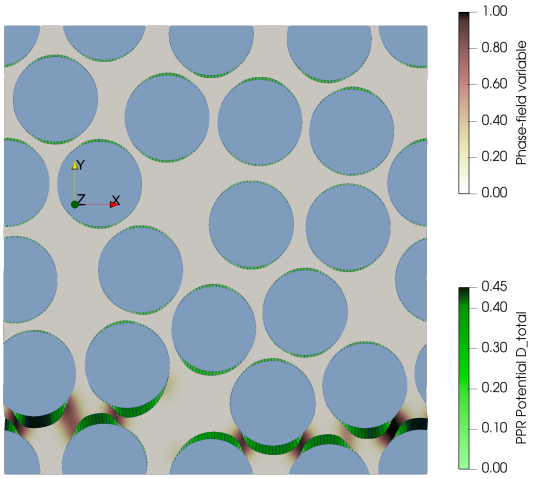


(a) $\alpha = \beta = 15$ and a PF linear softening law, for a prescribed displacement of 0.596 %.

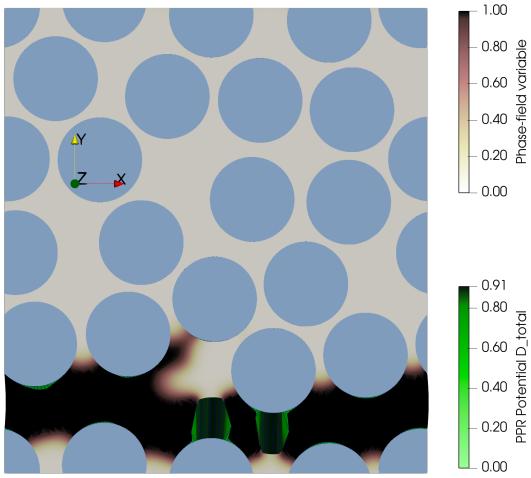


(b) $\alpha = \beta = 15$ and a PF linear softening law, for a prescribed displacement of 0.992 %.

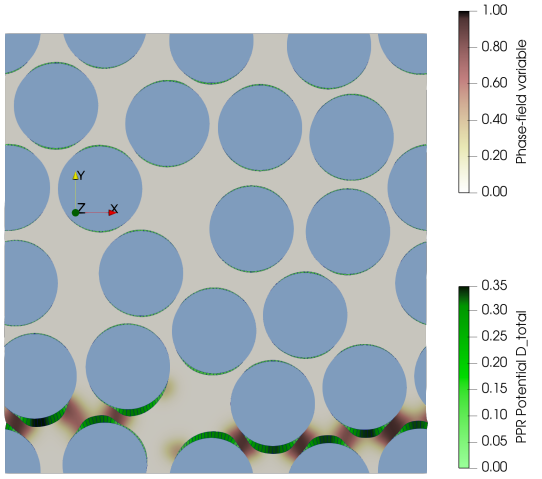


(c) $\alpha = \beta = 2$ and a PF exponential softening law, for a prescribed displacement of 0.416 %.

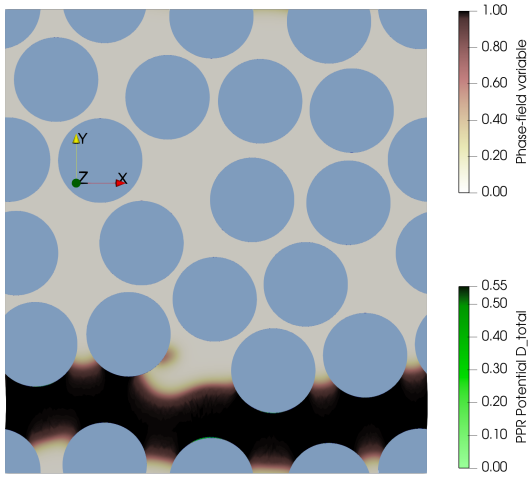


(d) $\alpha = \beta = 2$ and a PF exponential softening law, for a prescribed displacement of 0.992 %.

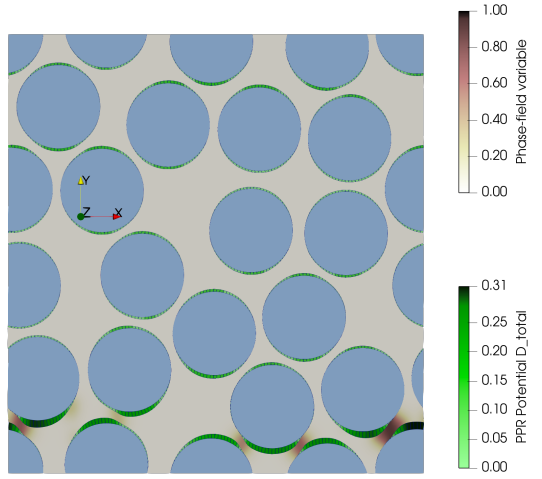


(e) $\alpha = \beta = 15$ and a PF exponential softening law, for a prescribed displacement of 0.56 %.

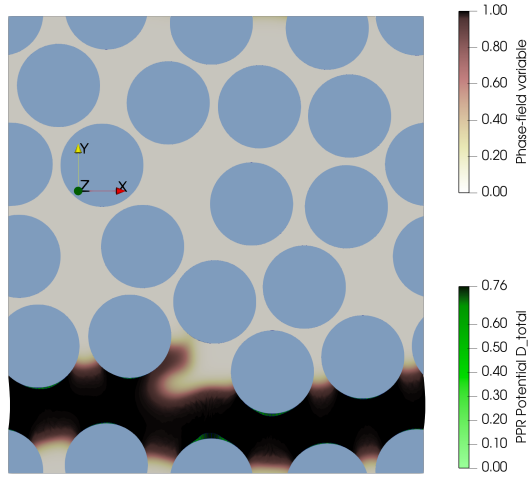


(f) $\alpha = \beta = 15$ and a PF exponential softening law, for a prescribed displacement of 0.992 %.

Figure 7.20: Phase-field distribution in the matrix, plotted in the deformed configuration at the peak response and at the end of the simulation (scale factor of 10), of an *PF + intCZM* RVE model with TRI6 continuum elements, for a PPR cohesive strength of 15 MPa and for three distinct combinations of the softening laws.

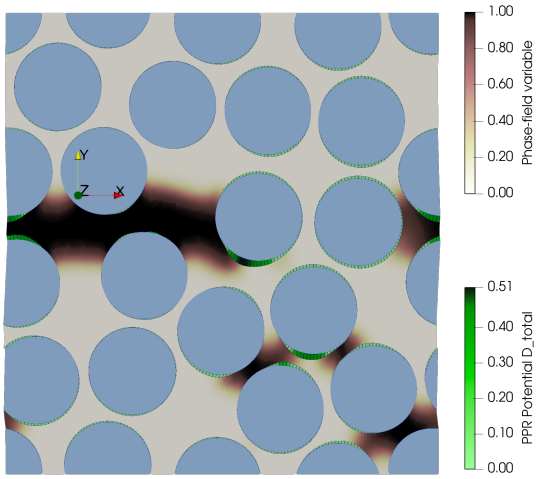


(a) $\alpha = \beta = 15$ and a PF linear softening law, for a prescribed displacement of 0.653 %.

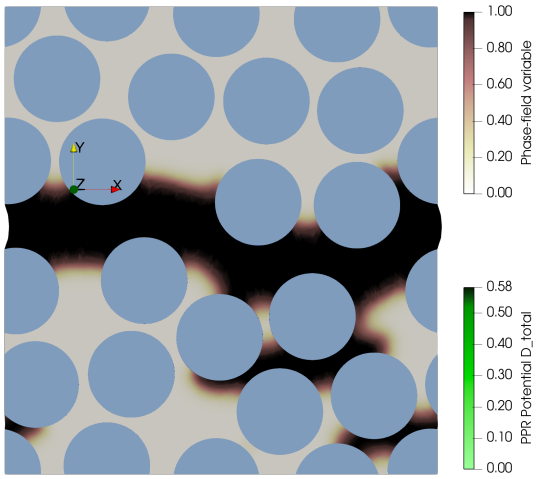


(b) $\alpha = \beta = 15$ and a PF linear softening law, at a for a prescribed displacement of 0.796 %.

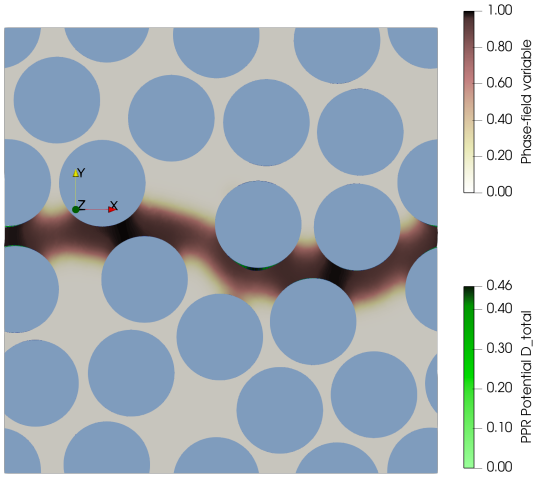


(c) $\alpha = \beta = 2$ and a PF exponential softening law, for a prescribed displacement of 0.285 %.

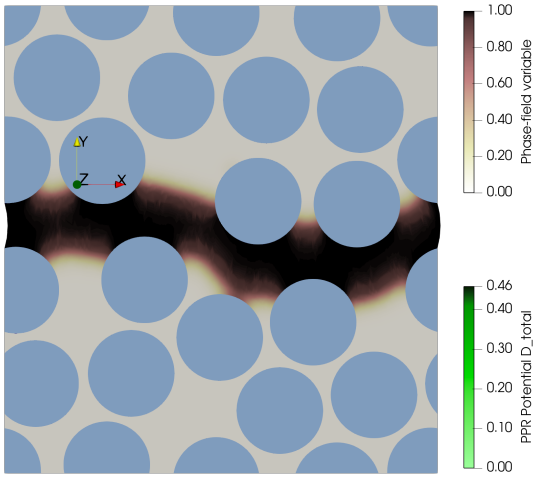


(d) $\alpha = \beta = 2$ and a PF exponential softening law, for a prescribed displacement of 0.796 %.

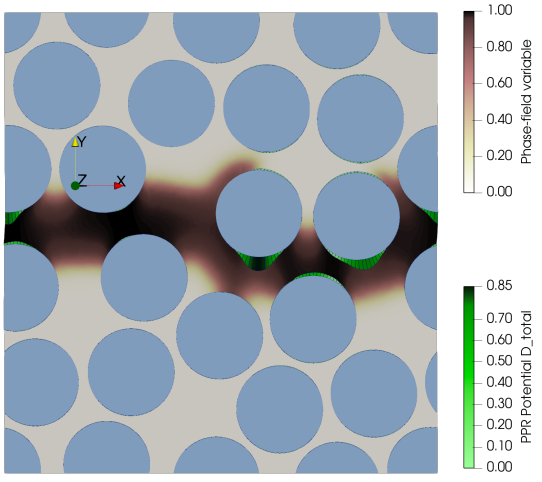


(e) $\alpha = \beta = 15$ and a PF exponential softening law, for a prescribed displacement of 0.637 %.

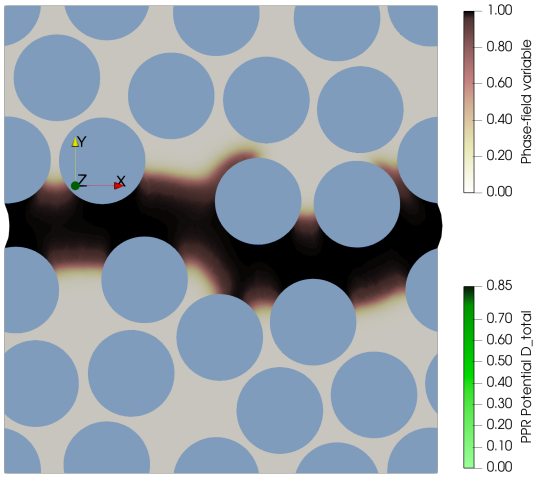


(f) $\alpha = \beta = 15$ and a PF exponential softening law, for a prescribed displacement of 0.796 %.

Figure 7.21: Phase-field distribution in the matrix, plotted in the deformed configuration at the peak response and at the end of the simulation (scale factor of 10), of an *PF + intCZM* RVE model with TRI6 continuum elements, for a PPR cohesive strength of 30 MPa and for three distinct combinations of the softening laws.

**Non-phase-field models**

To identify the influence of interfacial debonding on the RVE response, additional simulations with the phase-field deactivated are performed, retaining the PPR cohesive elements along the fibre-matrix interfaces (*inCZM*). These *intCZM* models are executed for the three cohesive strengths previously considered. The resulting homogenised stress-strain response are plotted in Figure 7.22 alongside the corresponding *PF* + *intCZM* responses from Figure 7.14 for comparison. All *intCZM* models ran until a prescribed strain of 1.8 % at the top edge.

As can be seen in Figure 7.22, the *intCZM* models consistently predict higher RVE strengths than the equivalent *PF* + *intCZM* models. Specifically, for $\sigma_{n/t}$ = 15, 30, and 45, the peak homogenised stress with only interfacial damage simulated are 26.5, 39.7 and 52.3 MPa, respectively. For the same cohesive strengths, the peak resistances reported for the models with phase-field activated in the matrix are 23.0, 32.9, and 28.2 MPa. The largest discrepancy occurs for $\sigma_{n/t}$ = 45 MPa (85 % increase in predicted resistance), where the *PF* + *intCZM* response if matrix-dominated and the absence of a matrix damage mechanism for the *intCZM* formulation prevents crack coalescence, yielding an unrealistically high peak RVE strength. For 15 and 30 MPa, the predicted strength corresponds to the end of the simulation where the curve has plateaued, and is only 16 % and 20 % higher, respectively. These two cases are dominated (15 MPa) or partially-dominated (30 MPa) by interfacial debonding for the *PF* + *intCZM* simulations, which is the sole damage mechanism represented in *intCZM*. These results reflect the evolution of damage in fibre-reinforced composites. Interfacial debonding alone (without an auxiliary matrix damage mechanism, such as phase-field) leads to isolated fibre-matrix gaps unable to connect into a continuous crack path. As a consequence, the *intCZM* RVE model behaves as a purely elastic matrix from which the fibres progressively debond. This phenomenon can give rise to a plateauing load or even load recovery as an increase in the prescribed displacement induces new interface openings. For the lowest cohesive strength ($\sigma_{n/t}$ = 15 MPa), the stress-strain response does not exhibit a clearly defined peak stress before the 2 % strain limit, but instead increases until the end of the simulation. For the two highest cohesive strengths (30 and 45 MPa), the load can drop locally as certain fibres debond, then plateau or increase as the RVE continues to deform and additional fibre-matrix interfaces become engaged.

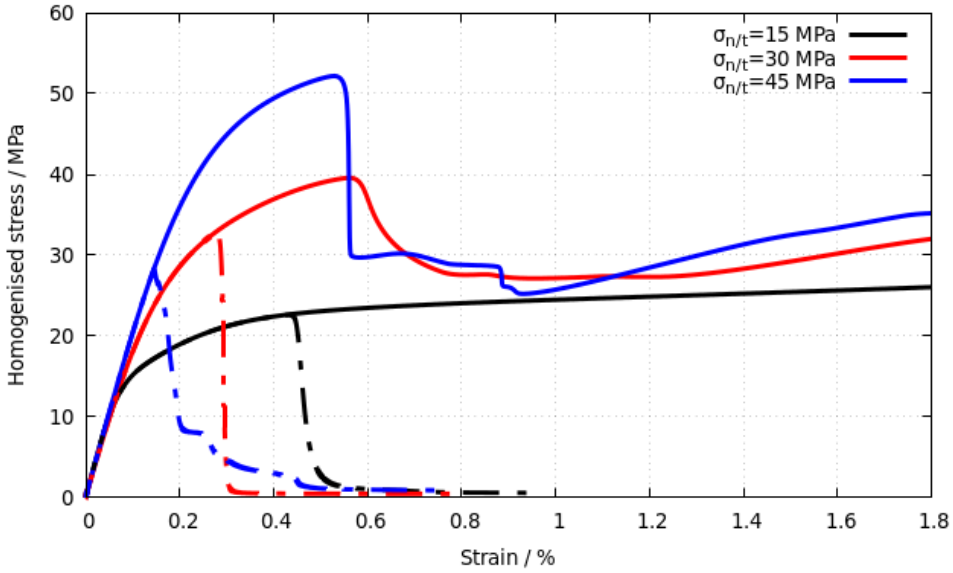


Figure 7.22: Homogenised stress-strain curves, for different values of the cohesive strength of the interface cohesive elements, for the quadratic *intCZM* RVE model (full lines), with respect to the hybrid configuration, *PF* + *intCZM* (dashed lines).

This is also evident in the distribution of the output damage variable, $D_{\text{total}}$, associated with

the PPR cohesive zone model (Figure 7.23). For $\sigma_{n/t} = 15$ MPa, the cohesive elements never reach $D_{\text{total}} = 1$ (Figures 7.23a and 7.23b). For higher cohesive strengths, the PPR damage variable reaches 1 at the peak response, with the normal gap at the fibre-matrix interfaces increasing with an increase in the prescribed displacement (Figures 7.23e and 7.23f and Figures 7.23e and 7.23f). For $\sigma_{n/t} = 45$ MPa the central region of the RVE is most effected, while for $\sigma_{n/t} = 30$ MPa the largest debonding occurs near the bottom fibres.

To conclude, the *intCZM* model, a mesh which contains only interfacial cohesive elements and with a purely elastic matrix, is insufficient to reproduce the matrix-dominated failure modes captured by the *PF* + *intCZM* model. The inability to faithfully reproduce the RVE strength stems from the lack of a matrix failure mechanism, such as phase-field diffuse field or cohesive elements inserted between the matrix TRI6 elements, which is required for realistic crack coalescence.

The parametric study of the cohesive properties associated with the PPR cohesive zone model within the *PF* + *intCZM* framework provides a solid foundation for simulating matrix cracking and interface debonding in composite RVEs. The potential-based approach allows the user to choose types of cohesive laws in addition to loading conditions, but the selected material parameters must be chosen with regard to their interaction with the matrix fracture mechanism. The global response thus depends on the coupled behaviour of the matrix phase-field and the interface cohesive elements, with the variation of the interfacial strength, initial slope indicator, and fracture energies, producing distinct peak response and fracture patterns.

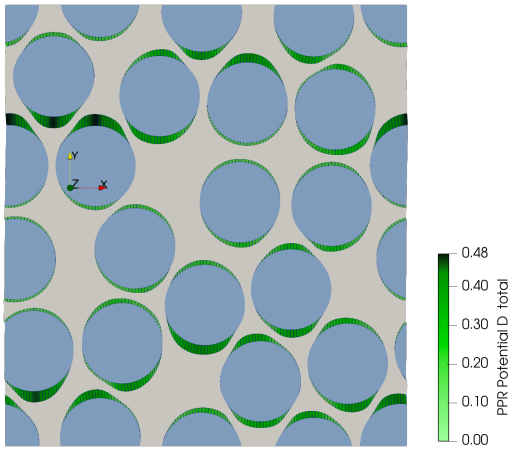


(a) $\sigma_{n/t} = 15$ MPa.

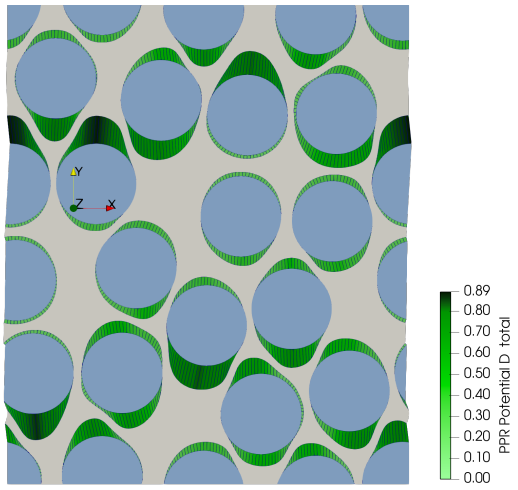


(b) $\sigma_{n/t} = 15$ MPa.

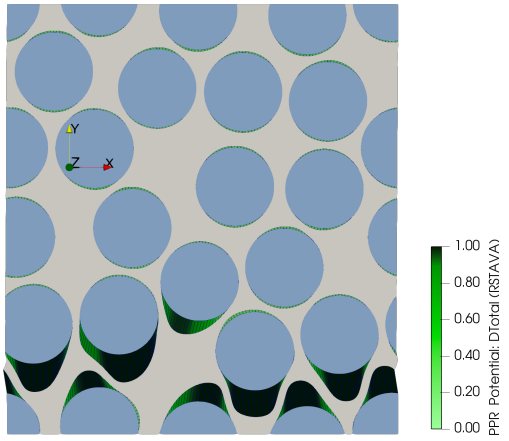


(c) $\sigma_{n/t} = 30$ MPa.

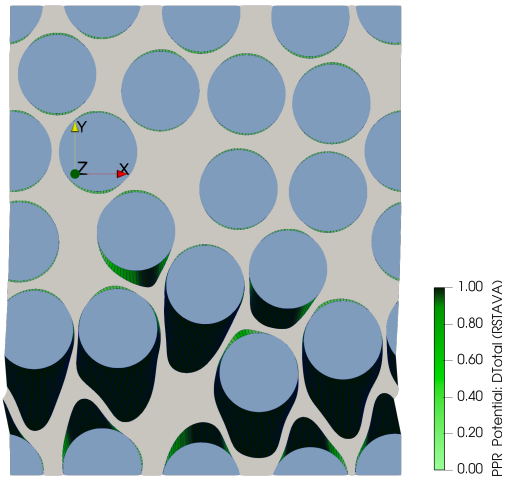


(d) $\sigma_{n/t} = 30$ MPa.

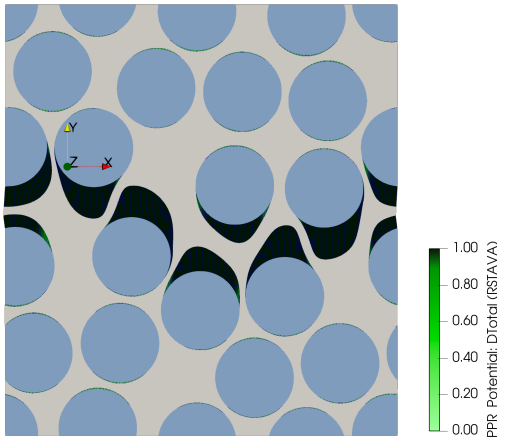


(e) $\sigma_{n/t} = 45$ MPa.

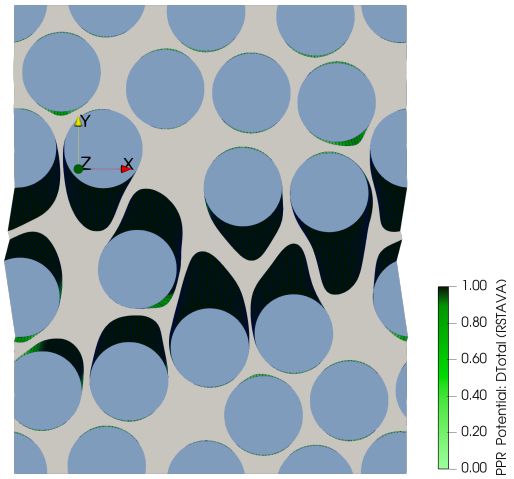


(f) $\sigma_{n/t} = 45$ MPa.

Figure 7.23: Phase-field distribution in the matrix (deformed configuration, scale factor of 10) at the peak response (1 % displacement) and at the end (2 % displacement) of the simulation, of an *intCZM* RVE model with TRI6 continuum elements, for a PPR cohesive strength of 15 MPa and for three distinct values of the PPR cohesive strength ($\sigma_{n/t}$): 15, 45 and 60 MPa.

### 7.2.4 Parametric study of FRP fracture with allCZM + intCZM and dynamics

This Section compares two fracture modelling strategies for the same RVE linear mesh: the hybrid phase-field matrix with cohesive elements along the interfaces (*PF* + *intCZM*), and the entirely cohesive model in which the zero-thickness PRR cohesive elements are inserted not only along the fibre-matrix interfaces but also between every pair of adjacent continuum elements of the matrix and fibre (*allCZM* + *intCZM*). For the latter, the phase-field diffuse field in the matrix is replaced by explicitly pre-inserted cohesive elements within the matrix, using the Python script of Chapter 5. The main purpose lies in understanding how the two modelling approaches affect the global response of the composite RVE, its overall failure patterns, and its global stress-strain response.

The linear elastic properties of fibre and matrix can be found in Tables 7.1 and 7.2, respectively. All PPR cohesive materials considered (fibre-fibre, fibre-matrix, and matrix-matrix) employ identical properties for the normal and tangential directions to simplify the comparisons with the models from the previous Section. Since the RVE is loaded in predominantly mode I, the normal component is expected to govern the overall response. The tangential properties are equal to the normal ones as to allow a direct comparison with the phase-field formulation implemented in `LINKS`. Matrix-matrix cohesive properties are given in Table 7.6[5]. The material properties of the fibre-matrix interface cohesive elements can be seen in Table 7.7. Due to limitations in the Python script, it produces cohesive elements between fibre-fibre continuum elements. As a result, extremely large values of the cohesive strength ($5{\cdot}10^6$ MPa) and associated compatible fracture energy (50 MPa·mm) were chosen to ensure no separation or damage. Thus, the impact of these elements can be neglected and the fibre elements behaved essentially as purely elastic.

Table 7.6: Cohesive zone model material properties for the matrix-matrix cohesive elements, adopted in the parametric study of an *allCZM* + *intCZM* RVE model, for a linear meshed RVE.

| $\rho$ / tonne·mm$^{-3}$ | $\phi_{n/t}$ / MPa·mm | $\sigma_{n/t}$ / MPa | $\alpha = \beta$ / - | $\lambda_{n/t}$ / - | $\alpha_p$ |
|---|---|---|---|---|---|
| $1.3 \cdot 10^{-9}$ | 0.002 | 45 | 2 | 0.01 | 1 |

Table 7.7: Cohesive zone model material properties for the fibre-matrix interface cohesive elements, adopted in the parametric study of an *allCZM* + *intCZM* RVE model, for a linear meshed RVE.

| $\rho$ / tonne·mm$^{-3}$ | $\phi_{n/t}$ / MPa·mm | $\sigma_{n/t}$ / MPa | $\alpha = \beta$ / - | $\lambda_{n/t}$ / - | $\alpha_p$ |
|---|---|---|---|---|---|
| $1.3 \cdot 10^{-9}$ | 0.004 | $\{15, 30, 45, 60\}$ | 2 | 0.01 | 1 |

All simulations are performed using a dynamic formulation. Initial dynamic simulations with Rayleigh damping coefficients set to 0.001, and a spectral radius ($\rho_\infty$) associated with the solver of 0.7. However, the early increments observed large oscillations, which made the stress-strain curves deviate from the static/non-dynamic response (see Figure 7.24). The amplitude of the initial transient oscillations increases with the cohesive strength of the interface elements, although these oscillations also decay more rapidly than lower strengths. Raising the interface strength increases the effective stiffness of the RVE, leading to high-frequency elastic oscillations at the early time steps. Rayleigh coefficients dampen high-frequency modes more strongly (Xu et al. (2019)).

To mitigate this behaviour, some lower values of the Rayleigh coefficients and spectral radius were tested, as well as a more refined incrementation (Figures 7.26a and 7.26b). The smaller increment size (time increment) reduced the amplitude of the initial oscillation from approximately

[5]Initial simulations with a penalty factor of 100 of the matrix-matrix cohesive elements ended immediately after the peak response. Setting the penalty factor to $\alpha_p = 1$ successfully addressed this issue and produced equivalent results and conclusions.

30 down to about 1, therefore preventing eventual damage initiation in the first increments at any cohesive interface which would affect the mechanical response.

As observed in Figure 7.25, the *allCZM* + *intCZM* models predict higher strength of the RVE compared to the *PF* + *intCZM* baseline for the same interfacial strength. The peak homogenised stresses obtained with the *allCZM* + *intCZM* model are 23.0, 37.9, 40.5, and 40.4 MPa for a interface cohesive strengths of 15, 30, 45, and 60 MPa, respectively. For reference, note that the *PF* + *intCZM* and the pure *intCZM* (interface-only) models produced the peak stresses seen in Figure 7.14. The higher discrepancy between observed peak strengths occurs for lower cohesive interface strengths, because, in these cases, the *PF* + *intCZM* model, predicts matrix-dominated fracture while the *allCZM* + *intCZM* formulation prevents natural crack coalescence and therefore predicts higher apparent strengths. For those cases (45 and 60 MPa), the diffuse matrix phase-field is replaced by pre-inserted cohesive elements which prevent a natural crack coalescence and result in substantially different peak stresses. Two reasons may be offered. The intrinsic cohesive zone discretisation requires the potential crack surfaces to be defined a priori, whereas the variational phase-field formulation permits cracks to nucleate and propagate along energetically favourable paths which are determined by the stress field as the specimen is loaded. In addition, the damage driving criteria differ for the PF and PPR-CZM. This specific PF formulation, the phase field-cohesive zone model, computes damage from bulk stress measures ($\sigma_1$), while the PPR potential-based CZM determines damage locally at each cohesive element according to its normal and tangential traction values. This may result in damage nucleating in different places at the mesh and distinct crack propagation, despite the same fracture toughness being defined. Note that the regularisation parameter of the phase-field, $l = 0.001$, was selected based upon mesh resolution. A faithful energetic equivalence between the phase-field and cohesive zone model discretisation for an heterogeneous composite microstructure would require a more careful calibration. As a final remark, the stress values have different definitions and so a value of 45 MPa in the PF formulation is not directly equivalent to 45 MPa of cohesive strength in the CZM.

Figures 7.27 and 7.28 display the spatial distribution of the cohesive damage output, $D_{\text{total}}$, for the fibre-matrix and matrix-matrix cohesive elements. The *allCZM* + *intCZM* model can produce either matrix-dominated or interface debonding-dominated response, depending on the cohesive strengths and fracture energies of the each type of cohesive element. If the intra-matrix elements activate first and coalesce, the fibre-matrix interfaces remain largely intact, while, conversely, if the interfaces are weaker, debonding dominates. As expected, as the interface cohesive strength increases, the influence of the intra-matrix elements becomes more relevant. For $\sigma_{n/t} = 45$ and 60 MPa, the simulations terminate with a perpendicular crack formed entirely by *allCZM* matrix cohesive elements. In these cases, $D_{\text{total}} = 1$ for several matrix-matrix cohesive interfaces, while the interfacial cohesive elements remain undamaged. This behaviour replicates the matrix-dominated fracture observed with *PF* + *intCZM* (see Figures 7.15 and 7.16). For $\sigma_{n/t} = 15$ and 45 MPa, the interface cohesive elements play a larger role in the fracture response, with the matrix-matrix cohesive elements essentially only bridging the gap between fibre-matrix interfaces. In addition, the interface cohesive elements do not exhibit significant unloading, after the peak response (i.e., the gap actually increases), in contrast with the *PF* + *intCZM* simulations.

When comparing the *allCZM* + *intCZM* directly with *PF* + *intCZM*, for the same cohesive strength, the interface elements have a much larger impact in the fracture response for *allCZM* + *intCZM* models (Figures 7.15 and 7.27).

Furthermore, the spatial patterns of the activated matrix cohesive elements produced by the *allCZM* + *intCZM* models are irregular and tortuous, not following the ideal path parallel to the loaded top edge. This contrasts with the more spatially coherent, continuous damage bands obtained for the *PF* + *intCZM* simulations. Here, the discrete nature of pre-inserted cohesive interfaces restricts the possible crack propagation paths to bulk element boundaries. The activation of these cohesive interfaces is thus dependent on the local tractions and the local mesh connectivities. In contrast, the phase-field formulation is a continuous scalar field, where crack paths evolve along energeti-

cally favourable directions.

The main differences in the RVE responses observed between the parametric studies of Sections 7.2.3 and 7.2.4 is due to several factors. A relevant contribution is the underlying difference between the implementation of each modelling approach. Although both are cohesive models, the phase-field approach employed has fewer parameters to change and does not allows for independent control over normal and tangential properties. On the other hand, the PPR potential-based CZM is highly sensitive to the initial slope parameter, $\lambda_{n/t}$, which must be calibrated, alongside adjustments of the fracture energies to be compatible with the strength values selected.

**Closing remarks**

For completeness, the average CPU time per increment found for the quadratic RVE meshes with a *PF* + *intCZM* configuration and for the linear RVE meshes with a *allCZM* + *intCZM* configuration differ from the values reported for the *PF*-only meshes in the mesh sensitivity study of Section 7.2.1. For the TRI6 meshes used in Sections 7.2.2 and 7.2.3, the measured average time is 15.9 s per increment, which is consistent with the 16.2 s shown in Figure 7.2. By contrast, the linear meshes fully modelled with CZM shown in Section 7.2.4 resulted in an average time of 5.7 s per increment, substantially higher than the 2.8 s registered in the convergence study. This discrepancy can be primarily attributed to the mesh size and the configuration chosen: the higher times correspond to the quadratic TRI6 discretisation (*mesh2 - TRI6*), while the lower values refer to linear elements (*mesh2 - QUAD4-FBAR*). In addition, note that the insertion of cohesive elements between every matrix-matrix interface adds significantly to the number of elements, nodes and degrees of freedom of the finite element problem. This leads to a much larger global stiffness matrix, which is more computationally expensive to compute. In contrast, the phase-field approach to bulk fracture preserves the original mesh but introduces an additional scalar field and leads to a coupled problem. When a staggered solution scheme is employed (as in this work), the multi-physics problem is partitioned into two smaller blocks (mechanical and phase-field), reducing the complexity and size of the problem.

Table 7.8 compares the two main models used throughout this Section: *PF* + *intCZM*, and *allCZM* + *intCZM*. The *PF* + *intCZM* approach is, in general, preferable, since it combines robustness to numerical issues with a physically consistent damage evolution, and is faster per increment than a fully cohesive discretisation. The diffuse phase-field naturally captures the complex bulk crack nucleation and propagation. The *allCZM* + *intCZM* approach may also be advantageous when mesh refinement is difficult to achieve, or in situations with well per-defined failure models were crack paths can be reasonably anticipated. In all cases, a rigorous calibration of the material parameters, while ensuring compatible values for the material strengths and fracture energies is required.

Table 7.8: Summary of the comparison between the hybrid configuration (*PF + intCZM*) and the fully cohesive zone modelling approach (*allCZM + intCZM*) for composite RVE analysis.

| | **PF + intCZM model** | **allCZM + intCZM model** |
|---|---|---|
| **Configuration** | Hybrid approach combining continuous phase-field for matrix with discrete cohesive interfaces | Fully cohesive zone approach with discrete traction-separation laws for all potential crack surfaces |
| **Damage criterion** | Damage is computed from principal stresses | Damage is determined locally based on local tractions and the predefined TSL |
| **Failure mechanism** | Matrix cracks follow energetically favourable paths; interface debonding predefined at boundaries | Predefined crack surfaces constrain natural crack coalescence |
| **Crack topology** | Spatially coherent and continuous damage bands | Irregular and tortuous crack patterns |
| **Parameter sensitivity** | Moderate sensitivity to length-scale parameter; additional sensitivity to interface cohesive parameters | High sensitivity to penalty parameters, strength ratios, and fracture energies |
| **Computational cost** | Faster approach, but requires fine mesh to resolve regularization | Higher cost per increment due to increased number of elements, nodes and DOFs from cohesive elements |

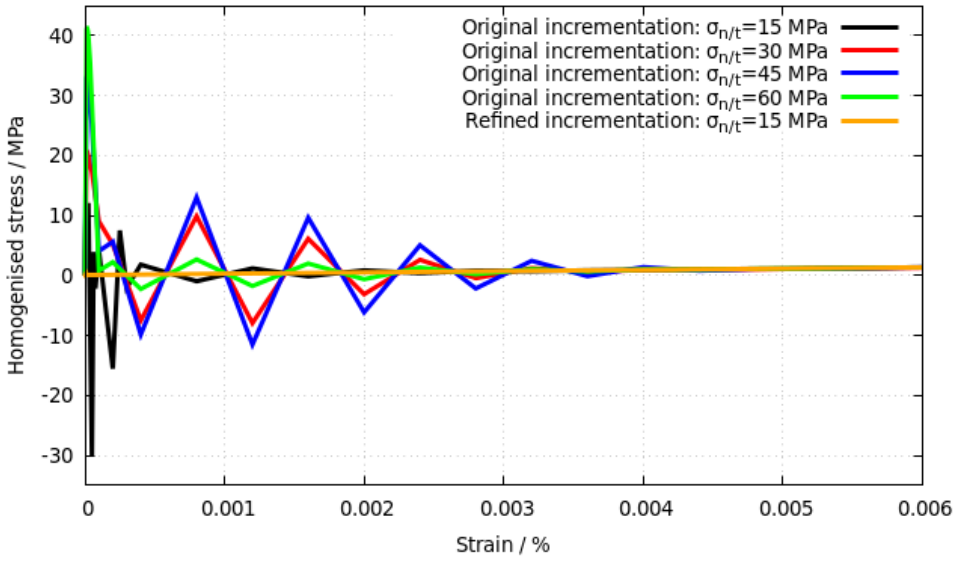


Figure 7.24: Detail of the homogenised stress-strain curves, showing early-increment oscillations for the linear *allCZM + intCZM* RVE model.

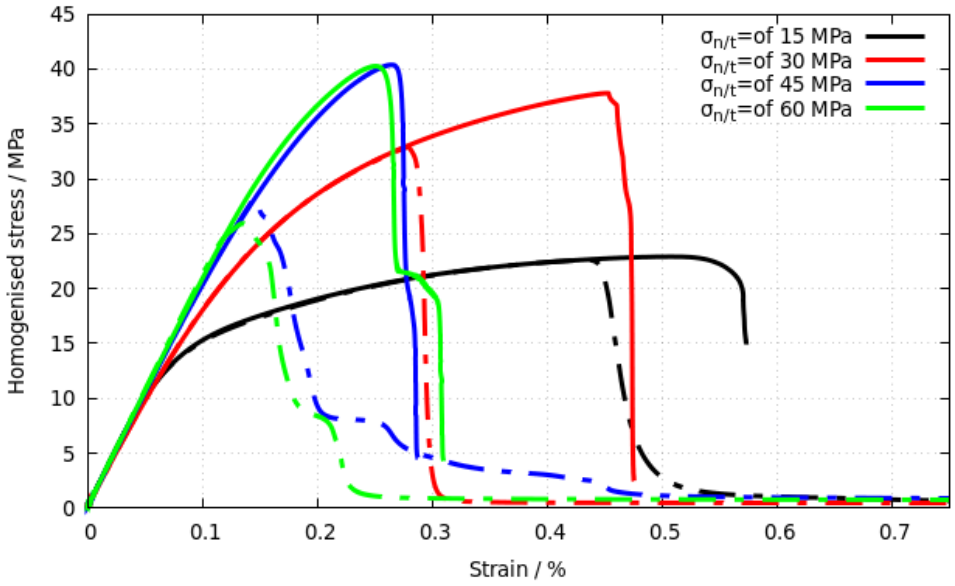


Figure 7.25: Homogenised stress-strain curves, for different values of the cohesive strength of the interface cohesive elements, for the linear *allCZM* + *intCZM* RVE model (full lines), in comparison with the *intCZM* models (dashed lines).

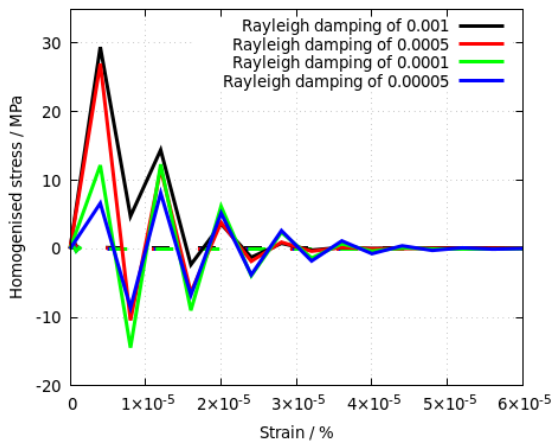


(a) Rayleigh damping variation, for $\rho_\infty = 0.7$

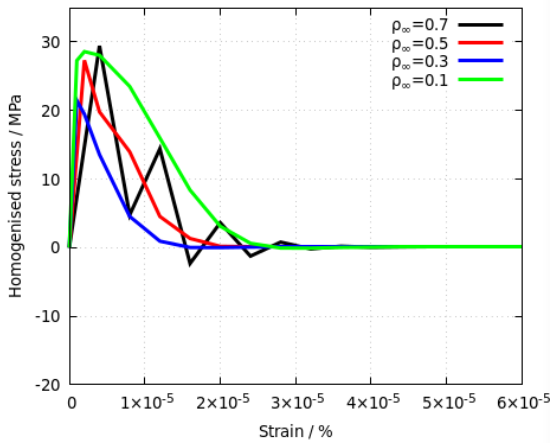


(b) Spectral radius variation, for a Rayleigh damping of 0.001

Figure 7.26: Detail of homogenised stress-strain curves, for the parametric study of the dynamic parameters of the linear *allCZM* + *intCZM* RVE model with a cohesive interface strength of 30 MPa: Rayleigh damping (7.26a) and spectral radius, $\rho_\infty$ (7.26b). Full lines correspond to an incrementation of $15 \cdot 10^{-5}$ and dashed lines to an incrementation of $30 \cdot 10^{-6} + 12 \cdot 10^{-5}$.

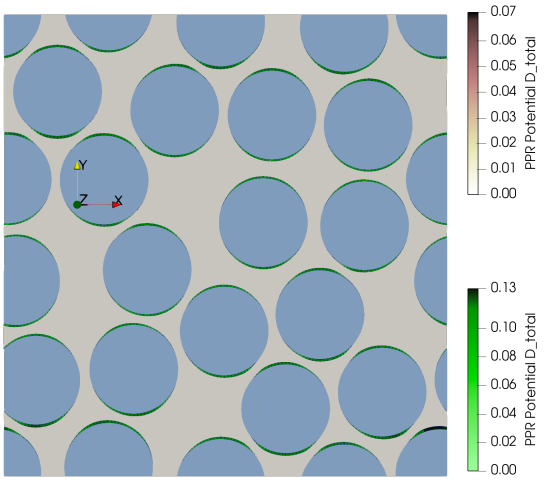


(a) $\sigma_{n/t}$ = 15 MPa at a load factor of 0.99 (or a prescribed displacement of 0.396 %).

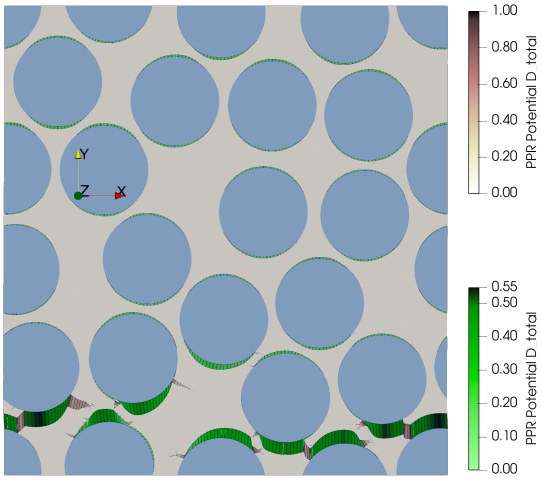


(b) $\sigma_{n/t}$ = 15 MPa at a load factor of 1.432 (or a prescribed displacement of 0.573 %).

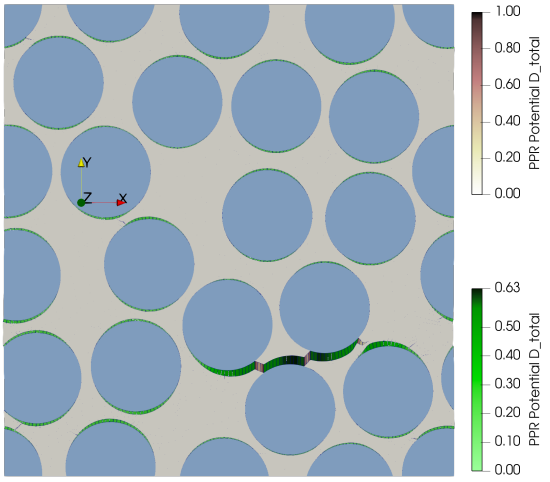


(c) $\sigma_{n/t}$ = 30 MPa at a load factor of 1.158 (or a prescribed displacement of 0.463 %).

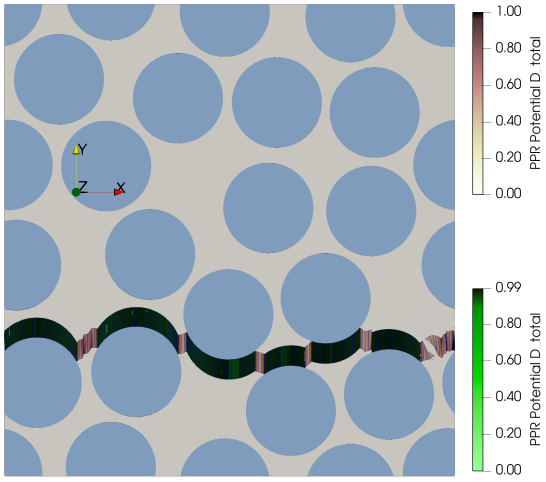


(d) $\sigma_{n/t}$ = 30 MPa at a load factor of 1.189 (or a prescribed displacement of 0.475 %).

Figure 7.27: Cohesive damage distribution in the fibre-matrix (green colouring) and matrix-matrix (red colouring) element interfaces, plotted in the deformed configuration at the peak response and at the end of the simulation (scale factor of 10), for an *allCZM* + *intCZM* RVE model with TRI6 continuum elements, employing two distinct values of the PPR cohesive strength ($\sigma_{n/t}$): 15 and 30 MPa.

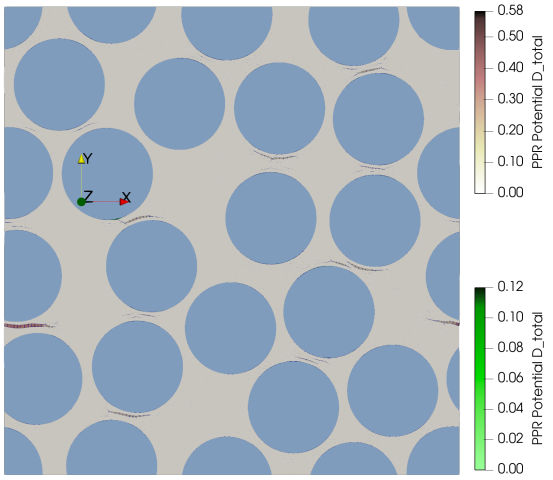


(a) $\sigma_{n/t}$ = 45 MPa at a load factor of 0.67 (or a prescribed displacement of 0.388 %).

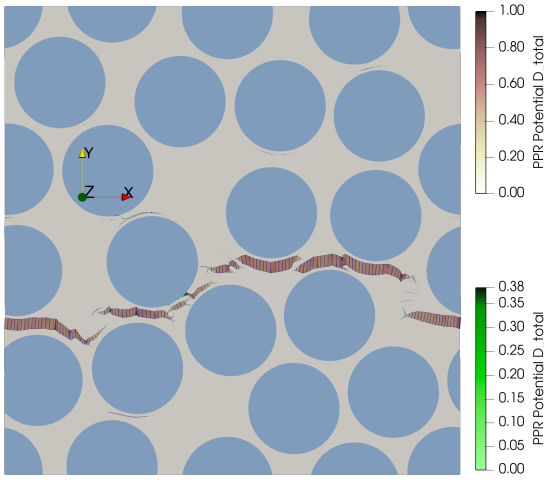


(b) $\sigma_{n/t}$ = 45 MPa at a load factor of 0.715 (or a prescribed displacement of 0.286 %).

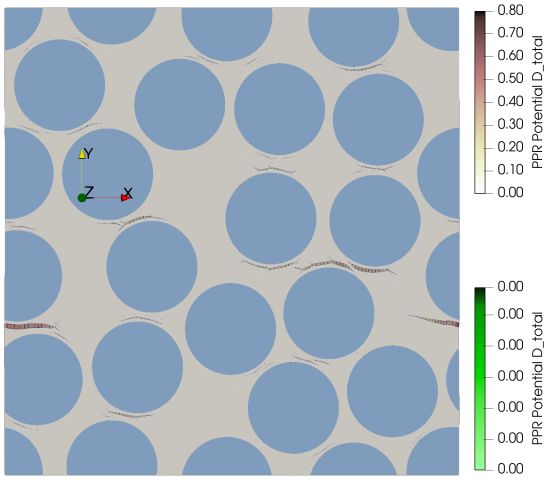


(c) $\sigma_{n/t}$ = 60 MPa at a load factor of 0.658 (or a prescribed displacement of 0.263 %).

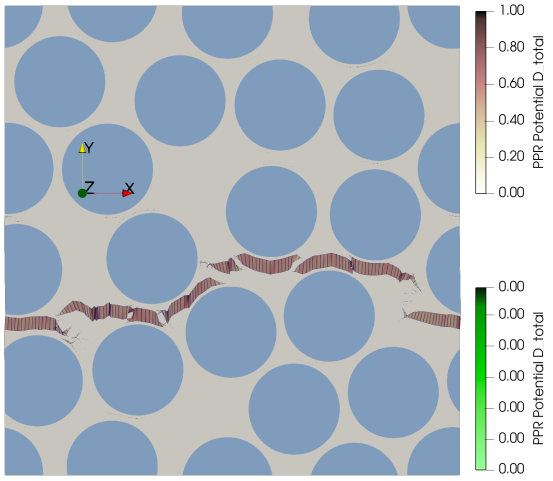


(d) $\sigma_{n/t}$ = 60 MPa at a load factor of 0.775 (or a prescribed displacement of 0.31 %).

Figure 7.28: Cohesive damage distribution in the fibre-matrix (green colouring) and matrix-matrix (red colouring) interfaces, plotted in the deformed configuration at the peak response and at the end of the simulation (scale factor of 10), for an *PF + intCZM* RVE model with TRI6 continuum elements, employing two distinct values of the PPR cohesive strength, $\sigma_{n/t}$, 45 and 60 MPa.

# Chapter 8

# Conclusions

The work developed during this Master's Dissertation focuses on the interplay between two distinct failure mechanisms, cohesive zone models and phase-field fracture, in the context of composite microstructures. The theoretical basis and finite element implementation of each damage model is presented and thoroughly used through benchmark tests to asses the influence of specific numerical schemes and fracture material parameters. Chapter 2 reviews first-order continuum mechanics and the formulation of the finite element method. Chapter 3 introduces the Park-Paulino-Roesler cohesive zone model and its finite element implementation, while Chapter 4 addresses the phase-field formulations within their variational framework.

The implementation and improvement of a Python preprocessing routine to pre-insert cohesive elements between material interfaces is tackled in Chapter 5, as well as the enforcement of the required boundary conditions to ensure the microstructures simulated represent the entire macro-scale model. This numerical tool is a significant contribution, with the current implementation capable of greatly reducing the preprocessing time compared with the legacy version. Added robustness with respect to two-dimensional mixed meshes is also of interest, with the capability to automate the insertion of cohesive elements along fibre-matrix interfaces particularly useful for micro-scale simulates of representative FRPs

Preliminary studies on macro-scale meshed models are detailed in Chapter 6. These benchmark examples allow for predictions of the global strength. The parametric variations of the eight cohesive properties in the PPR model demonstrate the flexibility of the potential-based CZM to capture mode I, II and mixed-mode and mixed fracture. Careful calibration of CZM parameters is crucial to ensure numerical stability and physically realistic predictions of the global system response. The initial slope parameter, in particular, must be fine-tuned to control the elastic behaviour and reduce the artificial compliance from the inserted cohesive elements. In addition, adjusting the shape parameters can recover cohesive laws to specific material and loading conditions

The benchmark simulations with a phase-field formulation frequently experience premature solver termination and, in the case of the perforated cantilever plate, fail to reach full separation. Similar numerical issues are encountered by the fully CZM modelling approach, due the presence of multiple energetically equivalent crack paths. For the phase-field models, a length-scale parameter of 0.1 allowed the solver to select a crack path, although not the expected path, and proceed until eventual failure. These observations underline the interplay between the regularisation length-scale, the mesh resolution and the solver robustness.

Chapter 7 conducts a thorough analysis and comparison of the distinct failure mechanism in the mechanical behaviour of composites. A mesh sensitivity study is initially conducted, with the more refined quadratic model achieving the best balance between accuracy and computational time. With regards to the failure of heterogeneous microstructures, both damage models, phase-field and cohesive zone model, are then combined for the same RVE mesh (PF-only approach, hybrid approach with PF and CZM in hte interfaces, and a fully CZM modelling approach), varying

the fracture properties to assess the overall response. All these configurations produce promising results, demonstrating the capabilities of each approach model to simulate distinct failure mechanisms. The phase-field only approach reliably captures complex bulk crack topologies, but fails to represent interface debonding and, as result, generally predicts higher apparent strengths. On the other hand, the explicit modelling of matrix damage via cohesive elements reproduces a detailed discrete description of interface behaviour, but is more time-consuming, while also encountering more numerical difficulties and exhibiting greater sensitivity to the initial slope parameter. The hybrid approach combines both modelling approaches, with PF handling bulk fracture accurately while cohesive elements capture fibre-matrix debonding. Calibrating appropriately the strengths and fracture energies of each damage model allows control over whether failure is matrix- or interface-dominated and generally offers improved numerical robustness and reduced parameter sensitivity. In summary, the PF + CZM hybrid approach is here recommended for most practical RVE applications due to its modelling flexibility and physical consistency.

## 8.1 Future works

Keeping in mind the work developed during this Master's Dissertation, possible avenues for future improvements and achievements are listed hereafter.

Firstly, a considerable priority is to extend and refine the Python preprocessing routine. This tool should support selective pre-insertion of cohesive elements (e.g., matrix-matrix only, or matrix-matrix and fibre-matrix interfaces, while excluding fibre-fibre interfaces) rather than an automatic insertion across the entire domain. Full support for three-dimensional finite element meshes and mixed 2D/3D meshes needs to be implemented and validated. Performance optimisation of the Python data structures employed must be equally carried out to ensure efficient preprocessing of large meshes.

Secondly, a more through parametric study of the fracture models is recommended. Future simulations should systematically map the parameter space (FP length-scale parameter, interface strength and fracture energy/toughness). This will provide a more detailed description of the transition between matrix- and interface-dominated failure.

Thirdly, an extension to fibre-reinforced thermoplastics is suggested, provided that the ductile, temperature- and rate-dependent behaviour of these materials is accounted for. These models must additionally be validated against manufacturing specific defects and calibrated with dedicated micromechanical experiments.

Finally, leveraging data-driven methods with well-structured databases of high-fidelity microstructural simulations can offer clear advantageous, such as the reduction of the testing campaign time and the associated material waste. Through training on large and diverse databases, machine and deep learning algorithms can provide relatively fast predictions of global responses (apparent strength, stiffness, critical energy release) and dominant failure modes.

# Appendix A

# Energy decompositions for the phase-field models

Phase-field crack/damage growth is driven by the amount of strain energy stored in the solid, characterised by the undamaged elastic strain energy density $\psi_0$. To prevent crack growth under compression, the driving force for fracture, i.e., the undamaged elastic strain energy, can be decomposed in an active (positive or degradable) component due to tension ($\psi_0^+$ or $\psi_0^D$) and an inactive (negative or residual) component due to compression ($\psi_0^-$ or $\psi_0^R$) (Miehe et al. (2010)). For a generalised anisotropic formulation, the elastic strain energy density is given as

$$\psi(\boldsymbol{\varepsilon}(\boldsymbol{u}), g(\phi)) = \psi^+(\boldsymbol{\varepsilon}(\boldsymbol{u}), \phi) + \psi_0^-(\boldsymbol{\varepsilon}(\boldsymbol{u})) = g(\phi)\psi_0^+(\boldsymbol{\varepsilon}(\boldsymbol{u})) + \psi_0^-(\boldsymbol{\varepsilon}(\boldsymbol{u})). \tag{A.1}$$

As a result, the stress field, formulated in Equation (4.37), can be rewritten as

$$\boldsymbol{\sigma}^* = \frac{\partial \psi}{\partial \boldsymbol{\varepsilon}} = g(\phi)\boldsymbol{\sigma}^+ + \boldsymbol{\sigma}^-, \quad \boldsymbol{\sigma}^\pm = \frac{\partial \psi_0^\pm}{\partial \boldsymbol{\varepsilon}}, \tag{A.2}$$

and the corresponding evolution law of the crack phase-field is written as

$$G_c \delta_\phi \gamma = -g'(\phi)\psi_0^+. \tag{A.3}$$

For an isotropic elastic undamaged material, the Lamé constants and the bulk modulus $\kappa$ are given as a function of the Young's modulus $E$, the Poisson's ratio $\nu$ and the number of space dimensions $n$ (e.g., 3), such that

$$\lambda = \frac{E\nu}{(1+\nu)[1-(n-1)\nu]}, \tag{A.4}$$

$$\mu = \frac{E}{2(1+\nu)}, \tag{A.5}$$

$$\kappa = \lambda + \frac{2\mu}{n} = \frac{E}{n[1-(n-1)\nu]}. \tag{A.6}$$

Several strain energy splits exist, in particular, the volumetric-deviatoric split and the spectral decomposition exclusive for the AT1 and AT2 models.

## A.1 Standard formulation

As proposed originally for the AT2 model, the standard or isotropic formulation for the fracture driving force is given as

$$\psi_0^+(\boldsymbol{\varepsilon}) = \frac{1}{2}\boldsymbol{\varepsilon} : \mathbf{E}_0 : \boldsymbol{\varepsilon} = \frac{1}{2}\lambda \,\mathrm{tr}^2(\boldsymbol{\varepsilon}) + \mu \,\mathrm{tr}(\boldsymbol{\varepsilon}^2), \quad \psi_0^-(\boldsymbol{\varepsilon}) = 0, \tag{A.7}$$

where $\mathbf{E}_0$ is the undamaged elastic stiffness forth-order tensor, $\lambda$ and $\mu$ are the Lamé parameters. Note that the active component recovers the behaviour for the initial Helmholtz free energy potential $\psi_0$ for an isotropic elastic solid.

The isotropic phase-field damage model is as follows

$$\boldsymbol{\sigma}^* = \frac{\partial \psi}{\partial \boldsymbol{\varepsilon}} = g(\phi)\boldsymbol{\sigma}, \quad \boldsymbol{\sigma} = \frac{\partial \psi_0}{\partial \boldsymbol{\varepsilon}} = \mathbf{E}_0 : \boldsymbol{\varepsilon}, \tag{A.8}$$

$$Y = -\frac{\partial \psi}{\partial \phi} = -g'(\phi)\bar{Y}, \quad \bar{Y} = \frac{\partial \psi}{\partial g} = \frac{1}{2}\boldsymbol{\sigma} : \mathbf{C}_0 : \boldsymbol{\varepsilon}, \tag{A.9}$$

where $\boldsymbol{\sigma}$ is the effective stress tensor.

The history-dependent variable is given as

$$\mathscr{H} = \max_{t\in[0,\tau]} \psi_0(\boldsymbol{\varepsilon}). \tag{A.10}$$

## A.2 Volumetric-deviatoric energy split

The model was first proposed by Amor et al. (2009) to avoid crack interpenetration during unilateral contact under compression. The decomposition of the elastic strain energy density into deviatoric and volumetric parts is such that

$$\psi_0^+(\boldsymbol{\varepsilon}) = \frac{1}{2}\kappa\langle \mathrm{tr}(\boldsymbol{\varepsilon})\rangle_+^2 + \mu|\boldsymbol{\varepsilon}_{\mathrm{dev}}|^2, \tag{A.11}$$

$$\psi_0^-(\boldsymbol{\varepsilon}) = \frac{1}{2}\kappa\langle \mathrm{tr}(\boldsymbol{\varepsilon})\rangle_-^2. \tag{A.12}$$

with

$$|\boldsymbol{\varepsilon}_{\mathrm{dev}}|^2 = \boldsymbol{\varepsilon}_{\mathrm{dev}} : \boldsymbol{\varepsilon}_{\mathrm{dev}}, \tag{A.13}$$

and $\boldsymbol{\varepsilon}_{\mathrm{dev}}$ is defined as

$$\boldsymbol{\varepsilon}_{\mathrm{dev}} = \boldsymbol{\varepsilon} - \frac{\mathrm{tr}(\boldsymbol{\varepsilon})\boldsymbol{I}}{3}. \tag{A.14}$$

The damaged stress tensor can be obtained as

$$\boldsymbol{\sigma}^* = g(\phi)\left[\kappa\langle \mathrm{tr}(\boldsymbol{\varepsilon})\rangle_+ \boldsymbol{I} + 2\mu\boldsymbol{\varepsilon}_{\mathrm{dev}}\right] - \kappa\langle \mathrm{tr}(\boldsymbol{\varepsilon})\rangle_- \boldsymbol{I}, \tag{A.15}$$

with the residual stresses are given as

$$\boldsymbol{\sigma}_{\mathrm{R}}(\boldsymbol{\varepsilon}) = \kappa\langle \mathrm{tr}(\boldsymbol{\varepsilon})\rangle_- \boldsymbol{I}. \tag{A.16}$$

This energy split introduces the necessary asymmetry in traction and compression, without adding residual stresses for $\mathrm{tr}(\boldsymbol{\varepsilon}) > 0$. A drawback is its inability to independently define separate shear strengths for two loading scenarios (Vicentini et al. (2024)). The volumetric-deviatoric is only valid in the context of the AT1 and AT2 models.

## A.3 Spectral energy split

Formulated by Miehe et al. (2010), the spectral decomposition is an alternative to the volumetric-deviatoric split, which employs the concept of eigenvalues and eigenvectors of the strain tensor, such that

$$\psi_0^+(\boldsymbol{\varepsilon}) = \frac{1}{2}\lambda\langle \mathrm{tr}(\boldsymbol{\varepsilon})\rangle_+^2 + \mu\boldsymbol{\varepsilon}^+ \cdot \boldsymbol{\varepsilon}^+ \tag{A.17}$$

$$\psi_0^+(\boldsymbol{\varepsilon}) = \frac{1}{2}\lambda\langle \mathrm{tr}(\boldsymbol{\varepsilon})\rangle_-^2 + \mu\boldsymbol{\varepsilon}^- \cdot \boldsymbol{\varepsilon}^-, \tag{A.18}$$

with the spectral decomposition of the positive and negative parts of the strain tensor given as

$$\boldsymbol{\varepsilon}^{+} = \sum_{i=1}^{n} \langle \varepsilon_i \rangle_{+} \boldsymbol{e}_i \otimes \boldsymbol{e}_i \tag{A.19}$$

$$\boldsymbol{\varepsilon}^{-} = \sum_{i=1}^{n} \langle \varepsilon_i \rangle_{-} \boldsymbol{e}_i \otimes \boldsymbol{e}_i \tag{A.20}$$

where $\varepsilon_i$ is the strain principal strain, and $\boldsymbol{e}_i$ is the corresponding principal strain direction ($I = 1,2,3$).

The residual stress tensor is given:

$$\boldsymbol{\sigma}_{\mathrm{R}}(\boldsymbol{\varepsilon}) = \lambda \langle \mathrm{tr}(\boldsymbol{\varepsilon}) \rangle_{-} \boldsymbol{I} + 2\mu \boldsymbol{\varepsilon}^{-} \tag{A.21}$$

Note that for a positive crack opening ($\mathrm{tr}(\boldsymbol{\varepsilon})$) there might be non-zero residual stresses. The spectral decomposition of the strain tensor allows crack closing, in reverse loading conditions (Miehe et al. (2010)).

# Appendix B

# Exponential softening curves for the damage models

This Appendix briefly summarises the exponential softening law used in the numerical applications. A comparison is made between the PPR potential-based cohesive zone model, and in the phase field - cohesive zone model (PF-CZM), where the shape parameters of each model are related to replicate the same softening behaviour across both models.

According to Wu (2024), an exponential softening curve is generally described as

$$t(\Delta) = \sigma \exp\left(-\frac{\sigma}{\phi}\Delta\right), \tag{B.1}$$

with $\Delta$ being the crack opening, $\sigma$ the maximum strength, and $\phi$ the fracture energy for the respective fracture mode.

The corresponding initial slope, $k_0$ is given as

$$k_0 = -\frac{\sigma^2}{\phi}, \tag{B.2}$$

and the final crack opening is assumed as infinite: $\delta \to \infty$.

## B.1 PPR potential approximation

For mode I fracture, the extrinsic PPR potential can be simplified as (Muñetón-López and Giraldo-Londoño (2024))

$$\psi(\Delta_n) = \phi_n\left(1 - \left(1 - \frac{\Delta_n}{\delta_n}\right)^{\alpha}\right), \quad \Delta_n \in [0, \delta_n], \tag{B.3}$$

with the corresponding traction-separation law given as

$$t_n(\Delta_n) = \frac{\partial \Psi}{\partial \Delta_n} = \sigma_n\left(1 - \frac{\sigma_n}{\alpha\phi_n}\right)^{\alpha-1}. \tag{B.4}$$

From the above equation, it is clear that setting the shape parameter as $\alpha = 2$ yields a linear softening response, while for values greater or lower than 2 the softening branch becomes convex or concave, respectively. To replicate the exponential softening response found for the phase-field cohesive zone model (PF-CZM) model, it is necessary to select a value for the shape parameter, $\alpha$, that best approximates the response in Equation B.4 to Equation B.1.

Muñetón-López and Giraldo-Londoño (2024) arrived at a value of 15, after performing a polynomial fit between the shape parameters of the phase-field model ($d$, $b$, and $a_3$) to the normal shape parameter of the PPR potential model ($\alpha$). The values for the phase-field shape parameters that best

resemble an exponential softening response have been previously studied in literature (Wu (2017, 2024)), such that: $d = 2.5$ and $b = 2^{5/3} - 3$. Assuming these values, the result obtained here for $\alpha$ is 14.216, very close to the one from the article (Muñetón-López and Giraldo-Londoño (2024)). This value is independent of the material properties chosen ($\phi_n$, $\sigma_n$, $\lambda_n$).

# Appendix C

# Rayleigh damping

For the Rayleigh proportional damping model, the global damping matrix,

$$\mathbf{C} \equiv c_{\mathrm{M}}\mathbf{M} + c_{\mathrm{K}}\mathbf{K}_0, \tag{C.1}$$

is a linear combination of the mass matrix $\mathbf{M}$ and the initial tangent stiffness matrix $\mathbf{K}_0$. Thus, it is controlled via mass and stiffness coefficients respectively defined as $c_M \ \left[s^{-1}\right]$ and $c_K \ [s]$. For further details on the impact of these parameters, the reader is directed to Vieira de Carvalho (2023).

For a each $r$ mode of vibration, the Rayleigh damping ratio is given as

$$\xi_r = \frac{c_{\mathrm{M}}}{2\omega_r} + \frac{c_{\mathrm{M}}\omega_r}{2}, \tag{C.2}$$

where the first term provides hyperbolic damping for small frequencies, and the second term provides proportional damping for high frequencies.

# Bibliography


Sunday C. Aduloju and Timothy J. Truster. On topology-based cohesive interface element insertion along periodic boundary surfaces. *Engineering Fracture Mechanics*, 205: 10 – 13, 2019. ISSN 00137944. doi: 10.1016/j.engfracmech.2018.10.037. URL https://www.scopus.com/inward/record.uri?eid=2-s2.0-85056244903&doi=10.1016%2fj.engfracmech.2018.10.037&partnerID=40&md5=768f6b17bba63a74c5e038edb7ec496a. Cited by: 5.

Hanen Amor, Jean-Jacques Marigo, and Corrado Maurini. Regularized formulation of the variational brittle fracture with unilateral contact: Numerical experiments. *Journal of The Mechanics and Physics of Solids*, 57:1209–1229, 2009. URL https://api.semanticscholar.org/CorpusID:51695868.

G. I. Barenblatt. The formation of equilibrium cracks during brittle fracture. generzal ideas and hypotheses. axially-symmetric cracks. *Journal of Applied Mathematics and Mechanics*, 23:622–636, 1959. URL https://api.semanticscholar.org/CorpusID:119998777.

G.I. Barenblatt. The mathematical theory of equilibrium cracks in brittle fracture. volume 7 of *Advances in Applied Mechanics*, pages 55–129. Elsevier, 1962. doi: 10.1016/S0065-2156(08)70121-2. URL https://www.sciencedirect.com/science/article/pii/S0065215608701212.

Pei-Liang Bian, Hai Qing, Siegfried Schmauder, and Tiantang Yu. A unified phase-field method-based framework for modeling quasi-brittle fracture in composites with interfacial debonding. *Composite Structures*, 327:117647, 2024. ISSN 0263-8223. doi: 10.1016/j.compstruct.2023.117647. URL https://www.sciencedirect.com/science/article/pii/S0263822323009935.

Javier Bonet and Richard D. Wood. *Nonlinear Continuum Mechanics for Finite Element Analysis*. Cambridge University Press, 2 edition, 2008. ISBN 978-0-521-83870-2 978-0-511-75544-6. doi: 10.1017/CBO9780511755446.

Michael J. Borden, Clemens V. Verhoosel, Michael A. Scott, Thomas J.R. Hughes, and Chad M. Landis. A phase-field description of dynamic brittle fracture. *Computer Methods in Applied Mechanics and Engineering*, 217-220:77–95, 2012. ISSN 0045-7825. doi: 10.1016/j.cma.2012.01.008. URL https://www.sciencedirect.com/science/article/pii/S0045782512000199.

B. Bourdin, G.A. Francfort, and J-J. Marigo. Numerical experiments in revisited brittle fracture. *Journal of the Mechanics and Physics of Solids*, 48(4):797–826, 2000. ISSN 0022-5096. doi: 10.1016/S0022-5096(99)00028-9. URL https://www.sciencedirect.com/science/article/pii/S0022509699000289.

Blaise Bourdin, Jean-Jacques Marigo, Corrado Maurini, and Paul Sicsic. Morphogenesis and propagation of complex cracks induced by thermal shocks. *Phys. Rev. Lett.*, 112:014301, Jan 2014. doi: 10.1103/PhysRevLett.112.014301. URL https://link.aps.org/doi/10.1103/PhysRevLett.112.014301.

Andrea Braides. *Gamma-Convergence for Beginners*. Oxford University Press, 07 2002. ISBN 9780198507840. doi: 10.1093/acprof:oso/9780198507840.001.0001. URL https://doi.org/10.1093/acprof:oso/9780198507840.001.0001.

G.T. Camacho and M. Ortiz. Computational modelling of impact damage in brittle materials. *International Journal of Solids and Structures*, 33(20):2899–2938, 1996. ISSN 0020-7683. doi: 10.1016/0020-7683(95)00255-3. URL https://www.sciencedirect.com/science/article/pii/0020768395002553.

Pedro Ponce Camanho, Carlos Dávila, and Marcelo De Moura. Numerical simulation of mixed-mode progressive delamination in composite materials. *Journal of Composite Materials*, 37(16): 1415–14380, 08 2003. doi: 10.1177/0021998303034505.

António Manuel Couto Carneiro. *Modeling and Analysis of Rough Contact by Computational Homogenization*. PhD thesis, Faculdade de Engenharia da Universidade do Porto, 12 2021. URL https://hdl.handle.net/10216/122021.

Bernard D. Coleman and Morton E. Gurtin. Thermodynamics with internal state variables. *The Journal of Chemical Physics*, 47(2):597–613, 07 1967. ISSN 0021-9606. doi: 10.1063/1.1711937. URL https://doi.org/10.1063/1.1711937.

José Henrique Comprido Nascimento, Igor André Rodrigues Lopes, and F.M. Andrade Pires. Multiscale modeling of advanced discontinuous fiber-reinforced composites. Master's thesis, Faculdade de Engenharia da Universidade do Porto, 07 2023. URL https://hdl.handle.net/10216/151931.

Alexandre D. Costa Amaro, A. Francisca Carvalho Alves, and F.M. Andrade Pires. Multi-scale modelling and analysis of the behaviour of pc/abs blends with emphasis on interfacial/bulk damage. Master's thesis, Faculdade de Engenharia da Universidade do Porto, 07 2023. URL https://hdl.handle.net/10216/151464.

M. A. Crisfield and G. Alfano. Finite element interface models for the delamination analysis of laminated composites: Mechanical and computational issues. *International Journal for Numerical Methods in Engineering*, 50(7):1701–1736, 2001. doi: 10.1002/nme.93. URL https://onlinelibrary.wiley.com/doi/abs/10.1002/nme.93.

Weicheng Cui and M.R. Wisnom. A combined stress-based and fracture-mechanics-based model for predicting delamination in composites. *Composites*, 24(6):467–474, 1993. ISSN 0010-4361. doi: 10.1016/0010-4361(93)90016-2. URL https://www.sciencedirect.com/science/article/pii/0010436193900162.

E.A. de Souza Neto, D. Perić, M. Dutko, and D.R.J. Owen. Design of simple low order finite elements for large strain analysis of nearly incompressible solids. *International Journal of Solids and Structures*, 33(20):3277–3296, 1996. ISSN 0020-7683. doi: https://doi.org/10.1016/0020-7683(95)00259-6. URL https://www.sciencedirect.com/science/article/pii/0020768395002596.

E.A. de Souza Neto, D. Peric, and D.R.J. Owen. *Computational Methods for Plasticity: Theory and Applications*. Wiley, 2008.

Guido Dhondt and Klaus Wittig. Calculix: a free software three-dimensional structural finite element program. Available from: http://www.calculix.de, 1998. Accessed on 2025-09-02.

Wanderson F. dos Santos, Igor A. Rodrigues Lopes, Francisco M. Andrade Pires, and Sergio P.B. Proença. Exploring novel mechanical metamaterials: Unravelling deformation mode coupling

and size effects through second-order computational homogenisation. *International Journal of Solids and Structures*, 292, 2024. ISSN 00207683. doi: 10.1016/j.ijsolstr.2024.112724. URL https://www.scopus.com/inward/record.uri?eid=2-s2.0-85186585269&doi=10.1016%2fj.ijsolstr.2024.112724&partnerID=40&md5=0a999b259b41b427a394bf065477502b. Cited by: 11; All Open Access, Hybrid Gold Open Access.

D.S. Dugdale. Yielding of steel sheets containing slits. *Journal of the Mechanics and Physics of Solids*, 8(2):100–104, 1960. ISSN 0022-5096. doi: 10.1016/0022-5096(60)90013-2. URL https://www.sciencedirect.com/science/article/pii/0022509660900132.

Ahmed Elmasry, Wiyao Azoti, Sherif A. El-Safty, and Ahmed Elmarakbi. A comparative review of multiscale models for effective properties of nano- and micro-composites. *Progress in Materials Science*, 132, 2023. ISSN 00796425. doi: 10.1016/j.pmatsci.2022.101022. URL https://www.scopus.com/inward/record.uri?eid=2-s2.0-85139852077&doi=10.1016%2fj.pmatsci.2022.101022&partnerID=40&md5=8e7bc1df4af868a47f3b606d3550a82f. Cited by: 48.

G.A. Francfort and J.-J. Marigo. Revisiting brittle fracture as an energy minimization problem. *Journal of the Mechanics and Physics of Solids*, 46(8):1319–1342, 1998. ISSN 0022-5096. doi: 10.1016/S0022-5096(98)00034-9. URL https://www.sciencedirect.com/science/article/pii/S0022509698000349.

Michel Frémond and Boumediene Nedjar. Damage, gradient of damage and principle of virtual power. *International Journal of Solids and Structures*, 33(8):1083–1103, 1996. ISSN 0020-7683. doi: 10.1016/0020-7683(95)00074-7. URL https://www.sciencedirect.com/science/article/pii/0020768395000747.

Huajian Gao and Patrick Klein. Numerical simulation of crack growth in an isotropic solid with randomized internal cohesive bonds. *Journal of the Mechanics and Physics of Solids*, 46(2):187–218, 1998. ISSN 0022-5096. doi: 10.1016/S0022-5096(97)00047-1. URL https://www.sciencedirect.com/science/article/pii/S0022509697000471.

Christophe Geuzaine and Jean-François Remacle. Gmsh: A 3-d finite element mesh generator with built-in pre- and post-processing facilities. *International Journal for Numerical Methods in Engineering*, 79(11):1309–1331, 2009. doi: 10.1002/nme.2579. URL https://onlinelibrary.wiley.com/doi/abs/10.1002/nme.2579.

I.M. Gitman, H. Askes, and L.J. Sluys. Representative volume: Existence and size determination. *Engineering Fracture Mechanics*, 74(16):2518–2534, 2007.

Guilherme Fonseca Gonçalves. Predicting the failure of structures with second-order homogenisation and nonlocal damage models. Master's thesis, Faculdade de Engenharia da Universidade do Porto, 07 2024.

S. Goutianos, B.F. Sørensen, and M.D. Thouless. Mixed-mode cohesive laws and the use of linear-elastic fracture mechanics. *Engineering Fracture Mechanics*, 252:107792, 2021. ISSN 0013-7944. doi: 10.1016/j.engfracmech.2021.107792. URL https://www.sciencedirect.com/science/article/pii/S0013794421002356.

Alan Arnold Griffith. The phenomena of rupture and flow in solids. *Philosophical Transations of the Royal Society of London*, 221:163–198, 1921. doi: 10.1098/rsta.1921.0006.

L. Hamitouche, M. Tarfaoui, and A. Vautrin. An interface debonding law subject to viscous regularization for avoiding instability: Application to the delamination problems. *Engineering Fracture Mechanics*, 75(10):3084 – 3100, 2008. ISSN 00137944. doi:

10.1016/j.engfracmech.2007.12.014. URL https://www.scopus.com/inward/record.uri?eid=2-s2.0-40949106800&doi=10.1016%2fj.engfracmech.2007.12.014&partnerID=40&md5=a3db67371bcc05cc64ab28ce0332b56b. Cited by: 60.

R. Hill. A self-consistent mechanics of composite materials. *Journal of the Mechanics and Physics of Solids*, 4:213–222, 1965.

Andrea Infuso, Mauro Corrado, and Marco Paggi. Image analysis of polycrystalline solar cells and modelling of intergranular and transgranular cracking. *Journal of the European Ceramic Society*, 34(11):2713 – 2722, 2014. ISSN 09552219. doi: 10.1016/j.jeurceramsoc.2013.12.051. URL https://www.scopus.com/inward/record.uri?eid=2-s2.0-84901273774&doi=10.1016%2fj.jeurceramsoc.2013.12.051&partnerID=40&md5=4500a54c3a4b6f4717118fb8bc679f87. Cited by: 35; All Open Access, Green Open Access.

L. M. Kachanov. Time of the rupture process under creep conditions, izy akad. *Nank S. S. R. Otd Tech Nauk*, 8:26–31, 1958. URL https://cir.nii.ac.jp/crid/1572543025657048960.

Philip K. Kristensen, Christian F. Niordson, and Emilio Martínez-Pañeda. An assessment of phase field fracture: crack initiation and growth. *Philosophical Transactions of The Royal Society A Mathematical Physical and Engineering Sciences*, 379:20210021, 06 2021. doi: 10.1098/rsta.2021.0021.

Charlotte Kuhn, Alexander Schlüter, and Ralf Müller. On degradation functions in phase field fracture models. *Computational Materials Science*, 108:374–384, 2015. ISSN 0927-0256. doi: 10.1016/j.commatsci.2015.05.034. URL https://www.sciencedirect.com/science/article/pii/S0927025615003602. Selected Articles from Phase-field Method 2014 International Seminar.

Hao Long, Lihong Liang, and Yueguang Wei. Failure characterization of solid structures based on an equivalence of cohesive zone model. *International Journal of Solids and Structures*, 163:194–210, 2019. ISSN 0020-7683. doi: 10.1016/j.ijsolstr.2019.01.008. URL https://www.sciencedirect.com/science/article/pii/S0020768319300186.

Oscar Lopez-Pamies, John E. Dolbow, Gilles A. Francfort, and Christopher J. Larsen. Classical variational phase-field models cannot predict fracture nucleation. *Computer Methods in Applied Mechanics and Engineering*, 433:117520, 2025. ISSN 0045-7825. doi: 10.1016/j.cma.2024.117520. URL https://www.sciencedirect.com/science/article/pii/S0045782524007746.

E. Lorentz and S. Andrieux. A variational formulation for nonlocal damage models. *International Journal of Plasticity*, 15(2):119–138, 1999. ISSN 0749-6419. doi: 10.1016/S0749-6419(98)00057-6. URL https://www.sciencedirect.com/science/article/pii/S0749641998000576.

Juan Macías, Albertino Arteiro, Fermin Otero, Pedro Camanho, and Jose Reinoso. Micro-mechanical analysis of composite materials using phase-field models of brittle fracture. *European Journal of Mechanics - A/Solids*, 102:105069, 07 2023. doi: 10.1016/j.euromechsol.2023.105069.

Jean-Jacques Marigo, Corrado Maurini, and Kim Pham. An overview of the modelling of fracture by gradient damage models. *Meccanica*, 51:3107–3128, 2016. doi: 10.1007/s11012-016-0538-4.

T.D. Marusich and M. Ortiz. Modelling and simulation of high-speed machining. *International Journal for Numerical Methods in Engineering*, 38(21):3675 – 3694, 1995. ISSN 00295981. doi: 10.1002/nme.1620382108. URL https://www.scopus.com/inward/record.uri?eid=2-s2.0-0029408920&doi=10.1002%2fnme.1620382108&partnerID=40&md5=505da25d1b2adb902be47fb8488b8ff5. Cited by: 515; All Open Access, Green Open Access.

A.R. Melro, P.P. Camanho, F.M. Andrade Pires, and S.T. Pinho. Micromechanical analysis of polymer composites reinforced by unidirectional fibres: Part i – constitutive modelling. *International Journal of Solids and Structures*, 50(11):1897–1905, 2013a. ISSN 0020-7683. doi: 10.1016/j.ijsolstr.2013.02.009. URL https://www.sciencedirect.com/science/article/pii/S0020768313000747.

A.R. Melro, P.P. Camanho, F.M. Andrade Pires, and S.T. Pinho. Micromechanical analysis of polymer composites reinforced by unidirectional fibres: Part ii – micromechanical analyses. *International Journal of Solids and Structures*, 50(11):1906–1915, 2013b. ISSN 0020-7683. doi: 10.1016/j.ijsolstr.2013.02.007. URL https://www.sciencedirect.com/science/article/pii/S0020768313000723.

A. Mesgarnejad, B. Bourdin, and M.M. Khonsari. Validation simulations for the variational approach to fracture. *Computer Methods in Applied Mechanics and Engineering*, 290:420–437, 2015. ISSN 0045-7825. doi: 10.1016/j.cma.2014.10.052. URL https://www.sciencedirect.com/science/article/pii/S004578251400423X.

C. Miehe, Fabian Welschinger, and M. Hofacker. Thermodynamically consistent phase-field models of fracture: Variational principles and multi-field FE implementations. *International Journal for Numerical Methods in Engineering*, 83:1273 – 1311, 09 2010. doi: 10.1002/nme.2861.

Nicolas Moës, John Dolbow, and Ted Belytschko. A finite element method for crack growth without remeshing. *International Journal for Numerical Methods in Engineering*, 46(1):131–150, 1999. doi: 10.1002/(SICI)1097-0207(19990910)46:1<131::AID-NME726>3.0.CO;2-J. URL https://onlinelibrary.wiley.com/doi/abs/10.1002/%28SICI%291097-0207%2819990910%2946%3A1%3C131%3A%3AAID-NME726%3E3.0.CO%3B2-J.

Gergely Molnár and Etienne Barthel. How glass breaks – damage explains the difference between surface and fracture energies in amorphous silica. *arXiv preprint arXiv:2412.11817*, 12 2024. doi: 10.48550/arXiv.2412.11817. URL https://arxiv.org/abs/2412.11817.

Joern Mosler and Ingo Scheider. A thermodynamically and variationally consistent class of damage-type cohesive models. *Journal of the Mechanics and Physics of Solids*, 59(8):1647–1668, 2011. ISSN 0022-5096. doi: 10.1016/j.jmps.2011.04.012. URL https://www.sciencedirect.com/science/article/pii/S0022509611000743.

Rogelio A. Muñetón-López and Oliver Giraldo-Londoño. A phase-field formulation for cohesive fracture based on the park–paulino–roesler (ppr) cohesive fracture model. *Journal of the Mechanics and Physics of Solids*, 182:105460, 2024. ISSN 0022-5096. doi: 10.1016/j.jmps.2023.105460. URL https://www.sciencedirect.com/science/article/pii/S0022509623002648.

Yousef Navidtehrani, Covadonga Betegón, and Emilio Martínez Pañeda. A unified abaqus implementation of the phase field fracture method using only a user material subroutine. *Materials*, 14:1913, 04 2021. ISSN 1996-1944. doi: 10.3390/ma14081913. URL https://www.mdpi.com/1996-1944/14/8/1913.

Alan Needleman. A continuum model for void nucleation by inclusion debonding. *Journal of Applied Mechanics-transactions of The Asme - J APPL MECH*, 54(3):221–224, 09 1987. doi: 10.1115/1.3173064.

M. Ortiz and A. Pandolfi. Finite-deformation irreversible cohesive elements for three-dimensional crack-propagation analysis. *International Journal for Numerical Methods in Engineering*, 44(9):1267 – 1282, 1999. ISSN 00295981. doi: 10.1002/(SICI)1097-0207(19990330)44:9<1267::AID-NME486>3.0.CO;2-7. URL https://www.scopus.com/

inward/record.uri?eid=2-s2.0-0033097151&doi=10.1002%2f%28SICI%291097-0207%2819990330%2944%3a9%3c1267%3a%3aAID-NME486%3e3.0.CO%3b2-7&partnerID=40&md5=cb9315ef82b0558126d5113f52244bea. Cited by: 1304.

Marco Paggi and Peter Wriggers. Stiffness and strength of hierarchical polycrystalline materials with imperfect interfaces. *Journal of the Mechanics and Physics of Solids*, 60 (4):557 – 572, 2012. ISSN 00225096. doi: 10.1016/j.jmps.2012.01.009. URL https://www.scopus.com/inward/record.uri?eid=2-s2.0-84856719496&doi=10.1016%2fj.jmps.2012.01.009&partnerID=40&md5=0584597f830ac2fe3acb120391709f47. Cited by: 57; All Open Access, Green Open Access.

Kyoungsoo Park and Glaucio Paulino. Computational implementation of the ppr potential-based cohesive model in abaqus: Educational perspective. *Engineering Fracture Mechanics*, 93:239–262, 10 2012. doi: 10.1016/j.engfracmech.2012.02.007.

Kyoungsoo Park and Glaucio H. Paulino. Cohesive zone models: A critical review of traction-separation relationships across fracture surfaces. *Applied Mechanics Reviews*, 64:1002, 11 2011. doi: 10.1115/1.4023110.

Kyoungsoo Park, Glaucio H. Paulino, and Jeffery R. Roesler. A unified potential-based cohesive model of mixed-mode fracture. *Journal of the Mechanics and Physics of Solids*, 57(6):891–908, 2009. ISSN 0022-5096. doi: 10.1016/j.jmps.2008.10.003. URL https://www.sciencedirect.com/science/article/pii/S0022509608001713.

Kim Pham and Jean-Jacques Marigo. From the onset of damage to rupture: construction of responses with damage localization for a general class of gradient damage models. *Continuum Mechanics and Thermodynamics*, 25(2):147–171, March 2013. ISSN 1432-0959. doi: 10.1007/s00161-011-0228-3. URL https://doi.org/10.1007/s00161-011-0228-3.

Kim Pham, Hanen Amor, Jean-Jacques Marigo, and Corrado Maurini. Gradient damage models and their use to approximate brittle fracture. *International Journal of Damage Mechanics*, 20(4):618–652, 2011. doi: 10.1177/1056789510386852. URL https://doi.org/10.1177/1056789510386852.

A. Quintanas-Corominas, J. Reinoso, E. Casoni, A. Turon, and J.A. Mayugo. A phase field approach to simulate intralaminar and translaminar fracture in long fiber composite materials. *Composite Structures*, 220:899–911, 2019. ISSN 0263-8223. doi: 10.1016/j.compstruct.2019.02.007. URL https://www.sciencedirect.com/science/article/pii/S0263822318339928.

E. Ramm. Finite element procedures in engineering analysis, k-j. bathe, prentice-hall, 1982. no. of pages: 735. *International Journal for Numerical and Analytical Methods in Geomechanics*, 7(4):500–500, 1983. doi: 10.1002/nag.1610070412. URL https://onlinelibrary.wiley.com/doi/abs/10.1002/nag.1610070412.

Igor A. Rodrigues Lopes. *Multi-Scale Modelling and Analysis of Multi-Phase Solids Using Second-Order Computational Homogenisation at Finite Strains with Parallel Computing*. PhD thesis, Faculdade de Engenharia da Universidade do Porto, 06 2019.

Igor A. Rodrigues Lopes, Francisco Manuel Andrade Pires, and F. J. P. Reis. A mixed parallel strategy for the solution of coupled multi-scale problems at finite strains. *Computational Mechanics*, 61 (1-2):157–180, 2018. doi: 10.1007/s00466-017-1472-6. URL http://link.springer.com/10.1007/s00466-017-1472-6.

Igor A. Rodrigues Lopes, Bernardo P. Ferreira, and Francisco M. Andrade Pires. On the efficient enforcement of uniform traction and mortar periodic boundary conditions in computational homogenisation. *Computer Methods in Applied Mechanics and Engineering*, 384:113930, 2021. ISSN 0045-7825. doi: 10.1016/j.cma.2021.113930. URL https://www.sciencedirect.com/science/article/pii/S004578252100267X.

Igor A. Rodrigues Lopes, Miguel Vieira de Carvalho, João A. Marques da Silva, Rui P. Cardoso Coelho, and Francisco Manuel Andrade Pires. Second-order homogenisation of crystal plasticity and martensitic transformation. *European Journal of Mechanics - A/Solids*, 102:105104, 2023. ISSN 0997-7538. doi: 10.1016/j.euromechsol.2023.105104. URL https://www.sciencedirect.com/science/article/pii/S0997753823001961.

J.C.J. Schellekens and R. Borst, de. On the numerical integration of interface elements. *International Journal for Numerical Methods in Engineering*, 36(1):43–66, 1993. ISSN 0029-5981. doi: 10.1002/nme.1620360104.

Joachim Schöberl. Netgen, an advancing front 2d/3d-mesh generator based on abstract rules. *Computing and Visualization in Science*, 1:41–52, 1997.

Mohammadmehdi Shahzamanian, Zhutian Xu, and Peidong Wu. Scripts to insert cohesive elements at the interfaces between matrix and precipitates with irregular shapes in representative volume elements in abaqus. *Applied Sciences (Switzerland)*, 13(22), 2023. ISSN 20763417. doi: 10.3390/app132212281. URL https://www.scopus.com/inward/record.uri?eid=2-s2.0-85186125119&doi=10.3390%2fapp132212281&partnerID=40&md5=21537f802aa677d60881f6d1a9469dd1. Cited by: 3; All Open Access, Gold Open Access.

Imad Shakir Abbood, Sief aldeen Odaa, Kamalaldin F. Hasan, and Mohammed A. Jasim. Properties evaluation of fiber reinforced polymers and their constituent materials used in structures – a review. *Materials Today: Proceedings*, 43:1003–1008, 2021. ISSN 2214-7853. doi: 10.1016/j.matpr.2020.07.636. URL https://www.sciencedirect.com/science/article/pii/S2214785320357618. International Conference on Advanced Materials Behavior and Characterization (ICAMBC 2020).

Kyongchan Song, Yingyong Li, and Cheryl Rose. *Continuum Damage Mechanics Models for the Analysis of Progressive Failure in Open-Hole Tension Laminates*. 2011. doi: 10.2514/6.2011-1861. URL https://arc.aiaa.org/doi/abs/10.2514/6.2011-1861.

Ellad B Tadmor, Michael Ortiz, and Rob Phillips. Quasicontinuum analysis of defects in solids. *Philosophical magazine A*, 73(6):1529–1563, 1996. doi: 10.1080/01418619608243000.

A. Turon, C.G. Dávila, P.P. Camanho, and J. Costa. An engineering solution for mesh size effects in the simulation of delamination using cohesive zone models. *Engineering Fracture Mechanics*, 74(10):1665–1682, 2007. ISSN 0013-7944. doi: 10.1016/j.engfracmech.2006.08.025. URL https://www.sciencedirect.com/science/article/pii/S0013794406003808.

Viggo Tvergaard and John W. Hutchinson. The relation between crack growth resistance and fracture process parameters in elastic-plastic solids. *Journal of the Mechanics and Physics of Solids*, 40(6):1377–1397, 1992. ISSN 0022-5096. doi: 10.1016/0022-5096(92)90020-3. URL https://www.sciencedirect.com/science/article/pii/0022509692900203.

Viggo Tvergaard and John W. Hutchinson. The influence of plasticity on mixed mode interface toughness. *Journal of the Mechanics and Physics of Solids*, 41(6):1119–1135, 1993. ISSN 0022-5096. doi: 10.1016/0022-5096(93)90057-M. URL https://www.sciencedirect.com/science/article/pii/002250969390057M.

Clemens Verhoosel, Joris Remmers, and Miguel Gutierrez. A dissipation-based arc-length method for robust simulation of brittle and ductile failure. *International Journal for Numerical Methods in Engineering*, 77:1290 – 1321, 02 2009. doi: 10.1002/nme.2447.

Francesco Vicentini, Camilla Zolesi, Pietro Carrara, Corrado Maurini, and Laura De Lorenzis. On the energy decomposition in variational phase-field models for brittle fracture under multi-axial stress states. *International Journal of Fracture*, 247:291–317, 10 2024. doi: 10.1007/s10704-024-00763-w.

M. Vieira de Carvalho, I.A. Rodrigues Lopes, and F.M. Andrade Pires. A multi-scale formulation for polycrystalline materials accounting for cohesive micro-cracks: Homogenisation of the traction-separation law. *International Journal of Plasticity*, 171:103780, 2023. ISSN 0749-6419. doi: 10.1016/j.ijplas.2023.103780. URL https://www.sciencedirect.com/science/article/pii/S0749641923002644.

Miguel Vieira de Carvalho. *Multi-Scale Modelling of Polycrystalline Materials: Slip Plasticity, Martensitic Transformation and Intergranular Fracture*. PhD thesis, Faculdade de Engenharia da Universidade do Porto, 2023. URL https://hdl.handle.net/10216/149034.

Miguel Vieira de Carvalho, Rui Pedro Cardoso Coelho, and Francisco M. Andrade Pires. On the computational treatment of fully coupled crystal plasticity slip and martensitic transformation constitutive models at finite strains. *International Journal for Numerical Methods in Engineering*, 123(21):5155 – 5200, 2022. ISSN 00295981. doi: 10.1002/nme.7059. URL https://www.scopus.com/inward/record.uri?eid=2-s2.0-85134213252&doi=10.1002%2fnme.7059&partnerID=40&md5=8cf16451b718bed0a45703c3bc973110. Cited by: 11.

José Vila-Chã, Bernardo Ferreira, and Francisco Andrade Pires. An adaptive multi-temperature isokinetic method for the rve generation of particle reinforced heterogeneous materials, part i: Theoretical formulation and computational framework. *Mechanics of Materials*, 163:104069, 09 2021. doi: 10.1016/j.mechmat.2021.104069.

Jian-Ying Wu. A unified phase-field theory for the mechanics of damage and quasi-brittle failure. *Journal of the Mechanics and Physics of Solids*, 103:72–99, 2017. ISSN 0022-5096. doi: 10.1016/j.jmps.2017.03.015. URL https://www.sciencedirect.com/science/article/pii/S0022509616308341.

Jian-Ying Wu. A generalized phase-field cohesive zone model (μPF-CZM) for fracture. *Journal of the Mechanics and Physics of Solids*, 192:105841, 2024. ISSN 0022-5096. doi: 10.1016/j.jmps.2024.105841. URL https://www.sciencedirect.com/science/article/pii/S0022509624003077.

Jian-Ying Wu and Yuli Huang. Comprehensive implementations of phase-field damage models in abaqus. *Theoretical and Applied Fracture Mechanics*, 106:102440, 2020. ISSN 0167-8442. doi: 10.1016/j.tafmec.2019.102440. URL https://www.sciencedirect.com/science/article/pii/S0167844219306871.

Jian-Ying Wu and Vinh Phu Nguyen. A length scale insensitive phase-field damage model for brittle fracture. *Journal of the Mechanics and Physics of Solids*, 119:20–42, 2018. ISSN 0022-5096. doi: 10.1016/j.jmps.2018.06.006. URL https://www.sciencedirect.com/science/article/pii/S0022509618302643.

Jian-Ying Wu, Vinh Phu Nguyen, Chi Thanh Nguyen, Danas Sutula, Sina Sinaie, and Stéphane P.A. Bordas. Chapter one - phase-field modeling of fracture. volume 53 of *Advances in Applied Me-*

*chanics*, pages 1–183. Elsevier, 2020. doi: 10.1016/bs.aams.2019.08.001. URL https://www.sciencedirect.com/science/article/pii/S0065215619300134.

Junjie Xu, Yuli Huang, and Zhe Qu. The high-frequency oscillation in systems with rayleigh damping model. 06 2019. URL https://www.researchgate.net/publication/335950537_The_high-frequency_oscillation_in_systems_with_Rayleigh_damping_model.

Xiaopeng Xu and Alan Needleman. Void nucleation by inclusion debonding in a crystal matrix. *Modelling and Simulation in Materials Science and Engineering*, 1(2):111, 01 1993. doi: 10.1088/0965-0393/1/2/001.

Xiaopeng Xu and Alan Needleman. Numerical simulations of fast crack growth in brittle solids. *Journal of the Mechanics and Physics of Solids*, 42(9):1397–1434, 1994. ISSN 0022-5096. doi: 10.1016/0022-5096(94)90003-5. URL https://www.sciencedirect.com/science/article/pii/0022509694900035.

Lin Ye. Role of matrix resin in delamination onset and growth in composite laminates. *Composites Science and Technology*, 33(4):257 – 277, 1988. ISSN 0266-3538.

O.C. Zienkiewicz and R.L. Taylor. *The Finite Element Method: Its Basis and Fundamentals*. The Finite Element Method. Butterworth-Heinemann, 2013. ISBN 9780080951355. URL https://books.google.pt/books?id=7UL5Ls9hOF8C.